PHOTONEUTRON SPECTROSCOPY WITH MONOCHROMATIC PHOTONS

PHOTONEUTRON SPECTROSCOPY OF NUCLEI NEAR MASS 200 USING MONOCHROMATIC PHOTONS

by

JOHN ELTON McFEE, B.Sc.

A Thesis

Submitted to the School of Graduate Studies

in Partial Fulfilment of the Requirements

for the Degree

Doctor of Philosophy

McMaster University

September 1977

DOCTOR OF PHILOSOPHY
(Physics)

McMASTER UNIVERSITY,
Hamilton, Ontario

TITLE: Photoneutron Spectroscopy of Nuclei Near Mass 200

AUTHOR: John Elton McFee, B.Sc. (University of New Brunswick)

SUPERVISOR: Dr. W.V. Prestwich

NUMBER OF PAGES: xvii, 350

ABSTRACT

A new technique has been developed for the study of photoneutron reactions in the 6 to 11 MeV photon energy range. The technique consists essentially of illuminating a target with a beam of neutron capture gamma rays and observing the neutrons with a high resolution helium-3 detector. Using this method, bismuth, lead, thallium, gold and tantalum targets were studied. Q-values, cross sections and reduced widths were obtained and the systematic variation of the latter two with respect to photon energy, residual excitation energy and neutron energy were investigated. In the case of gold and tantalum, previously undiscovered energy levels in the residual nuclei were determined. Based on these systematics, evidence is presented to suggest that the reactions occur predominantly off resonance and may have substantial direct or semidirect components. Fore-aft neutron emission asymmetry in lead has also been studied and a theoretical model has been derived in order to obtain approximations of the E2/E1 mixing ratios. Direct evidence of parity mixing is presented.

ACKNOWLEDGEMENTS

I would like to express my sincerest gratitude to Dr. Bill Prestwich for the deep enthusiasm and insight that he has shown towards this project. His unique approach to physics has immensely clarified my understanding of the subject and has taught me to look at the field with greater interest, and with a sense of humour. I would also like to thank Dr. Terry Kennett for his many enlightening conversations concerning this project and other topics, and for the assistance that he and Dr. A.F.M. Ishaq provided in the early stages of the work.

Countless others have provided me with the support required to complete a project of this magnitude and I apologize in that I can only acknowledge a few. I thank Dr. Andy Robertson for imparting to me his general knowledge of experimental physics. I thank Mr. E. Beaver, K. Chin and G. Cormick who provided much help with the electronics. I must credit Dr. Evans Hayward with the suggestion to study emission asymmetry in 208-lead. The staff of the McMaster Nuclear Reactor has been cordial and quick to render assistance and the McMaster Computer Centre has made my stay a long and interesting one.

I am particularly grateful to Mrs. Dorothy Matthews both for cheerfully typing this manuscript in an excellent fashion and at the same time, correcting my many mistakes in spelling and grammar. I should also like to thank Mr. Nick Barkman for proofreeding this manuscript.

Finally, I must apologize to Dr. Prestwich for not having determined the volume of a photon, but I assure him that the quest is still underway.

TABLE OF CONTENTS

LIST OF ILLUSTRATIONS

LIST OF ILLUSTRATIONS

LIST OF ILLUSTRATIONS

LIST OF ILLUSTRATIONS

LIST OF ILLUSTRATIONS

LIST OF TABLES

LIST OF TABLES

CHAPTER 1

1.1 Introduction

This thesis contains a description of a unique method for performing high resolution photoneutron spectroscopy. It also contains a discussion of the deduced properties of such reactions for selected targets and photon energies. Before we can deal in depth with these topics, however, we must first answer several important questions, among them:

Of what interest are photoneutron reactions?

What is the current status of research for such reactions?

Does the new method provide unique and useful data?

What are the criteria for target and energy selection?

In this Chapter we shall endeavour to answer these questions and in Chapter 7 we shall expand on the fourth one.

Because of the minute size of a nucleus, it is necessary in order to study its internal detail to probe it with particles whose wavelengths are smaller than the nuclear radius. This inherently, then, involves generating small, high velocity particles, with wavelengths less than 10^{-15}m, allowing them to impinge on the nucleus, and

detecting the outgoing radiation. Practically every conceivable type of particle has been employed; be it hadron or lepton, charged or uncharged. Reactions involving incident and outgoing hadrons are faced with the problem that since the strong interaction is not well understood, the interaction Hamiltonian for certain initial and final state wavefunctions must be approximated by the use of optical model potentials. This has met with reasonable success through the Distorted Wave Born Approximation, but it is only applicable to direct reactions. Charged relativistic leptons, notably electrons, make good projectiles due to the fact that the weak interaction has such a short range, that for essentially all impact parameters the interaction is purely Coulomb in nature. Since the electromagnetic field of the extremely relativistic electron closely resembles that of a photon, the nucleus is essentially excited by absorption and emission of virtual photons. The Hamiltonian is thus well defined and the nuclear properties come into play through the model dependent matrix elements used to determine the nuclear four-current. A large amount of very beautiful

work using inelastic electron scattering has been done in recent years to study giant collective resonances but the procedures have been faced with a few major problems. In order to observe such resonances one must subtract the large continuum arising from the radiative tail of the elastic scattered peak. This increases the uncertainty in shape, cross section and centroid determination and prohibits the determination of off-resonance cross sections. Furthermore, since virtual photons can be longitudinally polarized, E0 collective vibrations can be excited and these have certain properties such as energy centroids and angular distributions, very similar to isoscalar E2 resonances.

Photonuclear reactions are complementary in many ways to hadron and charged lepton induced reactions in that all three can be used to study giant collective resonances (Sa74). They are, in fact, quite similar to inelastic electron scattering experiments, exciting the nucleus via real photons as opposed to virtual photons. The photoabsorption process, being electromagnetic in nature, can be readily described theoretically (Chapter 2),

although modelling the deexcitation process is not so easy if hadrons are emitted. Since real photons cannot excite E0 resonances, there is no confusion over E2-E0 assignments with photoabsorption experiments. Photon energies can be determined with good precision and as we shall soon see, it is possible in certain instances to observe the off-resonance cross section.

For reasons discussed later, this thesis is concerned primarily with heavy nuclei (A~200) and photon energies from 7 to 11 MeV. For such nuclei, with photo-excitation energies in excess of the neutron separation energy, the photoabsorption process consists almost entirely of photoneutron emission. From a theoretical viewpoint, photoneutron reactions can be used to study the single particle nature of nuclei as well as the collective motions of nucleons within the nucleus. On a more applied basis, a detailed knowledge of the absolute values of photoneutron cross sections may be necessary for detailed modelling of secondary production of neutrons in nuclear reactors.

With the above in mind, we turn to a discussion of the methods of studying such reactions.

1.2 Experimental Methods for Photoneutron Reactions

Photoneutron experiments generally differ from one another in two aspects - choice of photon source and choice of detection system. We shall deal with each in turn.

1.2.1 Photon Sources

Photon sources may be subdivided into two distinct groups - photons produced by electromagnetic processes and those produced by nuclear excitation. The former can be generated by bremsstrahlung or positron annihilation in flight and their energy can thus be controlled at will. In practice, however, the best attainable energy spread is of the order of 70 to 100 keV (Ru75) using a bremsstrahlung monochromator. Nuclear gamma rays can be generated continuously in time since they are produced using nuclear reactors and electrostatic particle generators; whereas electromagnetic radiation, being produced by pulsed electron generators, may have duty cycles as low as 10^{-3}.

The early work on the systematics of the giant dipole resonance and certainly the bulk of photonuclear experiments to date have been achieved using bremsstrahlung, produced

when electron beams generated by a synchroton, betatron or linear accelerator are allowed to impinge on a radiator target. The ensuing bremsstrahlung spectrum is a continuous one, decreasing from a maximum at zero energy to zero at the maximum incident electron energy, E_o. In most experiments of this type, the neutron yield is measured as the endpoint energy is increased in small increments. For a given endpoint, the yield, $Y(E_o)$, is given by

$$Y(E_o) = b \int_0^{E_o} I(E_o,E)\ \varepsilon(E)\sigma(E)\ dE \qquad (1.1)$$

where b is a constant dependent on detector characteristics

ε is the detector efficiency

I is the spectral shape

and σ is the total cross section for producing a neutron; that is

$$\sigma = \sigma(\gamma,n) + 2\sigma(\gamma,2n) + \sigma(\gamma,pn) + \ldots\ldots$$

The procedure to obtain the cross section in an interval $E_o - \Delta E$ to E_o is to multiply Y by the inverse matrix of the bremsstrahlung spectrum. This has been discussed by

Spicer (Sp69) and studied in detail by Penfold and Leiss (Pe58). One consequence of such an analysis is that the energy resolution can be no better than ΔE, usually 500 keV. In addition, there are several inherent sources of uncertainty in the determination of the cross section :

1) statistical uncertainties
2) uncertainties in detector efficiency
3) uncertainties in the beam monitor response function
4) uncertainties in neutron multiplicity corrections and
5) for $\Delta E < 0.5$ MeV, uncertainties in the detailed shape of the spectral tip.

This method has the added disadvantage in that the effective photon flux is decreased further than that suggested by the duty cycle alone since only a very small portion of the total spectrum is used for a given endpoint energy, due to the small incremental steps used.

A major breakthrough in the use of bremsstrahlung sources has been the bremsstrahlung monochromator, a device which can be used to select a very small energy

interval out of the continuous photon spectrum. This method, which was initially employed by Axel and co-workers at the University of Illinois, consists of deflecting the electron beam from the circular betatron orbit and allowing it to radiate in a thin external target. The electrons are analysed magnetically and the neutrons produced in the (γ,n) reaction are detected in coincidence with the analysed electrons. The technique is limited by chance coincidence rate and there is a trade-off in that increased energy resolution requires a decrease in photon flux. Practical photon rates, for an energy resolution of about 1%, are approximately a factor of 1000 lower than the standard bremsstrahlung threshold method.

Because roughly only one photon is produced for every 10^{10} electrons, positron annihilation in flight methods require a much higher intensity electron generator, such as a linear accelerator. With this technique, positrons are created in a shower when an electron beam strikes a high Z target, placed either at the end of the accelerator or after the first section. In the former case,

monoenergetic positrons are then selected and focussed using slits and magnets onto an annihilation target, whereas in the latter case the positrons are accelerated to the desired energy and then magnetically removed from the annihilation target. If a positron of energy E annihilates in flight, two photons each of energy mc^2 are isotropically emitted in the centre of mass system. If the positron is furthermore extremely relativistic, photons emitted in the forward hemisphere are confined to a very narrow cone in the laboratory system with a continuous energy distribution that is a maximum at $E + 1/2\ mc^2$. The backward emitted photons travel in a similar cone and have a continuous spectrum peaked at $1/2\ mc^2$ which is similar to the forward spectrum reflected about an energy of $(E + mc^2)/2$. The photon energy is dependent on polar angle but as the positron energy is increased the peaks at either end of the spectrum become sharper and the cone of emission decreases in angle. As an example, for 19 MeV positrons incident on beryllium the full width half maximum (realizing that the peak is asymmetrical) is approximately 250 keV and the full

width quarter maximum is 875 keV. Aside from the energy resolution and problems of low duty cycles associated with annihilation in flight facilities, there are two other problems to be faced. The first is that in targets of practical thickness the photon spectrum is modified by ionization losses and multiple scattering of positrons. Secondly, positrons radiate in the annihilation target, producing bremsstrahlung. This can be decreased to some extent by using a low Z target since σ_π/σ_β varies as Z^{-1}. In practice, however, the bremsstrahlung background must be subtracted by allowing negatons to strike the target and assuming that bremsstrahlung production is the same for them as for positrons.

The two chief means of producing photons by nuclear excitation are proton induced photon emission and neutron capture. The three primary reactions which constitute the former class are the $^{19}F\ (p,\alpha\gamma)\ ^{16}O$, $^{7}Li\ (p,\gamma)\ ^{8}Be$ and $^{3}H\ (p,\gamma)\ ^{4}He$ reactions. The $^{19}F\ (p,\alpha\gamma)$ reaction, which has been used in a resonance fluorescence experiment by Reibeland Mann (Re60), produces three gamma rays at energies of 6.14, 6.92 and 7.12 MeV. Their

relative intensities can be varied by altering the incident proton energy but the 7.12 MeV γ dominates for proton energies near 2 MeV. The energy spread is of the order of 130 keV due to the α particle emission. The ^{7}Li (p,γ) produces 17.6 MeV photons with an energy spread of approximately 12 keV but it has the misfortune of being contaminated by a broad band of photons centered about 14.2 MeV. The ^{3}H (p,γ) reaction produces photons which are continuously variable from 20 MeV upwards by alteration of the incident proton energy. Energy spread is principally limited by the thickness of the gas target, being as low as 40 keV. The reaction has been chiefly used by Stephens et al. (Wo58, Ca60) who have found it to possess one major inconvenience. There is a large neutron background from the $^{3}H(p,n)^{3}He$ reaction once its threshold is attained (E_{γ} = 20.6 MeV).

Neutron capture gamma rays have been used by Donahue and coworkers (We61, Gr64, Hu67) to study (γ,n) reactions, by Ben-David, Moreh and collaborators to study (γ,γ) reactions, and they are the source of photons for the present work. B. Arad (Ar73) has written an excellent

review article on the use of such sources. Neutrons are normally generated by a nuclear reactor and a neutron capture target is either placed in the core or is struck by an external beam. Energy spread is chiefly determined by Doppler broadening due to the thermal motion of the source atoms and may be expressed as

$$\frac{\Delta E}{E_\gamma} = \left(\frac{2kT}{Mc^2}\right)^{1/2} \qquad (1.2)$$

with k Boltzmann's constant, T the temperature in degrees Kelvin, and M the mass of the source nucleus.

The energy spread is typically found to be of the order of a few electron volts. The chief drawback to the method is that the photon energies for a given source material are fixed and although different materials may be used to cover a wide range, energies cannot be continuously varied. The Compton monochromator (Kn66) is one attempt to circumvent this problem. Here the neutron capture photons are Compton scattered from a low Z scatterer and thus by appropriate choice of angle, the photon energy may be varied from $m_o c^2/2$ to the maximum photon energy. Energy spread, mainly determined by angular considerations is

approximately 2.5%

Neutron capture gamma rays as they pertain to the present experiments are discussed further in later sections.

1.2.2 Photoneutron Detection Methods

Detection methods for neutrons whose energy exceeds approximately 1 keV fall into two broad categories - those based on nuclear recoil and those based on neutron induced reactions. Both types include certain detectors that possess some energy resolution - proton recoil chambers, belonging to the first group and ^{3}He detectors to the second. In addition, both types can be used for time of flight analysis in order to gain energy information. The means of detection of photoneutrons is generally tailored to satisfy restrictions imposed by the photon source and the experimental philosophy. Normally until present day, systems with monochromatic or nearly monochromatic photon sources have employed detectors with little or no energy information.

Bremsstrahlung monochromators, because of the requirements for fast coincidence, are forced to utilize

high speed neutron detectors such as organic scintillators. These possess lower efficiency and generally smaller solid angles than do flat response type BF_3 detectors and have no useful energy information. Thus energy information is restricted to a knowledge of the incident photon energy - useful for cross section determinations but of limited use to study branching to excited states of the residual nucleus.

Bremsstrahlung threshold techniques can make use of neutron time of flight. Since 1 MeV neutrons travel at a rate of approximately 70 ns/m, and the best practical electronic timing resolution is of the order of 1 ns, flight paths of several meters length must be used to ensure reasonable energy resolution up to about 3 MeV. Because the flight time detector must then subtend very small solid angles, efficiency is very low and hence the use is restricted to high rate machines. Furthermore, since organic scintillators are often used as flight time detectors, careful corrections must be made to determine the energy dependence of the efficiency if cross sections are to be determined. Bremsstrahlung threshold facilities,

by utilizing time of flight methods, can observe neutron emission by sharp resonances in the target nucleus, but such observations become complicated when the bombarding energy exceeds that of the first excited state. The spectra are generally unravelled by subtracting a background spectrum taken at an energy less than that required to populate the first excited state and then the procedure may be bootstrapped to higher energies.

One consequence of the low detection efficiency of time of flight techniques is that they cannot generally be used with positron annihilation in flight systems. These generally employ high efficiency neutron detectors such as large gadolinium doped liquid scintillators or BF_3 detectors. Because of the inherent lack of neutron energy information, positron annihilation facilities are restricted to a similar set of experiments as are the bremsstrahlung monochromators.

Nuclear excitation photon sources can in certain cases utilize most of the neutron detection techniques described previously. Proton capture facilities may use neutron time of flight if the proton source is pulsed.

but here again detector solid angle is very critical and flight paths must be made long enough to achieve resolution at least equal to the source energy spread.

Because of the continuous nature of neutron capture photons from a nuclear reactor, accompanying neutron detectors used in the previous work of Donahue and associates have been BF_3 detectors surrounded by wax. Since these detectors possess no energy information and a given photon source generally has several discrete energy groups, it becomes a complicated procedure to determine cross sections for different energy photons. This had been done by subtracting neutron rates due to different sources with similar energy photons by assuming a cross section smoothly varying with energy. As discussed in Chapter 2, this assumption may not necessarily be valid.

In recent years developments have been made in the design of high resolution ^3He neutron detectors (Cu69a, Sh72). Such detectors may possess energy resolution as low as 15 keV for thermal neutrons and 27 keV for 1 MeV neutrons with the possibility of a further decrease using pulse risetime techniques. The efficiency may be made

almost as high as the intrinsic efficiency ($\sim 10^{-4}$ for 1 MeV neutrons) since solid angles may be made very large. Thus a beam of continuous high rate neutron capture photons could be combined with a high efficiency, high resolution neutron detector to study photoneutron reactions. This is the method used in this thesis and it is described in section 1.3.

1.2.3 Contrast of Experimental Methods

The basic methods of photoneutron research have been described in the previous two sections and their main features are summarized in Table 1.1. Before describing the method used in this work, we shall briefly contrast the merits, uses and pitfalls of these various techniques.

Electromagnetic sources, as we have seen, have energy resolution generally inferior to the nuclear excitation methods. The only electromagnetic source which can practically accept a high resolution neutron detector is the bremsstrahlung threshold technique. Here the neutron detector is actually used to measure photon energy and the analysis becomes complicated if the photon energy exceeds that required to populate the

first excited state of the residual nucleus. Photon rates generally are also lower than for nuclear excitation sources due primarily to low duty cycles.

Electromagnetic sources have the advantage over nuclear excitation sources in that their energy is continuously variable (the one exception is the $^{3}H(p,\gamma)$ reaction for $E_\gamma > 20$ MeV). Thus e.m. sources are well suited to continuous measurements of photoneutron cross sections as a function of E_γ. Due to the broad resolution such experiments generally average over resonance structure in all but the light or closed shell nuclei with average spacings of the order of 10 keV. An excellent example of such an experiment is the study of ^{208}Pb by Bowman et al. (Bo69). Here it is clear that using bremsstrahlung threshold and time of flight, resonances with an average spacing of 10 keV can be observed. Averaging over resonances may be advantageous, if one desires to study the collective properties of photon interactions, such as the giant resonances. In such a case one must average over the microstructure and in such instances e.m. sources automatically perform this function. Of course, these sources are also amenable to a study of angular distributions of

the photoeffect. One particular disadvantage with such methods is their inability to study the small continuum due to direct and semidirect processes (Chapter 2) between resonances. This is due mainly to chance background in time of flight systems and the broad energy spread of the sources.

All nuclear excitation sources, excepting the $^{3}H(p,\gamma)$ reaction, can only produce certain fixed energies of photons. Among the accelerator induced reactions, only the $^{19}F(p,\alpha\gamma)$ reaction yields photons of low enough energy to study the isoscalar E2 resonance (Chapter 2) in heavy nuclei. The remainder are mainly useful in the study of the giant dipole resonance. The $^{7}Li(p,\gamma)$ reaction has a low enough energy spread to permit observation of neutron groups corresponding to discrete states in the residual nucleus if used with a time of flight system. This would also be feasible with a high resolution ^{3}He detector but such experiments have not yet been done. It would also be possible utilizing the Li reaction, to observe the off resonance cross section for nuclei if their level densities were very low (since the excitation energy is high). All three reactions could be used for angular distribution studies.

The extremely narrow line width of neutron capture photons provides an excellent means for observing off resonance photonuclear interactions. Besides the fact that little data has been obtained concerning off resonance cross sections, they are of interest both in the study of direct and semidirect cross sections and as a means of resolving discrepancies between theory and experiments (Ja74, Bo64). To date, the only available means of studying such processes has been by determining the asymmetry of resonance shapes in time of flight photoneutron experiments or by applying a similar analysis to resonance neutron capture data and then utilizing the theorem of reciprocity. In doing so, approximations must be made such as the neglection of phase factors between the resonance and potential scattering amplitudes, and assumptions concerning resonance-resonance interference must be used.

In conjunction with a high resolution ^{3}He detector, branching to excited states of the residual nucleus can be observed and knowledge can be gained pertaining to the neutron decay process. Q-values, more accurate than from most

experiments, and branching ratios obtained in such a manner may be useful in the interpretation of bremsstrahlung threshold experiments. These partial cross sections for the population of various excited states are in themselves very interesting in that they have not been observed before for narrow photon energy bands and hence it would be interesting to see if trends exist with respect to nuclear mass, photon energy or residual nuclear excitation energy. Alternatively, since one cannot previously deduce whether a given energy capture photon interacts on or off resonance for a particular nucleus, electromagnetic source cross sections may be used to determine this. The latter statement follows from the fact that e.m. sources generally average over many resonances; and thus, if cross sections from (n,γ) sources are much lower than the e.m. cross sections it suggests off resonance interactions. Furthermore, the distribution of neutron intensities to various excited states may be used to study the nature of the reaction as can angular distribution measurements (Chapter 2). Neutron capture gamma rays, having energies in the 6 to 10 MeV range are expected to be useful in the

study of the low lying giant collective resonances such as the isoscalar E2 resonance. The highest energies available from neutron capture on stable isotopes are around 10.8 MeV (^{14}N) but it is possible to produce 8×10^4 year ^{59}Ni by neutron capture on stable ^{58}Ni in a high flux reactor. This isotope emits capture photons of energy 11.387 MeV allowing photoneutron reactions at energies which approach that of the giant dipole resonance in heavy nuclei.

We therefore see that the various methods of undertaking photoneutron experiments each have their own advantages and disadvantages and are in many respects complementary in the nature of the experiments that can be performed, and the data that can be acquired. We now discuss the method used in this thesis.

1.3 Photoneutron Spectroscopy Near Mass 200

1.3.1 Photoneutron Spectroscopy using Monochromatic Photons

As mentioned in the previous section, Donahue and associates have carried out measurements of photoneutron cross sections using monochromatic photons from neutron capture, but with neutron detectors which had no energy information. Our method, which has been previously

reported (Mc75, Mc76) is an extension of this technique making use of the recent Israeli advances in the technology of 3-Helium neutron spectrometers.

The experiments are shown schematically in Fig. 1.1. A monoenergetic photon incident on the target nucleus may bring about photodisintegration as long as the energy exceeds that of the neutron separation energy. The energies available from neutron capture lie between the photoneutron threshold and the centroid of the giant dipole resonance. This, in general, might be near the isoscalar E2 resonance, depending upon the target. Since the photon energy is well defined and the individual neutron groups can be resolved, it becomes possible to observe the decay of the intermediate state via the intensity distribution of the groups corresponding to states in the residual nucleus.

The actual experimental layout is discussed in detail in Chapter 3 and 4 and hence we shall merely outline it here. A photon source material such as nickel or chromium is packed in a holder which in turn is placed in the core of a nuclear reactor. The in-core position

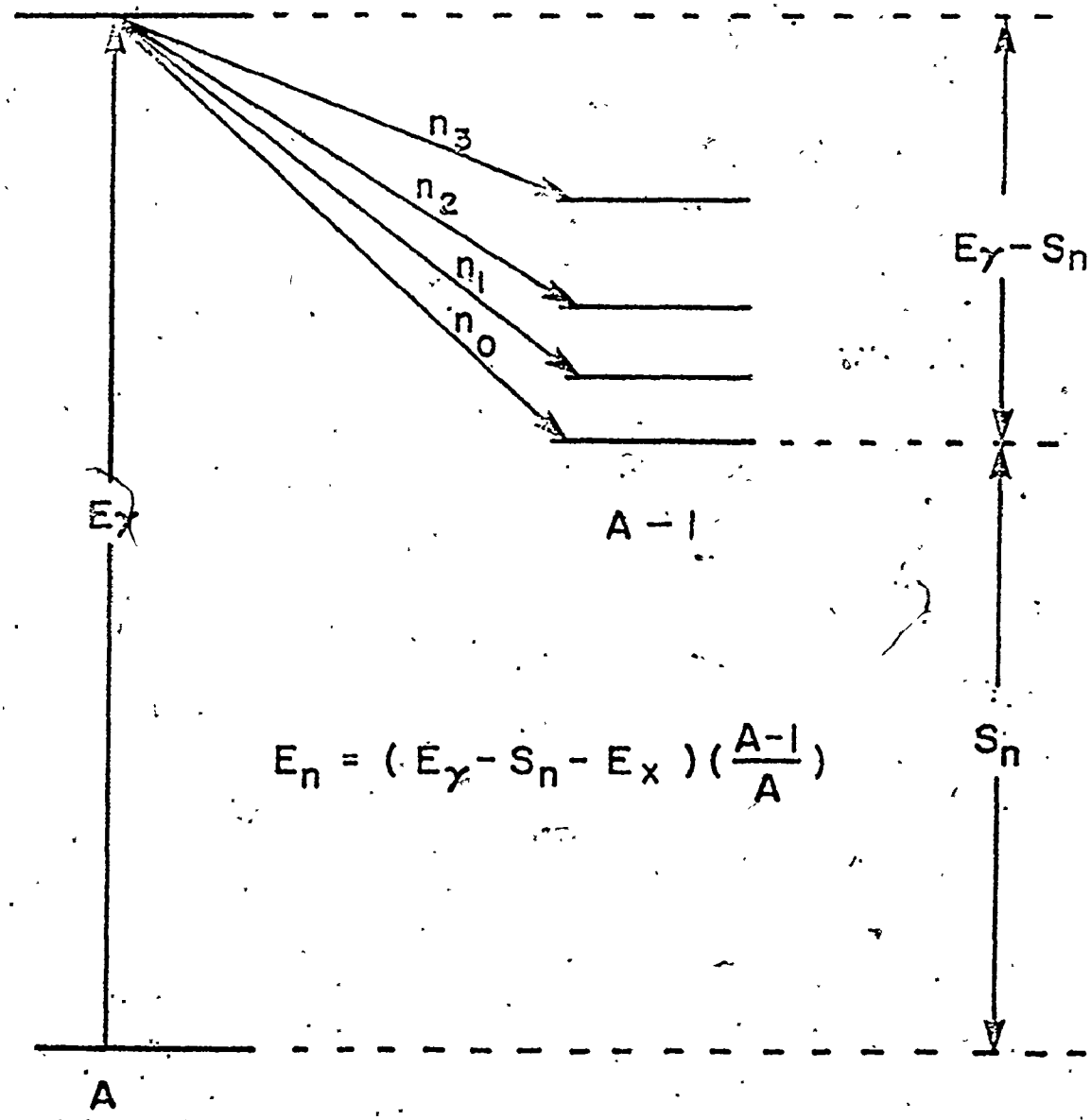

1.1 Schematic representation of a monochromatic photoneutron spectroscopy experiment. E_γ represents the photon energy, A the mass of the target nucleus and A-1 the residual nuclear mass. Neutron groups n_0, n_1 .... branch from the intermediate state leaving the residual nucleus in one of a number of excited states characterized in general by excitation energy, E_x.

differs from Donahue's adjacent source positioning, yielding a higher capture rate. The ensuing capture gamma rays are allowed to impinge on a target and the emitted photoneutrons are detected using a high resolution ^{3}He gridded ionization chamber.

Using this system two types of experiments have been done. Total counting in order to determine cross sections, branching ratios and intensity distributions has been done for targets near mass 200. Furthermore, for natural lead, the fore-aft asymmetry in the neutron emission rate has been studied to observe and model parity mixing during the photon interaction process. The reasons for this are discussed in section 1.3.2.

1.3.2 Photoneutron Reactions Near Mass 200

Our new technique for photoneutron spectroscopy has initially been directed toward a study of the nuclei surrounding the doubly closed shell nucleus 208-Pb. There are several general reasons why such a mass region has been chosen and there are specific reasons for the selection of the specific nuclei.

Lead-208 has proved to be of considerable interest to observers for many years, because of its simple closed shell configuration yet large number of constituent nucleons. It is one of the few nuclei, in this respect, which can be somewhat successfully described in photonuclear theories both in terms of the single particle (shell) models and in terms of the hydrodynamic and other collective models (Sp69). Many photoneutron cross section measurements have been made on this nucleus since the beginning of the last decade in order to try to test the compatibility of such theories and their validity in general (Fu60, Fu62a, Ve70b) but all such measurements have been averaged over a broad photon energy band or have been on-resonance measurements. Off-resonance cross sections in 208-lead are of particular importance since there have been discrepancies between values inferred from (γ,n) and (n,γ) resonance symmetries and considerable controversy over what the value actually is. In a study of the off resonance cross section near the 41 keV resonance, Bowman and associates (Bo69) have made assumptions which suggest a cross section of 12.5 mb, roughly two orders

of magnitude larger than that predicted by the direct capture model, and have suggested that the interaction is semidirect. Jackson, on the other hand, (Ja74) has in his analysis come to the conclusion that the off resonance cross section is approximately 1.3 mb, is in agreement with (n,γ) results and can be explained in terms of contributions from nearby resonances plus a small direct component. This controversy may be capable of being resolved using our method of photoneutron spectrocopy.

There has also been renewed interest in this nucleus in recent years following the discovery of the new giant resonances. (Bu72, Pi74) have found what appear to be giant collective states at 10.2, 10.6 and 11.2 MeV and have claimed they are formed in E0 or E2 interactions. A fourth state has also been observed at 8.85 and it has been argued by Pitthan that this resonance must be E0 since it has not been observed in the photoneutron experiments of Veyssiére et al. (Ve70b). Hayward, on the other hand, suggests (Ha74) that she and Fuller may have observed such a resonance in a previous photoneutron experiment (Fu62a). Since photons of energies 8.512, 8.533 and 8.999 MeV are available using chromium and nickel sources, it was felt that a measurement of the ratio of forward to backward angle

neutron emission would establish if parity mixing were occurring and possibly help confirm if such an E2 resonance were to exist. By using natural lead it might also be possible to determine if parity mixing were occurring significantly in the other lead isotopes as well.

Like ^{208}Pb, the nuclei surrounding it are expected to have low level densities, making the study of off resonance cross sections feasible. Furthermore, they are expected to have reasonably simple nuclear configurations which may yield interesting information. For example, the low lying states of ^{208}Bi may be interpreted as consisting of particle hole multiplets arising from the coupling of a single proton with a neutron hole outside the ^{208}Pb spherical core. If then, one can show that the proton states are populated as strongly as the neutron hole states, one has evidence for a compound or at least a multistep process.

As we move further from the closed shell region we find nuclei that are interesting for different reasons. The two natural thallium isotopes, 203 and 205, are intriguing in that the levels in the residual nuclei are

well known but little has been done concerning (γ,n) reactions. Gold and tantalum are quite the opposite. Photoneutron reactions have been performed several times on both but only 2 levels in ^{180}Ta and 6 levels in ^{196}Au are known. In addition, since the known levels in ^{196}Au have been determined by the decay of the 595 keV spin 12^- state and since the ground states of ^{196}Au and ^{197}Au are 2^- and $3/2^+$ respectively, the centrifugal barrier is expected to strongly inhibit (γ,n) population of many of these high spin intermediate states. It is therefore expected that a (γ,n) spectroscopy study of these nuclei could provide knowledge of the as yet unknown energy levels of the residual nuclei. Tantalum is of added interest in that it is a deformed nucleus (Chapter 2) and thus it is intriguing to see if its off resonance behaviour in photoneutron reactions is similar to that of the more spherical nuclei.

It is interesting to note that for a fixed neutron separation energy there may be a tradeoff between detection efficiency and the total (γ,n) cross section. The former decreases with neutron energy while the latter increases

with photon energy. In stating that the cross section increases we are assuming that we are observing only the averaged cross section and that the reaction takes place on the tail of the giant dipole resonance. At our photon energies and for the nuclei in question the reaction should occur near the isoscalar E2 resonance and on the giant dipole tail which should ensure non-negligible cross sections. Furthermore, if the reactions occur off resonance, as is expected (Chapter 2) the cross section may not appear to increase significantly with energy. Nevertheless, the nuclei studied in this thesis have neutron separation energies less than the energies of the most abundant photons; so that, photoneutron reactions can occur; and yet high enough; such that, the emitted neutrons can be detected with reasonable efficiency.

With all of the above thoughts in mind and with further considerations such as cost and others discussed in Chapter 4, it was decided to carry out an investigation of the isotopes of bismuth, lead, thallium, gold and tantalum, which ranged in mass from 209 to 181.

CHAPTER 2

THEORY OF PHOTONEUTRON REACTIONS

2.1 Giant Collective Resonances and Photoneutron Reactions

2.1.1 Giant Collective Resonances

In the independent particle approximation, a nucleus of mass A exhibits a shell structure with major shells separated by an energy of $\hbar\omega$. In the simplest case it is assumed that the nucleons move in the influence of a three dimensional simple harmonic oscillator potential well of depth $-V_o$ and that the potential is equal to zero at the nuclear radius, R. Then if

$$R = bA^{1/3} \qquad b \text{ a constant} \approx 1.4F \qquad (2.1)$$

it is simple to show classically that

$$\hbar\omega = (\hbar/b)\sqrt{2V_o/m}\,A^{-1/3} \qquad (2.2)$$

$$\approx 6.5\sqrt{V_o}\,A^{-1/3}$$

m is the nucleon mass

V_o in MeV

With a reasonable choice for V_o of 40 MeV (En66) we get

$$\hbar\omega \approx 41\ A^{-1/3} \qquad (2.3)$$

This may be shown quantum mechanically by assuming a square well potential and setting the radial wavefunctions (spherical Bessel functions) to zero at the nuclear radius. If one assumes that the nucleon-nucleon forces are of a two-body nature, then the first step in an excitation process, such as by an incident nucleon, is to excite one target nucleon.

If the target nucleon is excited to the continuum, a one hole state is created in the residual nucleus and the reaction is a pickup or knockout process. The Q-value for such a process is

$$Q \approx -S + \delta - n\hbar\omega \qquad (2.4)$$

with S, the binding energy of the least bound target nucleon

δ, the binding energy of the nucleon to projectile in pickup (= 0 for knockout)

n, the number of the shell containing the hole (topmost filled shell is n=0).

Hole states from the topmost filled shell have excitations in the residual nucleus of the order of 1 MeV and yield discrete peaks for closed shell nuclei. Hole states in the next major shell have residual nuclear excitations of approximately 10 MeV. Such final states are generally particle unstable and hence are broadened such that only the envelope of the group can be seen. This envelope is labelled a giant resonance. Such resonances may have under them a semidirect background (section 2.2) due to 2 hole - 1 particle (2h-1p) states and more complex configurations.

If the target nucleon is instead excited into a bound or quasibound state, it forms a 1p-1h state of the target and the event is inelastic scattering. The lowest excitations consist of transitions and rearrangements within the topmost shell and possess an excitation energy of approximately $0\hbar\omega$. Such excitations cannot occur in a closed shell nucleus where the top major shell is filled. Heavy nuclei, however, possess at least one opposite parity level from the above shell due to spin orbit coupling. Higher energy excitations also occur corresponding to transitions across successive major shells

with excitation energies $L\hbar\omega$ (L, = 1,2...) and parity change $(-)^L$.

Contrary to our simplistic model, actual nuclei have band widths of the same order as the shell spacing and the excited states are furthermore spread by residual interactions. It is possible, however, that the particle hole excitations might exhibit some residual clustering into groups having energy spacings of the order of $\hbar\omega$. In addition, constructive interference of 1p-1h excitations causes the excitation strength to be concentrated in a few levels within each band (Sa74) and such excitations may possess transition strengths many times the single particle estimates. These collective oscillations, commonly called giant collective resonances, tend to increase or decrease in energy with respect to other band members. If we consider the collective motion of protons and neutrons with spin up or down, we label excitations with protons and neutrons oscillating in phase (Fig. 2.1) as isoscalar (T=0). If they oscillate out of phase they are designated isovector (T=1) excitations. Likewise if spin up and spin down nucleons move in phase we have S=0 excitations and

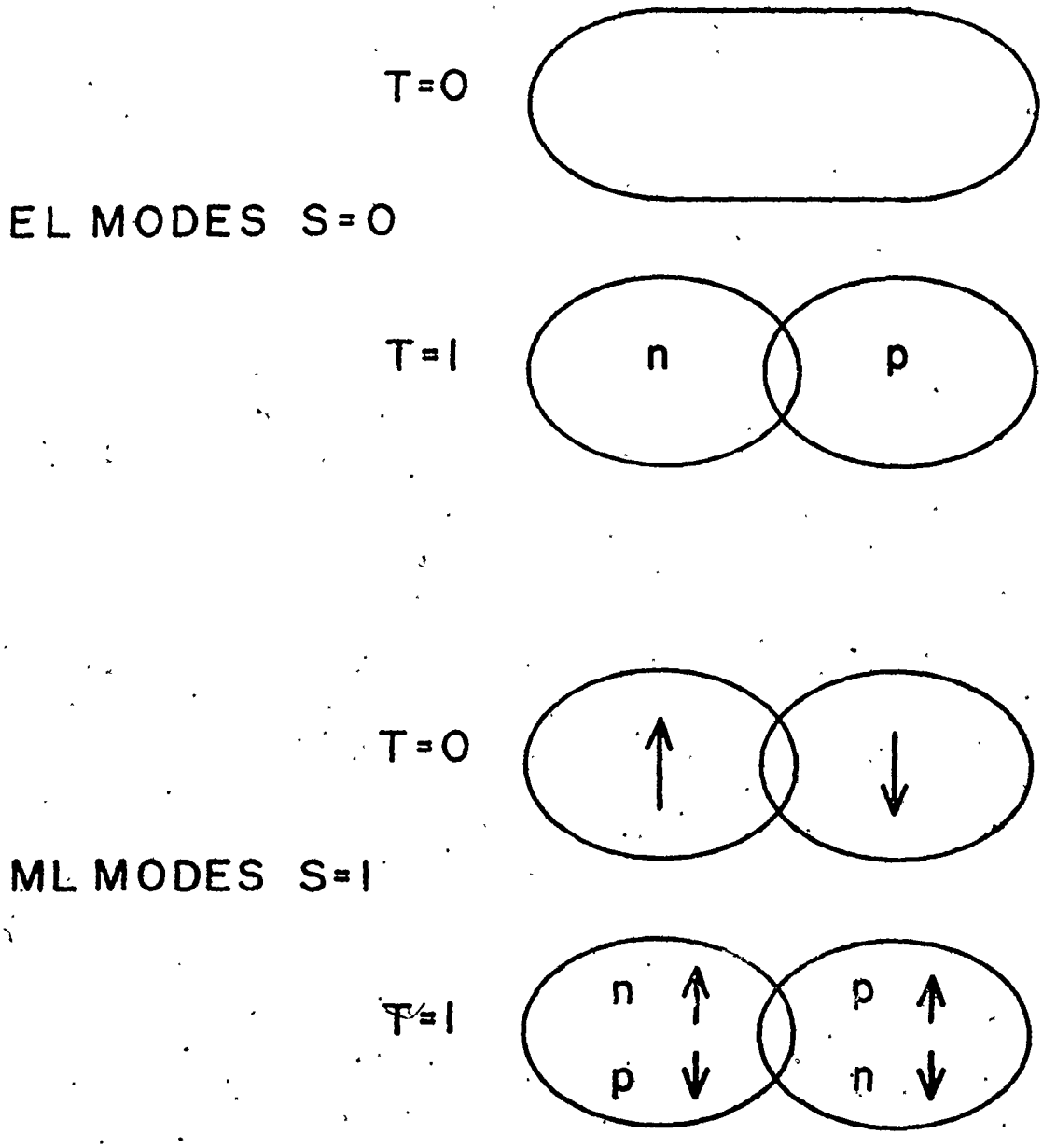

2.1 Fundamental modes of collective oscillation as characterized by a four fluid model. Proton, neutron, spin up and spin down fluids are represented by the symbols p, n, ↑ and ↓ respectively.

if they are out of phase, S=1 excitations. This is sometimes called the four fluid model of collective oscillations. The spin-isospin dependence of the nucleon-nucleon interaction yields attractive potentials and thus S=T=0 excitations decrease in energy while S=1 and T=1 states increase in energy due to the additional force required to separate the proton/neutron and spin up/down fluids. As an example, Table 2.1 shows the positions of the lowest order S=0 giant collective resonances for the simple harmonic oscillator potential with and without the inclusion of the two body residual interactions. Such excitations are shown schematically in Fig. 2.2. The S=0 states will be populated by electric multipole interactions (EL) whereas the S=1 states would be mainly excited by magnetic multipole (ML) radiation (Sa74).

Giant collective resonances possess certain sum rules which may be useful in recognizing such modes of excitation. The multipole operator for a system of A nucleons is given by

$$Q_{LM} = \sum_{i=1}^{A} e_i \, r_i^L Y_L^M(i) \qquad (2.5)$$

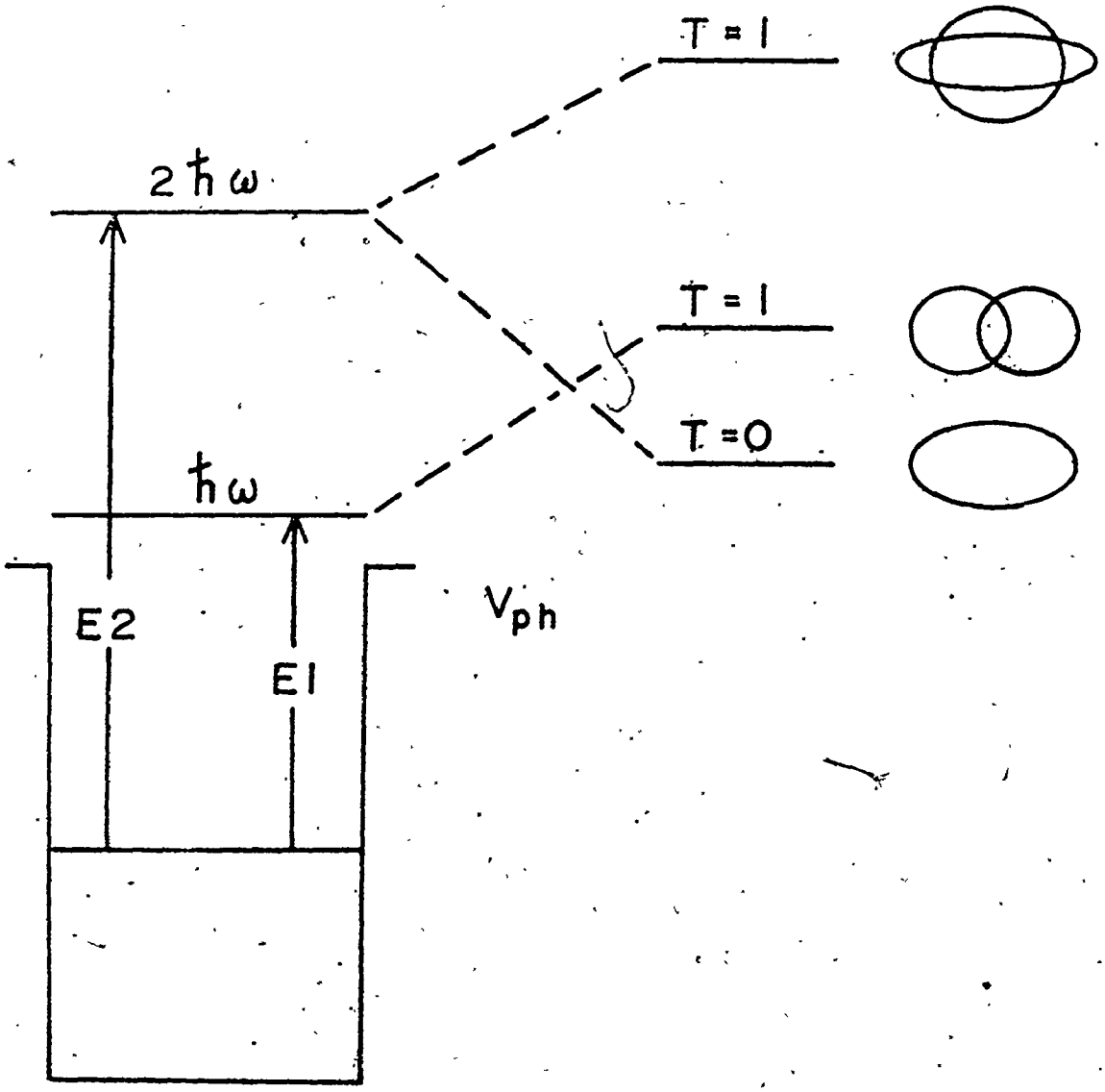

2.2 Lowest order electric multipole excitations. Levels on the left represent simple harmonic oscillator levels, and those on the right are the same levels in which the degeneracy has been removed by turning on the residual particle hole interaction. Shown also are the schematic modes of oscillation.

where e_i is the charge of the i^{th} nucleon (units of proton charge)

and r_i is its radial position.

Now, $$e_i = (1/2 + \tau_i) \tag{2.6}$$

where τ_i is the 3- component of the isospin operator for the i^{th} nucleon.

Thus

$$Q_{LM} = 1/2 \sum_i r_i{}^L Y_L{}^M(i) + \sum_i \tau_i r_i{}^L Y_L{}^M(i) \tag{2.7}$$

$$= Q_{0LM} + Q_{1LM}$$

where the first subscript stands for the mode of isospin excitation, T=0 or 1. The last statement follows from the fact that for the L=1 case we recognize the first term as containing just the center of mass coordinates (equivalent to protons and neutrons moving in phase). The second term then must be the operator for the out of phase fluids. For the simple harmonic oscillator shell model it can be shown that these operators can excite a nucleon by at most $L\hbar\omega$ and that the number of shells must be odd if L is odd and even if L is even. A linear energy

weighted sum rule which is almost model independent, may be defined as :

$$\sum_n (E_n - E_0) |\langle n|Q_{0L0}|0\rangle|^2 = S_L \qquad (2.8)$$

E_n being the energy of the n^{th} excited state. For example, if nucleon-nucleon forces are velocity independent and the target spin is 0, for L>1 we find that S_L is related to the L^{th} radial moment of the mass distribution :

$$S_L = \frac{A\hbar^2}{8\pi m} L(2L+1) \langle r^{2L-2} \rangle \qquad (2.9)$$

Similar expressions occur for L=0 and 1 except that in the former case the sum rule must be modified to conserve volume and in the latter case to fix center of mass. It should be borne in mind, however, that such sum rules may be heavily modified (section 2.2) due to the presence of potentials which do not commute with the multipole operators. Other types of sum rules also exist although these generally tend to be much more model dependent. For photon absorption, however, there exist a series of sum rules of the form :

$$S_N = \int E^N \sigma(E)\, dE$$

for E the excitation energy

N an integer (positive or negative)

$\sigma(E)$ the photon absorption cross section.

As we shall see in section 2.1.2, for absorption of photons of certain multipolarities one finds that values of S_N may be obtained which are model independent or nearly model independent for certain values of N.

Giant collective resonances may manifest themselves through many types of nuclear reactions. They have been observed using charged hadron projectiles, such as in (^{3}He,α) and (p,d) reactions, photons and charged leptons. The latter, usually employed in (e,e') experiments have certain similarities with photonuclear reactions in that electron inelastic scattering transfers virtual photons to the nucleus as opposed to the real photons transferred in a photonuclear reaction.

2.1.2 Photonuclear Reactions

Photonuclear reactions are one means of exciting giant collective resonances and as such have been used

extensively in the exhaustive studies of the E1 isovector or giant dipole resonance (GDR). Many papers and several excellent review articles (Le60, Fu62b, Ha65, Sp69) have been written on the theory of photonuclear reactions and their application to the study of the GDR. This section does not purport to cover the subject thoroughly but rather, it is hoped, will serve as a brief general review of such reactions.

At very low energies the only photon scattering that can occur is Thomson scattering or scattering by the whole nuclear charge. This is an E1 T=0 process and hence just involves motion of the center of mass. At higher energies the internal nuclear coordinates can be disrupted and excitation of nuclear levels can occur. Thus, up to the particle emission threshold of typically 6 to 14 MeV, only elastic and inelastic photon scattering occur and since each successive state can decay to all the states below it, the total width increases with photon energy more rapidly than the E^{2L+1} variation. Above the threshold, widths rapidly broaden and finally overlap. For medium and heavy nuclei this overlapping is thought

to occur in the giant resonance region whereas for light nuclei structure is seen throughout the entire region. The giant resonances (section 2.1.1) may be thought of as single particle resonances and as such are just envelopes of the true microstructure, provided that the levels do not overlap. Thus the photon excitation may reach either one of a series of narrow compound states (section 2.2) whose envelope is the giant resonance or the continuum between states composed of two and multistep direct processes (the np-nh states of section 2.1.1). If the photon energy spread is sufficiently narrow, one's position in energy with respect to the compound states and continuum can be determined by comparing the measured cross section with that of a beam with energy spread greater than the average level spacing.

Although several giant resonances have been confirmed, mainly from inelastic electron scattering data, the most prominent is the giant dipole resonance. It is known to be Lorentzian in shape for medium and heavy nuclei where levels overlap or are closely spaced. For light nuclei it is again an envelope of a fine structure

which, because of the nonstatistical nature of such nuclei, depends much more heavily on individual nuclear properties. In the energy region involved in this work (6 to 12 MeV) the only possible S=0 resonances that could be observed (Table 2.1) are the tail of the GDR ($80A^{-1/3}$ MeV) and the isoscalar E2 resonance (I2R) centered at $60A^{-1/3}$ MeV. These energies correspond to approximately 13.7 and 10.3 MeV respectively for A=200. We have omitted the isoscalar E0 (monopole or "breathing mode" resonance) which although, it possesses an energy equal to that of the I2R, cannot be excited by real photons as in a photonuclear excitation. The monopole resonance may possibly be excited by inelastic electron scattering wherein an extreme relativistic electron transfers virtual photons to the nucleus. Although real photons may only have transverse electric fields, such virtual photons may possess the longtitudinal electric fields which are required to excite the E0 resonance. Evidence for the existence of E0 resonances is discussed in Chapter 1. We must also consider S=1 resonances and in fact for ^{208}Pb there are suspected weak M1 resonances with widths of the

order of 20-50 eV at energies of 7.5 and 8.5 MeV (Bo70b, To72).

For energies in excess of the particle emission thresholds, elastic and inelastic scattering photon cross sections are small and thus the cross section is comprised predominantly of (γ,n) and (γ,p) cross sections. If the photon energy is sufficiently great, $(\gamma,2n)$ and (γ,np) reactions can also occur. In measuring the total photon absorption cross section at such energies for light nuclei both proton and neutron emission must be considered, whereas for heavy nuclei the Coulomb barrier strongly prohibits proton emission, and photoneutron emission essentially exhausts the cross section for nonfissionable materials. In this work, then, we can equate the photon absorption cross section to the photoneutron cross section. Self-conjugate nuclei form a special case in which the proton well is by happenstance adjusted to compensate for the Coulomb barrier, and thus the ratio of (γ,p) to (γ,n) cross sections varies from one to about five (Ha65). At energies much above the GDR resonance energy the main photoabsorption mechanism is the quasideuteron effect in

which a high energy, low momentum photon interacts with a colliding proton-neutron pair possessing high momentum. The pair is ejected from the nucleus with reaction kinematics similar to the deuteron disintegration.

The electromagnetic interaction is one of the best understood interactions and because of this, the process of photon absorption readily lends itself to theoretical description. The nonrelativistic interaction Hamiltonian for the electromagnetic interaction is given by (Fu62b) :

$$H = \sum_i - \frac{e_i}{M_i c} (\vec{P}_i \cdot \vec{A}) + \frac{e_i^2}{2M_i c^2} \vec{A} \cdot \vec{A} \qquad (2.10)$$

where the sum is over all charges; M_i, e_i, $\vec{P}_i$ are the mass, charge and momentum of the i^{th} nucleon; $\vec{A}$ is the vector potential of the e.m. field.

When used to evaluate matrix elements, the approximation is generally made that the photon wavelength is much greater than the nuclear radius and that the character of nucleon and meson currents can be neglected. Thus $\vec{P}_i \cdot \vec{A}$ can be replaced by a term proportional to $\vec{r}_i \cdot \vec{\mu}$ where $\vec{r}_i$ is the coordinate of the i^{th} nucleon and $\vec{\mu}$ is the photon

polarization vector. At high energies this approximation, known as Siegart's theorem, is not valid. For El oscillations the Hamiltonian can be separated into three parts, one describing the center of mass motion (responsible for Thompson scattering), one describing electric dipole oscillations of protons and a similar one for neutrons. Since, when a proton or neutron interacts with a photon the whole nucleus recoils, the motion of the nucleon after the center of mass motion is subtracted is equivalent to that of a nucleon with a different charge. This new charge, called an effective charge, manifests itself as the coefficients in front of the last two terms. For El radiation, we have

$$q_p = ((A-1)/A)^L + (-)^L ((Z-1)/A^L) \qquad (2.11)$$

$$q_n = (-)^L Z/A^L$$

where q_p, q_n are the proton and neutron effective charges (units of e). These effective charges are important in direct reactions where they can be used to deduce the ratio of (γ,particle) cross sections. These will just vary as the

square of the effective charges if all assumptions hold true, which explains why direct E1 photo alpha and photo-deuteron emission is highly suppressed. It should also be noted that for E2 transitions, the signs of the proton and neutron effective charges are the same whereas for E1 transitions they differ. As a consequence, for an absorption process which involves an E1-E2 admixture followed by direct emission, one expects neutron emission to be backward peaked with respect to 0. As we shall see in Chapter 7, this is found to be true for ^{208}Pb near 9 MeV photoexcitation energies.

We have briefly discussed sum rules for giant collective resonances in section 2.1.1 and these too manifest themselves in photoabsorption processes. If we consider incident E1 radiation and consider the nucleus as a simple harmonic oscillator (independent particle approximation) with k^{th} state wavefunction denoted by $|k\rangle$ and with energy relative to the ground state of $\hbar\omega_{k0}$, then we can define an oscillator strength, f_k (Le60, Fu62b, Ha65) :

$$f_k = \frac{2M\omega_{k0}}{\hbar} |\langle k|z|0\rangle|^2 \qquad (2.12)$$

where Z represents the electric dipole operator and M is the nucleon mass. It may then be shown by simple expansion that

$$\sum_k f_k = - \frac{M}{\hbar^2} \langle 0 | [[H,Z],Z] | 0 \rangle \qquad (2.13)$$

If the Hamiltonian commutes with the dipole operator then the sum in 2.13 will be equal to 1. The integrated photon absorption for the k^{th} level is proportional to f_k and thus the total integrated cross section is

$$\int \sigma(E)\,dE = \frac{2\pi^2 e^2 \hbar}{Mc} \sum_k f_k \qquad (2.14)$$

For nuclei, the sum is over all protons and neutrons, and the charge e must be replaced by the appropriate effective charges, yielding :

$$S_o = \int \sigma(E)\,dE = \frac{2\pi^2 e^2 \hbar}{Mc} \quad \frac{NZ}{A} = 0.06 \frac{NZ}{A} \text{ MeV-Barns} \qquad (2.15)$$

It can be shown (Ha65) that velocity dependent and attractive exchange forces tend to increase the dipole sum, whereas terms in the Hamiltonian proportional to $\vec{l}.\vec{l}$ decrease the classical sum rule although in a negligible manner.

In general, a factor, $\beta>1$, is included as a multiplier on the right hand side of equation 2.15 to account for such non-commutivity. The upper limit of the integral is normally taken as the meson production threshold. It is found experimentally that the integrated cross section up to 30 MeV varies roughly linearly from $Z=10$, $\beta\approx0.6$ to $Z=50$, $\beta\approx1.4$ where it becomes constant. In such sums, however, higher order multipoles are often neglected. The deviation at low Z may in addition be in part due to the fact that data is sparse above 30 MeV, (Ha65) and thus a substantial portion of the integrated cross section is not included.

Another nearly model independent sum rule is the inverse quadratic sum for isoscalar E2 radiation given by :

$$S_{-2} = \int \frac{\sigma(E)\,dE}{E^2} = \frac{\pi^2}{3Mc^2}\,\frac{e^2}{\hbar c}\,\frac{Z^2}{A^2}\,\langle r^2\rangle \approx \frac{256}{A^{1/3}}\,Z^2\ \mu b - MeV \qquad (2.16)$$

Besides the independent particle theory of giant collective resonances as discussed in section 2.1.1, there exists for dipole photoabsorption by heavy nuclei another

more physically picturesque model called the hydrodynamic model, originally proposed by Goldhaber and Teller (Go48). The original assumptions were essentially that oscillations are set up in constant density interpenetrating proton and neutron fluids such that the dipole vibration is produced at the extremes of the nucleus regions where proton and neutron fluids do not overlap. The restorative force was expected to be proportional to the surface area, as in the liquid drop model, and thus the giant dipole resonance energy would vary as $A^{-1/6}$. For heavy nuclei, where the model is supposed to be valid, this is not the case and thus a second model was developed by Steinwedel, Jensen and Jensen (St50). This model suggested that the vibrations took place within a rigid boundary and that the two fluids underwent density oscillations. On solution, the resonance energy was found to be $80A^{-1/3}$ in agreement with the isospin corrected shell model predictions and an integrated cross section of 0.86 $(2\pi^2 e^2 \hbar/Mc)$ NZ/A was obtained. There was no provision in the theory for increase of the dipole sum by attractive exchange forces. The model has been extended (Da58) to

describe deformed nuclei, something that the simple spherically symmetric shell model can not do. In this case, two peaks are expected; the lower energy corresponding to the long axis of the ellipsoid and the higher energy corresponding to the short axis ($E_{RES} \alpha\ R^{-1}$). These energies can, in fact, be used to determine the ratio of the axes and hence the quadrupole moment of the nucleus. Of the nuclei studied in the present work, ^{181}Ta exhibits such a deformed nature in (γ,n) cross section experiments (Be75).

As discussed in Chapter 1, the present work consists of a study of photoneutron emission by heavy nuclei ($A \sim 200$) for photon energies in the 7 to 11 MeV range. Neutron spectra from such nuclei may fall into one of two different classes. At high energies a characteristic evaporation spectrum is expected due to the excessive overlap of levels. Such a spectral shape has a form approximated by $E_n \exp(-E_n/T)$ with T being the nuclear temperature and E_n the neutron energy. At low photon energies where the density of intermediate states is lower, one expects discrete spectra of the form $E_\gamma - Q - E_x$, where E_γ is the

photon energy, Q is the photoneutron Q-value and E_x is the excitation energy of the residual nucleus. Since the present work is concerned with nuclei near the doubly magic closed shell nucleus ^{208}Pb, one might expect at such photon energies the latter type of spectrum due to low level densities. As we shall see in Chapter 6, this is indeed the case. Photoneutron emission for such heavy nonfissionable nuclei should, as mentioned previously, almost exhaust the photoabsorption cross section, and thus if the level density of intermediate states is low enough, one can measure the photoabsorption cross section both on and between compound resonances. The probability of an arbitrary photon energy with negligible energy spread yielding an excitation energy which overlaps with a resonance may be given in terms of the gamma ray photoexcitation strength function, $\vec{f}$, described by Bartholomew et al. (Ba73). It is defined as

$$\vec{f}_{XL}(E_\gamma) = \frac{<\Gamma_{XL}>}{E_\gamma^{2L+1}} \cdot \rho_J(E_\gamma) \qquad (2.17)$$

with E_γ, the photon energy

X , the mode of photoexcitation (magnetic or electric)

L , the photon multipolarity

ρ_J, the density of spin J states at energy E_γ

$\langle\Gamma_{XL}\rangle$ the average radiative width for XL photoexcitation from ground state to excitation energy E_γ and is assumed to be independent of J.

Since the probability of overlapping a resonance is just $\langle\Gamma\rangle.\rho_J$ where $\langle\Gamma\rangle$ is the total width and $\langle\Gamma_{XL}\rangle/\langle\Gamma\rangle$ of such interactions will be photoexcitation events, the probability of an on resonance photoexcitation is $f_{XL}.E_\gamma^{2L+1}$.

The gamma ray strength functions near 9 MeV have been determined from (γ,n) cross section experiments for nuclei observed in the present study and are found to yield peak resonance overlap probabilities of approximately 2×10^{-4} to 6×10^{-4} (Ba73). Thus it is reasonable to assume that photoneutron excitations in the present work should occur off resonance. This appears to be a conclusion of the experiments and is discussed in Chapter 7.

2.2 Direct, Semi-Direct and Compound Reactions

Considerable interest has been expressed (Ja74) over whether photoneutron reactions proceed via direct or compound mechanisms and thus we turn to a discussion of

such processes.

A direct reaction is one which proceeds without the formation of a compound nucleus. It proceeds very much faster than compound nuclear formation with correspondingly greater resonance widths and generally is thought to occur on the nuclear surface. It is a one-step process in which the incident particle (photon) interacts directly with the scattered nucleon (neutron) and is expected to be more likely to occur when the excitation energy greatly exceeds the nuclear Fermi energy.

Compound reactions generally occur at much lower excitation energies when, after a few internal collisions, the nucleon energy is sufficiently below that of the Fermi level that the nucleon does not have enough energy to escape. The nucleon "loses memory" of its origin, save that the nucleus has had its energy, angular momentum, and parity altered, and after many rearrangements of nuclear configurations, an exit channel occurs and a decay takes place. Thus, the probability of decay to each exit channel is assumed to be independent of the mode of formation.

This is clearly then, a multistep process.

The justification for using single particle potentials (such as an optical model potential) is the assumption of the existence of a virtual state of the incident particle in the field of the target nucleus. Experimentally, the states are observed to have widths of the order of several MeV and are called single particle resonances. In actual fact if one had sufficiently good resolution for observation of the nuclear cross section, one would see the very narrow compound resonances clustered in groups, the envelope of which would appear to form a resonance with a greater width. These wider resonances in turn would cluster in groups and their envelope would be the single particle resonance. These intermediate width resonances are due to the population of excitation modes with complexity between that of the single particle and compound states. The states are presumed to couple directly to the entrance channel and all channels of compound nuclear formation must proceed through them. They are thus labelled doorway states, and among the simplest examples are the 1p-1h excitations described in section 2.1. Such excitations

will lead to the formation of intermediate states of the form np-nh and these will be considered compound states if n is sufficiently large. Such compound states will be those that are strongly coupled to the doorway state. Only for n equal to 1 can we have direct photoneutron reactions. Reactions which populate intermediate states for which n is small (including the special case of doorway states) are labelled semidirect reactions.

We see then that direct and compound reactions differ sharply in their mechanisms, the former being due to an average nuclear potential and the latter being due to the same average potential followed by the effects of the residual two body interaction (section 2.1.1). Thus it would be expected that the properties of such reactions should differ drastically. One such property is the distribution of reduced widths (section 2.3). For compound nuclear formation, Brink (Br55) has suggested that due to the high density of states at any particular excitation energy, the central limit theorem of statistics would yield a Gaussian distribution of reduced width amplitudes, γ,

with mean zero and variance $\langle\gamma^2\rangle$. For a single channel process the total width is just the sum of one width which is in turn the square of the reduced width amplitude. By transformation of probability distributions we find the distribution for $\gamma^2 = x$ (Fi70)

$$P(x)dx = (2\pi x\langle x\rangle)^{-1/2} \exp(-x/2\langle x\rangle)dx \qquad (2.18)$$

This is expected and has been verified for low energy neutron reduced widths where only one exit channel is available. For multichannel processes the total width is the sum of squares of partial width amplitudes, each of which is sampled from a Gaussian distribution and thus we get :

$$P_\nu(x)dx = \bar{\Gamma}^{-1}(\nu/2)(\nu/2\langle x\rangle)^{\nu/2} \; x^{(\nu-2)/2} e^{-\nu x/2\langle x\rangle} dx \qquad (2.19)$$

where $\bar{\Gamma}$ is the incomplete gamma function and ν is the number of channels or, in statistical terminology, the number of degrees of freedom. This distribution is called a chi-squared distribution for ν degrees of freedom and by computing $P_\nu(x)$ as a function of x for

different values of ν it can be easily shown that the distribution narrows as the number of degrees of freedom increase.

Reactions which proceed via a direct mechanism should be expected to yield reduced widths which are narrowly distributed. The reasons for this are centered around the fact that the process takes place through the influence of an average potential which should be approximately the same for all states. Thus the reduced width amplitudes and hence the reduced widths should be similar. Although the distribution of widths is not expected to be sampled from a χ^2- distribution, if an estimate of the ν is obtained and found to be large, it implies a narrow distribution and hence possible indication of a direct (or semidirect) interaction.

Given a set of reduced widths, it is possible to obtain an estimate of the number of degrees of freedom of the parent distribution (assuming of course that parent distribution is a member of the χ^2- family). Estimates may be obtained by use of the maximum likelihood method (Ke46) but it has been pointed out (Bo63) that finite

sample size could bias the estimate. Recently, Lycklama and associates (Ly69) have derived an estimate of ν with only a slight ($\sim$ 1%) bias and have obtained the result :

$$\langle \nu \rangle = \left(\frac{n-3}{n}\right) \left\langle \frac{2}{\sigma^2} \right\rangle - \frac{2}{n} \qquad (2,20)$$

$$\left\langle \sigma^2 \right\rangle = \frac{1}{n} \sum_i (x_i - \bar{x})^2 \qquad \bar{x} = \frac{1}{n} \sum_i x_i = 1$$

x_i are the reduced widths normalized to a mean of 1

n is the number of reduced widths in the sample.

This is the equation used in the present work to obtain an estimate of ν. It should be pointed out that experimentally determined estimates of the number of degrees of freedom will always be greater than the true value. This is because detection instruments possess finite sensitivity and resolution and hence do not observe small reduced widths. This effect is most pronounced for distributions for which the number of degrees of freedom is small since here the probability is greatest for the occurrence of small widths. Corrections can be made but such corrections and subsequent

estimations are model dependent. If ν is large, of course, the effect of instrument sensitivity will decrease.

It is also possible to determine the nature of the photoneutron reaction by comparison with a reaction whose mechanism is known. Pickup reactions such as (p,d) and (d,t) are known to be direct type reactions and like (γ,n) reactions transfer one neutron to the nucleus. Among the proof that such reactions are direct is the ability to calculate such cross sections by use of the distorted wave Born approximation or DWBA method. This method effectively assumes that the initial wavefunction is the product of an optical model wavefunction describing the incoming proton (or deuteron) and a shell model wavefunction describing the neutron bound to the target nucleus. The final wavefunction is the product of the wavefunction of the outgoing particle in an optical potential multiplied by a wavefunction to describe its internal motion. Experimentally measured neutron pickup reactions may be expressed in the form :

$$\left(\frac{d\sigma}{d\Omega}\right)_{expt} = S \left(\frac{d\sigma}{d\Omega}\right)_{DWBA} \qquad (2.21)$$

with, S the spectroscopic factor (Mo71), and $\left(\frac{d\sigma}{d\Omega}\right)_{DWBA}$, the calculated DWBA cross section for a pickup of neutrons of orbital angular momentum, ℓ_n. Since DWBA calculations are based on the assumption that the neutron is in a single particle state such as a shell model state, the experimental cross section will be less than the calculated one if the assumption is not completely true. Thus S is in effect the fractional contribution of a single particle state or states with a given ℓ_n- value to the total wave-function describing the state of neutron plus residual nucleus. It is then expected that if the neutron reduced widths and spectroscopic factors were highly correlated, then the photoneutron reaction cross section would have a large direct component. Lane has said that alternatively, a positive correlation implies that a single state dominates the two reaction channels, this state being a doorway state (La71).

It should be pointed out that if the intermediate state spin is ambiguous (that is, if two or more possible spins can be populated) then one may find no correlation. This is due to the fact that the same final states may not be accessible for a neutron of given angular momentum from the different states (Bo70a). Thus for targets which are not even-even, although a correlation will indicate a direct or semidirect contribution, a lack of correlation or even an anticorrelation does not rule out such a contribution. A linear correlation coefficient, r, between the spectroscopic factors S_i and the neutron reduced widths, x_i, may be defined as :

$$r = \sum_i (x_i - \bar{x})(S_i - \bar{S}) \Big/ \sqrt{\sum_i (x_i - \bar{x})^2 \sum_i (S_i - \bar{S})^2} \qquad (2.22)$$

with $\bar{x} = \frac{1}{N} \sum_i x_i$ $\qquad$ $\bar{S} = \frac{1}{N} \sum_i S_i$

and N, the number of widths considered.

A value of 1 will be obtained for r for complete correlation, 0 for no correlation and -1 for complete anticorrelation. The experimental correlation coefficient may then be compared with a probability distribution for

a parent population which is completely uncorrelated and a probability, $P_c(r,N)$ can be found for uncorrelated data to have as high or higher a measured coefficient. Obviously, the smaller P_c, the more confident one is that a correlation exists. Derivation of P_c is straightforward and is given in many standard texts on statistical theory (Be69). The result is :

$$P_c(r,N) = 2 \int_{|r|}^{1} P_r(\rho,N-2)\,d\rho$$

$$P_r(r,N-2) = \frac{1}{\sqrt{\pi}} \frac{\Gamma[N-1)/2]}{\Gamma(N/2-1)} (1-r^2)^{(N/2-1)} \qquad (2.23)$$

where P_r is the probability that a random sample of uncorrelated data points from a parent distribution with 0 correlation coefficient, would yield a coefficient between r and r+dr. Although P_c is derived from a normal distribution, not a χ^2, this will yield a conservative estimate for strong correlations and a somewhat liberal estimate for strong anticorrelations.

P_c can be computed by expanding the integral (Be69). This probability, of course, neglects experimental error in the values of the reduced widths, since it assumes that every width is a sample from the true distribution. This will not be a serious problem if uncertainties are

small and similar since on the average such experimental errors will tend to cancel one another.

Thus we are presented with two methods of determining the type of reaction mechanism for each photon energy and nuclear mass. The results of such analysis are discussed in Chapter 7.

2.3 Transmission Coefficients and Penetrabilities

Transmission coefficients and penetrabilities play an important part in the analysis of photoneutron reduced widths and angular distributions, and thus a review of their definitions and properties is useful. Although these quantities may be derived with full mathematical rigour (Pr62) using R-matrix theory, it is perhaps more instructive to utilize a less vigorous descriptive approach.

We consider within an energy interval ΔE a series of randomly spaced neutron resonances of a spin and parity, 0^+, for which the total resonance widths, Γ_K, are much more narrow than the spacing, D_o. Thus the single level Breit-Wigner formula holds. We further neglect potential scattering and write the single level cross section for decay via a neutron of angular momentum ℓ (EM63):

$$\sigma_{c\ell}^{K} = \pi\lambda\!\!\!^{-2}\,(2\ell+1)\,\frac{\Gamma_{n\ell}^{K}\,\Gamma_{K}}{(E-E_o)^2+\Gamma_K^2/4} \qquad (2.24)$$

with $\lambda\!\!\!^{-2}$ = $\hbar^2/2mE$

E_o = the resonance energy

$\Gamma_{n\ell}^{K}$ = the partial neutron width for orbital angular momentum ℓ .

The average of equation 2.24 may readily be obtained if $\Gamma_{n\ell}^{K} << \langle D_o \rangle$, yielding :

$$\langle\sigma_{c\ell}\rangle = \pi\lambda\!\!\!^{-2}(2\ell+1)\;2\pi\frac{\langle\Gamma_{n\ell}\rangle}{\langle D_o\rangle} \qquad (2.25)$$

We can furthermore compare $\langle\sigma_{c\ell}\rangle$ with the cross section for the interaction of a neutron of angular momentum ℓ with an average nuclear potential, derived from partial wave analysis (Ro67):

$$\sigma_{c\ell} = \pi\lambda\!\!\!^{-2}(2\ell+1)\;(1-|N_\ell|^2) \qquad (2.26)$$

where $N_\ell = \exp(2i\phi_\ell)$ is the complex reflection factor and ϕ_ℓ is the phase shift of the partial wave of orbital momentum ℓ.

We define the transmission coefficient for decay of the compound nucleus , by :

$$T_\ell(E) = 2\pi \frac{\langle \Gamma_{n\ell} \rangle}{\langle D_o \rangle} \qquad (2.27)$$

Thus

$$\langle \sigma_{c\ell} \rangle = \pi \lambda^2 (2\ell+1) T_\ell(E) \qquad (2.28)$$

In general for a compound nucleus of spin J, we define the transmission coefficient in the same fashion as 2.27, replacing D_o by D_J. It is assumed, as is normally done (Pr62), that T_ℓ is a function only of ℓ and E and not J.

If in the simplest case, which will serve to illustrate more complex situations, we consider an s-wave neutron in a square potential, and realize that resonances occur when the logarithmic derivative of the wavefunction is approximately zero, then we have :

$ka = (n+1/2)\cdot\pi$ n integer,

k the neutron wave number

a the well radius.

Now $D = k\Delta k\hbar^2/m = (k\hbar/m)(\pi/a)\hbar$. (2.29)

The first term $k\hbar/m$ is the neutron velocity in the well, v, and $2a/v$ is the neutron transit time across the well. Thus we have

$$D\ t_o \approx 2\pi\hbar \qquad (2.30)$$

Also the theory of Fourier transforms relates the level width Γ_c and the lifetime τ by the expression

$$\Gamma_c \tau = \hbar \qquad (2.31)$$

and then we get :

$$\Gamma_c \approx \frac{D}{2\pi}\left(\frac{t_o}{\tau}\right) \qquad (2.32)$$

The last factor is obviously the barrier penetration factor for neutron emission from the well since it is the transit time divided by the lifetime. For neutrons, this factor will be solely dependent on the centrifugal barrier and is a function of $\rho = ka$. This may be extended in general (Pr62) to include neutrons of different orbital

angular momenta and can be expressed analytically. For the lowest few orbital angular momenta, ℓ, the penetration factor or penetrability, P_ℓ, is given by :

$$\begin{aligned} P_0 &= \rho \\ P_1 &= \rho^3/(\rho^2+1) \\ P_2 &= \rho^5/(\rho^4+3\rho^2+9) \\ P_3 &= \rho^7/(\rho^6+6\rho^4+45\rho^2+225) \end{aligned} \tag{2.33}$$

The first term, then, which is equal to $\hbar/\tau_o$, is the frequency with which the nucleon traverses the well or alternatively the frequency at which a nucleon configuration forms which corresponds to an exit channel. We denote the first term, $2S_\ell D$, where $S_0 = \frac{1}{4\pi}$ and call it a strength function and thus we have :

$$\Gamma_c = 2S_\ell D P_\ell \tag{2.34}$$

For an actual nucleus the situation is more complex than that of the single particle neutron resonance and S is no longer merely a constant. Still, for a distribution of resonances of given spin and parity within an energy

interval ΔE, we may separate the average width into a strength function and a penetrability and thus we have :

$$\langle \Gamma_c^J \rangle = 2 S_\ell P_\ell \langle D_J \rangle \qquad (2.35)$$

Insertion in equation 2.27 yields :

$$T_\ell = 4\pi S_\ell P_\ell \qquad (2.36)$$

$$\langle \sigma_{c\ell} \rangle = \pi \lambda^2 (2\ell+1)(4\pi S_\ell P_\ell)$$

Normally it is desirable to remove the penetrability term from an averaged cross section in order to study the strength function, since there is no information about the nucleus (aside from the radius) contained in the former term. When distributions of intensities are studied in order to determine reaction mechanisms, (section 2.2), the penetrability is normally removed from the individual intensities. The quantity remaining is called the reduced width and the average of these for the same spin and parity, yields the strength function. The removal of the penetrability is also done since the distributions of reduced widths are the quantities normally generated by the various theories (Br55, Po56).

As can be seen from equation 2.33, removal of the penetration factor is only possible if the orbital angular momentum is known, and in general for the present experiments this is not the case. In section 6.3 we have assumed, in order to estimate the fractional content of the various ℓ-wave neutrons from a given transition, that the neutron decay channel cross section can be given by equation 2.28. Here, the various values of T_ℓ^j, where j is $\ell \pm 1/2$, are taken from the compilation of Auerbach and Perey (Au62). The two have determined the transmission coefficients using a Perey-Buck optical potential consisting of a real and imaginary part. The real part is the sum of a two body non-local Woods-Saxon term and a local Thomas spin-orbit term, while the imaginary term is a two body non-local derivative Woods-Saxon potential. The parameter set is a universal one derived from a wide range of masses. The authors have then solved the wave equations for the partial wave phase shifts, ϕ_ℓ, and have thus determined the T_ℓ^j by the use of equations 2.26 and 2.28. An example of the coefficients for mass 200 is plotted in Fig. 2.3. In making the assumption that the decay channel cross

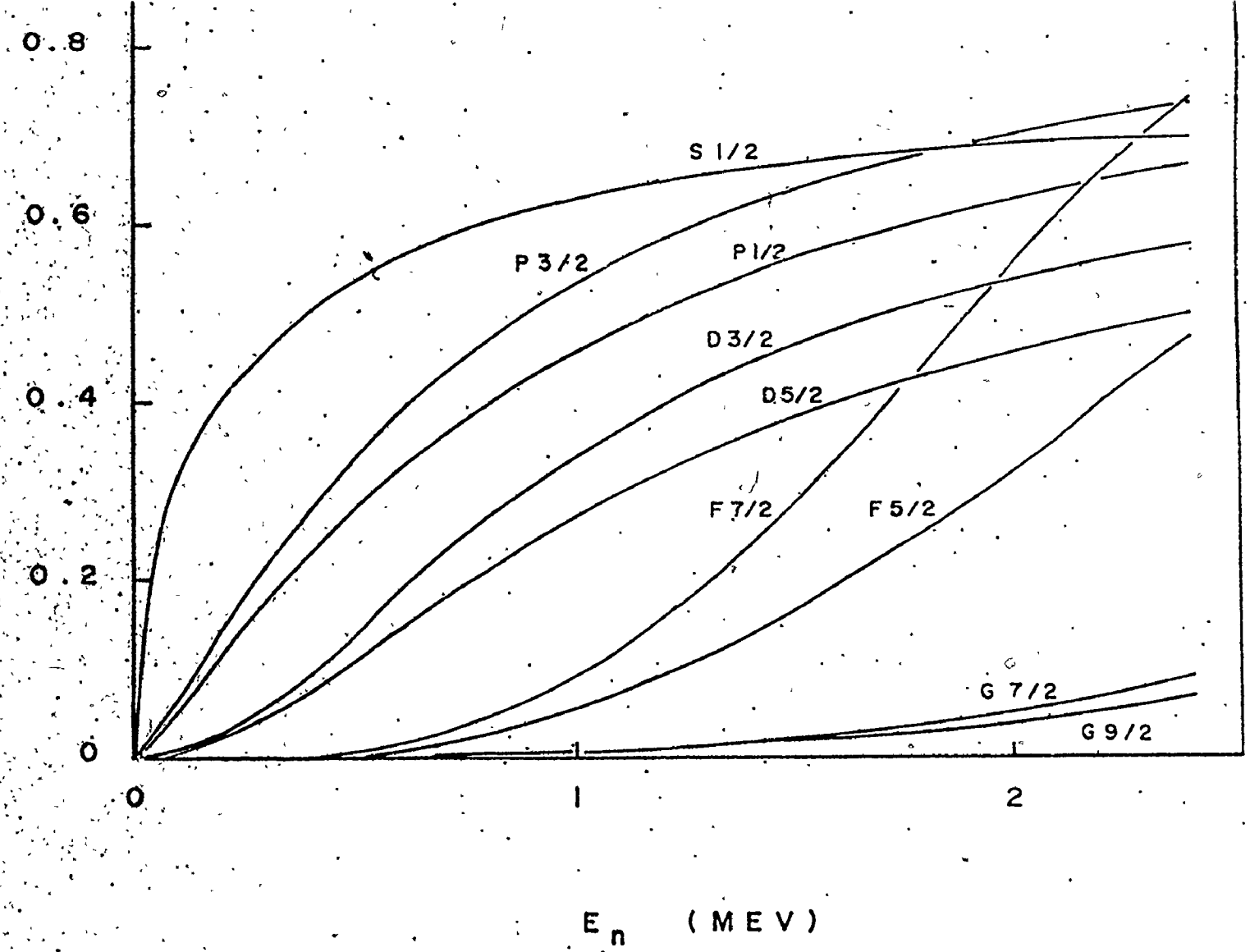

2.3 Transmission coefficients as a function of neutron energy for various ℓ-values. Coefficients are calculated using a Perey-Buck optical potential and are from a tabulation of Auerbach (Au62). A mass of 200 is assumed.

section is governed by the transmission coefficients, we are in effect assuming the decay is determined by the properties of the neutron in the average optical potential of the residual nucleus. Obviously, the local effects due to the specific states excited by the incident photon have been neglected and the assumption will introduce some errors. If the optical potential is a good estimate of the average nuclear potential, though, one should not expect such local fluctuations to alter the average trends of the decay intensities. The same assumptions have been used in section 2.4 in order to estimate the angular distribution coefficients for the (γ,n) differential cross section. As is noted in section 6.4, the assumption appears to have some validity.

2.4 Photoneutron Angular Distributions

In this discussion, which serves as background material for section 6.4, we follow closely the notation of Carr and Baglin (Ca71). If we consider an incident photon, γ, which excites a target nucleus A to a state A* which then decays via emission of a neutron to a specific state in the residual nucleus A-1, then we may

write the reaction as :

$$\gamma + A \rightarrow A^{*} \rightarrow n + (A-1)$$

The reaction seen schematically in figure 1,1 can be described by several quantum numbers :

$j_A^{\pi_A}$ are the spin and parity of the target state

p is the nature of the excitation, p =0 for magnetic, p =1 for electric

L is the multipolarity of the excitation

J^{π} are the spin and parity of the excited state

ℓ is the orbital angular momentum of the neutron

$j=1/2$ is the neutron spin (intrinsic parity is positive)

$j_{A-1}^{\pi_{A-1}}$ is the spin and parity of the residual nucleus.

We define the channel spin S such that :

$$\vec{s} = \vec{j} + \vec{j}_{A-1}$$

where $\vec{J} = \vec{\ell} + \vec{s}$

Each mode of excitation, pL, can in general reach several excited states, each of which can decay through several decay channels determined by ℓ and s, and there may

be many distinct combinations of excitation and decay channel for a given reaction. Each combination, denoted a reaction channel, is specified by a set of values $t = \{p, L, J^{\pi}, \ell, s\}$ and there are several restrictions imposed upon these values :

1) $|j_A - L| \leq J \leq j_A + L$

2) $\pi = \pi_A (-1)^{p+L+1}$

3) $|j_{A-1} - j| \leq s \leq j_{A-1} + j$

4) $|J-s| \leq \ell \leq J+s$

5) ℓ odd if $\pi \neq \pi_{A-1}$; ℓ even if $\pi = \pi_{A-1}$.

We must also note that two reaction channels, t_1 and t_2, can interfere but that different channel spins cannot. With the above in mind and after some manipulation (Ca71) we have for the differential cross section :

$$\frac{d\sigma}{d\Omega} = \lambda^2 [2(2j_A+1)^{-1}(1/4) \sum_{t_1,t_2} (\sum_{\nu} A_{t_1 t_2 \nu} P_{\nu} \mathrm{Cos}\theta)$$

$$\times \mathrm{Re}\{\langle \ell_1 s \beta^1 | R^{J_1}_{\pi_1} | p_1 L_1 \beta \rangle \, ^* \langle \ell_2 s \beta^1 | R^{J_2}_{\pi_2} | p_2 L_2 \beta \rangle\}$$

here

β, β^1 specify the internal structure of the initial and final nuclear states

$2\pi\lambda$ is the center of mass photon wavenumber

$\langle \ell s \beta^1 | R_\pi^J | pL\beta \rangle$ is the reaction matrix and its elements contain all the information about the nuclear structure.

The first summation extends over all possible t_1, t_2 and the values of ν are specified by :

$$\max(|\ell_1-\ell_2|, |L_1-L_2|, |J_1-J_2|) \leq \nu \leq \min(\ell_1+\ell_2, L_1+L_2, J_1+J_2) .$$

The coefficients $A_{t_1 t_2 \nu}$ are functions of the Racah-coefficients and angular momentum terms for a given set of values of t_1, t_2 and ν. They may be calculated directly and have been tabulated (Ca71, Ma74).

It must be realized that for the experiments described in section 5.4 and 6.4, even for the simplest case of $j_A^{\pi A} = 0^+$, $j_{A-1}^{\pi A-1} = 1/2^-$, there are 16 matrix elements with nonvanishing coefficients and thus a minimum 16 independent angles are required to determine them uniquely. Thus, it is necessary to make some simplifying

assumptions in order to achieve our objective of determining the amount of E2/E1 admixing.

Although there are some concentrations of M1 strength in 208- lead at 7.5 and 8.5 MeV photon energy (Bo70b, To72) these are small,having a width of only 20 to 50 eV. Because of this we have neglected any M1 contributions in the angular distribution calculations and thus write E in place of p=1. We have next assumed that a matrix element $\langle \ell s \beta^1 | R^J_\pi | EL\beta \rangle$ may be separated into a photon component $R^J_{\pi p} | EL\beta \rangle$ and a nuclear component $\langle \ell s \beta^1 | R^{J*}_{\pi n}$, where in future the parameters β and β^1 will be suppressed for clarity. It is furthermore assumed that $\langle EL \rangle^2$ is given by :

$$\frac{\langle E2 \rangle^2}{\langle E1 \rangle 2} = \alpha$$

and that $\langle \ell s \rangle^2$ can be related to the transmission coefficient, T^j_ℓ :

$$\langle \ell s \rangle^2 = T_\ell^{\ell \pm 1/2}$$

where the positive or negative sign is determined by the channel spin, s. By expressing $\langle \ell s \rangle^2$ in terms of the

the optical model transmission coefficients, we are effectively stating that the probability of neutron emission from the excited state is governed by the average optical model potential corresponding to the residual nucleus. Obviously this ignores any local structure effects due to the specific excited state but might be expected to yield reasonable average results. Lastly, it is assumed that $\langle \ell S \beta^1 | R_\pi^J | pL\beta \rangle$ is equal to $\langle \ell S \beta^1 | R_\pi^J | pL\beta \rangle^*$ which is equivalent to neglecting the phase factors of the matrix elements. This last assumption is difficult to justify but it might be hoped that if the number of matrix elements is sufficiently large, as is normally the case, the phase effects would on the average cancel one another at least in a manner to yield meaningful qualitative results. As we shall see in section 6.4 this appears to be reasonable since similar values of α are obtained for the same nucleus and photon but for different transitions.

As an example, we shall apply the above assumptions to the case of a photoneutron reaction from a nuclear state of spin parity 0^+ to one of spin parity $1/2^-$ as is shown

schematically in Fig. 2.4. Since L is $\leq$ 2 we must have $\nu \leq 4$. Using the tables of coefficients (Ca71), writing $R(L\ell s)$ for $\langle \ell s \beta^1 | R_\pi^J | EL\beta \rangle$ (J is uniquely determined for fixed L) and $A_\nu = \sum_{t_1 \neq t_2} 2A_{t_1 t_2 \nu} + \sum_{t_1 = t_2} A_{t_1 t_2 \nu}$

we get :

$$A_0 = 3|R(101)|^2 + 3|R(121)|^2 + 5|R(211)|^2 + 5|R(231)|^2$$

$$A_1 = 9.487\, R^*(101)R(211) - 1.342 R^*(121)R(211) + 9.859 R^*(121)R(231)$$

$$A_2 = 4.243\, R^*(101)R(121) - 1.5|R(121)|^2 + 2.5|R(211)|^2 - 1.75 R^*(211)R(231) + 2.857|R(231)|^2$$

$$A_3 = 7.746\, R^*(101)R(231) + 8.05 R^*(121)R(211) - 4.382 R^*(121)R(231)$$

$$A_4 = 13.997\, R^*(211)R(231) - 2.857|R(231)|^2$$

where we have neglected all M1 matrix elements. Now utilizing the remainder of the assumptions namely :

$$|R(121)|^2 = |R(101)|^2\, T_2^{3/2} / T_0^{1/2}$$

$$|R(211)|^2 = |R(101)|^2\, \alpha\, T_1^{3/2} / T_0^{1/2}$$

$$|R(231)|^2 = |R(101)|^2\, \alpha\, T_3^{5/2} / T_0^{1/2}$$

Writing T_{23} for $T_2^{3/2}$, etc.... we obtain :

$$A_0 = 3\ (1+T_{23}/T_{01}) + 5\alpha\ (T_{13}/T_{01}+T_{35}/T_{01})$$

$$A_1 = \pm\sqrt{\alpha}\sqrt{\frac{T_{13}}{T_{01}}}\left(9.487-1.342\sqrt{\frac{T_{23}}{T_{01}}} + 9.859\sqrt{\frac{T_{23}T_{35}}{T_{01}T_{13}}} \right)$$

$$A_2 = 4.243\sqrt{\frac{T_{23}}{T_{01}}} - 1.5\,\frac{T_{23}}{T_{01}} + \alpha\,\frac{T_{13}}{T_{01}}\left(2.5-1.75\sqrt{\frac{T_{35}}{T_{13}}} + 2.857\,\frac{T_{35}}{T_{13}} \right)$$

$$A_3 = \pm\sqrt{\alpha}\sqrt{\frac{T_{13}}{T_{01}}}\left(7.746\sqrt{\frac{T_{35}}{T_{13}}} + 8.05\sqrt{\frac{T_{23}}{T_{01}}} - 4.382\sqrt{\frac{T_{23}}{T_{01}}\,\frac{T_{35}}{T_{13}}} \right)$$

$$A_4 = \alpha\,\frac{T_{13}}{T_{01}}\left(13.997\sqrt{\frac{T_{35}}{T_{13}}} - 2.857\ \frac{T_{35}}{T_{13}} \right)$$

In the above expression we have set $|R(101)|^2 = 1$ with no loss of generality since in calculating the ratios of cross sections at different angles, this term cancels out. The choice of positive and negative signs in the A_1 and A_3 terms arise because the phase factor for E2 and E1 mixing is not known. The asymmetry parameter, A, as defined in section 6.4 for a single angle 0 is given by :

$$A = \frac{I(\pi-\Theta)-I(\Theta)}{I(\pi-\Theta)+I(\Theta)} = \frac{\frac{d\sigma}{d\Omega}(\pi-\Theta) - \frac{d\sigma}{d\Omega}(\Theta)}{\frac{d\sigma}{d\Omega}(\pi-\Theta) + \frac{d\sigma}{d\Omega}(\Theta)} = \frac{\sum_{\nu\,odd} A_\nu\ P_\nu(\cos\Theta)}{\sum_{\nu\,even} A_\nu\ P_\nu(\cos\Theta)}$$

due to symmetry properties of P_ν.

Thus, the choice of sign for $\sqrt{\alpha}$ merely determines whether A is positive or negative. The sign chosen for each case, then, is that corresponding to the sign of A as determined from the data.

In a similar manner we can derive expressions for the 0^+ to $3/2^-$ photoneutron reaction and 0^+ to $5/2^-$ reaction and we shall merely state these results.

$$\underline{J_A^{\pi A} = 0^+ \ , \ J_{A-1}^{\pi A-1} = 3/2^-}$$

$$A_0 = 3\left(1+\frac{T_{23}}{T_{01}} + \frac{T_{25}}{T_{01}}\right) + \frac{5\alpha}{T_{01}}(T_{11}+T_{13}+T_{35}+T_{37})$$

$$A_1 = \sqrt{\alpha}\sqrt{\frac{T_{11}}{T_{01}}}\left(9.487 - 1.342\sqrt{\frac{T_{23}}{T_{01}}} + 9.859\sqrt{\frac{T_{23}T_{35}}{T_{01}T_{11}}} - 4.025\sqrt{\frac{T_{25}T_{13}}{T_{01}T_{11}}} + 8.05\sqrt{\frac{T_{25}T_{37}}{T_{01}T_{11}}}\right)$$

$$A_2 = -1.5\,\frac{T_{23}}{T_{01}} + 4.243\sqrt{\frac{T_{23}}{T_{01}}} + 1.5\,\frac{T_{25}}{T_{01}} + \frac{\alpha}{T_{01}}(2.5\,T_{11}+2.857T_{35}-2.5T_{13} +0.714T_{37}-1.75T_{35}-4.286\sqrt{T_{13}T_{37}})$$

$$A_3 = \sqrt{\alpha}\sqrt{\frac{T_{11}}{T_{01}}}\left(7.746\sqrt{\frac{T_{35}}{T_{11}}} + 8.05\sqrt{\frac{T_{23}}{T_{01}}} + 5.367\sqrt{\frac{T_{25}T_{37}}{T_{01}T_{11}}} - 4.382\sqrt{\frac{T_{23}T_{35}}{T_{01}T_{11}}} - 2.683\sqrt{\frac{T_{25}T_{13}}{T_{01}T_{11}}}\right)$$

$$A_4 = \frac{\alpha}{T_{01}}\left(-2.857T_{35} + 4.286T_{37} + 13.997\sqrt{T_{11}T_{35}} - 5.714\sqrt{T_{13}T_{37}} \right)$$

$$\underline{J_A^{\pi A} = 0^+,\ J_{A-1}^{\pi A-1} = 5/2^-}$$

$$A_0 = 3\left(1 + \frac{T_{25}}{T_{23}} + \frac{T_{49}}{T_{23}}\right) + \frac{5\alpha}{T_{23}}\left(T_{11}+T_{35}+T_{13}+T_{37}+T_{511}\right)$$

$$A_1 = \sqrt{\alpha}\sqrt{\frac{T_{11}}{T_{23}}}\left(8.05\sqrt{\frac{T_{35}}{T_{11}}} + 5.27\sqrt{\frac{T_{25}T_{37}}{T_{23}T_{11}}} - 4.025 - 8.05\sqrt{\frac{T_{25}T_{13}}{T_{23}T_{11}}} + 9.487\sqrt{\frac{T_{49}T_{511}}{T_{23}T_{11}}} - 2.535\sqrt{\frac{T_{49}T_{37}}{T_{23}T_{11}}}\right)$$

$$A_2 = 1.5 - 0.429\frac{T_{25}}{T_{23}} + 4.454\sqrt{\frac{T_{25}T_{49}}{T_{23}}} - 1.071\frac{T_{49}}{T_{23}} + \frac{\alpha}{T_{23}}\left(-2.5T_{11} + 0.714T_{35} + 0.714T_{13} - 1.31T_{37} + 2.381T_{511} - 4.286\sqrt{T_{11}T_{35}} - 5.611\sqrt{T_{13}T_{37}} - 3.182\sqrt{T_{37}T_{511}}\right)$$

$$A_3 = \sqrt{\alpha}\sqrt{\frac{T_{11}}{T_{23}}}\left(5.367\sqrt{\frac{T_{35}}{T_{11}}} - 2.342\sqrt{\frac{T_{25}T_{37}}{T_{23}T_{11}}} - 2.683 + 0.383\sqrt{\frac{T_{25}T_{13}}{T_{23}T_{11}}} + 7.825\sqrt{\frac{T_{25}T_{511}}{T_{23}T_{11}}} - 6.639\sqrt{\frac{T_{49}T_{13}}{T_{23}T_{11}}} - 2.711\sqrt{\frac{T_{49}T_{511}}{T_{23}T_{11}}} + 5.071\sqrt{\frac{T_{49}T_{37}}{T_{23}T_{11}}}\right)$$

$$A_4 = \frac{\alpha}{T_{23}} (4.286T_{35} - 2.857T_{37} - 1.429T_{511} - 11.664\sqrt{T_{13}T_{511}}$$

$$- 5.714\sqrt{T_{11}T_{35}} + 1.247\sqrt{T_{13}T_{37}} + 7.636\sqrt{T_{37}T_{511}}$$

For the experiments of section 6.4, these are all the cross sections we need derive. For the case of $^{207}Pb(\gamma,n)^{206}Pb$, where the initial state has a spin-parity of $1/2^-$ it is not possible to use the above method since there is more than one intermediate state and the relative fractional contributions of them are not known. Thus the present analysis can only be used for even-even targets.

It is now possible, then, for the ^{208}Pb and ^{206}Pb targets, to calculate the asymmetry parameter as a function of α for each resolved neutron group using the optical model transmission coefficients tabulated by Auerbach and Perey (Au62). A typical excitation scheme is shown in figure 2.4 for the ground state to ground state transition ($0^+ \rightarrow 1/2^-$) for an 8999 keV photon incident on a 208-lead target. In section 6.4 values of A calculated from the fore-aft asymmetry experiment are compared with such plots in order to calculate α for different energy photons incident on 208- and 206-lead.

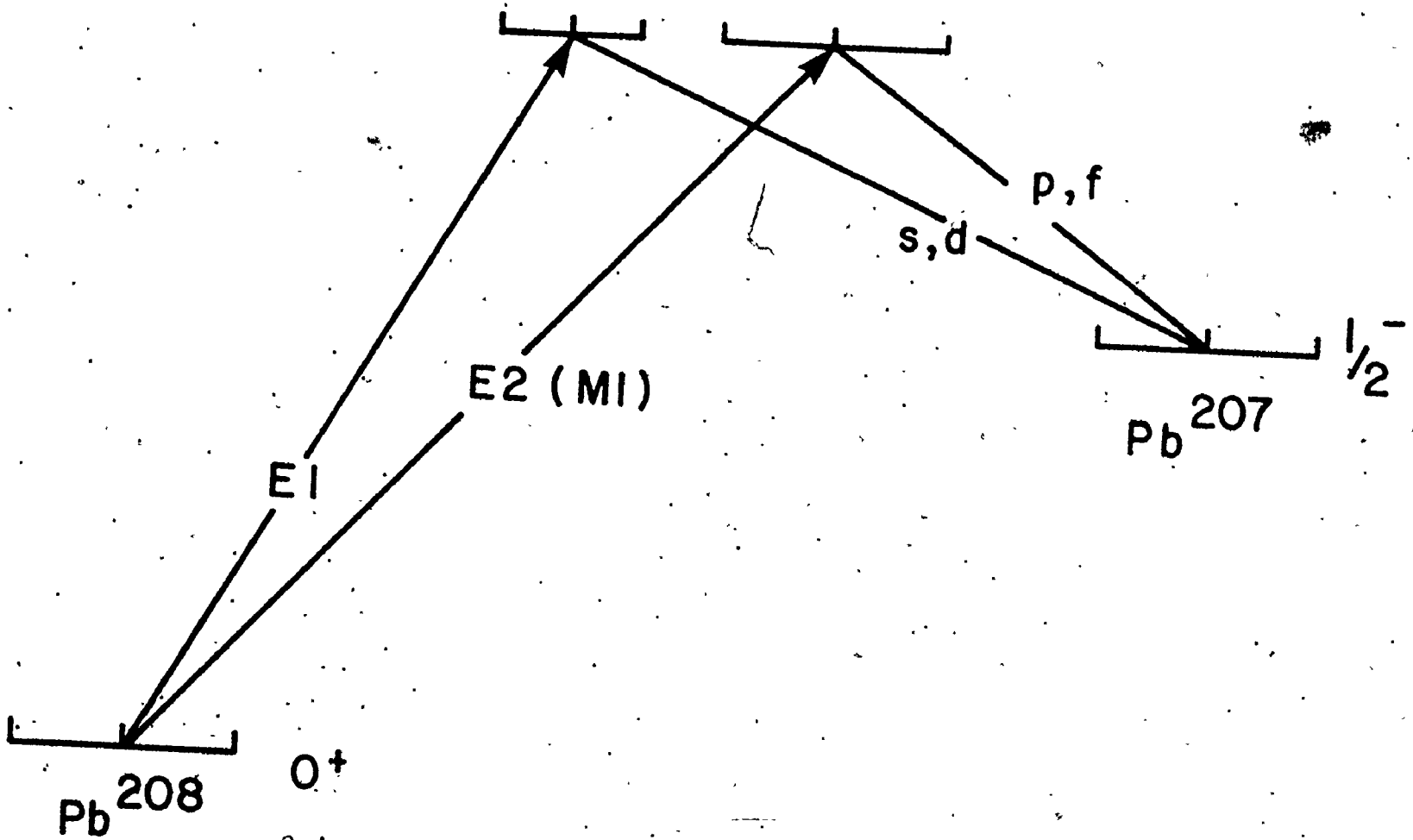

2.4 Schematic representation of parity mixing in photoneutron reaction $^{208}Pb(\gamma,n_o)^{207}Pb$.

CHAPTER 3

THE HELIUM-3 NEUTRON SPECTROMETER

3.1 Introduction

The fast neutron spectrometer which played such an integral part in this work is a very complex instrument. Its use has only become feasible for high resolution work in recent years due to optimization of many design parameters. In order to appreciate these advances in spectrometer design and at the same time be able to devise methods to further improve the detector response, one must thoroughly understand the theory behind such devices.

This chapter, then, is devoted to a discussion of the general theory of helium-3 neutron spectrometers and its application to the particular detector used in this work. Sections are included on the optimization of the response function by pulse risetime selection and on the determination of detector efficiency.

3.2 The Theory of Helium-3 Neutron Spectrometers

This section presents a brief survey of the theory

of ^{3}He ionization chambers and proportional counters particularly as it pertains to the device used in these experiments. Due to the complex nature of the subject, this survey is by no means complete. For a more detailed description of the theory of such devices, the reader should refer to the book by Rossi and Staub (Ro49) and the excellent work by Wilkinson (Wi50) upon which much of this material is based.

3.2.1 The ^{3}He (n,p) T Reaction

As stated in Chapter 1, there are two basic methods which are used to detect neutrons of energies greater than a few keV. The ^{3}He spectrometer, both as an ionization chamber and as a proportional counter, belongs to the second class; the neutron induced reaction spectrometer. This type of detector operates by collecting the charge produced in a material by ionizing particles created in a nuclear reaction of the type:

$$n + A \rightarrow B + C + Q$$

A neutron in interacting with nucleus A produces two nuclei, B and C and an amount of energy Q is released. If

neither of the products are produced in excited states the total energy $Q+E_n$, where E_n is the incident neutron energy, is divided among the kinetic energies of the products. The kinetic energies of the individual products are dependent on the emission angle but their combined energy is always equal to $Q+E_n$. As Batchelor and Morrison (Ba60) point out, there are several conditions which should be fulfilled by the neutron reaction in order to make the spectrometer useful. The cross section should be reasonably large and smoothly varying with energy, since sharp resonances make data analysis very difficult. There should be no appreciable contribution from the reaction itself which leaves the products in excited states or from other reactions with different Q-values, since this greatly complicates the spectra by increasing the number of peaks. If it is desirable to look at low energy neutrons, the Q-value should be positive. The Q-value should also be small, since the energy spread of the measuring device, ΔE_n, usually varies as the total energy deposited in the detector, E_n+Q, whereas energy resolution is defined as $\Delta E_n/E_n$. Finally, the substance should exist in some form that can be incorporated into an energy sensitive detector.

No reaction which has been explored to date possesses all of the above qualities. If one studies the neutron cross section catalogues (Hu58,Go66) it becomes readily apparent, as indeed one might expect, that the first two requirements restrict us to neutron reactions on light nuclei. Boron-10, which is used in BF_3 neutron detectors has a smoothly varying (n,α) cross section but with several broad peaks and a large (2790 keV) Q-value (Go72). Nitrogen-14 would be ideal since it has a smooth flat cross section and a low positive Q-value of 626 keV (Go72) but unfortunately it has a very small cross section of the order of millibarns in the fast neutron range and hence sees only limited use in high flux applications. Lithium-6 has a broad resonance near 2 MeV for the (n,α) reaction and a +4.783 keV Q-value (Wa71). One of the light elements, however, turns out to be almost ideal. It is helium-3. It has a Q-value of 764 keV (Go72) which is low enough to allow good energy resolution for neutrons up to a few MeV. As can be seen in Fig. 3.1 (Ba64), the cross section is smooth and devoid of resonance structure and this in fact is the case from .001 eV up to at least 5 MeV. Also, in the

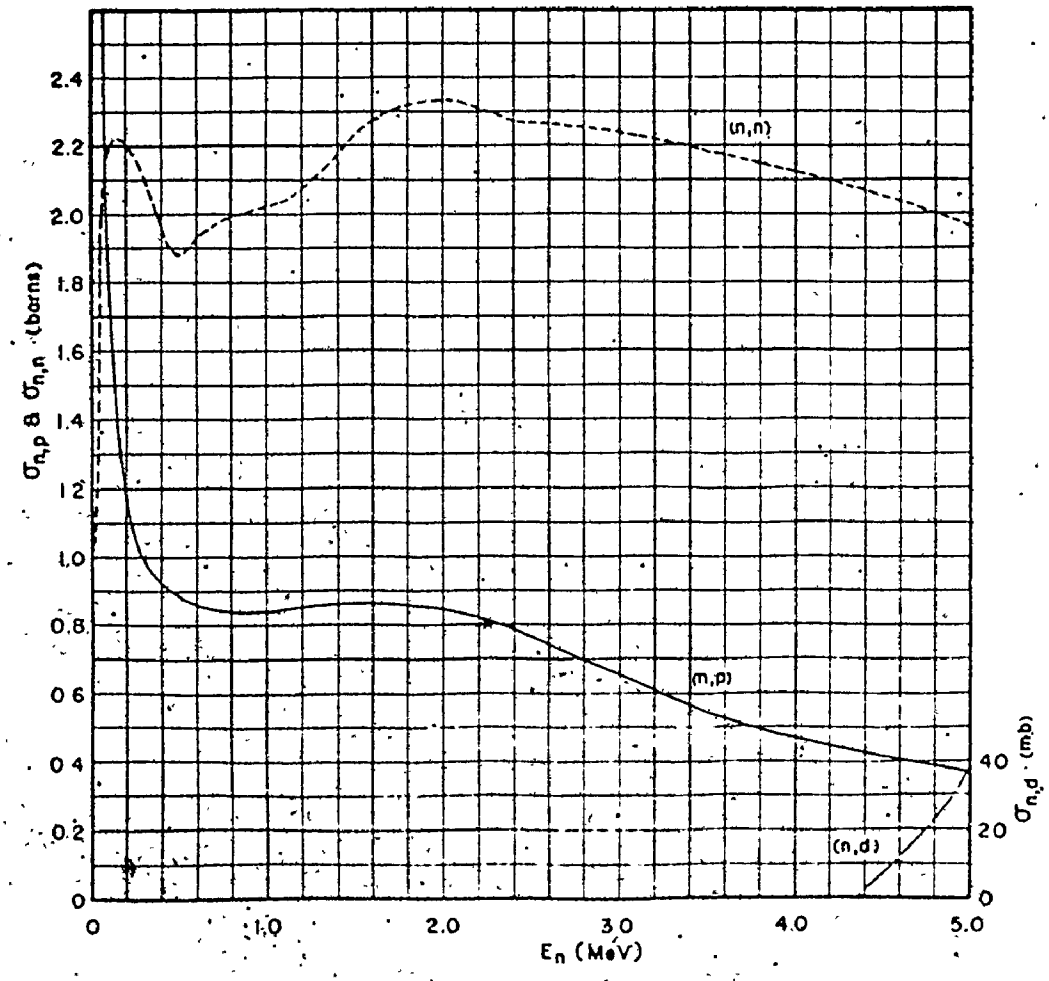

3.1 The neutron cross sections of helium-3. After Batchelor and Parker (Ba64).

range from 0.2 MeV to 3 MeV the cross section does not vary greatly and thus detector efficiency would be roughly constant.

There are three major disadvantages to the reaction , the latter two of which have direct bearing on the present experiment. At approximately 4.4 MeV the $^{3}He(n,d)^{2}H$ reaction begins to compete with the (n,p) cross section but this is of little consequence to the present work due to its high threshold and low values up to 5 MeV. At neutron energies less than 100 keV the (n,p) cross section rises enormously. Since there are usually a reasonable number of thermal and epithermal neutrons produced around any experiment which generates neutrons, this large cross section will create a large peak at the Q-value energy which can, because of finite detector resolution, obscure low energy neutron groups. Thus, special precautions must be taken to minimize such a peak. This will be discussed in a later section. The last disadvantage of ^{3}He, as can be seen in Fig. 3.1 is that there is a comparatively large neutron elastic scattering cross section over the entire useful energy

region. Thus, a monoenergetic neutron can elastically scatter off a ^{3}He nucleus and escape from the detector leaving the ^{3}He nucleus with an energy of anywhere from 0 to 3/4 E_n with equal probability. Provided the neutron energy is less than 1.018 MeV this causes no problems since the maximum recoil energy is less than the Q value for the (n,p) reaction (see Fig. 3.2a). For neutron energies greater than 1.018 MeV, part of the recoil spectrum will appear in the region above zero neutron energy (Fig. 3.2b). If there are a large number of discrete neutron groups the recoil spectra will add to give a rapidly rising continuum under the peaks which may seriously interfere with analysis of the data (Fig. 3.2c). In addition, if the spectrum of neutrons is continuous to begin with, then the analysis becomes very difficult, requiring complicated deconvolution procedures and in many cases is not at all feasible.

In most cases the ^{3}He spectrometer consists of a mixture of ^{3}He, a stopping gas and a gas used to increase ion collection time, placed in a proportional counter or ionization chamber. Although many books and

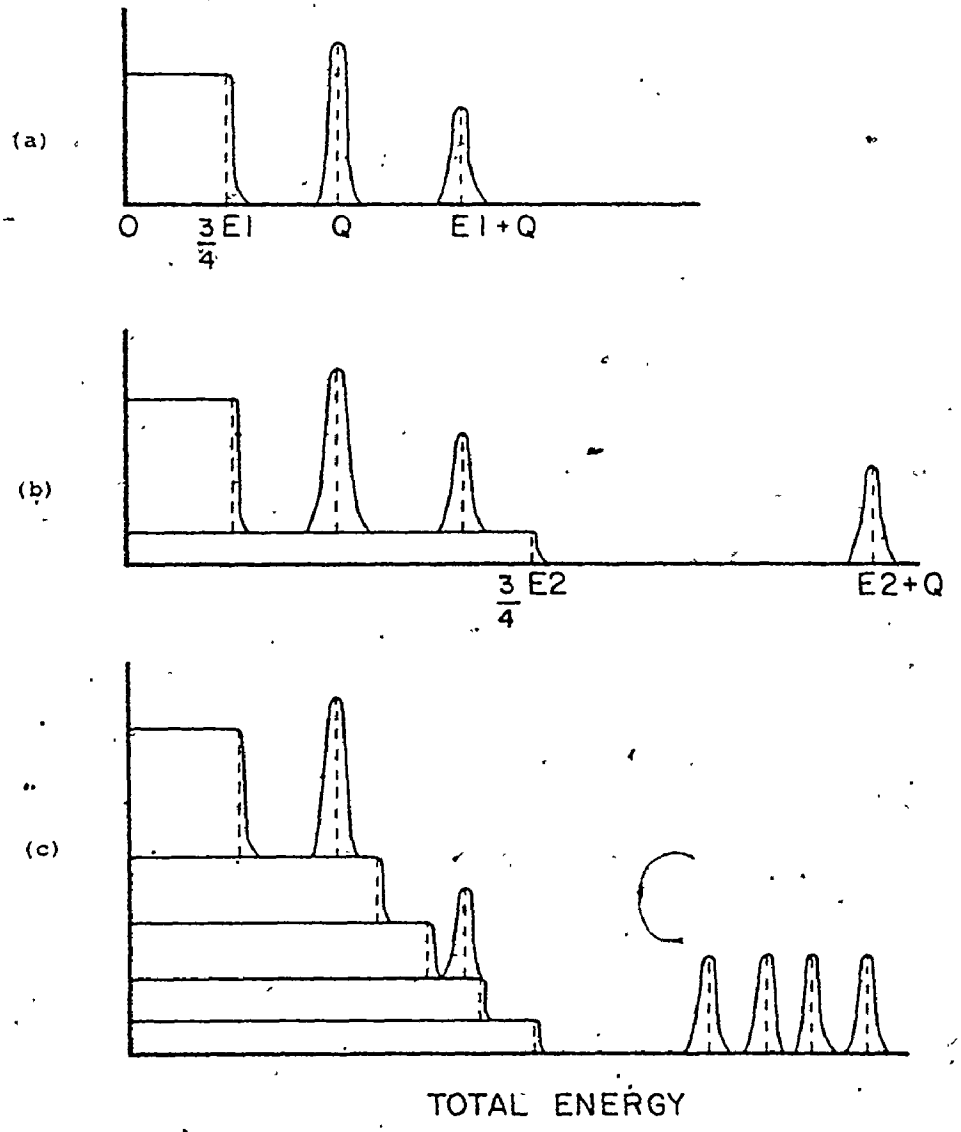

3.2 Effect of helium-3 recoils on detector response. Detector is assumed to be irradiated by monoenergetic neutrons of the same intensity. E_1, E_2 are the incident neutron energies and Q is the $^3He(n,p)$ Q-value. Figure (a) shows the effect of one monoenergetic group with energy less than 4/3 Q. Figure (b) is the same as (a) except that an additional group with energy $E_2 > 4/3\ E_1$ is added. Figure (c) shows the effect of multiple groups. Note that the helium-3 recoil area is roughly constant for each neutron group.

articles have been written on the subject of proportional and ionization counters, it is necessary to briefly describe the fundamentals of such devices.

3.2.2 Classification of Ionization Chambers and Proportional Counters

Ionization chambers and proportional counters belong to a class of detectors which, by employing electrostatic fields to separate positive and negative ions produced in a gas, can be used to detect charged particles. In order to understand the difference between the two devices, let us consider an idealized detector, as shown in Fig. 3.3a which consists of two hollow cylinders with a gas between them, the inner one of which is at a potential $+V_o$ with respect to the outer one. If we assume n electrons are ionized in the gas by an interacting particle, the number of electrons that reach the inner cylinder determines what type of detector it is and this will be, as shown in Fig. 3.3b, a function of the bias voltage, V_o. The region between V_1 and V_2 is the ionization chamber region and is characterized by all n electrons being collected without gas amplification (the production of secondary electrons by acceleration

(a)

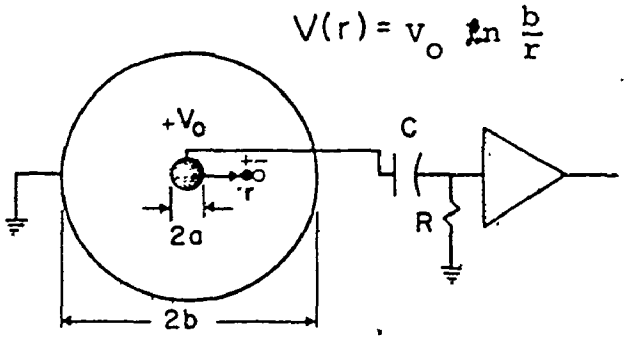

(b)

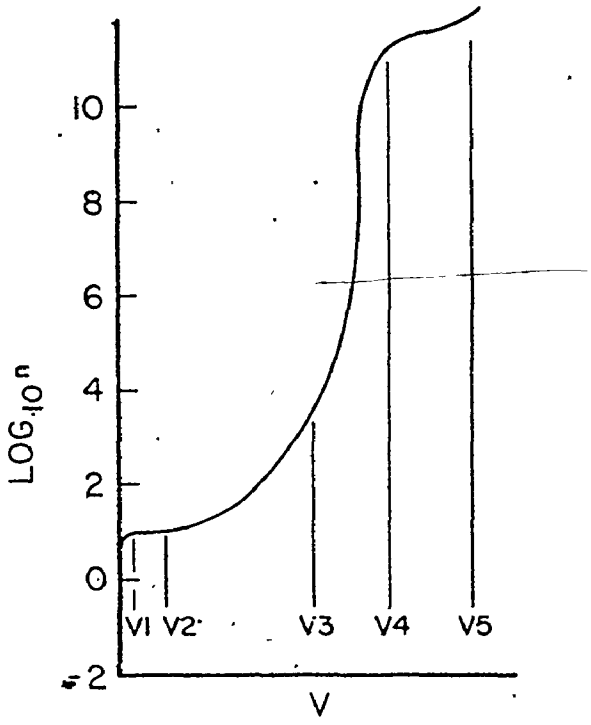

3.3 Cylindrical chambers. Figure (a) illustrates the geometry for a cylindrical chamber. Figure (b) shows the characteristic curve for the log of the number of electrons, n, produced per primary electron, as a function of bias voltage V (equivalent to V_o in Figure a). The various regions are discussed in the text. n is assumed to be 10

of the initial electrons and ions). The region from V_2 to V_3 is the proportional counter region in which each initial electron produces its own electron avalance and gasamplification is independent of the initial number of electrons liberated. This will be the case provided that n is low enough so that the interaction between avalanches is negligible. In the former case, by fulfilling certain conditions, the output pulse can be made proportional to the number of electrons initially liberated. In the latter, this is always the case (Wi50). The other regions such as 0 to V_1, the region of recombination, and V_4 to V_5, the Geiger region, will not be discussed since the output pulses cannot be made proportional to the number of initial electrons. In all cases, cylindrical geometry is not necessary.

3.2.3 Ionization

We look firstly at the process of ionization in gases. As the charged particle which we are trying to detect traverses the detector volume, it produces electrons and heavy positive ions by interactions with its electric field. If the particle comes to rest in

the detector then the range-energy relationship is unimportant since the resulting electrical pulse can be made proportional to the number of ion pairs formed. If the average energy required to produce an ion pair, W, is also constant over the entire track length, then the pulse height can be made accurately proportional to the particle energy. Although W is not constant as a function of electron energy in many gases such as methane and air, it is constant to within 1% for argon (Wi50), which is the stopping gas used in the detector of this experiment. The total number of initial electrons produced has a statistical variation with a variance of N (Co67), N being the mean number of ion pairs formed. For argon with a value for W of about 28.2 eV (Wi50, Co67), a 1 MeV incident particle is seen to have a detection energy spread of 5.3 keV neglecting the Fano factor due to statistical fluctuation, and less than 10 keV due to lack of constancy of W, for a total energy spread due to the ionization process of 11.3 keV. This assumes, as previously stated, that the track length lies entirely in the volume of the detector. If this is not the case,

then a fraction of the total energy is lost and thus the event does not produce a full energy pulse. This is called the wall effect and will be discussed in section 3.4.

3.2.4 Behaviour of Ions in Gases

When ions are formed in a gas they tend to move randomly in the same manner as the gas molecules and with an average agitation energy which is equal to thermal energy. Upon application of an electric field, the agitation energy increases and the ions drift along the field lines. Since heavy ions suffer large energy loss upon collision with gas molecules, their agitation energy becomes only slightly greater than thermal energy and an elementary calculation (Ki68) shows that the average drift velocity, v, is given by

$$|v| = \mu E \qquad \ldots (3.1)$$

$$\mu = q\lambda/mc \qquad \ldots (3.2)$$

and for an ideal gas

$$\lambda = kT/\sqrt{2}\sigma P \qquad \text{(Re65)} \qquad \ldots (3.3)$$

where

μ is the ion mobility

E is the electric field strength

P is the gas pressure in atmospheres

T is the gas temperature

λ is the mean free path of the ion

c is the average agitation velocity

q is the ion charge

m is the ion mass

σ is the collision cross section

k is Boltzmann's constant

and thus $|v| = (qkT/\sqrt{2}mc\sigma)E/P$ ... (3.4)

The above equations implicitly assume that the ions collide elastically with the gas molecules and lose appreciable energy during each collision and are thus thermalized after a few collisions. The latter is not the case for electrons because of their low mass and hence low energy loss per collision. Thus the mean agitation energy for electrons is considerably greater than thermal energy and its ratio relative to $3/2kT$ is usually denoted η. It is due to the high agitation energies and the onset of inelastic collisions at higher field strengths that the electron mobility is a

complicated function of E/P. The drift velocities for electrons are, however, of the order of 100 to 1000 times faster than those of heavy positive and negative ions and therefore in the design of a detector with a fast response, it is necessary to ensure that the electrons do not become attached to neutral molecules, forming heavy negative ions. The molecules which most readily attach themselves to electrons are the electronegative gases such as oxygen, the halogens and water vapour and great care should be taken to eliminate them from the detector since even a few parts per million of such gases can greatly affect the detector response.

Sometimes, however, impurities in a gas can actually improve the electron mobility as is the case for an argon-polyatomic gas mixture. For example, the mobility of electrons in argon can be increased by roughly a factor of ten merely by adding five to ten percent of CO_2 to it. This occurs for two reasons. In the first place, many low lying vibrational and rotational states in the polyatomic gas cause η and hence c of equation 3.2 to decrease by allowing inelastic

collisions. Secondly, in the case of argon, the collision cross section drops sharply as a function of electron energy and thus λ increases (Ramsauer effect). It is interesting to note that λ becomes so large that the electron mobility in the A-CO_2 mixture is just slightly smaller than that in the same partial pressure of CO_2 alone.

3.2.5 Ionization Chambers

Ionization chambers fall into two major classifications - current chambers and pulse chambers. If sufficiently high ion production rates are obtainable, the current in the detector can be directly measured and will be proportioned to the intensity incident upon the detector. Such devices, called current chambers, require much higher fluxes than are found in photoneutron experiments and hence won't be considered any further.

Pulse ionization detectors operate on the principle of detecting single events by inducing an electrical pulse in the chamber. The simplest such detector is the parallel plate chamber as illustrated in Fig. 3.4a. If an ion-electron pair are produced at a distance x_o

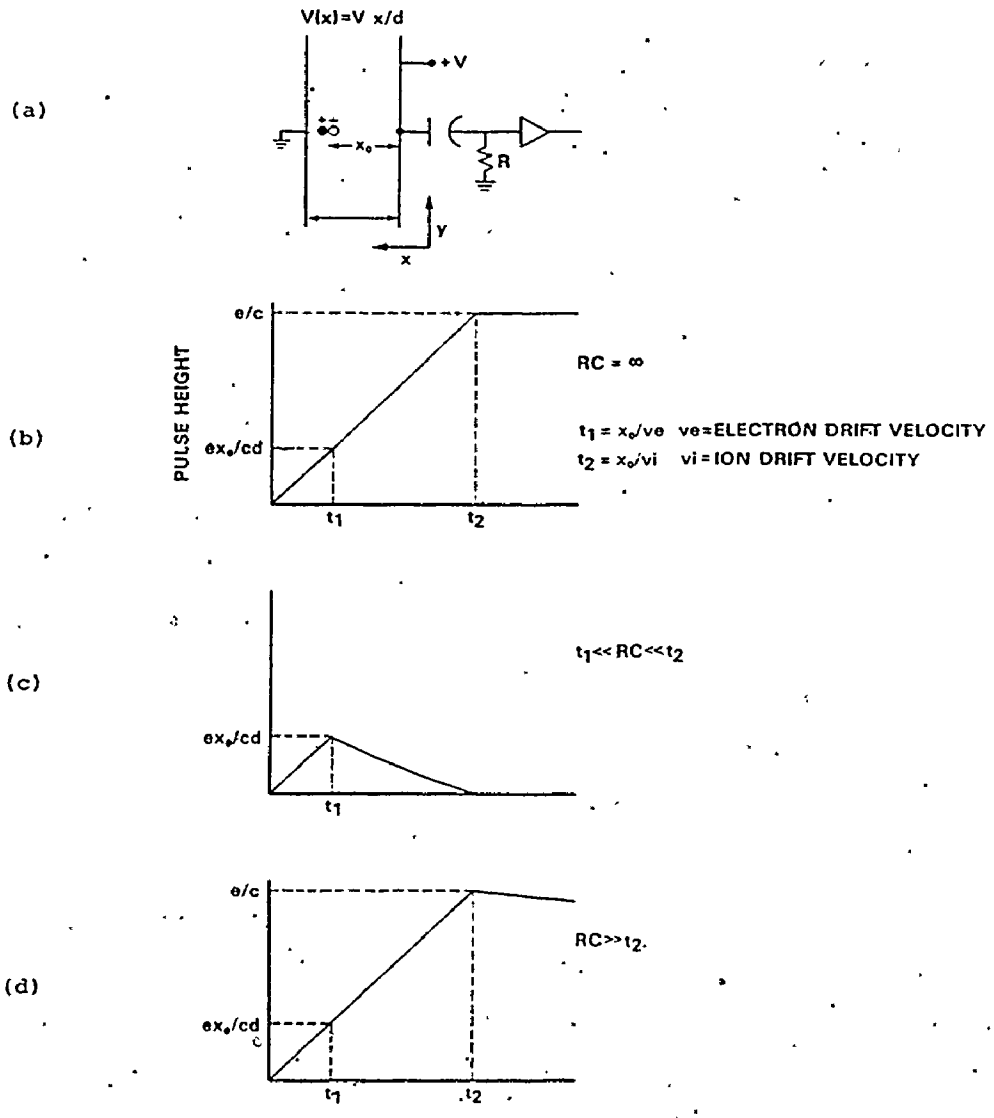

3.4 Systematics of a parallel plate ionization chamber. Figure (a) illustrates the geometry. Figure (b) shows the pulse height as a function of time for infinite time constants, where C is the combined capacitance of chamber and series capacitance. Figure (c) depicts the same graph when RC is much greater than the electron collection time, t_1, but much less than the ion collection time, t_2. Figure (d) shows the same thing except that RC >> t_2.

from the collector plate, each will induce a charge and hence a voltage on the collector and a charge of equal magnitude but opposite sign on the cathode. The magnitude of the charge induction can be calculated by energy perturbation (Wi50, Ni74) or, in a more sophisticated manner, by the use of Green's electrostatic theorem (Wi50), but the end result states that the charge induced on a given electrode is proportional to the potential difference between the point at which the inducing charge exists and the other electrode. Thus, for the parallel plate chamber, since $V(x)=V_o x/d$, a charge q at position x induces a charge $q(1-\frac{x}{d})$ at the collector. Now the total voltage, V, induced on the collector is given by

$$V(t) = \frac{1}{C}(q_-(t)+q_+(t)) \qquad \ldots \qquad (3.5)$$

where q_- is the charge induced by the electron

q_+ is the charge induced by the positive ion

and C is the chamber capacitance.

During the time required for the electron to drift to the collector, t_1, the positive ion moves very little, since its mobility is several hundred times less than

that of the electron and hence, if v is the electron drift velocity:

$$x_o - x = vt \qquad \ldots \qquad (3.6)$$

$$v(t) = \frac{e}{C}\left(-\left(1 - \frac{x}{d}\right) + \left(1 - \frac{x_o}{d}\right)\right) = -\frac{e}{C}\frac{vt}{d} \qquad \ldots \qquad (3.7)$$

The pulse thus rises linearly, as shown in Fig. 3.4b, until $t=t_1$ at which time $V = -\frac{e}{C}\frac{x_o}{d}$. After this point the pulse continues to rise slowly until $t=t_2$ at which time $V = -e/C$. It can be seen, therefore, that in order for the pulse height to be proportional to the number of ion pairs we must make the total time constant, RC, of the amplifier plus chamber long with respect to t_2, the positive ion transit time, which may be of the order of milliseconds. A detector operating in such a fashion is called a slow chamber and has many disadvantages, such as the inability to do fast counting, pulse pile up and microphonics. It is almost never used. Instead, if the clipping time is short with respect to t_2 but long with respect to t_1, all the electron pulse will be detected but no positive

ion contribution will occur due to their small displacement during this time and their slow motion. The inherent problem in this type of chamber, called a fast chamber, is that the maximum pulse height is a function of ion formation position; in fact, it is linear in the case of a parallel plate chamber.

There are two solutions to the problem of position dependence of pulse height. It will soon be seen that the detector in this experiment employs both such methods.

The first method is the use of a cylindrical chamber (Fig. 3.3a) instead of the parallel plate design. Following the same analysis that was used for the parallel plate chamber it is found that for an ion pair formed at a radius, r, from the center of a detector with anode radius a and collector radius b, the pulse shape is as shown in Fig. 3.5 and the maximum pulse height is given by

$$V = \frac{e}{C} \frac{\ell n\ r/a}{\ell n\ b/a} \qquad (3.8)$$

It can be seen that for $a \ll r < b$ which is usually true for

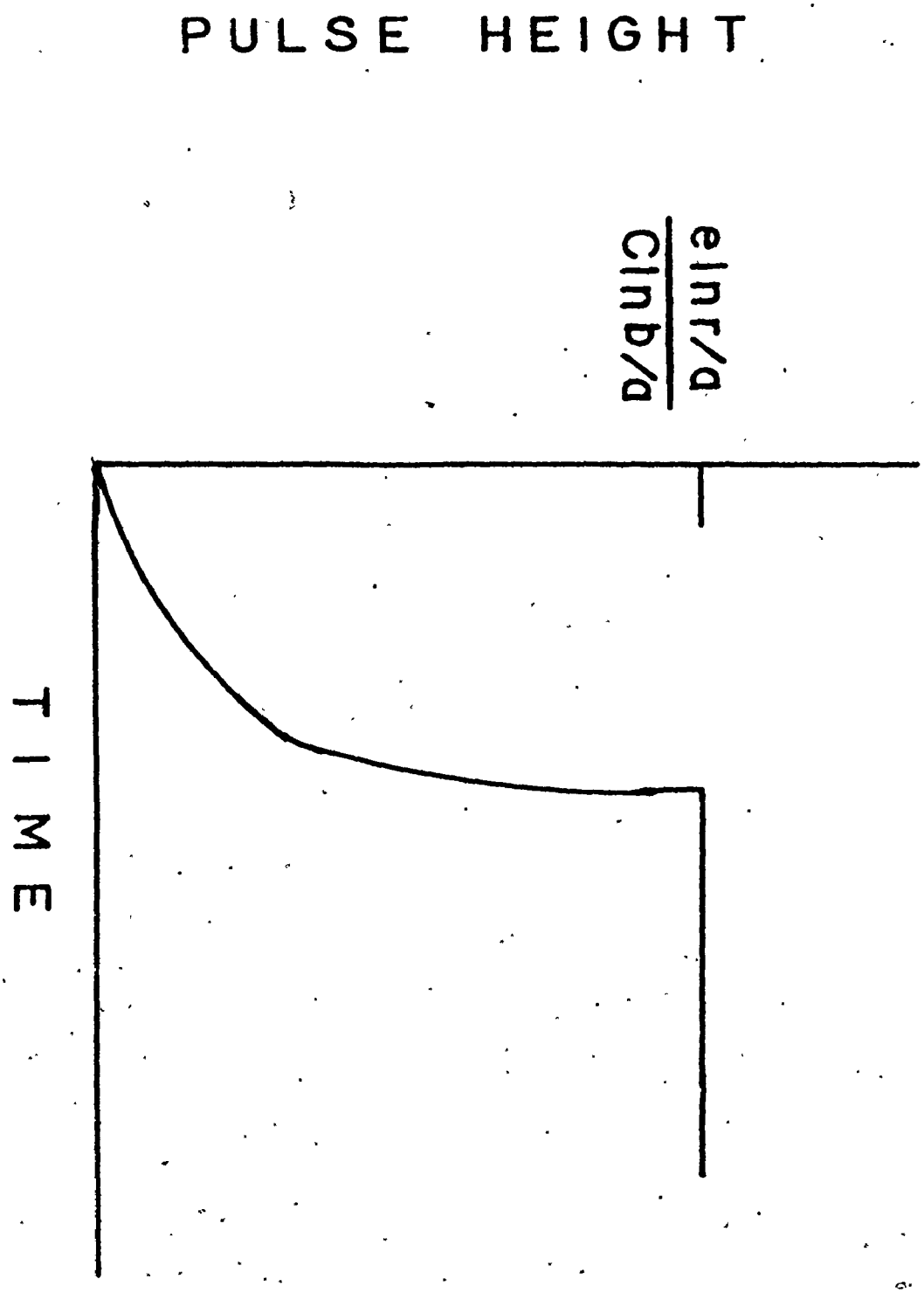

3.5 Pulse height as a function of time for the cylindrical geometry of Figure 3.3.a when operated in an ion chamber mode.

most detectors with thin anode wires, V is a slowly varying function of the position of ion formation. The inner radius cannot be made infinitely small, however, both for obvious physical reasons and also because gas multiplication can occur in the high electrostatic fields near the central wire, making the ionization chamber behave like a proportional counter. The alternative of lowering V_o is undesirable since it causes the drift velocity to decrease and hence the pulse rise time to increase.

It should be noted that the actual pulse profile observed in a parallel plate or cylindrical detector is actually the sum of all pulses from ion pairs formed along the track. For a cylindrical detector axial tracks will consist of a sum of single electron pulses all with the same risetime whereas radial tracks will be a sum of pulses with different risetimes due to the dispersion in radius of ion formation. Thus axial tracks will have a more narrow distribution of risetimes than radial ion tracks.

Pulse height can also be made independent of the

position of ion formation by use of a chamber with a grid (often called a Frisch grid after O.R. Frisch), as shown schematically in Fig. 3.6 for the parallel plate case. If a grid of wires of radius r, separation ξ, is placed close to the collector and a voltage, intermediate to the cathode and collector voltage, is placed upon it, then the induction of the positive ion formed at a distance, a, from the anode will no longer be $-e(b+C)/(a+C)$ because some of the lines of force will end on the grid instead of the collector. The electron will then travel to the collector and give its full pulse, so long as it is not collected by the grid. Total electron collection can be achieved if the cathode voltage V_-, collector voltage, V_C, and grid voltage, V_G are such that (Wi50)

$$\frac{V_C - V_G}{V_G - V_-} \frac{a}{C} \geq \frac{1 + \frac{2\pi r}{\xi}}{1 - \frac{2\pi r}{\xi}} \tag{3.9}$$

Also important is the grid inefficiency, which is related to the fraction of lines of force from the

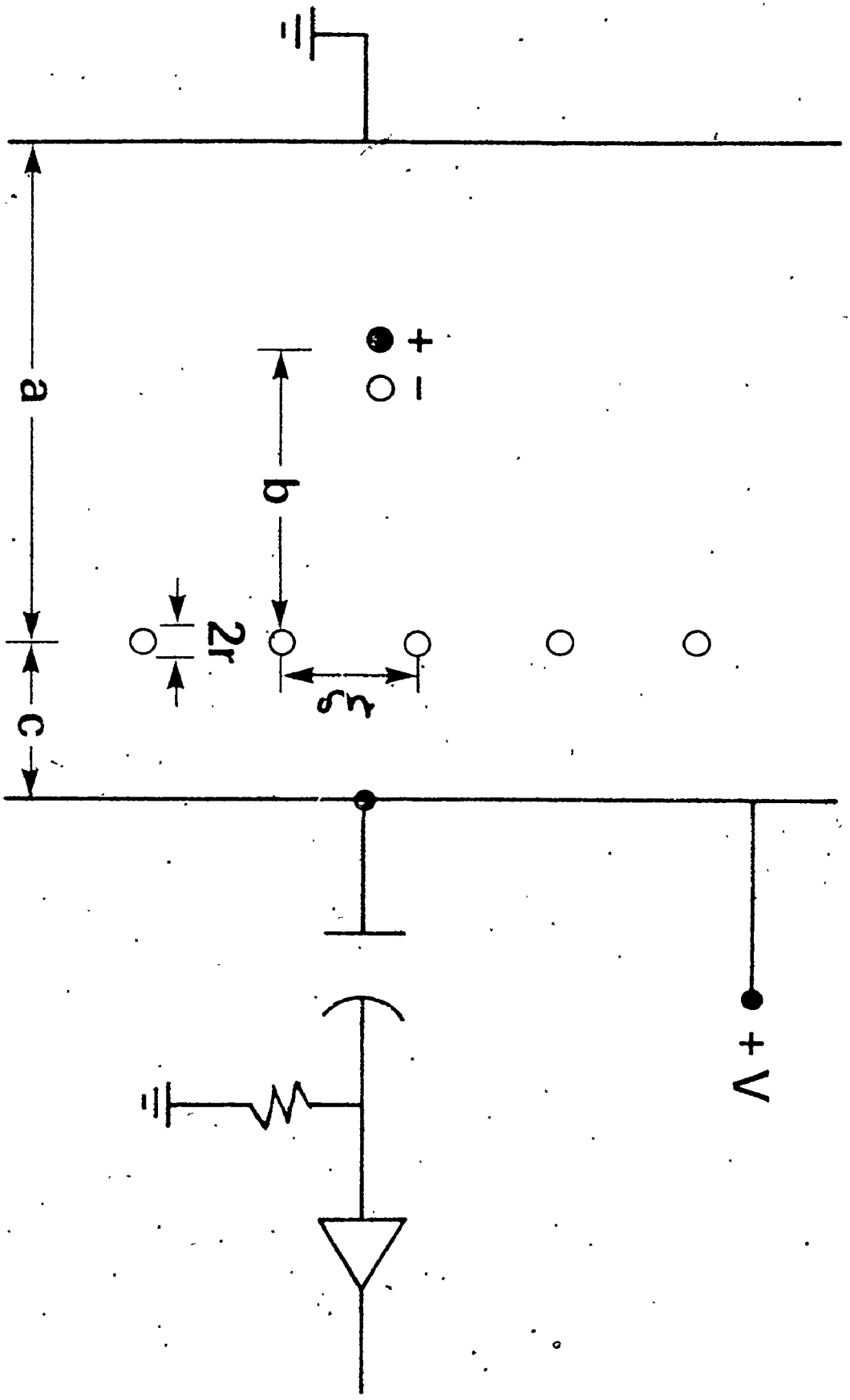

3.6 Schematic of a gridded parallel plate ion chamber.

positive ion to the grid and collector which finish on the collector. This is a complicated function of r/ξ and C/ξ (Wi50) and it is desirable to keep the inefficiency as low as possible. In most counters it is physically easy to minimize the grid inefficiency and loss of electrons due to the grid. It is also desirable to keep the collector to grid distance as small as possible since any event occurring between grid and collector will be subject to the induction effect. As is done in the case of the FNS-1 spectrometer, both a grid and a cylindrical design are employed. In this case the cylindrical design is used mainly to speed up electron collection time and hence minimize risetime dependent amplifier gain effects.

It can be easily seen that for a fast gridded cylindrical chamber with grid very close to the anode, pulse risetime is just dependent on ion track length and orientation, and the electron mobility.

Most ionization chambers, in addition to possessing collector electrodes and possibly Frisch grids, also have guard electrodes. These electrodes usually

surround both ends of the anode as shown in Fig. 3.7a and are held at the same potential as the collector electrode (usually positive high voltage). Guard electrodes serve three purposes. First, they allow no direct path across a solid insulator from a high to a low voltage electrode thus preventing a breakdown which might cause a spurious pulse. Secondly, they make the electric field more uniform over the collecting volume as seen in Fig. 3.7b. And thirdly, they define accurately the active volume of the detector by not allowing electrons formed outside the active volume to be collected.

Finally, it should be remarked that the collecting electrode is usually placed at high voltage. Since a decoupling capacitor is required, this has the disadvantage of increasing input capacitance, but nevertheless, it still has two advantages. The first is that of physical convenience. The outer case does not have to be shielded for safety purposes. Also, if the collecting electrode is at high voltage, it is assured that all electrons will be on a line of force leading to it. This may

(a)

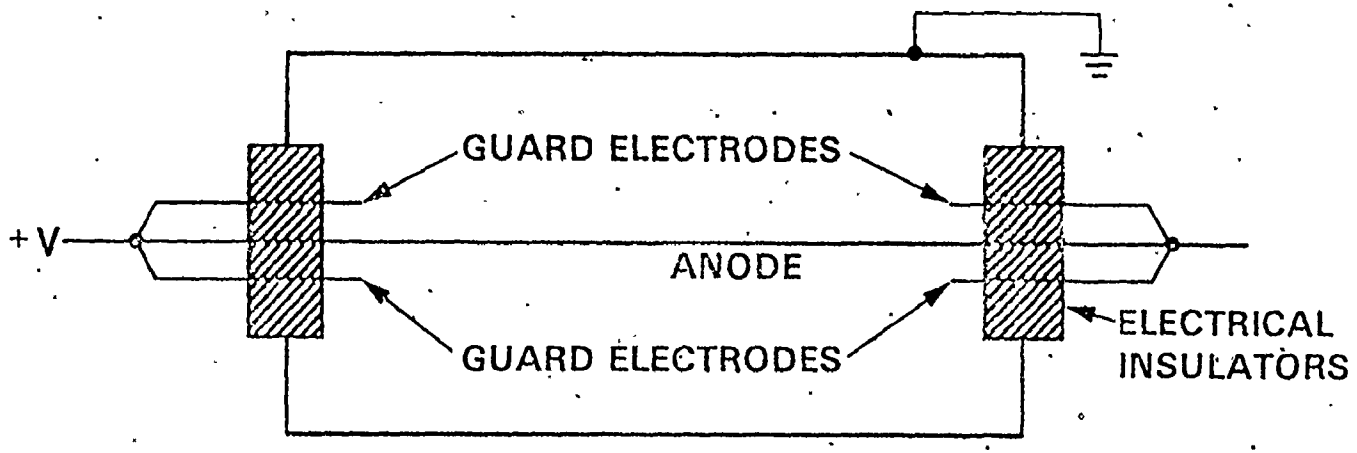

SIDE VIEW OF A CYLINDRICAL CHAMBER

(b)

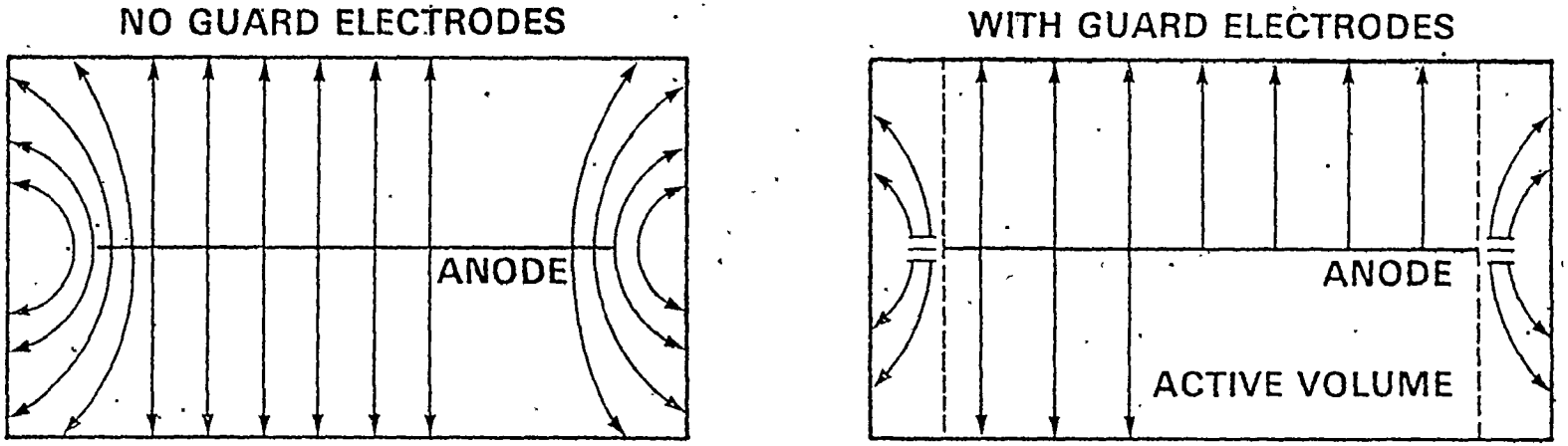

SIDE VIEW OF A CYLINDRICAL CHAMBER
ARROWS ARE FIELD LINES

3.7 The effect of guard electrodes on a cylindrical chamber.

not be the case in a poorly designed chamber with high potential on the non-collecting electrode.

3.2.6 Proportional Counters

Proportional counters are usually always co-axial cylinders, but the mechanism for pulse formation is greatly different than that for ionization chambers. The electrostatic field near the cathode is made large enough that electron multiplication takes place in the immediate vicinity of the wire and hence most ion pairs are formed in the region where $q_+(0) \approx e$ (equation 3.5). Thus, it is seen that the pulse due to electron collection is small and the majority of the pulse comes from the much slower positive ion movement. In addition, since most of the ionization is formed near the wire the induction effect is the same for all the positive ions and the amount of ionization is independent of track position. This means that all pulses will have the same form and the same fraction will be recorded even if the amplifier clipping time is much less than the positive ion collection time which is usually the case to avoid microphonics. By modifying equation 3.5 to

the form:

$$V(t) = - \frac{e+q(t)}{C} \qquad (3.10)$$

and then applying the analysis that was used for parallel plate ionization chambers we can find an expression for the pulse height as a function of time:

$$P(t) = \frac{-e}{C} \frac{\ln \left(\frac{2V_o Mt}{a^2 \ln b/a} + 1 \right)}{2 \ln b/a} \qquad t<t_2 \qquad (3.11)$$

$$= \frac{-e}{C} \qquad t \geq t_2$$

where M is gas multiplication factor

all other terms are as defined for cylindrical ionization chamber.

This pulse shape is shown in Fig. 3.8.

3.2.7 Comparison of the Advantages of Ionization and Proportional Chambers

Proportional counters, with their inherent gas multiplication, are able to detect very low energy particles; in some cases, even single electrons whose

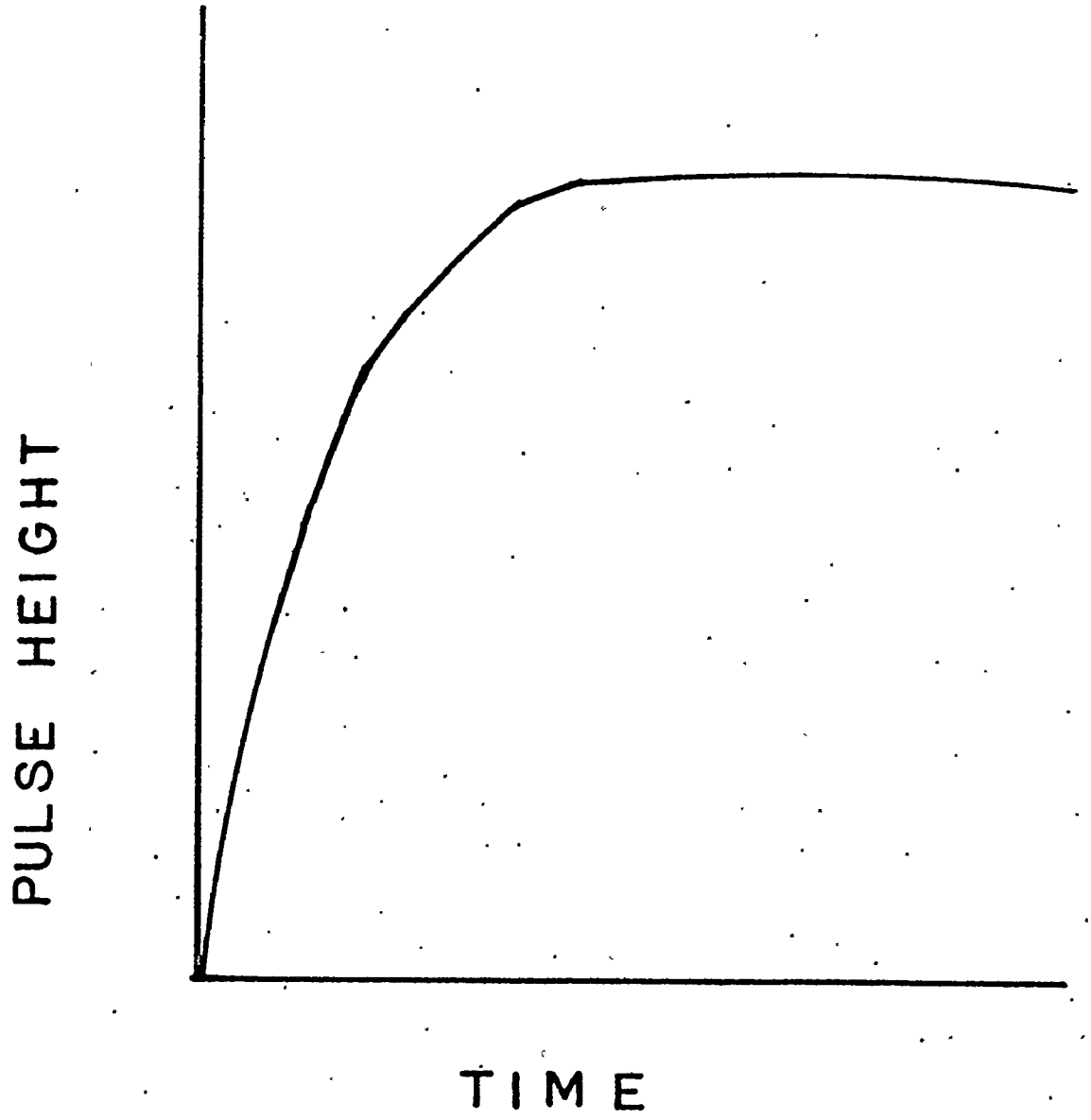

3.8 Pulse height as a function of time for a cylindrical proportional counter.

energy is insufficient to produce ionization. However, when high pressure gas fillings are required, as in ^{3}He detectors to increase detection efficiency, better energy resolution is achieved with an ionization chamber. This is due primarily to the fact that the positive ion drift velocity is proportional to the electrostatic field and inversely proportional to the gas pressure (Wi50). In order to increase the positive ion mobility and hence decrease the drift time, it is necessary to increase the electrostatic field if the gas pressure is increased. This, however, is limited by two factors. First, the field must be kept low enough so that the detector continues to operate in the proportional region. Secondly, the space charge of the positive ion sheath depresses the local field intensity and hence lowers the positive ion drift velocity, an effect that increases with increasing field and pressure. Since this saturation effect is dependent on the orientation of the initial ionization track (being smallest for axial tracks near the anode), there exists a risetime distribution which is quite large due to the low ion drift velocity. In

some high pressure ^{3}He proportional counters this risetime distribution can vary from 0.5 μsec to over 10 μsec (Sh71) and there is therefore a very significant energy spread due to the risetime dependence of gain which narrow band pulse amplifiers exhibit (Hu53).

Ionization chambers do not make use of gas multiplication and hence the problems associated with the induction effect and low drift velocity of positive ions can be eliminated by use of a gridded cylindrical chamber. One does not have to worry about problems associated with the electron avalanche; namely, anode wire uniformity, anode voltage stability and statistical variation of the multiplication constant. Since there is no multiplication to limit the electrostatic field strength, it can be varied to yield fast pulse risetime and minimize recombination. Because of the grid, the anode pulses are due entirely to electron collection from the initial ionization tracks and hence there is a much narrower risetime distribution than for proportional counters and an inherently narrower energy spread. Pulse risetime in an ionization chamber is more sensitive to

track length and orientation and thus, in the case of ^{3}He detectors, risetime discrimination is more effective in the removal of wall effect pulses and the ^{3}He recoil distribution.

The main disadvantage of ion chambers is the low signal amplitude which thus allows the preamplifier to noise limit the energy resolution at low neutron energies. With the latest FET preamplifiers available, however, this effect can be kept to less than 10 keV FWHM (Cu71a).

3.3 The FNS-1 Neutron Spectrometer

The neutron detector, model FNS-1 manufactured by Seforad Applied Radiation Ltd. of Emek Hayarden, Israel, was a fast ionization chamber consisting essentially of 6 atmospheres of ^{3}He, 3 atmospheres of argon and a small percentage of methane enclosed in a stainless steel-walled cylindrical chamber. The operational principles of 3-helium detectors are discussed in section 3.2 and their response functions are discussed in section 3.4.

The dimensions of the detector are shown in Fig. 3.9. The ^{3}He gas was a special low tritium grade

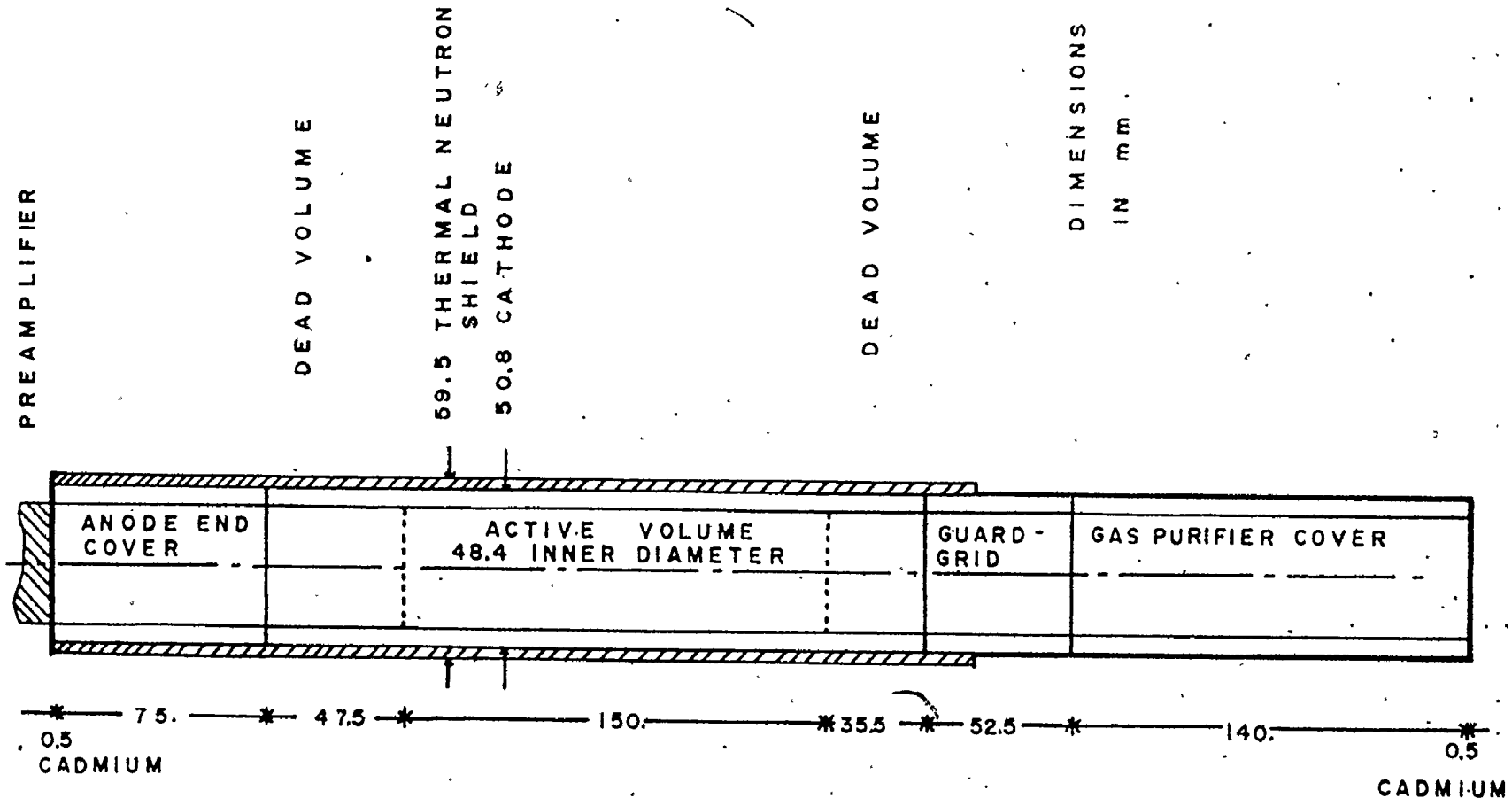

3.9 Dimensions of the Seforad FNS-1 helium-3 spectrometer.

since electronegative gases such as tritium, even in minute quantities, can increase pulse risetime by the formation of heavy negative ions. The argon was used as a stopping gas in place of krypton or xenon since with an atomic number of 18 versus 36 and 54 respectively, it would be less sensitive to gamma rays and hence pile up which might occur in high gamma fields. The methane was added to increase the electron drift velocity and thus decrease the pulse risetime. The pressures used were found to be an optimum by Cuttler (Cu71a) since for higher gas pressures although detection efficiency increases and the wall effect decreases, the electron drift velocity decreases which causes energy resolution to deteriorate. Although stainless steel has a higher average atomic number than beryllium or aluminium and hence a greater gamma ray sensitivity, its superior chemical properties for machining, welding and outgassing recommended its use.

The electrical connections of the detector are shown schematically in Fig. 4.3. Electrons from the initial ionization process were collected at the anode

which resided at a positive potential of 3000 volts with respect to the case. A Frisch grid, used to eliminate the induction effect, and two guard electrodes were also employed. A cylindrical geometry was utilized for reasons explained in section 3.2, the main one of which was the decreased electron collection time. The bias network which originally required two separate power supplies - one for the grid (+ 850 V) and another for the guard electrodes and anode (+ 3000 V) - was modified to allow all electrodes to operate from a single supply.

The SR 101 preamplifier, supplied by the company and rigidly attached to the spectrometer, consisted of two stages - the first a low noise charge sensitive preamplifier and the second a voltage amplifier of gain ten. The first stage, which was effectively a low noise FET with an integrating feedback capacitor, was used to integrate the charge produced by the ionizing particles. Its gain, which was governed by the reciprocal of the integrating capacitor, was approximately 1 volt/pico Coulomb and as such yielded a 5 mV pulse height for

a thermal neutron. Since this was about ten times smaller than a Ge(Li) detector signal (3 eV/electron-hole pair versus 30 eV/ion pair) the gain of ten voltage amplifier was employed. Nevertheless, the inherent resolution due to preamplifier noise would correspond to about 1 keV for the Ge(Li) and 10 keV for the ^{3}He detector. The preamplifier was AC coupled to the ion chamber since it was convenient to operate the anode at high voltage for reasons discussed in section 3.2.

A calcium getter, capable of being heated electrically to 150° C, was sealed in the detector in order to eliminate electronegative impurities should the need arise. It was found in these experiments that it was not necessary to use the calcium purifier.

Finally, a thermal neutron shield consisting of 2 mm of boron nitride powder sandwiched between two 0.5 mm sheets of cadmium surrounded the active volume to reduce the detector sensitivity to thermal and epi-cadmium neutrons. The reduction in rate of MeV neutrons was found to be no greater than 0.5% for the cadmium and 2.1% for the boron nitride and was probably significantly

less since the total cross sections were used in these calculations and in fact at these energies elastic scattering accounts for most of the total cross-section. The reduction of thermal and epithermal neutrons due to the shield was estimated by the manufacturer to be approximately 50 to 100 depending on the epithermal spectrum and thus made peak extraction at low neutron energies much easier.

3.4 The Response Function of a Helium-3 Spectrometer

As mentioned in section 3.2 if both proton and triton are stopped within the active volume of a Helium-3 spectrometer and if the detector is an idealized fast ionization chamber, then the pulse height out of the detector will be directly proportional to the sum of the neutron energy, E_n, and Q-value and thus for monoenergetic neutrons, a delta function will occur in the spectrum of the detector at $E_n + Q$. This in fact does not occur for any real detector and the deviations from a delta function can be considered as arising from four major causes:

1) systematics of the ionization chamber
2) electronic effects

3) ^{3}He recoils

4) wall and end effects

The first group of effects have been discussed in section 3.3 and it suffices to say that for a well designed gridded ionization chamber, such as we are here considering, the only modification of the original delta function is an energy broadening due to statistical fluctuation of ionization and a lack of constancy of the average energy required to produce an electron-ion pair. This amounts to approximately 11 keV for a 1 MeV neutron (Wi50) and is approximately 6 keV for thermal neutrons (Cu71b).

Electronic effects again tend to broaden the full energy peak and these effects are produced both by the amplifier and the preamplifier. The preamplifier has an inherent Nyquist or thermal noise component, Gaussian in shape, whose width adds in quadrature with the intrinsic resolution of the detector. This component is, of course, independent of incident neutron energy and for the FNS-1 spectrometer preamplifier this amounts to approximately 10 keV. This gives a minimum energy spread for thermal

neutrons of approximately 14 keV due to preamplifier and chamber effects.

The amplifier also produces a broadening of the pulse height but unlike the preamplifier it is asymmetrical in energy and it is a function of neutron energy. This broadening is due to the dependence of the amplifier gain on pulse risetime, and as was mentioned in section 3.2 is minimized by the use of a Frisch grid. It should be quite obvious that for a gridded chamber, the pulse risetime will be proportional to the ion track length and will also be a function of track orientation, being longer for radial tracks and shortest for axial tracks. In addition, axial tracks will have a risetime independent of track length whereas radial tracks will not. For thermal and low energy neutrons, with short ion track lengths, this difference in risetime is small and hence the broadening is small. For high energies, however, this effect is significant and turns out in fact, as shown in section 3.6, to yield an energy dependence of the form:

$$\delta = A + B\, E_n \qquad (3.12)$$

where A, B are constant

E_n is the neutron energy

and δ is the full width half maximum (fwhm)

instead of the normal :

$$\delta = \sqrt{A + B E_n} \qquad (3.13)$$

associated with electronic and statistical broadening such as is observed in Ge(Li) detectors. This broadening due to risetime variation can be improved by risetime selection and this is discussed in section 3.7.

The previous two effects produced only a spread in energy resolution whereas the effect of ^{3}He recoils and the wall and end events is to produce a continuum on the low energy side of the full energy peak.

The effect of the elastic scattering of neutrons has been mentioned in section 3.2.1. For monoenergetic neutrons of energy E_n the ^{3}He(n,n)^{3}He reaction produces recoiling ^{3}He nuclei in a continuous energy range from 0 to 3/4 E_n which can interfere with low energy neutron groups if E_n exceeds 1 MeV. Due to the double charge that they carry, helium-3 recoils are stopped in a shorter distance than protons or tritons of equivalent

energy. Again, as for protons and tritons, axially directed ^{3}He recoils produce pulses of short rise-time independent of track length and radial recoils produce track length dependent risetimes. Thus, ^{3}He recoils can be discriminated against by the use of pulse risetime discrimination as described in section 3.7.

Wall and end effects are complementary processes in which at least one of the proton or ^{3}H tracks partially lies outside the active volume of the detector. In the wall effect, an ion is formed inside the active volume and leaves the active volume before coming to rest, whereas in the end effect an ion is formed outside the active volume and comes to rest inside it. A typical thermal neutron spectrum emitted by an americium-beryllium source and incident on the FNS-1 spectrometer is shown in Fig. 3.10. The spectrum can be simply understood if one assumes that the detector diameter is greater than the combined proton-triton range and thus only one of the two reaction products can reach the wall. Since the initial particles have effectively no kinetic energy, the proton snd triton must be ejected in opposite

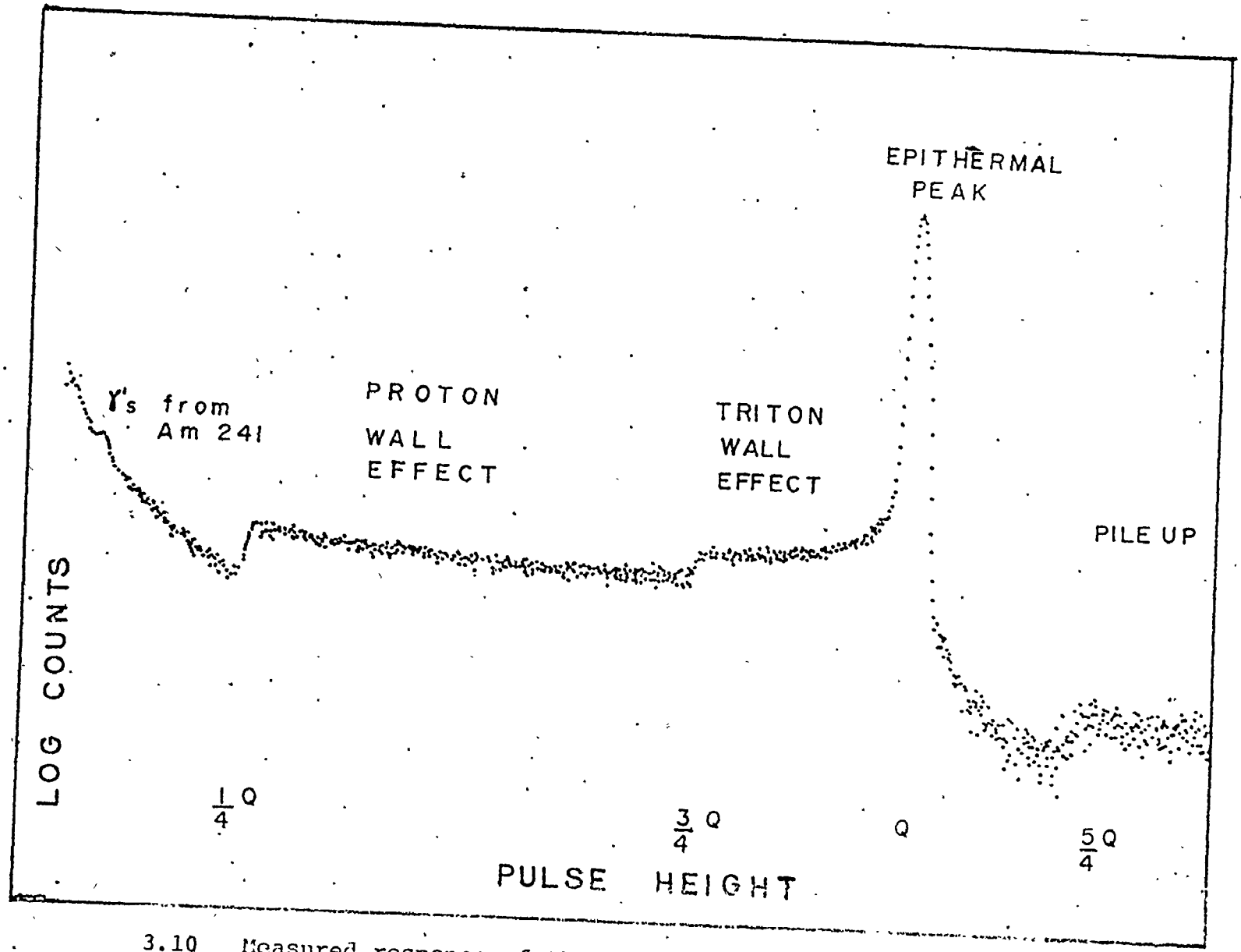

3.10 Measured response of the FNS-1 spectrometer to thermalized neutrons from an americium -beryllium source. Pulse height is expressed in fractions of the $^{3}He(n,p)$ Q-value.

directions, the proton having energy 3/4 Q and the triton have energy 1/4 Q, where Q is the Q-value (764 keV). For a homogeneous distribution of neutrons and an isotropic emission of protons and tritons there is a small probability for either proton or triton to be close enough to the wall that it will not leave full energy in the detector. If the ionization is constant along the track length, then for the case of the proton striking the wall (proton wall effect) the spectrum will consist of the full triton energy plus a fraction of the proton energy from zero up to the full proton energy. This will be a continuous distribution of equal probability. A similar situation exists for the triton wall effect. Actually the condition of constant ionization along the track length does not hold true due to energy loss of the charged particle and detailed calculations of the wall effect for thermal neutrons have been done by Shalev (Sh69).

The calculation of wall effect for fast neutrons is considerably more complex since the reaction products can be emitted at varying angles with respect to one

another and the energy and hence range of each particle is a function of emission angle. Thus no well defined edge occurs for the proton and triton wall effects and since the specific ionization can vary considerably over the ion track, the continuum due to the wall effect is generally not flat. Batchelor et al. (Ba55) have carried out a detailed calculation of the wall and end effects for fast neutrons incident on a cylindrical ^3He chamber. The spectrum arising from the $^3He(n,p)T$ reaction for neutrons of energy E_n can be written:

$$S(E) = (1-p)\delta(E-E_t) + P(E,E_n) + P^1(E,E_n) \qquad (3.14)$$

where

$E_t = E_n + Q$ is the maximum energy released

$Q = 764$ keV is the $^3He(n,p)^3H$ Q-value

p is the wall effect fraction and is given by:

$$p = \int_0^{E_t} P(E,E_n)dE \qquad (3.15)$$

$P(E,E_n)$ is the wall effect spectrum

$P^1(E,E_n)$ is the end effect spectrum

and $(1-p)\delta(E,E_t)$ is the fraction of events in the full energy peak.

Batchelor has shown that if effects arising from the circular ends are small compared with that of the main surface and if the energy-range relationship is linear and possesses the same constant of proportionality for protons and tritons then $P(E,E_n)$ and $P^1(E,E_n)$ can be evaluated for three cases:

(1) incident neutrons parallel to the axis of the detector

$$P(E,E_n) = 1/E_t[(2R/a)A(E) + (2R/b)B(E)] \quad (3.16)$$

$$P^1(E,E_n) = 1/E_t[(2R/b)B(E_t-E)] \quad (3.17)$$

(2) incident neutrons normal to the axis of the detector

$$P(E,E_n) = 1/E_t[(4R/\pi a + 2R/b)A(E) + (2R/a)(1-2/\pi)B(E)] \quad (3.18)$$

$$P^1(E,E_n) = 1/E_t[(2R/b)A(E_t-E)] \quad (3.19)$$

(3) isotropic neutrons

$$P(E,E_n) = 1/E_t[(2R/a+2R/b)\{(\pi/4)A(E) + (1-\pi/4)B(E)\}] \quad (3.20)$$

$$P^1(E,E_n) = 1/E_t[2R/b\{(\pi/4)A(E_t-E) + (1-\pi/4)B(E_t - E)\}] \quad (3.21)$$

where a is the radius of the active volume, and b its length, as determined from Fig. 3.9, and R is the range in the detector gas mixture of a proton of energy E_t. A(E) and B(E) have been numerically evaluated in 0.1 MeV steps for neutron energies of 0, 1/3, 2/3 and 1 MeV (Ba55) and are shown in Figures 3.11a and 3.11b. We can thus approximate the integral of equation 3.15 by the summation:

$$p = \sum_{E=o}^{E_t} P(E,E_n)\,\Delta E \qquad 3.22$$

The proton range, R, can be calculated by use of the known range of protons in dry air at 15°C and 1 atmosphere (Ev55) given in Table 3.1, and the fact that the range will be inversely proportional to the number of scattering centres and their charge. Thus for the 6 atmospheres of ^3He and 3 atmospheres of Ar (neglecting the trace quantities of polyatomic gases) at 20°C we find:

$$\frac{1}{R} = \frac{1}{R_{AR}} + \frac{1}{R_{HE3}} \qquad (3.23)$$

$$\frac{R_{AR}\cdot P_{AR}\cdot Z_{AR}}{T} = \frac{R_{AIR}\cdot P_{AIR}\cdot Z_{AIR}^{EFF}}{T_{AIR}} \qquad (3.24)$$

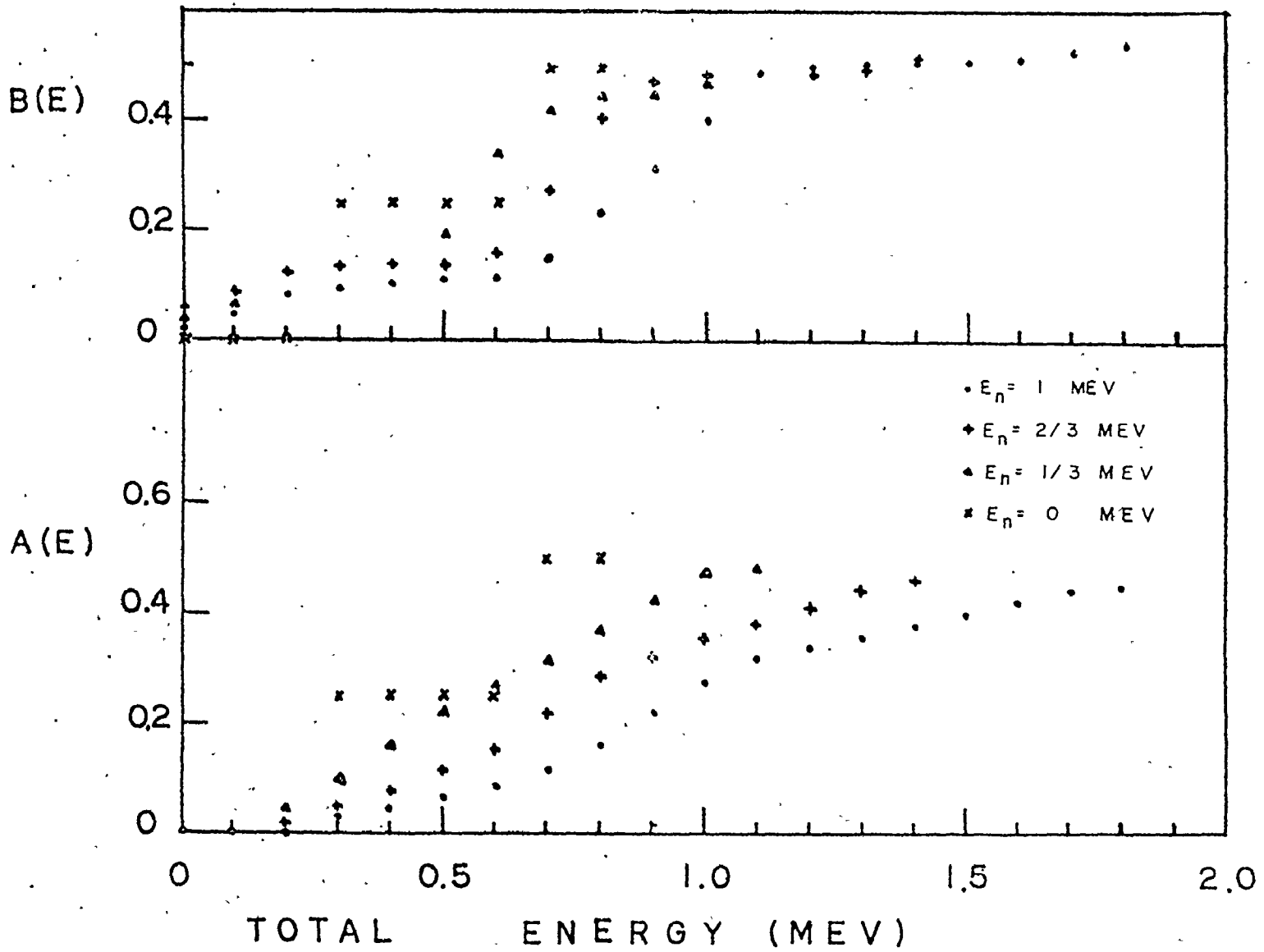

3.11 The coefficients of Batchelor et al. (Ba55) used in calculation of the wall effect. For further description see section 3.4.

$$\frac{R_{HE3} \cdot P_{HE3} \cdot Z_{HE3}}{T} = \frac{R_{AIR} \cdot P_{AIR} \cdot Z_{AIR}^{EFF}}{T_{AIR}} \qquad (3.25)$$

and R, R_{AR}, R_{HE3} and R_{AIR} are the ranges of protons in the detector gas mixture, argon, ^{3}He and air at the previously stated pressures and temperatures, namely:

$T = 293°K$

$P_{HE3} = 6$ atm

$P_{AR} = 3$ atm

$P_{AIR} = 1$ atm

$T_{AIR} = 288°K$

$Z_{AR} = 18$

$Z_{HE3} = 2$

$Z_{AIR}^{EFF} = Z_{N2}P_{N2} + Z_{02}P_{02} = 14.3$

$P_{N2} = .781$ = partial pressure of nitrogen in 1 atm of dry air at 15°C

$P_{02} = .209$ = partial pressure of oxygen in 1 atm of dry air at 15°C

Equations 3.23 through 3.25 yield the maximum proton ranges for various energies as shown in Table 3.1. By use of Table 3.1 and equations 3.14 through 3.21 the fraction of neutron events contributing to the full energy peak, 1-p, can be obtained. The results are shown in Fig. 3.12

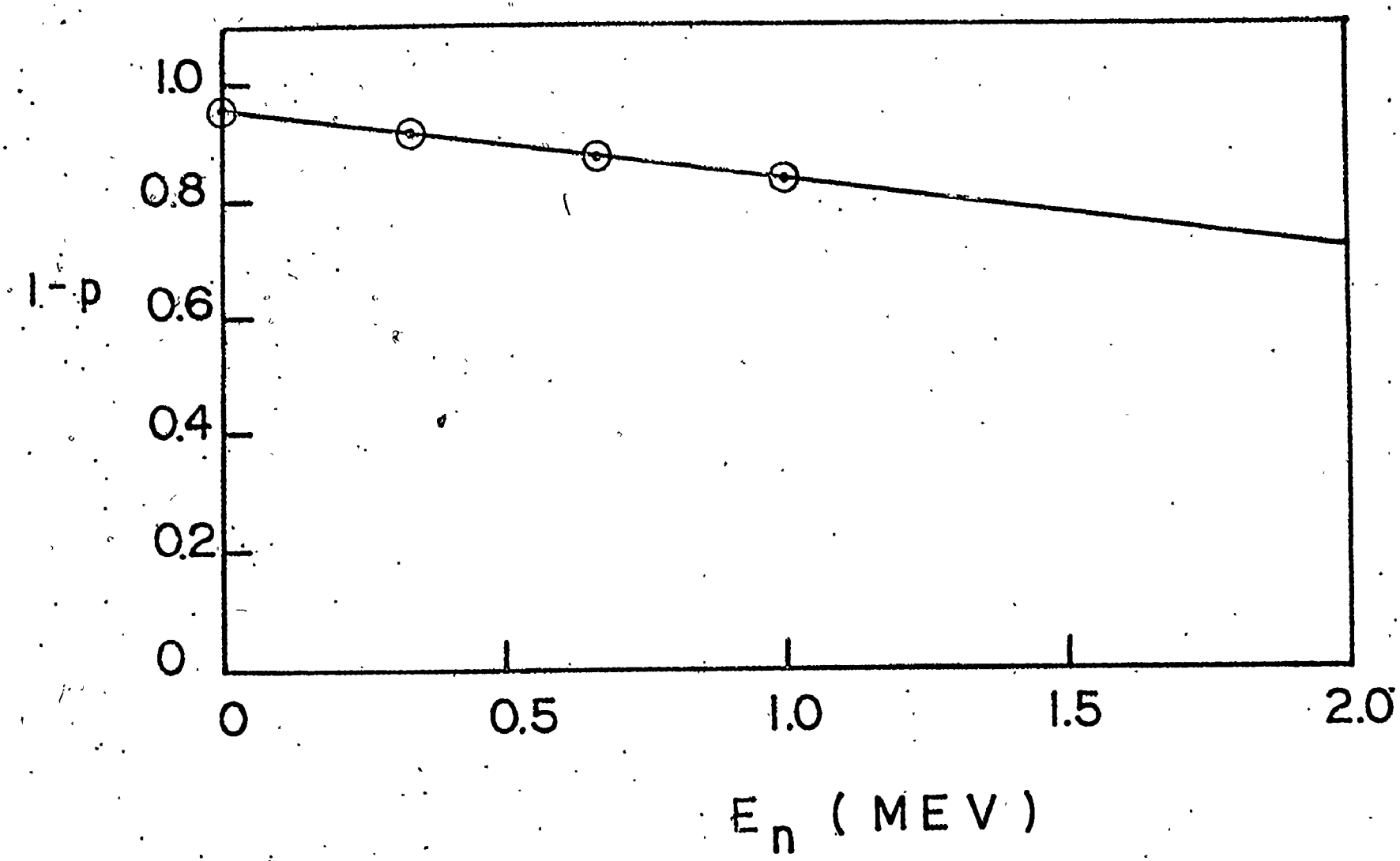

3.12 Plot of the fraction of ^{3}He (n,p) events occurring in the FNS-1 spectrometer which fall in the full energy peak as a function of neutron energy for the FNS-1 spectrometer. Based on a calculation described in the text.

for the case of incident neutrons perpendicular to the detector axis. It is interesting to note that the results differ by at most 4% between the three different geometrical cases presumably because of the short proton range even at 1 MeV neutron energy. It should be noted that, as Batchelor points out (Ba55), for neutron energies significantly in excess of 1 MeV, the assumptions made no longer hold and the theoretical curve should tend to deviate from experimental results. As will be seen in section 3.6, this deviation is small even up to 2.5 MeV. Also it should be added that although Batchelor suggests his theory is good to 12%, in our particular case, as shown in section 3.6, the theory seems to be in agreement with experiment to within 4% for E_n less than 2 MeV and 8.5% for E_n equal to 2.5 MeV. And finally it is noted that in our experimental geometry as detailed in section 3.5, we have neither one of the three geometrical cases but rather one that lies in between cases 1 and 2. The 4% disagreement between them, however, suggests that for our gas filling the wall effect is insensitive to geometry and that it is reasonable to use case 1.

It should also be noted that since the wall effect will occur more often for ion tracks with large radial components (neglecting the circular ends of the active volume), for a given neutron energy wall effect events which deposit most of their energy in the detector (and hence have comparatively long track lengths) will have longer risetimes than a substantial fraction of the full energy events. Thus, it may be possible by rejecting long risetimes for a given energy to eliminate some of the wall effect. This would require either a two dimension analysis or a difference amplifier to reject signals above a specified value of energy minus risetime. The former method was not used due to other reasons explained in section 3.7 and the latter method was not used due to a lack of equipment. Instead a simple discrimination against low risetimes was done which would accept most wall effect events. As seen in Fig. 3.18, this does not represent a serious problem since it can be approximated by an exponential tail in the spectral fitting program (Chapter 6).

Up until now we have discussed the detector response for neutrons. Helium-3 spectrometers, however,

do have some sensitivity to gamma rays. These can produce pulses by releasing electrons from either the metal walls or the gas filling. Electrons of energy greater than about 0.7 MeV which are ejected into the active volume have a specific ionization rate of approximately 1.5 MeV-cm^2/gm (Ev55) or approximately 9 keV/cm for the gas filling in question and thus can produce pulses from 0 to 135 keV. The actual pulse spectrum decreases in an approximately exponential manner (Cu71a) and pulse pile-up at high rates can extend the spectrum to well beyond 135 keV. For high rates then there is a reasonable probability that photon and neutron events will occur in coincidence leading to shifting and broadening of the neutron peaks. This effect can be evaluated by mixing a precision pulser with the detector signal and has been found to be negligible in this experiment.

For high neutron rates pulse pile-up will also occur and this is indeed observed in Fig. 3.10. Here we see above the thermal peak the start of a second continuum due to proton wall effect pulses occurring in the detector at the same time as full energy events.

3.5 Calculation of the Detector Efficiency

3.5.1 Energy Dependence of Efficiency

The efficiency is defined as that fraction of events per incident neutron flux that occur in the full energy peak for a given neutron energy. The calculation of efficiency may be broken up into two parts : a calculation of the energy dependence of the efficiency which will yield a relative efficiency as a function of energy and then a calculation of the absolute efficiency for one specific neutron energy. The latter is not needed in order to analyse ratios of neutron group intensities but is essential if photoneutron cross sections are to be determined. The relative efficiency, $\eta(E)$, normalized at a neutron energy of 1 MeV, can easily be calculated using the wall effect calculations detailed in section 3.4 and is given by :

$$\eta(E) = \frac{\sigma(E)}{\sigma(1\ \text{MeV})} \cdot \frac{(1-p(E))}{(1-p(1\ \text{MeV}))} \qquad 3.26$$

where $\sigma(E)$, $\sigma(1\ \text{MeV})$ are the $^3He(n,p)T$ cross sections at neutron energy E and 1 MeV respectively, and $(1-p(E))$, $(1-p(1\ \text{MeV}))$ are, as defined in section 3.4, the

fraction of interactions which occur in the full energy peak for neutron energy E and 1 MeV respectively. The $^{3}He(n,p)T$ cross section is shown in Fig. 3.1 and has been carefully described by Batchelor and Parker (Ba64) and the BNL325 Neutron cross section tabulations (Hu58, Go66). It is difficult to assign errors to the cross section curve, as pointed out in BNL325, but due to the plethora of data and smoothness of the cross section it is felt to be good to a few percent. The function (1-p), for neutrons perpendicular to the detector axis, has been calculated in section 3.4 and plotted in Fig. 3.12. Its accuracy at energies much in excess of 1 MeV neutron energy is uncertain due to assumptions made in the calculation, but, as will be seen in section 3.7, it appears to be accurate to about five percent up to 2 MeV. Using equation 3.26, $\eta(E)$ can be plotted and is shown in Fig. 3.13.

Two points about the relative efficiency should be noted. First, 1-p(E) and hence $\eta(E)$ is, as described in section 3.4, geometry independent to within a few percent for the particular detector in question and

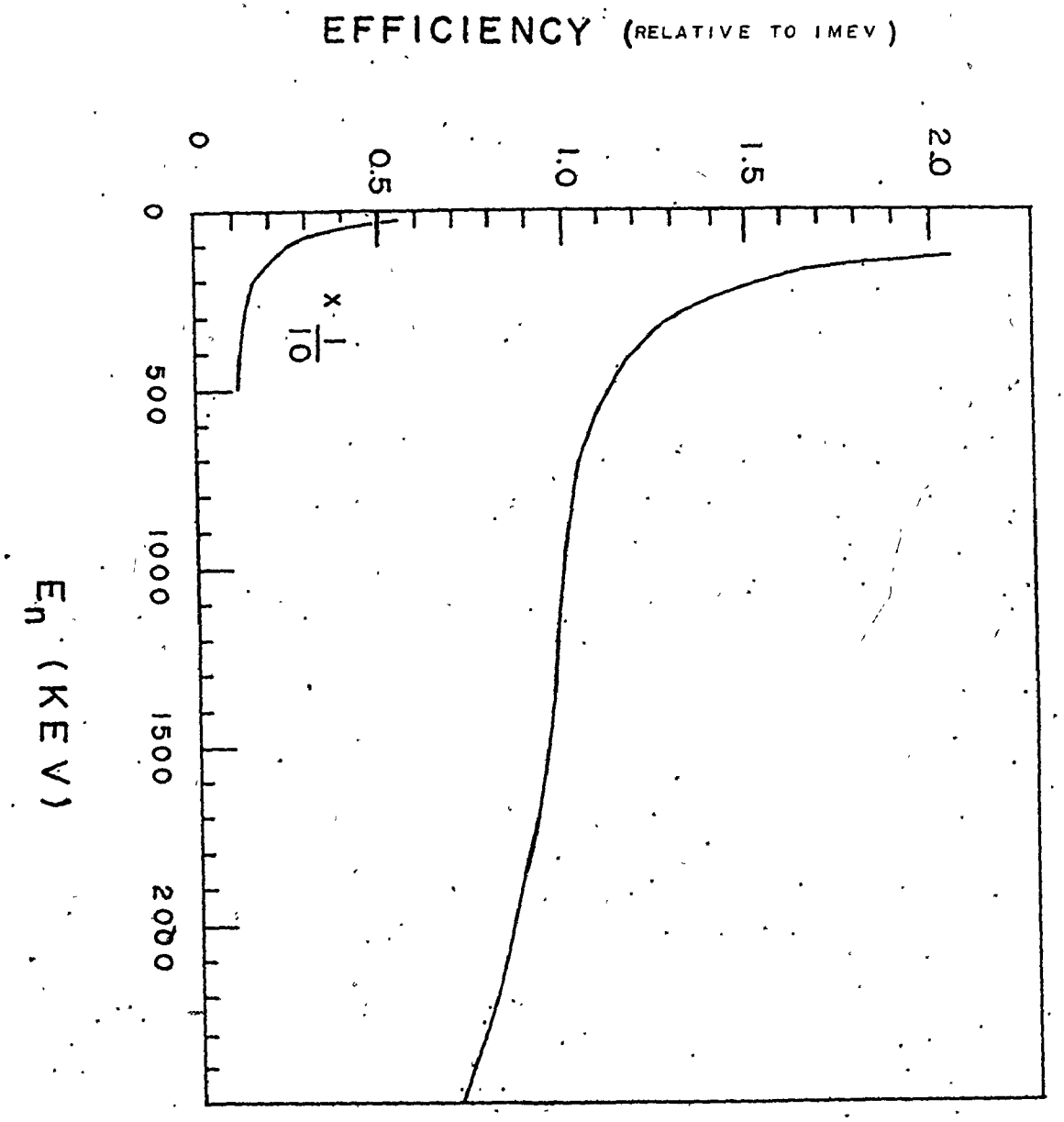

3.13 Theoretical efficiency of the FNS-1 spectrometer as a function of neutron energy. Efficiency is normalized to 1 MeV and is based on a calculation performed in the text. Efficiency reduced by a factor of 10 is also shown for lower energies.

hence $\eta(E)$ can be used for any geometry. Secondly, transmission of neutrons through the boron nitride and cadmium detector sheath has been neglected since it contributes at most only a 2.1% attenuation for the boron nitride and 0.5% for cadmium at neutron energies greater than 25 keV; $\eta(E)$ must then be multiplied by the ratio of the transmittance through the two filters and thus the correction will be correspondingly small. In actual fact, since elastic scattering accounts for a substantial fraction of the cross section for keV neutrons, this correction will be even smaller.

We now turn to the calculation of the absolute efficiency at a specific neutron energy which we will choose as 1 MeV since the relative efficiency is normalized at this energy. As stated previously, the energy dependence of the efficiency is insensitive to different geometrical situations. The absolute efficiency, however, is quite sensitive to geometry and thus the geometry in use must be accurately specified. Two types of experiments have been performed using two different detector geometries, one with the detector parallel to the incident photon

beam and one with the detector perpendicular to the beam.

3.5.2 Efficiency Calculation for Parallel Geometry

All experiments which measured absolute photoneutron cross sections employed this geometry which is shown in Fig. 3.14. The detector is situated parallel to the photon beam which is defined as the Z axis. The origin is defined as the center of am infinitesimal element of target, extending from $x_o' \rightarrow x_o' + dx_o'$, $y_o' \rightarrow y_o' + dy_o'$ and $z_o' \rightarrow z_o' + dz_o'$, but initially we shall assume a point source at the target center. We define $\ell(\theta,\phi)$ as an arbitrary path length through the detector which enters at position (r_1, θ,ϕ) and leaves at position (r_2,θ,ϕ) for a neutron emitted in the elemental solid angle $d\Omega(\theta,\phi)$. The equation of an arbitrary straight line corresponding to a neutron trajectory in the (θ,ϕ) direction is :

$$(x - x_o)^2 + (y - y_o)^2 = R^2 \qquad (3.27)$$

Equations 3.27 and 3.28 yield after simplification :

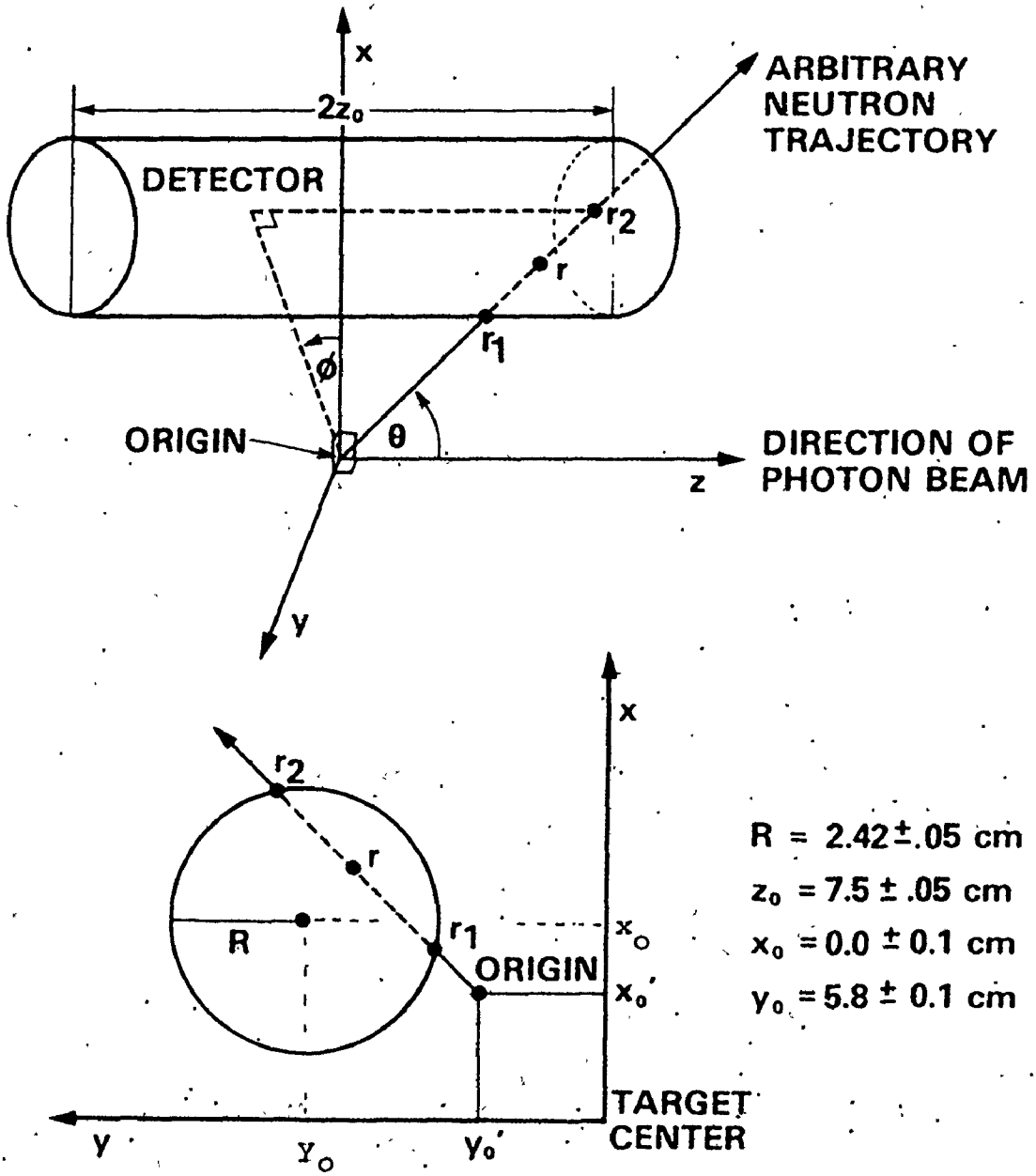

ORIGIN IS THE CENTER OF AN INFINITESMAL ELEMENT OF TARGET AT POSITION x_0', y_0', z_0' FROM TARGET CENTER

3.14 : Parallel geometry used to derive the efficiency curve of section 3.5.2. Symbols are defined in that section.

$$r = \frac{y_o \sin\phi + x_o \cos\phi \pm \sqrt{R^2 - (y_o \cos\phi - x_o \sin\phi)^2}}{\sin\theta} \quad (3.29)$$

The two roots of this equation, r_1 and r_2 ($r_2 > r_1$ by convention), are the radial coordinates of an arbitrary line intersecting the infinite cylinder. The boundary of the active volume in the positive Z direction is given by :

$$r_3 = z_o/\cos\theta \quad (3.30)$$

and thus we have for $0 \leq \theta \leq \pi/2$:

Case 1. $r_1 > r_3$ $\quad \ell(\theta,\phi) = 0$ (3.31)

Case 2. $r_2 > r_3 > r_1$ $\quad \ell(\theta,\phi) = r_3 - r_1$ (3.32)

Case 3. $r_3 > r_2 > r_1$ $\quad \ell(\theta,\phi) = r_2 - r_1$ (3.33)

The differential efficiency, $\frac{d^2\varepsilon(\theta,\phi)}{d\Omega}$, is given by

$$d^2\varepsilon(\theta,\phi) = n\sigma(1-p)\frac{d\Omega}{4\pi}\ell(\theta,\phi) \quad (3.34)$$

(for $n\sigma \ll 1$)

and $\quad d\Omega = \sin\theta\, d\theta d\phi \quad (3.35)$

giving

$$d^2\varepsilon = \beta \, \mathrm{Sin}\theta \, \ell(\theta,\phi) \, d\theta d\phi \tag{3.36}$$

where

$$\beta = \frac{n\sigma(1-p)}{4\pi} \tag{3.37}$$

n is number of ^3He nuclei per unit volume of detector

σ is the $^3He(n,p)T$ cross section at 1 MeV

$(1-p)$ is the fraction of full energy events per interaction at 1 MeV

Substitution of 3.36 into equations 3.31 to 3.33 leads to :

Case 1. $d^2\varepsilon = 0$ (3.38)

Case 2. $d^2\varepsilon = \beta(Z_o \mathrm{Tan}\theta + \sqrt{R^2-(y_o\mathrm{Cos}\phi - x_o\mathrm{Sin}\phi)^2})$ (3.39)

Case 3. $d^2\varepsilon = 2\beta\sqrt{R^2-(y_o\mathrm{Cos}\phi-x_o\mathrm{Sin}\phi)^2}\,\dfrac{-y_o\mathrm{Sin}\phi-x_o\mathrm{Cos}\phi)\,d\theta d\phi}{}$ (3.40)

Since for an unpolarized beam, differential cross sections are independent of azimuthal angle, ϕ, we are only interested in the dependence of efficiency on the polar angle, θ. We get :

$$\frac{d\varepsilon(\theta)}{d\theta} = \int_{\phi min}^{\phi max} \frac{d^2\varepsilon(\theta,\phi)}{d\theta d\phi}\, d\phi \qquad (3.41)$$

Case 1. $$\frac{d\varepsilon}{d\theta} = 0 \qquad (3.42)$$

Case 2. $$\frac{d\varepsilon}{d\theta} = \beta \int_{\phi min}^{\phi max} (Z_o \mathrm{Tan}\theta + \sqrt{R^2-(y_o\mathrm{Cos}\phi - x_o\mathrm{Sin}\phi)^2} - y_o\mathrm{Sin}\phi - x_o\mathrm{Cos}\phi)\, d\phi \qquad (3.43)$$

Case 3. $$\frac{d\varepsilon}{d\theta} = 2\beta \int_{\phi min}^{\phi max} \sqrt{R^2-(y_o\mathrm{Cos}\phi - x_o\mathrm{Sin}\phi)^2}\, d\phi \qquad (3.44)$$

By inspection, it is clear that ϕ min, ϕ max satisfy the equation :

$$(y_o\mathrm{Cos}\phi_m - x_o\mathrm{Sin}\phi_m) = \pm R \qquad (3.45)$$

or $$\mathrm{Cos}\phi_m = \frac{\pm Ry \pm x_o\sqrt{x_o^2+y_o^2-R^2}}{x_o^2+y_o^2} \qquad (3.46)$$

By noting that ϕ min $\leq$ ϕ max and $|\mathrm{Cos}\phi min| \neq |\mathrm{Cos}\phi max|$ except for $x_o = 0$, we get :

$$\text{Cos}(\phi \text{ min}) = \frac{Ry_o + x_o\sqrt{x_o^2 + y_o^2 - R^2}}{x_o^2 + y_o^2} \qquad (3.47)$$

$$\text{Cos}(\phi \text{ max}) = \frac{-Ry_o + x_o\sqrt{x_o^2 + y_o^2 - R^2}}{x_o^2 + y_o^2} \qquad (3.48)$$

Our target is not, however, a point source but rather a cube of side 2.5 ± 0.1 cm illuminated by a beam of roughly circular cross section. Thus, since the beam area is found to be smaller than the target area (see section 6.2.1) we want the differential efficiency averaged over the beam dimensions. This is given by :

$$\left\langle \frac{d\varepsilon(\theta)}{d\theta} \right\rangle = \frac{\int\int\int P(x_o', y_o', z_o') \frac{d\varepsilon}{d\theta}(x_o', y_o', z_o', \theta) dx_o' \, dy_o' \, z_o'}{\int_{x_o'} \int_{y_o'} \int_{z_o'} P(x_o', y_o', z_o') \, dx_o' dy_o' dz_o'} \qquad (3.49)$$

where

$$\frac{d\varepsilon}{d\theta} = \int_{\phi\min(x_o', y_o')}^{\phi\max(x_o', y_o')} \frac{d^2\varepsilon}{d\theta d\phi}(x_o', y_o', z_o', \theta, \phi) d\phi$$

$P(x_o', y_o', z_o')$ is the unnormalized probability of emission

of a neutron by an infinitesimal element of target extending from $x_o' \to x_o' + dx_o'$, $y_o' \to y_o' + dx_o'$ and $z_o' \to z_o' + dz_o'$. Elements of target within the beam in the x-y plane are equally likely to emit neutrons if we assume as a first approximation that the beam is of uniform intensity and circular with a radius such that it contains 50% of the beam intensity. Elements in the Z direction, however, will have a probability decreasing as $e^{-\mu d}$ due to the attenuation of photon flux by the target. Here d is the depth in the Z direction into the target (assuming the front face is d=o) and μ is the γ-ray absorption coefficient at the energy of concern taken from tables (St70). Also, d is given by :

$$d(z_o') = z_o + t/2 - z_o' \tag{3.50}$$

where t is the target thickness. Equation 3.49 then becomes :

$$\left\langle \frac{d\varepsilon(\theta)}{d\theta} \right\rangle = \frac{I}{t^2(-1+e^{+\mu t})} \int_{x_o'} \int_{y_o'} \int_{z_o'} e^{\mu z_o'} \frac{d\varepsilon}{d\theta}(\theta, x_o', y_o', z_o') dx_o' dy_o dz_o \tag{3.51}$$

Although this is a complicated equation, it can be solved numerically by first choosing an element of target and a polar angle, θ. Then for each angle ϕ either equation 3.42, 3.43, or 3.44 is chosen depending on the values of r_1, r_2 and r_3. An integration over ϕ is then performed remembering that ϕ_{min} and ϕ_{max} are functions of x_o' and y_o'. Finally integrations are performed over x_o', y_o' and Z_o' and the process is repeated for different values of θ. The results are shown in Fig. 3.15 for different target materials (different values of μ). It should be noted that the differential efficiency is symmetrical about $\theta=\pi/2$ and is quite insensitive to choice of μ. The efficiency is also found to be insensitive to beam area, since the same results, within the limits of error, are obtained by averaging across the beam area and averaging across the total target area as if it were completely illuminated by the beam. This is presumably due to the fact that the center of gravity of the beam and the center of the target are only displaced by approximately 3 mm.

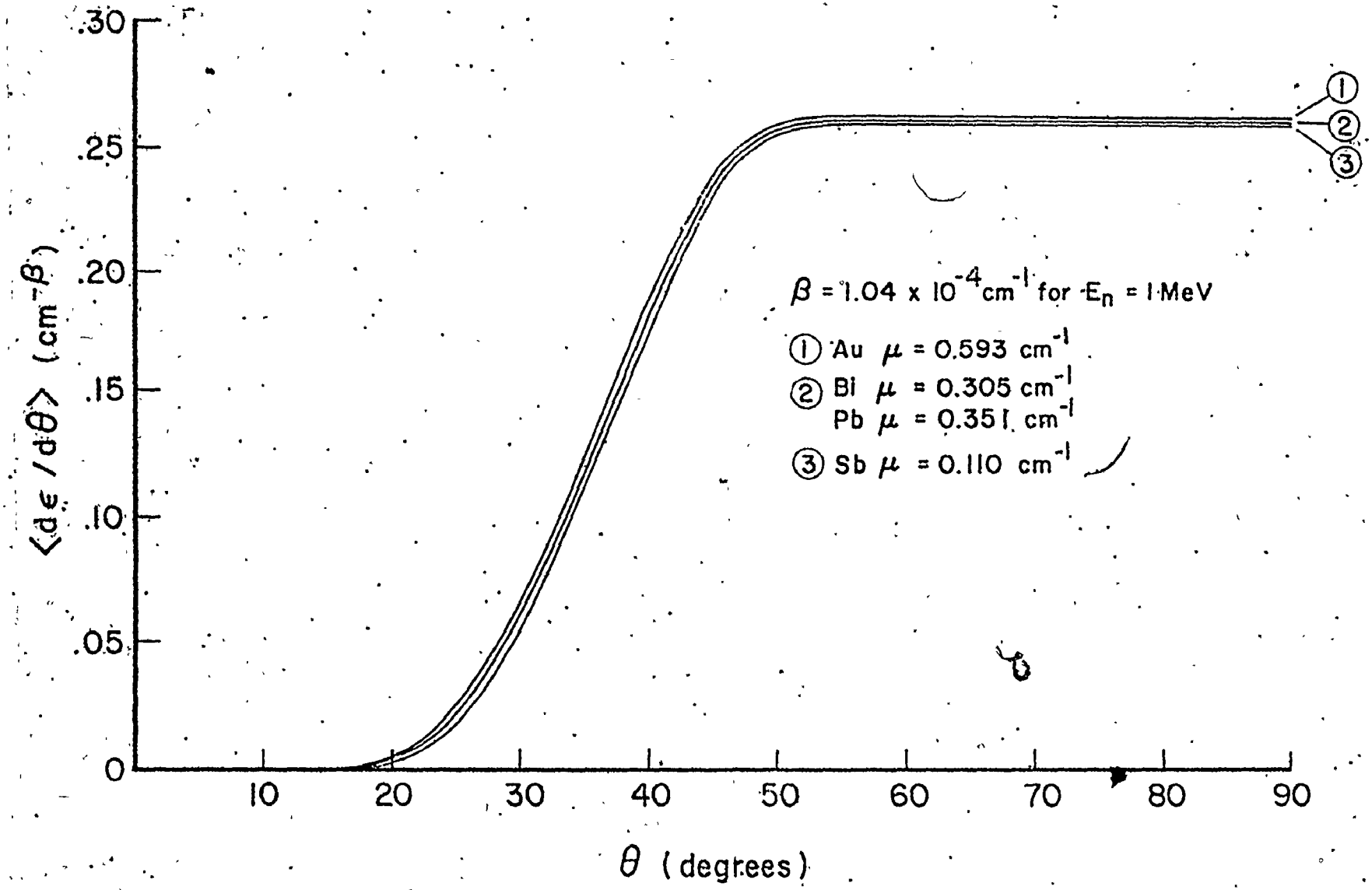

3.15 Average absolute efficiency of FNS-1 spectrometer calculated for parallel geometry as a function of polar angle. Units of efficiency are cm-β, where β is defined in section 3.5.2. Curves are shown for different target materials.

The average total efficiency is given by

$$\varepsilon = \int_0^{\pi} \left\langle \frac{d\varepsilon(\theta)}{d\theta} \right\rangle \, d\theta \qquad (3.52)$$

which requires a knowledge of the value of β.

$$\beta = \frac{n\sigma(1-p)}{4\pi} = \frac{PN_o\sigma(1-p)}{4\pi RT} \qquad (3.53)$$

where σ = 0.835 barns ± (4%) (Fig. 3.1)

$1-p$ = 0.835 ± (4%) (Fig. 3.12)

P = 6atm = pressure of ^3He in detector

N_o = 6.02×10^{23} $mole^{-1}$ = Avagadro's number

T = 295°K ± (5%) = temperature of ^3He

R = 0.08208 $\frac{liters - atm}{mole - °K}$

By integrating numerically 3.52 we thus find that $\varepsilon = 5.08 \times 10^{-5}$ at 1 MeV neutron energy.

It is interesting that a simple minded calculation yields a remarkably close result for ε. Here we assert that

$$\varepsilon = n^1\sigma(1-p) \langle t \rangle \cdot \frac{1}{2} \cdot \frac{\Omega_f}{\Omega_p} \qquad (3.54)$$

where $\langle t \rangle$ is the average chord length through the detector and n^1 is the number of ^3He atoms per unit volume of detector, Ω_p is solid angle subtended by a point source centrally located at the side of the detector, Ω_f is the solid angle averaged over the y dimension of the target. Ω_p and Ω_f may be obtained from Tables (Ma62) and the factor of 1/2 is included since these Tables reference solid angles as a fraction of 2π.

According to Dirac (Ca53), $\langle t \rangle$ is given by

$$\langle t \rangle = \frac{4V}{S} = \frac{4RZ_o}{R+2Z_o} \qquad (3.55)$$

where

V is the detector active volume

S is the surface area of the active volume

and thus we get

$\varepsilon = 5.6 \times 10^{-5}$ which differs by only 10% from the exact calculation.

The relative error in ε will be just the quadrature sum of relative errors in σ, (1-p) and T.

Variation in the other parameters by computer has shown to have a negligible effect in comparison, if we restrict the variation to the errors assigned to R, x_o, y_o, Z_o and t. This yields a relative error for ε of 7.5%.

3.5.3 Efficiency calculation for perpendicular geometry

An experiment to measure possible multipole mixing in natural lead utilized this type of geometry which is shown in Fig. 3.16. The procedure for calculation is much the same as for the parallel geometry case. We first examine a point source at the target center and find the values of r namely r_1, r_2 ($r_1 < r_2$) which are solutions for the intersection of an arbitrary straight line in the θ,Ø direction and a cylinder of infinite extent in the y direction and parallel to the y axis. We get thus :

$$\binom{r_2}{r_1} = \frac{x_o \text{Cos}\emptyset\text{Sin}\theta + Z_o \text{Cos}\theta (\pm)\sqrt{A}}{\text{Cos}^2\emptyset\text{Sin}^2\theta + \text{Cos}^2\theta}$$

where

$$A = (R^2 - x_o^2)\text{Cos}^2\theta + (R^2 - Z_o^2)\text{Cos}^2\emptyset\text{Sin}^2\theta + 2x_o Z_o \text{Cos}\emptyset\text{Cos}\theta\text{Sin}\theta \quad (3.56)$$

r_2 corresponds to the + root and r_1 to the - root

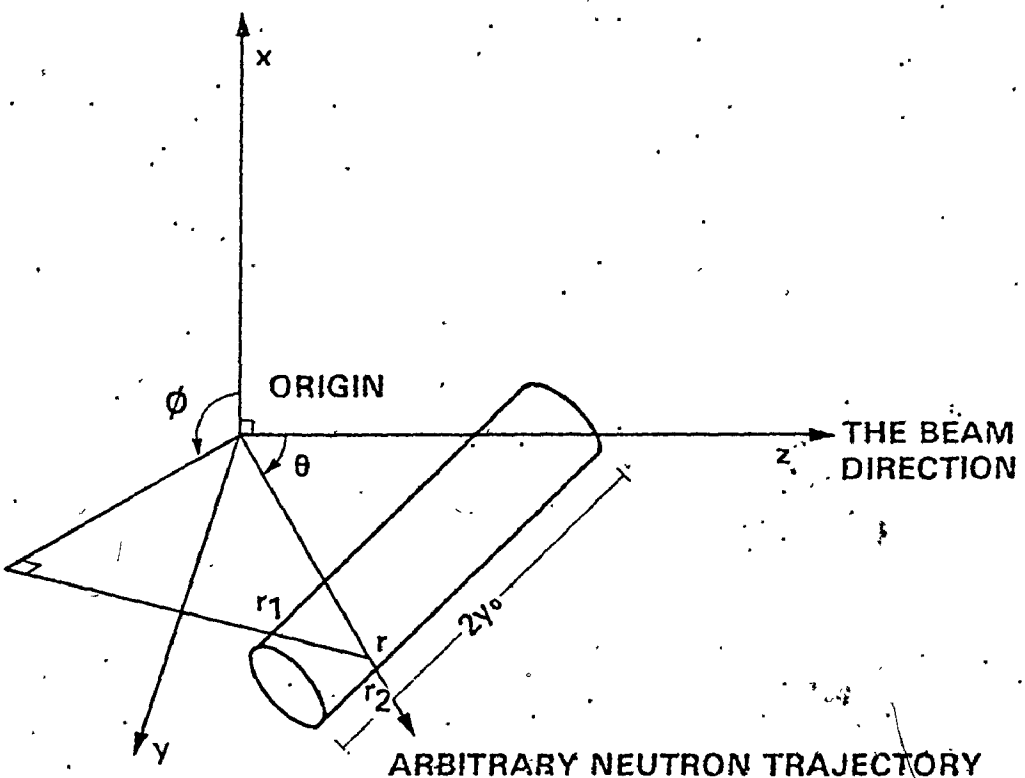

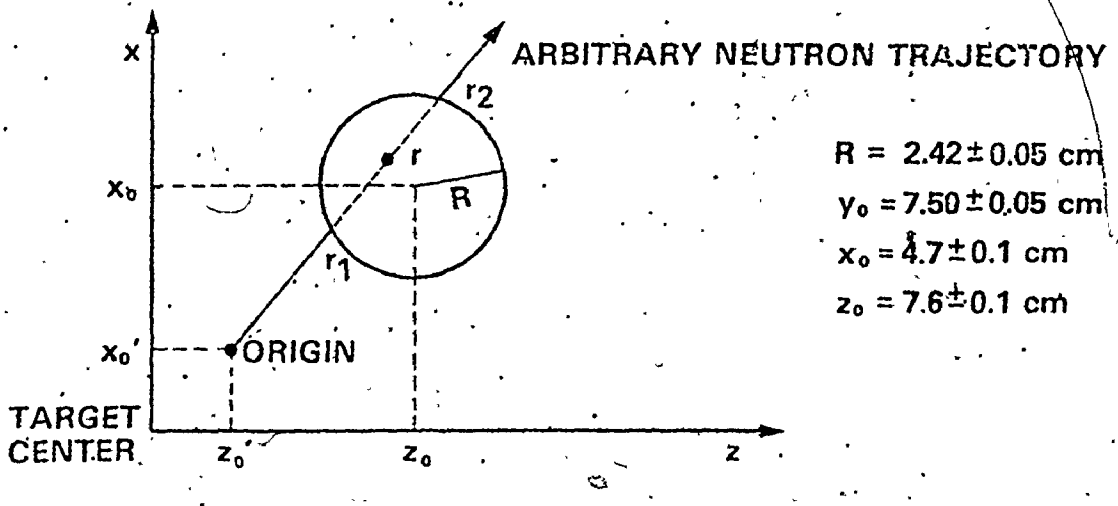

ORIGIN IS CENTRE OF INFINITESMAL ELEMENT OF TARGET AT A POSITION (x_0', y_0', z_0') FROM TARGET CENTRE

3.16 Perpendicular geometry used to derive the efficiency in section 3.5.3. Symbols are defined in that section.

$$r_3 = y_o / (\text{Sin}\phi\ \text{Sin}\theta) \qquad (3.57)$$

is the equation of the x=Z plane which forms the boundary for the active volume (we need consider only positive y since negative y will be identical). $\ell(\theta,\phi)$ and $d^2\varepsilon(\theta,\phi)$ are as defined in equations 3.31 to 3.37, except with no constraint on θ. The differential efficiency $d\varepsilon(\theta)/d\theta$ is now given by

$$\frac{d\varepsilon\theta}{d\theta} = 2 \int_{\phi min}^{\phi max} \frac{d^2\varepsilon(\theta,\phi)\,d\phi}{d\theta d\phi} \qquad (3.58)$$

where the factor of 2 accounts for the fact that we are integrating only for positive y and hence $o \leq \phi \leq \pi$. ϕ min, ϕ max (collectively denoted ϕm) are the roots of the equation :

$$R^2(\text{Cos}^2\phi m\text{Sin}^2\theta+\text{Cos}^2\theta) = (Z_o\text{Cos}\phi m\text{Sin}\theta-x_o\text{Cos}\theta)^2 \qquad (3.59)$$

namely :

$$\text{Cos}\phi m = \frac{\text{Cos}\theta}{\text{Sin}\theta} \cdot \frac{x_o z_o \pm R\sqrt{x_o^2+z_o^2-R^2}}{z_o^2 - R^2} \qquad (3.60)$$

If $\cos\phi_{min} > 1$ we chose $\phi_{min} = o$ since this corresponds to the case wherein a ring of constant θ intersects the detector only once for $o \leq \phi \leq \pi$, instead of twice. Again, for a finite target we must average the differential efficiency over all dimensions as in equations 3.49 to 3.51. In this case, however, the target is (2.54 ± 0.05)cm by $(2.54 \pm 0.05$cm) in the x and y directions but only (0.64 ± 0.05)cm thick in the Z direction. This has been evaluated numerically and is shown in Fig. 3.17. The efficiency is quoted in units of β since we require only the angular dependence for experiments utilizing this geometry. Although, as in section 3.6.2 β is accurate to 7.5%, the angular dependence has been found by variation of parameters within the errors assigned in Fig. 3.18 to be $\sim$ 2 to 4%.

3.6 The Measurement of Relative Efficiency and Energy Resolution

Because of assumptions made in the wall effect calculation (section 3.4) it was felt necessary to perform an experiment to measure the energy dependence of the detector efficiency. This was achieved by

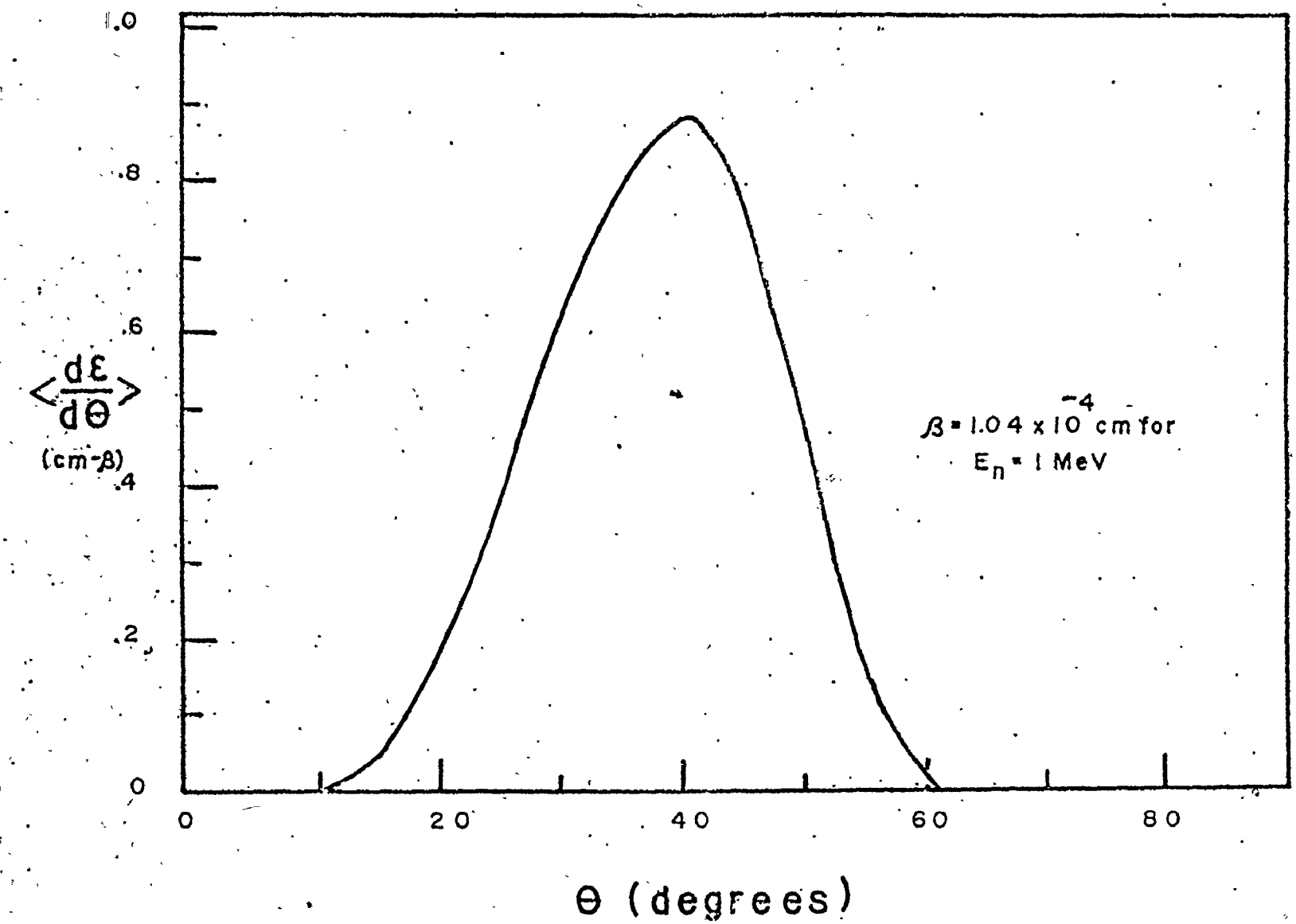

3.17 Average absolute efficiency of FNS-1 spectrometer calculated for perpendicular geometry as a function of polar angle. Units of efficiency are cm-β, where β is defined in section 3.5.2.

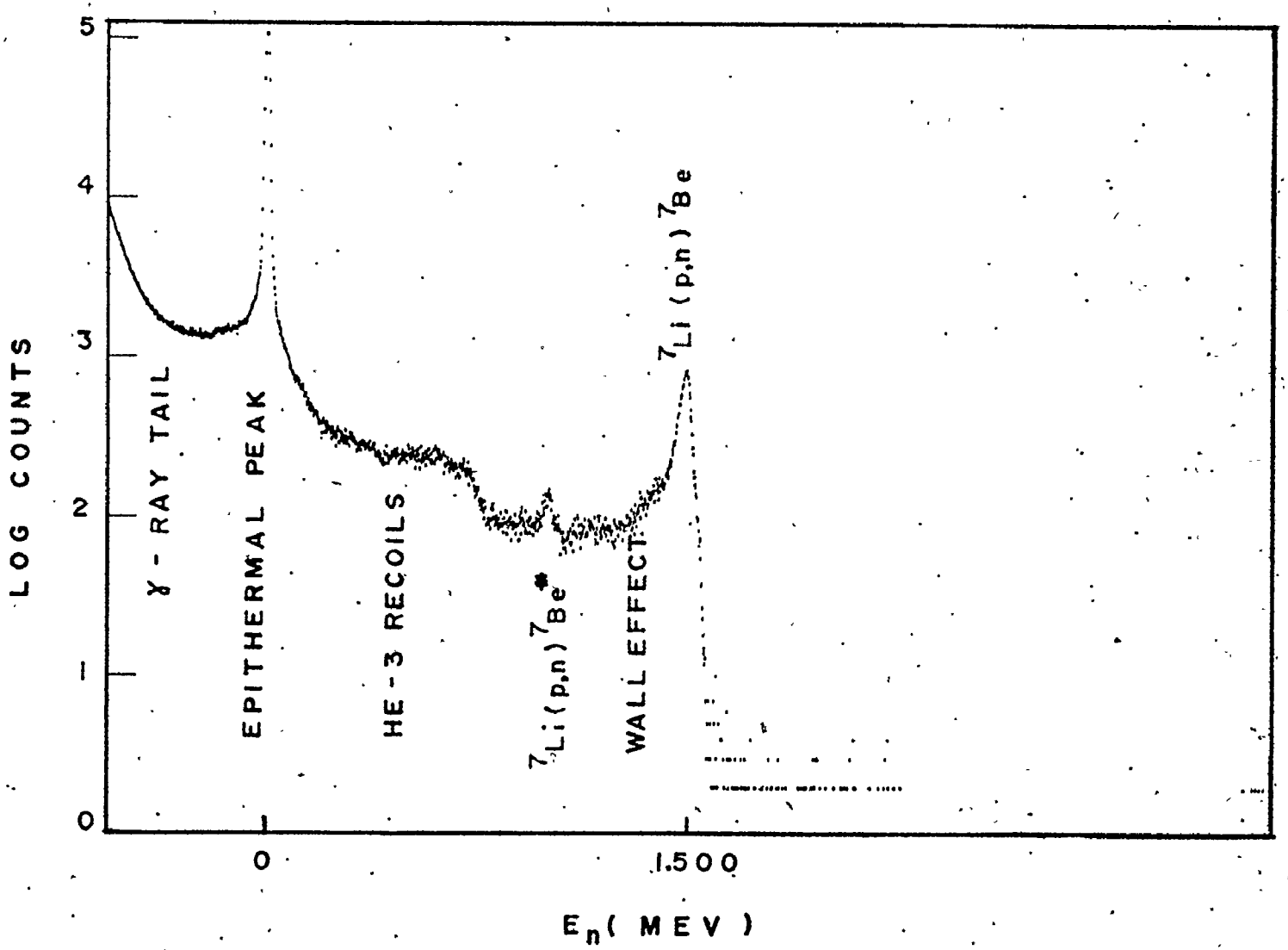

3.18 Measured response of the FNS-1 spectrometer to monoenergetic neutrons from the $^{7}Li(p,n)$ reaction. Proton energy is 3.2 MeV and details of the experimental arrangements are in section 3.6.

utilizing monoenergetic neutrons from the $^{7}Li(p,n)^{7}Be$ reaction.

A measurement of absolute efficiency was not done for two reasons. In the first place, the absolute efficiency calculation required no assumptions and it was felt that its accuracy of 7.5% was quite sufficient for the present experiments. Secondly, the absolute efficiency is very dependent upon source-detector geometry (section 3.5) and a measurement could not be performed for the arrangements used, since the neutron energy in neutron producing charged particle reactions is a function of emission angle.

The $^{7}Li(p,n)^{7}Be$ reaction has been studied in much detail and its use as a source of monoenergetic neutrons has been well documented by Gibbons and Newson (Gi60). A 10 μa proton beam was generated by the McMaster 3MV KN accelerator and was defocussed to produce a beam spot of approximately 1 cm diameter on the target in order to prevent evaporation of the LiF. The targets were composed of (50 ± 10) $\mu g/cm^2$ AnalaR grade natural LiF vacuum evaporated on 0.05 cm thick tantalum backings. In order to further prevent

target evaporation or burn-out, the targets were water cooled by thermal conduction between the tantalum backing and a copper faced target holder. The detector was positioned coaxially with the beam at 0° to the beam direction and 0.80 meters away from the target (target center to active volume center) in order that the energy spread due to reaction kinematics would be small. Also, since relative efficiency was found to be insensitive to geometry (section 3.5) the orientation would not seriously affect the measured variation. In order to monitor the neutron intensity at the detector position, a long counter was constructed similar in design to the long counter of Hanson (Al60) which had eight-one inch holes in its face. The monitor was placed 1.8 m behind the detector to minimize back scatter into the detector and was again coaxial to the beam.

The efficiency curve for the long counter has been measured by Hanson (Ha47, Al60) and is seen to deviate by only 10% from constancy over the energy interval of interest with an accuracy of about 2%. The long counter was also very insensitive to room

scattered neutrons since any thermal neutron flux was attenuated by a factor of 1000 in the middle 1.3 cm thick sheath of B_2O_3 and epithermal neutrons were well moderated in the 10 cm outer layer of paraffin and then absorbed.

At each energy, data were collected for approximately 2 to 4 hours in order to get at least one percent statistics in the neutron peak. A typical spectrum taken at a proton energy of 3.200 MeV is shown in Fig. 3.18 which clearly shows the neutron groups corresponding to the ground and first excited states of ^7Be. The wall effect, ^3He recoil spectrum, epithermal peak and gamma ray response can also be seen.

The epithermal neutron rate was sufficiently large to produce a sum peak of 1.528 MeV total energy which was clearly seen at low proton energies for which the maximum energy of neutron spectrum was less than 0.764 MeV. This sum peak, in conjunction with the epithermal peak was used to obtain the neutron energy calibration which had the advantage of not requiring a knowledge of the accelerator energy calibration.

As a further check the difference in energy of the ground state neutron group and excited state group were determined for energies above the $^{7}Li(p,n)^{7}Be$ threshold and were found to be in all cases, consistent to within 5 keV with the value quoted by Gibbons (Gi60).

Peak areas and centroids were determined by use of the nonlinear least squares fitting program JSPLOT, described in Chapter 6. The error for the centroid of a given peak was found to be $\sim$ 1 keV and for the area was $\sim$ 2.5%. These errors were seen to be greater than pure statistical errors and are presumably due to the deviation of the real peak shape from a Gaussian with low energy exponential tail. The measured efficiency is shown in Fig. 3.19 and is compared with the calculated efficiency from section 3.6. Errors are the quadrature sum of the uncertainty in monitor rate and peak area, approximately 4%, and agreement with the calculation is excellent. Also included in Fig. 4.20 are data collected by Dr. H. Franz and Dr. J.M. Cuttler (Fr73, Cu73) using the same model of detector and the same reaction. Their experiments and analysis procedures differed from ours in two aspects.

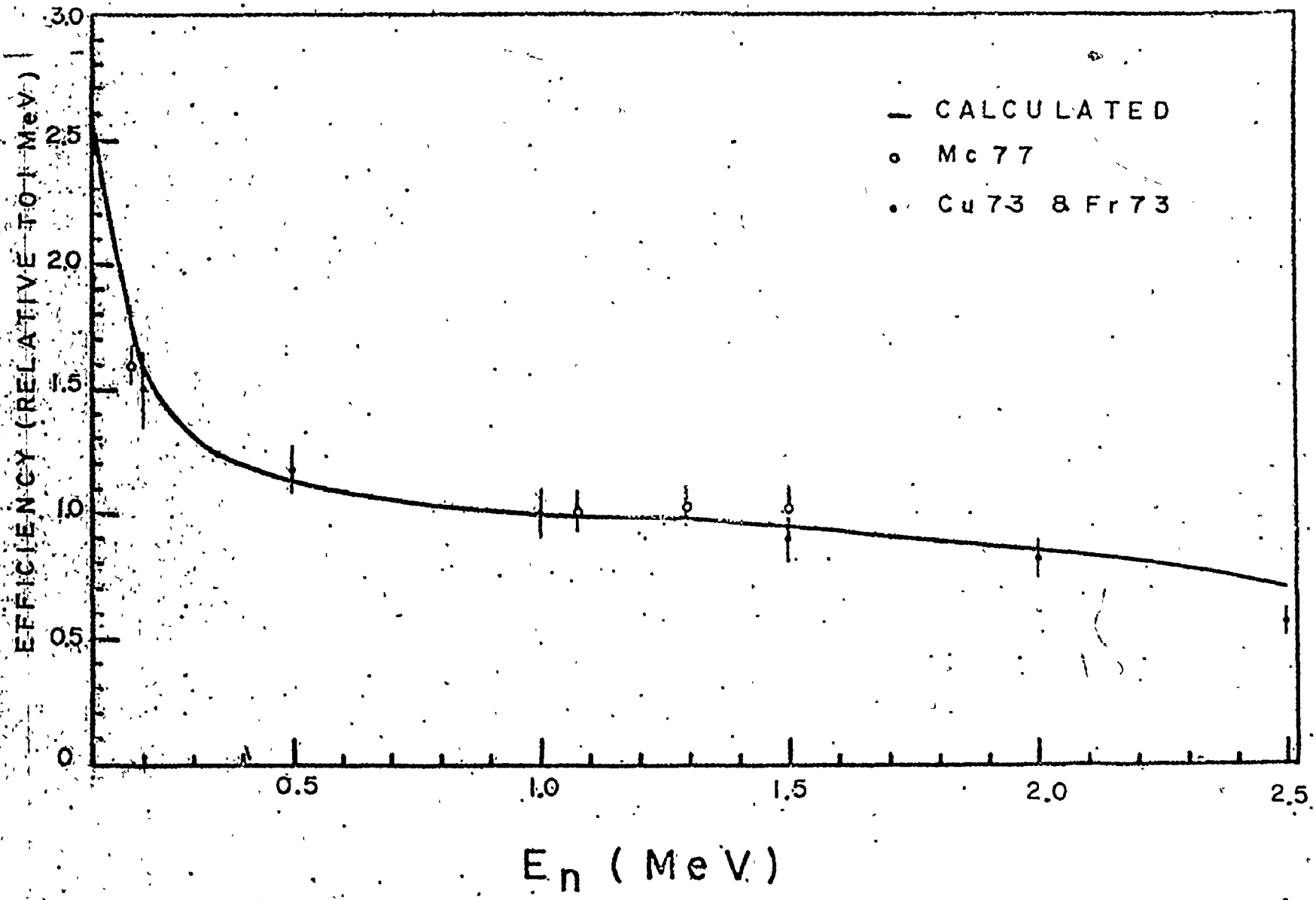

3.19 Measured relative efficiency of FNS-1 spectrometer compared to calculated efficiency. The latter is a copy of the curve of Figure 3.13. Open circles are from the experiments described in section 3.6. Closed circles are from the experiments of Franz and Cuttler.

First, they have normalized their efficiency to the total charge collected on a Faraday cup and secondly, they have determined the efficiency for peak height instead of area. This latter point has required us to multiply their results by the detector resolution at each neutron energy which we have determined as described below. Franz and Cuttler's measured relative efficiency is seen to be in excellent agreement with the calculated efficiency up to 2 MeV and is one standard deviation low at 2.5 MeV neutron energy. This suggests that the calculated efficiency is accurate to about 4% up to 2 MeV and is between 4 and 8.5% for neutron energies in the 2 MeV to 2.5 MeV range. To facilitate calculation of errors, the error was assumed to increase linearly between 2 and 2.5 MeV.

An attempt was made to determine the energy resolution of the detector (FWHM) by utilizing both the $^{7}Li(p,n)^{7}Be$ data and well isolated peaks from the photo-neutron data of Chapter 6. The latter data is shown in Fig. 3.20a. The errors are derived from the fitting program JSPLOT as described in Chapter 6 since the photon

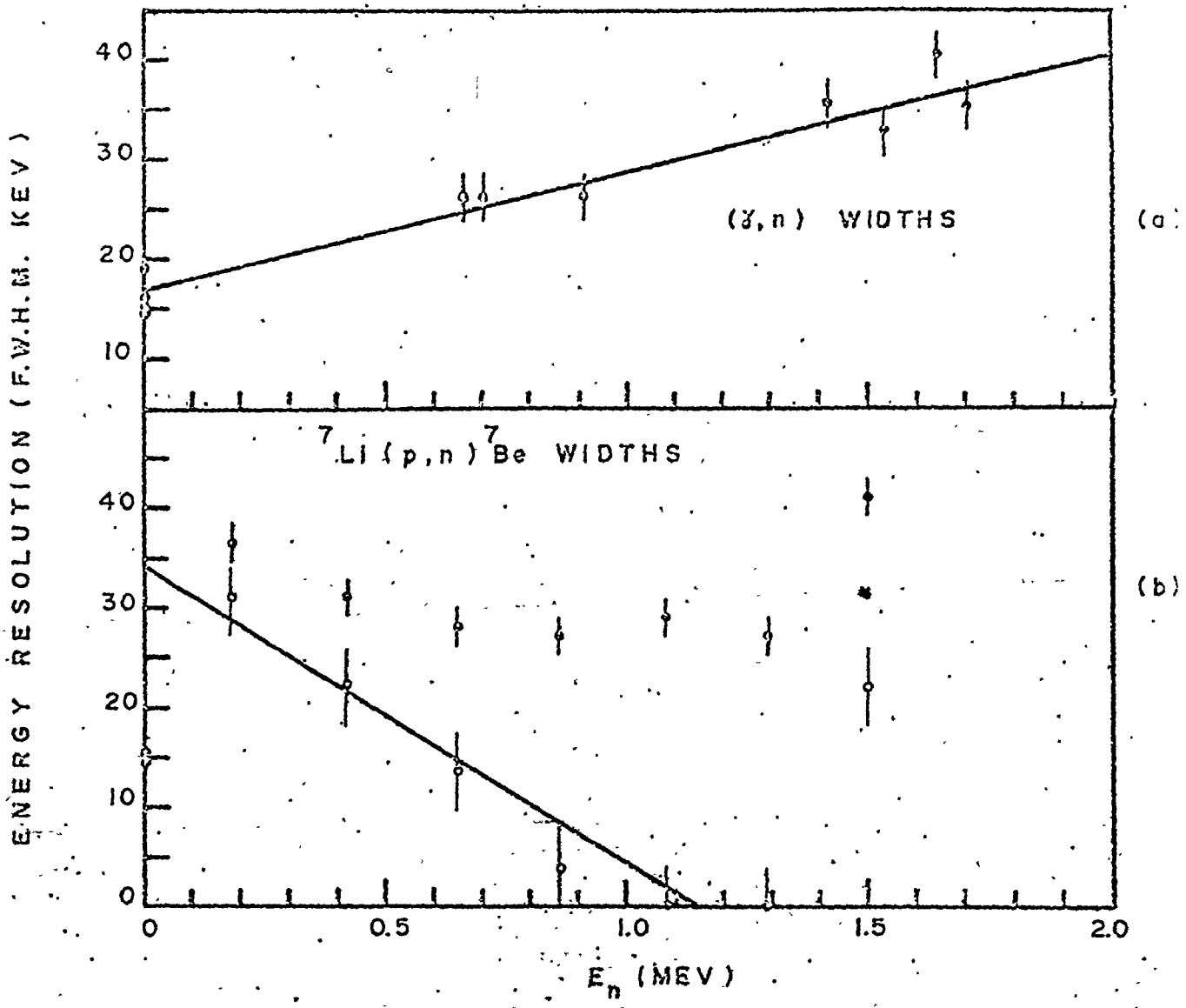

3.20 Measured energy resolution (full width at half maximum) of the FNS-1 spectrometer. Figure (a) shows a linear fit to peak widths derived from isolated peaks of photoneutron spectra. The closed circles of Figure (b) are the widths extracted from the ^{7}Li(p,n) experiments of section 3.6. The open circles represent the broadening due to finite thickness and have been calculated by subtracting the linear fit of Figure (a) from the ^{7}Li(p,n) widths. These points (excluding the last) due to finite target width have been fitted to a straight line.

widths are negligible. The data was fitted to a variety of functions using weighted linear and non-linear least squares fitting programs written by the author. The best fit obtained was a straight line of the form $\delta = A + BE_n$ with the terms as defined for equation 3.12. The best estimate coefficients, which yield a reduced $\chi^2 \sim 1$ for 6 degrees of freedom are $A = 16.8 \pm 1.1$ and $B = 12.0 \pm 1.1$ when δ is in keV and E_n is in MeV. This fitted line, which has an error per point of approximately 1 keV (from the variance-covariance matrix), is the one used previously to correct Franz and Cuttler's efficiency data.

The energy resolution data for the $^7Li(p,n)^7Be$ are shown as circles on Fig. 3.20b. First, it should be noted that there are more points than for the efficiency curve. This is due to an experiment which was being performed on the FN Tandem while the three middle points were being obtained. This produced a large quantity of high energy neutrons adjacent to our experiment which upset the neutron monitor. It was still possible, however, to observe the neutron peaks in

the spectra and extract the widths. The target thickness of 50 $\mu g/cm^2$ corresponds to an energy loss of approximately 5 keV (Cu71a) for protons of energy 2 MeV but Gibbons (Gi60) has noted that the true target thickness may be several times the measured average thickness due to the convoluted nature of the target surface. Furthermore, energy spread of the neutron groups is caused by energy straggling of protons in the target and although this is related to average thickness, the relationship is not clear. Thus the error in width of neutron groups is taken as the quadrature sum of the kinematic energy spread (1 keV) and the error assigned by JSPLOT, although the error may possibly be larger. It is clear that the widths decrease with energy and then increase again. This was assumed to be due to the sum of an energy straggling term which should decrease with energy and the detector resolution which increases with energy. To test this hypothesis, the straight line fit to the (γ,n) widths was subtracted in quadrature point by point from the $^{7}Li(p,n)^{7}Be$ widths. The result which

should be the energy straggling term is shown as open circles in Fig. 3.20b and clearly decreases in energy within experimental error (excepting the last point). Although a $1/E$ type relationship might appear to be reasonable, since it is proportional to the Bragg curve, in actual fact the best fit excluding the last point is a straight line in energy shown in Fig. 3.20b which yields a reduced χ^2 of 0.8 for 4 degrees of freedom or a confidence level of 95%. Since these data could not be easily used to extract the detector resolution, it was felt that it would be more accurate to use the (γ,n) widths.

3.7 Analysis of the Distribution of Risetimes

It was mentioned in section 3.4 that continuum events (wall effect, ^{3}He recoil) have different risetime distributions for a given energy than full energy (peak) events. It was also noted that the energy resolution at large neutron energies is due in large part to risetime dispersion and hence might be improved by risetime selection. Furthermore, for ion tracks with any radial component, risetime increases.

with track length and hence energy, allowing rejection of some of the huge epithermal peak by discriminating against short risetimes. Thus, although minimization of ^{3}He recoil events and epithermal events requires elimination of short risetimes, elimination of wall effect events requires rejection of long risetimes for a given neutron energy and thus there might exist an optimum. In order to investigate this, a two dimensional analysis (pulse risetime versus pulse height) was performed utilizing the $^{209}Bi(\gamma,n)^{208}Bi$ reaction and nickel neutron capture photons.

The experimental arrangement is described in Chapter 4 and the geometry chosen was the parallel geometry (section 3.5.2) used for the photoneutron cross section experiments. Bismuth was chosen because of its low number of well spaced levels. The electronics are described in detail in section 4.3.2. Data was collected in a 32 channel (time) by 512 channel (pulse height) array over a period of two weeks. The time resolution of the risetime pickoff circuit was less than one channel width or 0.25 μs (section 4.3.2). The quantity along the

time dimension is actually the difference in time between the leading edge of a pulse and the time at which it crosses zero. Although we shall refer to this as the "risetime", it should be noted that it is not equal to, but rather directly proportional to, the true pulse risetime.

The results are shown in Fig. 3.21 and several points are immediately obvious. Most of the continuum is contained in a narrow range of low risetimes (0.75 to 1.50 μs) and is presumably primarily ^{3}He recoils with wall effect events occurring at all risetimes. The full energy peak for epithermal neutrons is as expected at low risetime values (0.50 to 1.00 μs) with a very few epithermal events occurring at longer risetimes. The entire spectrum decreases with risetime and ends at approximately 4 μs, this presumably being of the order of the electron collection time of a radial ion track for the highest energy (1.530 MeV) neutrons available. The full energy peaks for the fast neutrons span a larger range of risetimes (predominantly 0.50 μs to 2.25 μs) and again as expected the high energy neutron

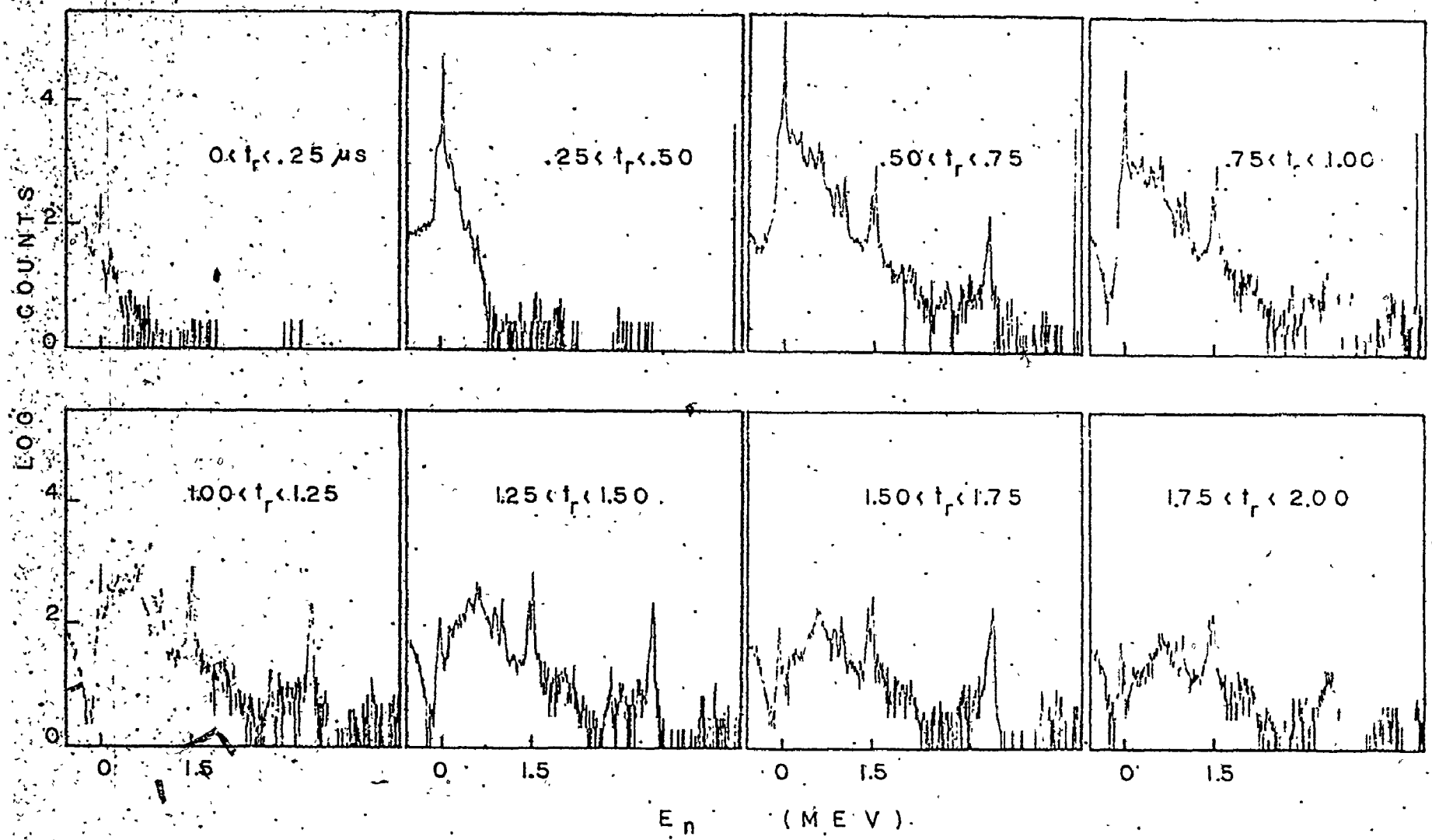

3.21 Spectrum of neutrons as a function of risetime, t_r. Neutrons are from the $^{209}Bi(\gamma,n)$ reaction using a nickel source and are detected by the FNS-1 spectrometer.

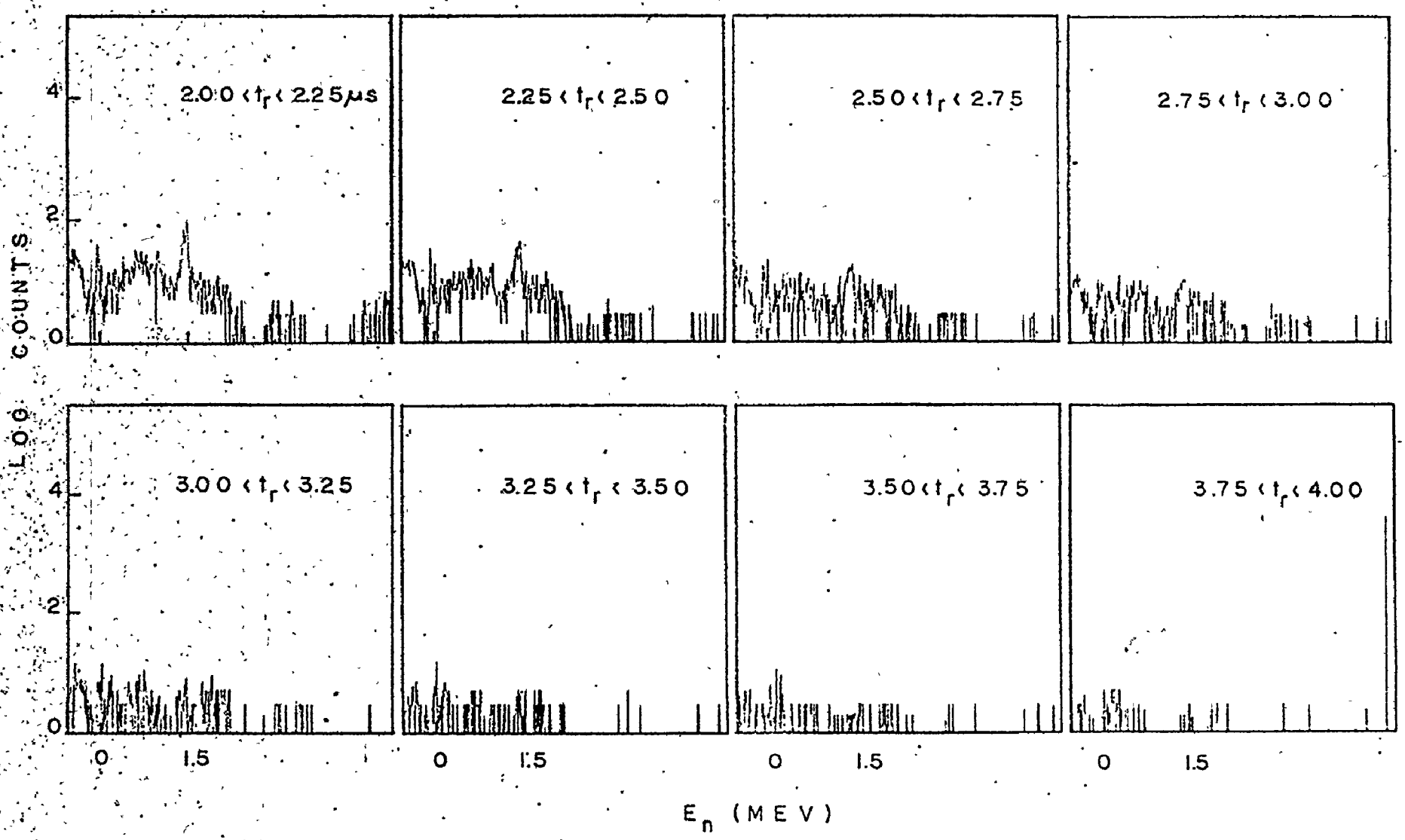
2.00 < t_r < 2.25 μs
2.25 < t_r < 2.50
2.50 < t_r < 2.75
2.75 < t_r < 3.00
3.00 < t_r < 3.25
3.25 < t_r < 3.50
3.50 < t_r < 3.75
3.75 < t_r < 4.00
LOG COUNTS
0
2
4
0
1.5
E_n (MEV)

groups exhibit maximum intensity at larger risetimes than the low energy groups. A low energy continuum (below .764 MeV) occurs predominantly in the lowest risetime group, 0 to 0.25 μs with a small contribution at longer risetimes. Almost all of the interactions for the photon energies (mainly 0.511 MeV) incident on the detector are Compton scattering events and are predominantly in the forward direction. Since most of the photons are from the photoneutron target and thus perpendicular to the detector axis, this implies that the electrons have radial tracks. Since the range for electrons of these energies (section 4.4) are much longer than the length of the active volume, this would imply that photon events would have long risetimes and these events are probably contained in the small, low energy continuum seen at longer risetimes. The low energy continuum at short risetimes, then, is possibly due in part to high specific ionization ^{3}He recoil events which reach the wall before expending their full energy. Also, argon recoils which have a maximum energy of 0.095 E_n probably contribute a substantial percentage of

continuum below 0.145 MeV (corresponding to E_n = 1.530 MeV) since the detector contains three atmospheres of argon with an elastic scattering cross section comparable to ^3He. These events would be expected, due to a very high specific ionization, to have an extremely short track length and hence risetime.

It can be seen, then, that by setting a threshold at low risetime, much of the continuum can be eliminated along with a large portion of the epithermal peak. It must be borne in mind that the epithermal peak should not be totally eliminated since it provides a useful reference for zero neutron energy. Also by setting a low risetime, the sensitivity of the detector for low energy neutrons is decreased which helps flatten the detector response to facilitate easier analysis of data. In order to simulate the effect of setting a discriminator level at low risetime, the two dimensional data were summed over various time channels and several of these pulse height spectra are shown in Fig. 3.22. The optimum case appears to be the spectrum summed from 0.75 to 4.0 μs since it has a small continuum with a small slope

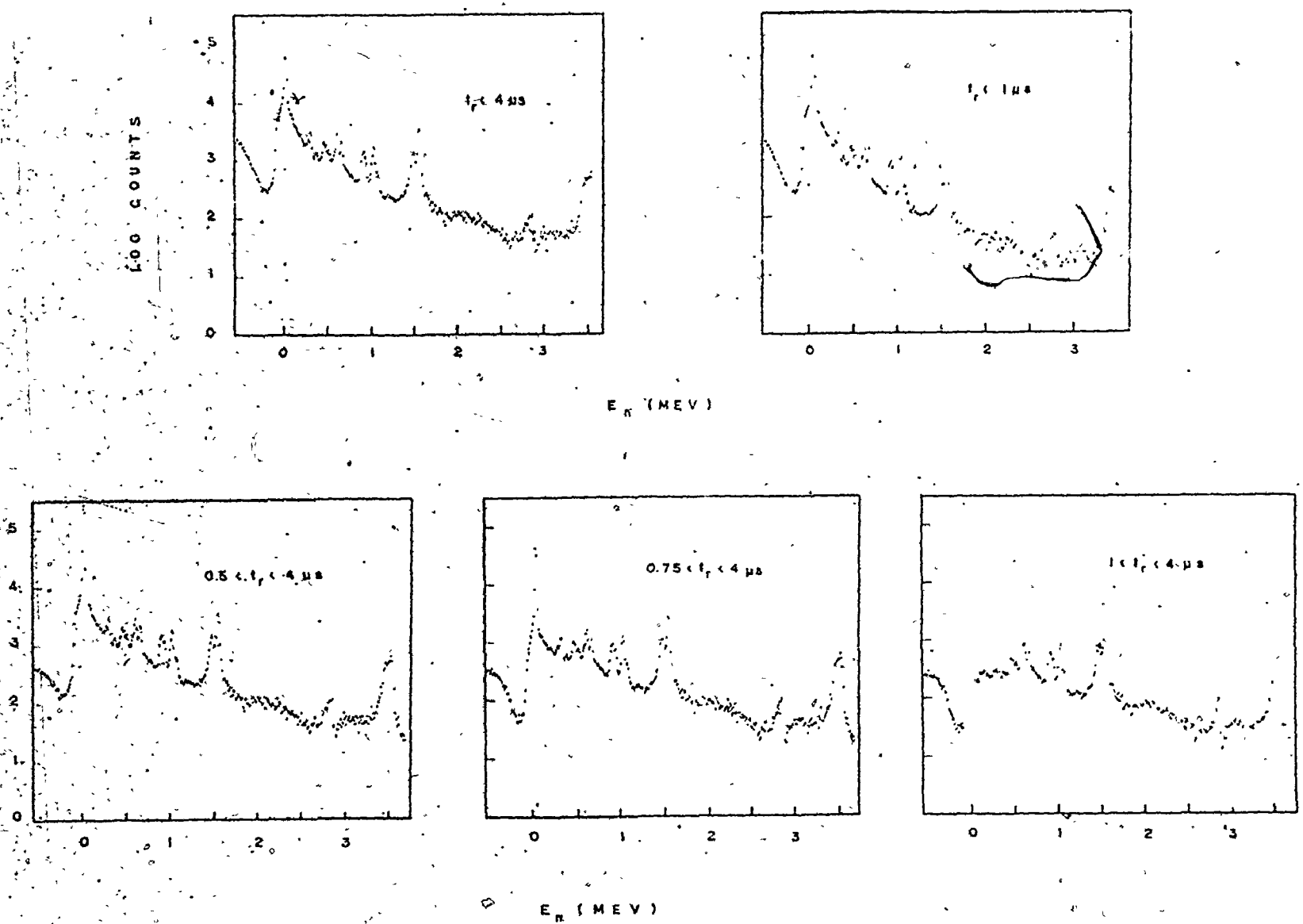

3.22 Spectrum of neutrons for various risetime windows. Neutrons are from the $^{209}Bi(\gamma,n)$ reaction using a nickel source and are detected by the FNS-1 spectrometer. These represent various time slices of Figure 3.2.1 totalized.

and a small epithermal peak which is still large enough to determine zero neutron energy. It should be noted that no significant improvement in energy resolution was observed by just rejecting low risetimes. A full energy peak is, as mentioned in section 3.4, the sum of narrow peaks of slightly different energies due to the dependence of amplifier gain on risetime. In the present experiment it was found by summation of time bins that the use of a time window to improve energy resolution would require such a loss in efficiency as to make the experiment unfeasible. The other alternative would be to apply a shift correction to each peak which would be a function of risetime and energy and then totalize the data. This, however, would require a large number of two dimensional monoenergetic calibration spectra, such as from a $^{7}Li(p,n)^{7}Be$ reaction, and much computer time. Since the improvement in energy resolution would only be of the order of 35% (14 keV) at 2 MeV neutron energy (Cu71a), this was not deemed worthwhile for the present experiment.

Thus, the implementation of risetime discrimination was carried out by rejecting those events with risetimes that occurred below a certain discriminator level. The electronics for this are described in section 4.3.3. The TAC range was shortened to 4 μs since very few events were seen to occur above this value and thus with an expanded timescale a threshold could be more easily set. As previously stated, optimum results were achieved by using a range of risetimes from 0.75 μs to 4.0 μs. This window was attained by use of the SCA remembering that 4.0 μs corresponded to a 10 volt TAC output. It was realized that the risetime discrimination would affect detector efficiency in an unpredictable manner and thus it would be necessary to determine this new efficiency. This was done by observing $^{209}Bi(\gamma,n)^{208}Bi$ spectra using photons generated by neutron capture on chromium with and without risetime rejection. The spectra were collected over a two week period and normalized to the same incident photon flux by use of the flux monitor (Chapter 4). The two spectra are shown in Fig. 3.23. In order to determine the efficiency as a function of

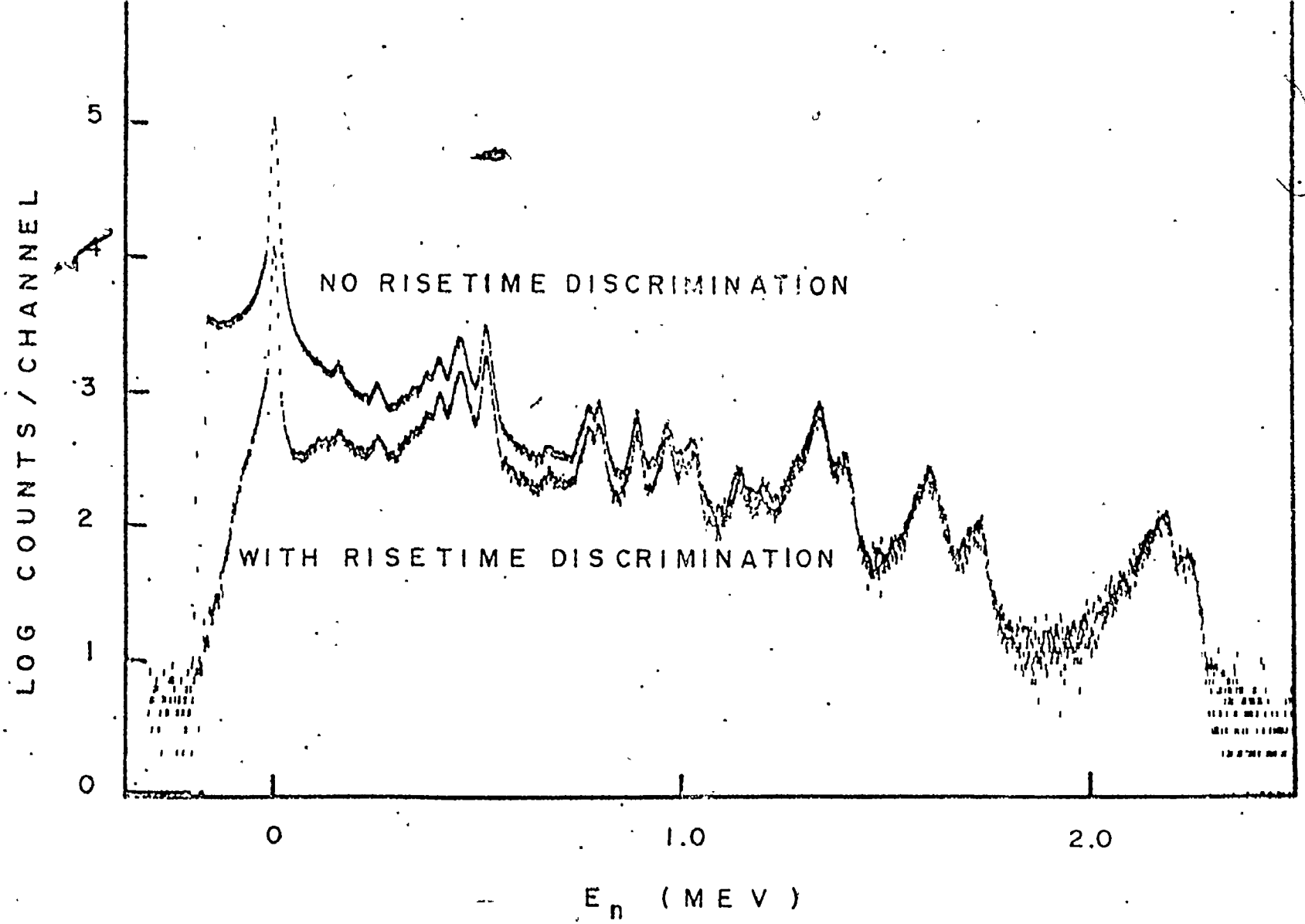

3.23 Comparison of spectra with and without risetime selection. Neutrons are from the ^{209}Bi(γ,n) reaction (chromium source) and are detected by the FNS-1 spectrometer. Window for the risetime selection is that used in the actual photonuclear experiments.

energy, peak areas were determined using the program JSPLOT, and the ratio, ρ_R, of the intensity with risetime rejection to intensity without risetime rejection at a given neutron energy, E_n, is shown in Fig. 3.24. The energy calibration procedure is explained in Chapter 6 as is the peak fitting program JSPLOT. The relative errors assigned to the efficiency ratio are the quadrature sum of the relative errors of the peak intensities with andwithout risetime discrimination. Relative errors for peak intensities were taken as the quadrature sum of the relative error in the beam monitor rate (Chapter 3) and the relative error due to the peak fitting program (Chapter 6) since error in timing was negligible. A variety of functions were fitted to the risetime ratio data and the best fit with a χ^2 of 1.5 for 26 degrees of freedom was obtained using a function of the form $A(1-e^{BE_n})$ as shown in Fig. 3.24. The standard deviation in the curve was found by variance-covariance analysis and is also plotted in Fig. 3.24.

The risetime ratio can now be used to determine the relative efficiency with risetime discrimination,

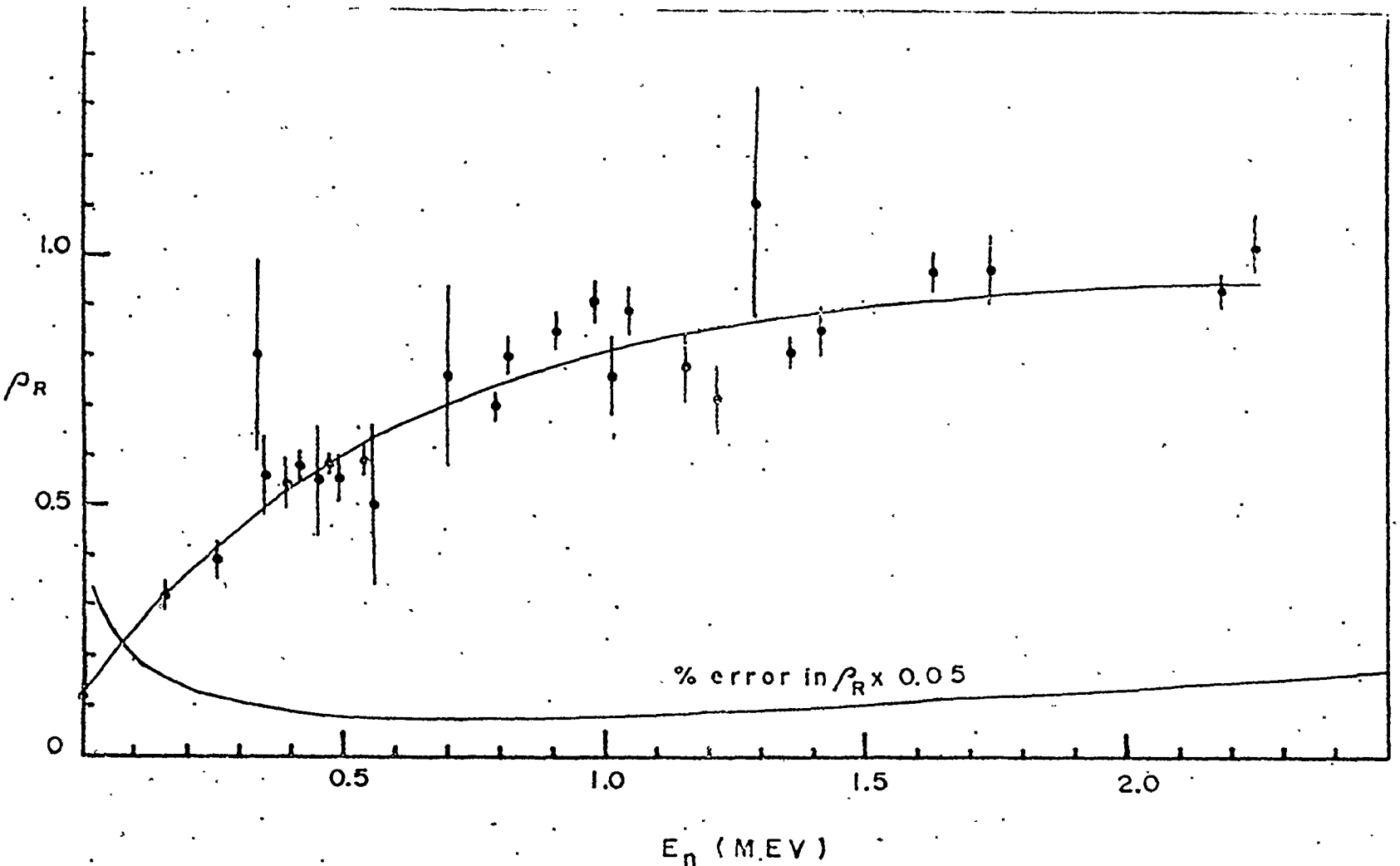

3.24 Ratio of efficiency of the FNS-1 spectrometer with risetime selection to efficiency without risetime selection as a function of neutron energy. Ratios are determined from the spectra of Figure 3.23 and have been fitted to an exponential form. The percentage uncertainty, reduced by a factor of 0.05, is also shown. Window for the risetime selection is that used in the actual photonuclear experiments.

η_R and η_R is given by :

$$\eta_R(E_n) = \rho_R \eta(E_n) \qquad (3.61)$$

and it is plotted in Fig. 3.25. To get the absolute efficiency for a given energy with risetime discrimination; η_R must be multiplied by the absolute efficiency at 1 MeV neutron energy. The relative error in η_R is found by quadrature addition of the relative errors in ρ_R and $\eta(E_n)$ and is also shown on Fig. 3.25. It must be remembered that η_R would apply only for the electronic configuration used in these experiments and any change in the risetime electronics or even the discriminator level set on the TAC output would require the determination of a new η_R. In addition since it was possible for the discriminator level to drift, it was necessary to periodically collect reference spectra ($^{209}Bi(\gamma,n)^{208}$ for a Cr source) and check that the relative intensities had not changed. Risetime discrimination was used for all targets when the chromium source was used and also for the enriched ^{208}Pb target with nickel capture gamma rays.

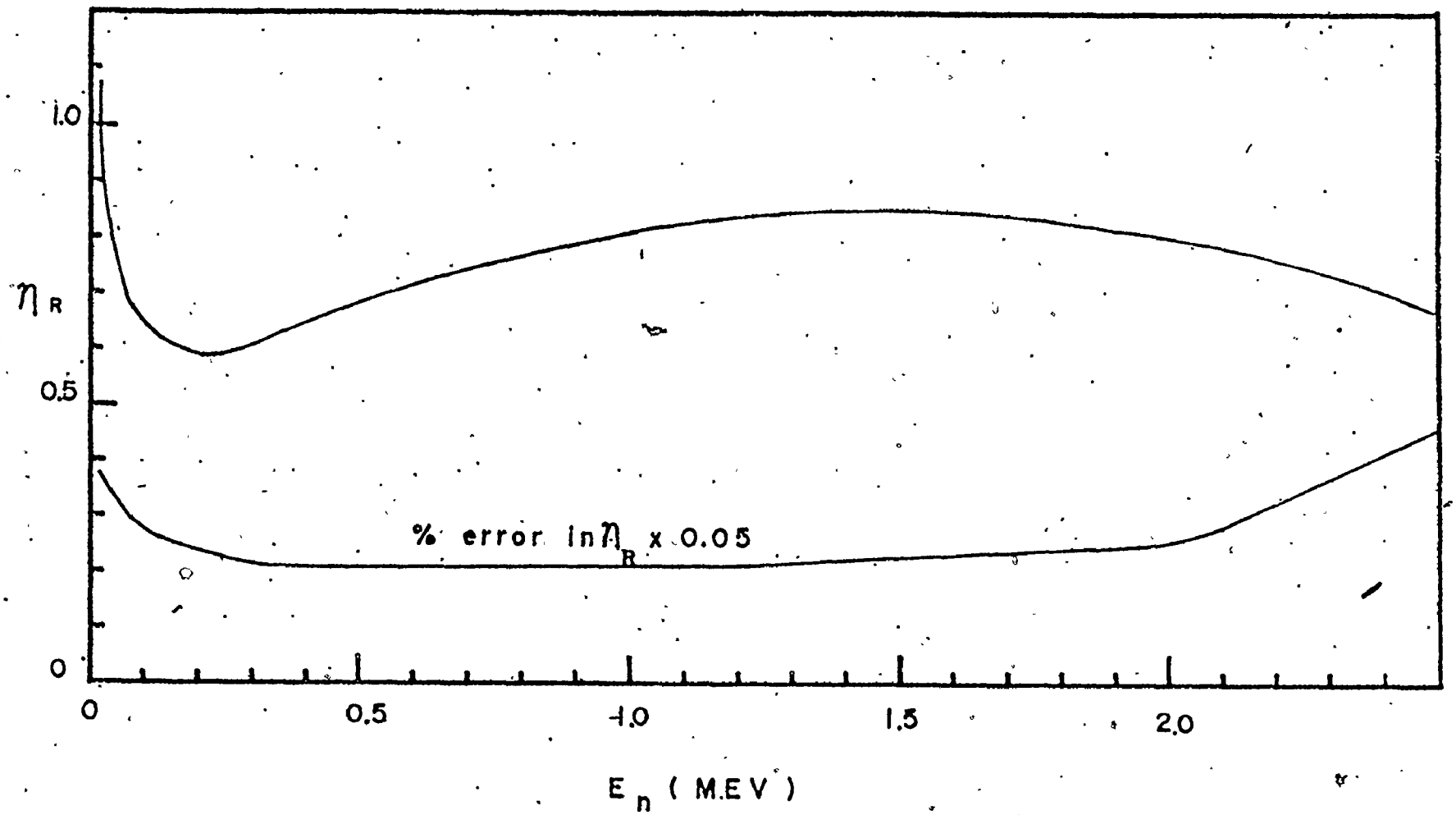

3.25 Relative efficiency of the FNS-1 spectrometer as a function of neutron energy when risetime selection is employed. This curve is the product of the curves of Figures 3.13 and 3.24. The percentage uncertainty, reduced by a factor of 0.05, is also shown. Window for the risetime selection is that used in the actual photonuclear experiments.

3.8 An anomaly in the detector response

Despite the agreement between the theoretical expectations and the observed detector response as mentioned previously, there existed one anomaly. As can be seen in Fig. 3.26 there were three flat topped peaks (labelled ANOM 1, 2 and 3) occurring in the spectra with total energy centroids of 3.55 ± 0.05, 4.3 and 4.54 ± 0.05 MeV. In actual fact, it was found that when sufficient statistics were collected the middle group was a doublet with centroids at 4.23 ± 0.05 and 4.32 ± 0.05 MeV total energy. It was further observed that the peaks were independent of source and target materials and in fact, completely independent of the reactor since they were observed with the same intensity in a different building. The width (FWHM) of the two smaller peaks was approximately 80 keV which was about 20 keV wider than that determined from photoneutron widths extrapolated to that energy (section 3.6). The doublet was observed to be approximately 160 keV in width and it is interesting to note that none of the peaks could be fitted very well to Gaussians or sums of

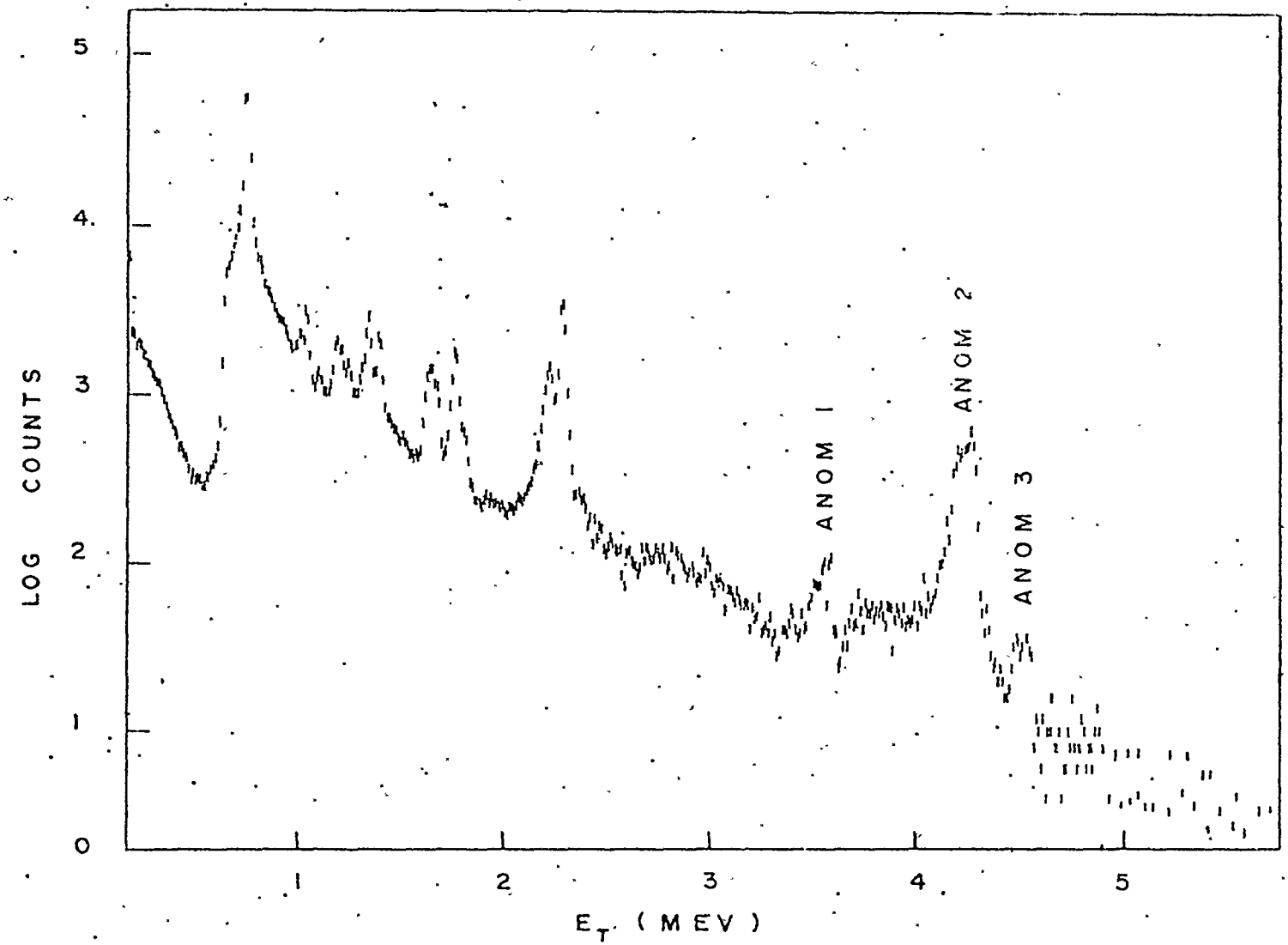

3.26 Spectrum taken by the FNS-1 spectrometer showing the three anomalous background peaks. Total energy deposited in the counter is plotted on the x-axis. Spectrum was collected over a two week period.

Gaussians with or without exponential tails. Furthermore, it was observed that the doublet actually consisted of several narrow peaks shifted in energy according to their risetime, somewhat similar to a normal fast neutron pulse. The anomalous peaks were not, however, observed in a 2.54 cm diameter by 10.16 cm length (active volume) non-gridded Harshaw proportional counter filled with 10 atm of ^{3}He.

In order to test the time interval distribution of the peaks, an energy window was set on the doublet and the SCA output signal was fed into a NOVA computer based pulse height analyser* which was programmed to measure time intervals between incoming pulses. The dwell period of the analyser was 20 sec/channel which gave a full scale range of 11.4 hours for the 2048 channels used. The resultant time interval distribution collected over a 115 hour period is shown in Fig. 3.27. The data was fitted to a variety of functions, the best being an exponential function which gave a reduced χ^2 of 1.02 for 59 degrees of freedom. This then suggested that the events were randomly distributed in time with a mean time between events of 192.3 ± 3.7 sec.

---

* designed and built by Gordon Cormick, M.Sc.

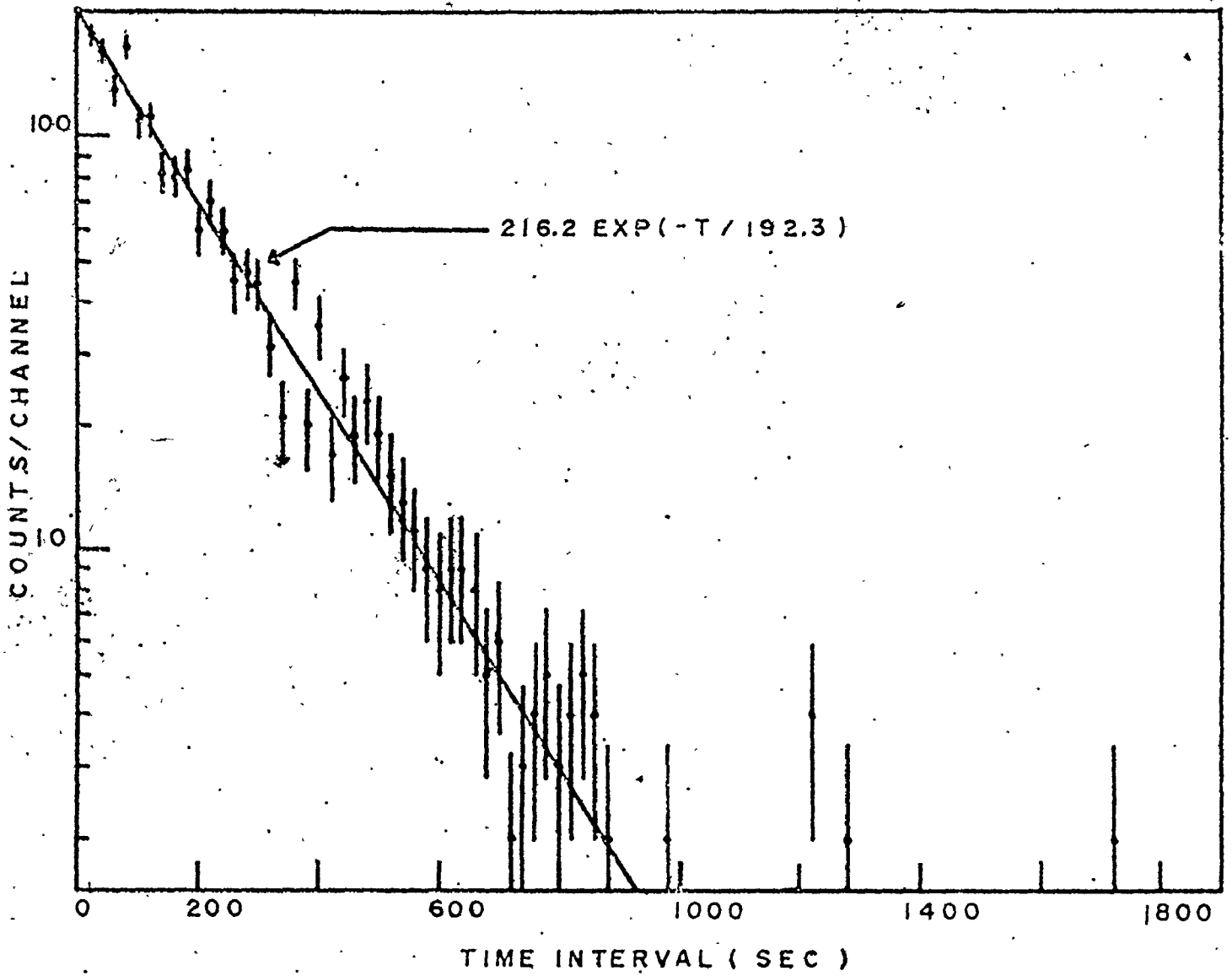

3.27 Time interval distribution of pulses from the second anomalous peak. Distribution has been fitted to the exponential form shown.

To date no ready explanation has been found for the existence of these peaks but several possibilities have been suggested:

1) Electronic effects
   a) high voltage discharge due to faulty or dirty insulation
   b) radiofrequency pickup by the preamplifier.
2) Internal ionizing radiation
   a) radioactive contaminants in the gas filling
   b) radioactive impurities in the detector walls, anode wire or insulators.
3) External ionizing radiation.

High voltage discharge appears to be a likely candidate although it is difficult to comprehend a discharge mechanism which would yield a broad risetime distribution, have three specific energy bands and be random in time. Nevertheless, such mechanisms can be complex and hence this possibility cannot be easily dismissed.

Radiofrequency pickup was quickly eliminated when the preamplifier was shielded with grounded aluminum

foil and no change in the count rate was observed.

A search was made in the literature for all possible radioactive contaminants that could produce ionizing radiation at the above energies. A list of all known natural alpha, beta and electron emitters and spontaneously fissionable nuclei were processed, omitting γ-rays since these deposit only a small amount of energy in the detector (section 3.4). The only possible contaminant that could be found was ^{226}Ra which emits alpha particles of energy 4.78 and 4.60 MeV and its daughter ^{210}Pb with an alpha of 3.72 MeV (Le67). This hypothesis possesses some flaws. In the first place, the energies of the α particles from ^{226}Ra and ^{210}Pb are greater than measured and the energy difference increases with energy. The first fact might be explained by charge recombination occurring due to the high specific ionization of the α particles but the second fact negates this possibility since specific ionization varies inversely as the particle velocity. The second fact also rules out energy loss due to the contamination being imbedded in the detector walls. In addition, three alpha groups with energies 5.3, 5.5 and

6.0 MeV which belong to daughters of radium, are missing. Although one could argue that this was due to diffusion of the ^{222}Rn daughter out of the detector, it is difficult to see why the ^{210}Pb, which is a daughter of ^{222}Rn, remained. And finally, the ratios of the intensities of the observed groups do not agree with those predicted from the ^{226}Ra decay chain. Thus it appears that internal radioactive contamination is not likely.

External sources of ionizing radiation were studied but again nothing could be found to fit the experimental observations. Cosmic radiation was the only possibility since the count rate did not vary from building to building. Since the cosmic ray flux at the earth's surface is comprised of approximately 80% muons and 20% electrons (Hi72), interactions involving these particles were examined. Practically no secondary muons occur at sea level at energies less than 100 MeV and only a few secondary electrons have energies less than 10 MeV (Ja48). Thus energy loss by ionization in the detector gas can be eliminated since the observed

energies are much greater than those calculated from the specific ionization curves (Ev55). Such reactions as :

$$^{3}He + \mu^{-} \rightarrow {}^{3}H + \nu \qquad (3.78)$$

and

$$^{40}Ar + \mu^{-} \rightarrow {}^{40}C\ell + \nu$$

have a finite probability of occurrence if the slow moving muon first forms a muonic atom in an S-shell orbital and then is captured by the nucleus. The charged ^{3}H or $^{40}C\ell$ atom will be monoenergetic since the muon is effectively at rest but unfortunately the energy attained is 1.88 MeV for ^{3}H and 0.127 MeV for $^{40}C\ell$ as shown by a simple calculation. Reactions of the type:

$$^{3}He + \mu^{-} \rightarrow {}^{2}H + n + \nu$$

and

$$^{40}Ar + \mu^{-} \rightarrow {}^{39}C\ell + n + \nu$$

can also occur but since these are three body breakups the energy is distributed among the three reaction products. The endpoint energies, from mass differences

are 99.384 MeV for the first reaction and 92.351 MeV for the second and thus one would expect a continuous distribution of energies for the neutron, deuteron and chlorine nuclei up to those endpoints.

The count rate was found not to change when 5 cm of lead was placed around the detector suggesting that any external source of radiation must be of very high energy. Lastly, it was noted that external radiation was an unlikely source of the three anomalous peaks since the peaks were not observed in the small ^{3}He detector previously described.

CHAPTER 4

THE EXPERIMENTAL SYSTEM

4.1 Introduction

When one is planning an experiment it is important to note that the process to be observed imposes certain constraints on the design. For photoneutron spectroscopy this places restrictions on the three major components of the experimental system; namely, the photon source, the detection system and the targets.

Since the photoneutron cross sections in the photon energy region of interest are small, it is necessary to have a strong source of gamma rays in order to ensure data collection times of a reasonable length. A highly-collimated beam is required to provide a well-defined geometry that will be inherently easy to analyse. Photon energies must be large enough to exceed the photoneutron Q-value of the targets and in addition the source should possess only a few monochromatic lines in order to simplify neutron spectra and to allow ready analysis of the photon energy dependence. It was realized that the latter two requirements could be fulfilled by utilizing a source of neutron capture gamma rays. Hence, a beam port facility,

which was able to reasonably fulfill all the necessary requirements, was designed and built employing natural nickel and chromium (n,γ) sources.

The neutron detection system should ideally possess both a high efficiency for detection of neutrons in the energy range of interest and at the same time have good enough energy resolution to be able to resolve most neutron groups. As stated in Chapter 1, time of flight techniques have associated with them very low efficiencies by virtue of their low duty cycles and the small solid angles subtended by the neutron detector. Thus it was decided to use a recently designed (Cu69a, Sh72) high resolution ^{3}He ionization chamber which could be placed very close to the target to yield a reasonable efficiency. The neutron detector has been fully described in Chapter 3 together with the theory of operation. Finally, pulse risetime discrimination was performed on the detector output in order to improve spectral response.

Due to the small photoneutron cross-sections, relatively massive targets, of the order of 25 to 200 grams, were required to obtain reasonable neutron detection rates. Thus the elements used had to be inexpensive. Secondly,

the targets must have photoneutron Q-values less than the highest energy photon of the sources but high enough to yield moderately low energy neutrons for which the detector has appreciable efficiency. Thirdly, the target materials should be capable of being readily formed into standard shapes. The targets should be monoisotopic or at least have few isotopes in order to facilitate easy data analysis. The targets should be wider than the beam and of a shape that would be easily produced and readily analysed. Lastly, the targets should be pure in order to avoid erroneous interpretation of data. Several targets in the mass range of interest were found to satisfy these requirements as were several others of lower atomic mass.

4.2 The Beam Port Facility

The experiments which were performed utilized the McMaster Nuclear Reactor, an enriched uranium light water cooled and moderated pool type reactor. The beam port facility, which has been described in a previous publication (Mc76), is shown in Fig. 4.1. Since the γ rays were to be generated by neutron capture in the source material, it was decided to place the source directly in the reactor core in order to obtain the highest possible neutron flux.

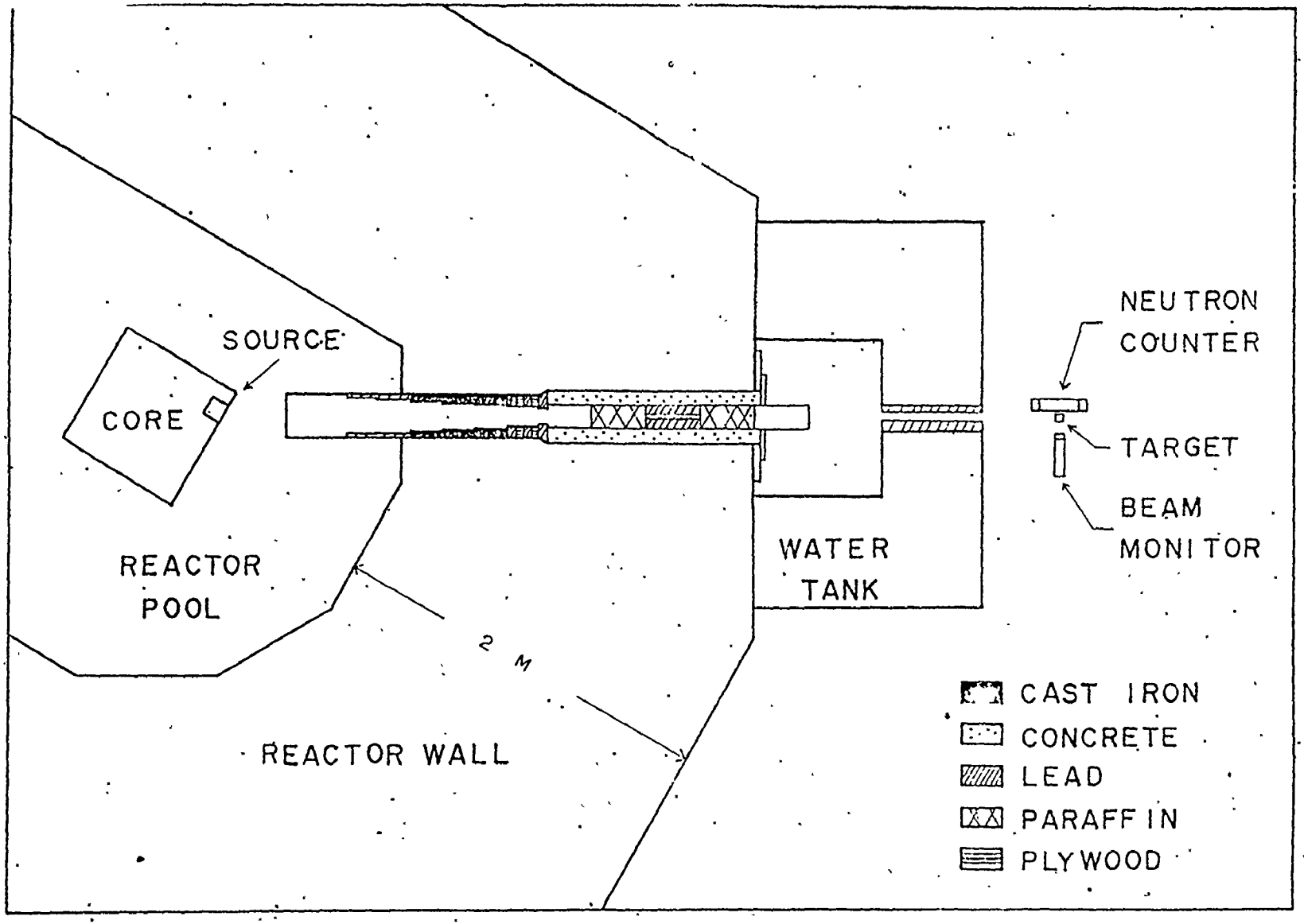

4.1 Overhead schematic view of the McMaster Nuclear Reactor monochromatic spectroscopy facility. Neutron counter is FNS-1 spectrometer. Counter target and monitor are not to scale. Parallel geometry is shown.

The position chosen for the source was collinear with a beam port and located at the outer corner of the core so that it could be viewed directly. The source container is shown in Fig. 4.2. It consisted of an outer sleeve designed to fit into a standard fuel element position or grid hole and an inner sample holder. The outer container possessed a locating hole designed to mate with a guide pin in the grid plate in order to prevent rotation. The neutron capture process and irradiation of the source by core gammas can generate considerable heat in the sample and it was thus considered necessary to cool the containers. This was achieved by designing the outer container with a hollow stem and placing holes in the top and bottom of the inner container. In operation water would flow under gravity through the cooling holes, down the stem and out the grid plug hole. Both containers were constructed of reactor grade aluminum and were sand blasted to remove surface dirt and impurities. There were two inner packages, each of dimensions 5-cm x 5-cm x 18-cm which could be placed inside the outer

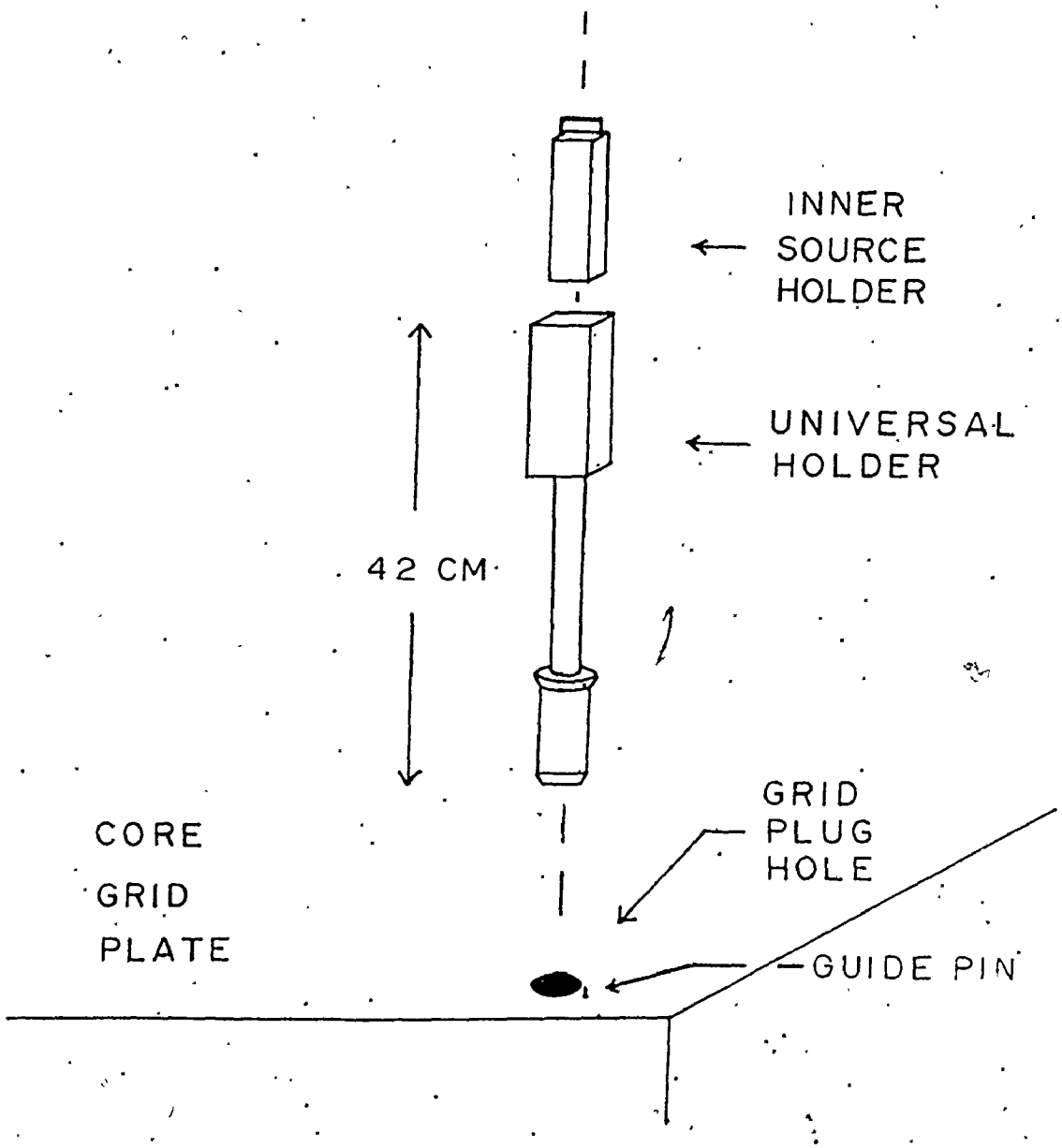

4.2 Exploded view of the photon source holder. Source material in inner holder is not shown.

container. One contained four 2.5-cm diameter x 15-cm long rods of 99.5% pure nickel* while the other contained an identical volume of 99.6% pure chromium**. In order to allow easy interchange of sources, the inner package was designed with a handle on top such that it could be removed with a standard fuel handling tool, while leaving the outer container in place. This ensured reproducible alignment of the different sources and the small packages were convenient for storage within the pool or for subsequent disposal. With the existing system, sources could be changed in several minutes and stored indefinitely in the reactor pool.

The neutron capture γ-ray beam was collimated by a series of stepped iron rings, barytes concrete and lead collimators to a diameter of approximately 2.5-cm as was determined by photographic methods at the target position. Neutrons were removed from the beam by two 25-cm long borated wax plugs. The targets were placed on a thin fixed position aluminum tray such that their centres were aligned with the centre of the beam, which previously had

---

* Refined by the International Nickel Corporation and designated INCO 200.

** Purchased from Materials Research Corporation, Orangeburg, N.Y. and designated VP Chromium.

been determined by the beam photographs and marked on the tray. Since aluminum has a photoneutron Q-value of approximately 13 MeV, it could only scatter photons and thermal neutrons from the beam. Its small mass, however, ($\sim$ 1.5g) ensured that this would be negligible. A thermal neutron flux of approximately $10^{13} cm^{-2} s^{-1}$ at the source position and a solid angle of the order of 10^{-5} steradians yielded photon beams of the order of $10^{6} s^{-1}$ at the target position. The actual measurement of the absolute photon flux and beam profile at the target position is discussed in sections 5.2 and 6.2.

4.3 Electronics

4.3.1 The Basic System

The ^{3}He detector described in Chapter 3 was designed to operate in its simplest usage with the same basic equipment employed by a Ge(Li) detector - namely, a preamplifier, pulse amplifier, bias supply, multichannel analyser and a pulser. The electronic configuration for such operation is shown in Fig. 4.3.

The preamplifier, which is an integral part of the detector, has been discussed in Chapter 3 and nothing further will be said about it here. A Power Designs Model

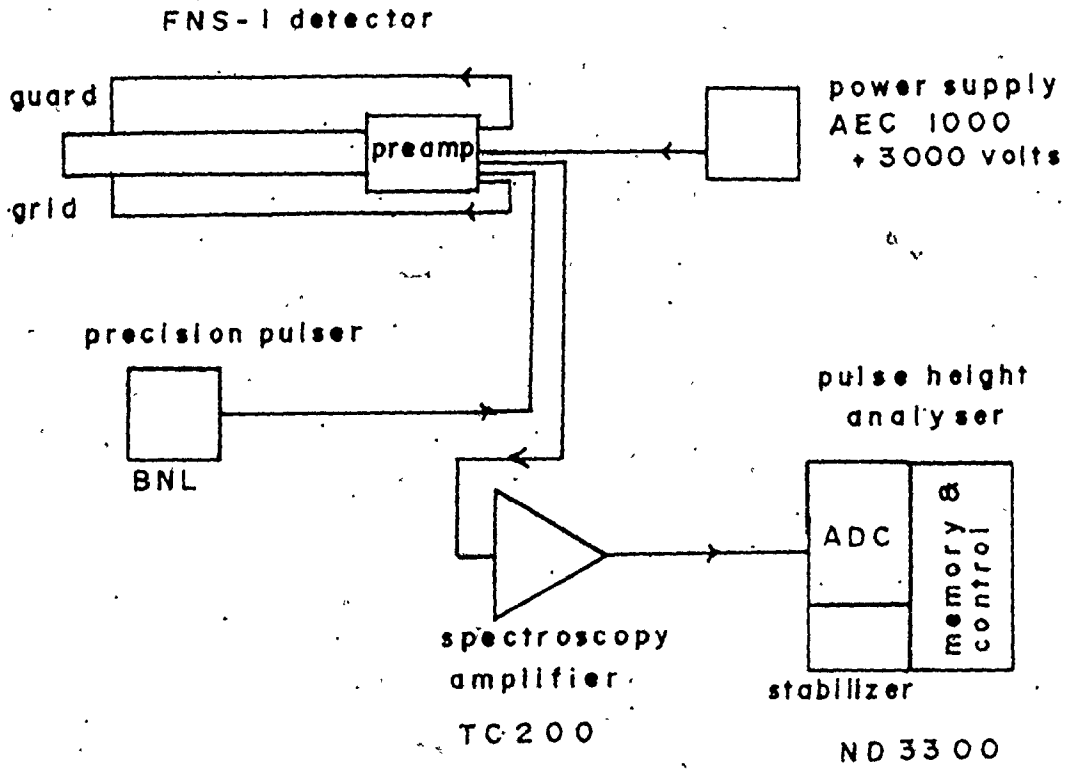

4.3 Basic electronics for neutron spectroscopy without risetime selection.

AEC 1000 high voltage supply was used to deliver a positive 3000 volt bias to the anode and guard and grid electrodes of the detector.

Besides its inherent amplification, a spectroscopy amplifier has two other important functions:

1) attenuation of high and low frequency noise
2) reduction of the probability of pulse pile up.

These latter two functions are achieved by pulse shaping techniques which often employ three stage active RC filtering - a first differentiation stage, an integration stage and a second differentiation stage which together act as a band pass filter to produce bipolar pulses. It is easy to see that the gain of a narrow band amplifier will be dependent on input pulse risetime unless the amplifier differentiating time constants are made appreciably longer than the maximum risetime.

Now, the pulses at the preamplifier output have a large variation in risetime - a range of approximately 0.2 to 1μs for thermal neutrons and 0.2 to 5μs for 1.5 MeV neutrons. This risetime variation, described in

Chapter 3 is due to finite collection time of electrons from the primary ionization tracks. Thus, the amplifier time constants should be made appreciably greater than 5μs to minimize the gain dependence on risetime. On the other hand, a short time constant is desirable to minimize sensitivity to microphonics and high counting rate and therefore a compromise must be made. Also,it has been shown (Gi53) that to optimize the signal to noise ratio for a given counting rate, the differentiating and integrating time constants should be equal.

With the above facts in mind, the amplifier that was chosen was a Tennelec TC200 spectroscopy amplifier which allowed independent variation of the three time constants from 0.2μs to 12.8μs. Also,the output from each amplification stage could be obtained for use in risetime discrimination, as will be explained later.

Using bismuth as a target and nickel as a source, the energy resolution for well resolved neutron groups was examined as a function of the three shaping time constants. The energy widths of the neutron groups were so small compared to the intrinsic resolution of the

detector (~ 8 eV vs 20 keV) that any significant variation of resolution due to amplifier time constants would be obvious. Following Gillespie's advice, the differentiating and integrating time constants were kept equal. It was found that the optimum energy resolution for neutrons over approximately 500 keV was equally obtainable with time constants of 6.4 and 12.8μs. Since there was no apparent difference in resolution between the two time constants, the lesser one was chosen for the above mentioned reasons.

A Nuclear Data 3300 multichannel analyser was used to encode and store the pulse height information. An ADC with a 2K ramp was employed and separate spectra were stored in 2048 channel groups. Gain and zero stabilization was achieved by locking two ADC stabilizers on the pulser and the intense thermal neutron peak.

The pulser was a precision pulser based on a "Brookhaven National Laboratories" design and capable of remaining stable in pulse height and rate over a period of several weeks. The pulser was introduced to fulfil three main purposes:

1) to produce a prominent, fixed-energy peak to be used in conjunction with the thermal peak for energy stabilization
2) to provide an independent check on the down-time of the multichannel analyser
3) to act as an indicator of gamma ray and thermal neutron pile-up effects

The adjustable pulse rate was kept at approximately the value of the thermal neutron rate in order that the ADC stabilizers would treat both zero and gain corrections at a similar rate and so that the pulser would not overflow analyser memory over a period of a few weeks. The pulser was adjusted such that the pulse shape at the preamplifier output was similar to that of thermal neutrons; that is, with a risetime of approximately 0.5μs (10% to 90%) and a fall time of approximately 1ms.

4.3.2 Electronics for Energy-Risetime Analysis

In part of the experiments it was decided to use pulse risetime selection in an attempt to decrease the thermal-epithermal neutron rate, ^{3}He recoils and the wall effect and to improve energy resolution. Since both very

short and very long risetimes were to be rejected for reasons described in Chapter 3, it was decided to examine the pulse height versus risetime distributions by means of a two dimensional analysis.

The basic method used was to clip the preamplifier output signal using an RC differentiator and trigger on the leading edge of the resultant signal in order to provide a time pickoff for the leading edge of the signal. A time-to-amplitude convertor (TAC) would then be employed to measure the time difference between the leading edge pickoff and a time pickoff related to the signal crossover. This time difference, then, should be proportional to the pulse risetime.

The electronics for this experiment are shown in Fig. 4.4. The spectroscopy amplifier was used in the same fashion as in section 4.3.1 with a 6.4μs integration and differentiation time constant. Since the Tennelec TC200 amplifier has the capability of being used as three separate RC amplifiers with independent time constants, it was decided to use its first differentiator for the short clipping amplifier and its integrator and second differentiator, for the crossover shaping amplifiers.

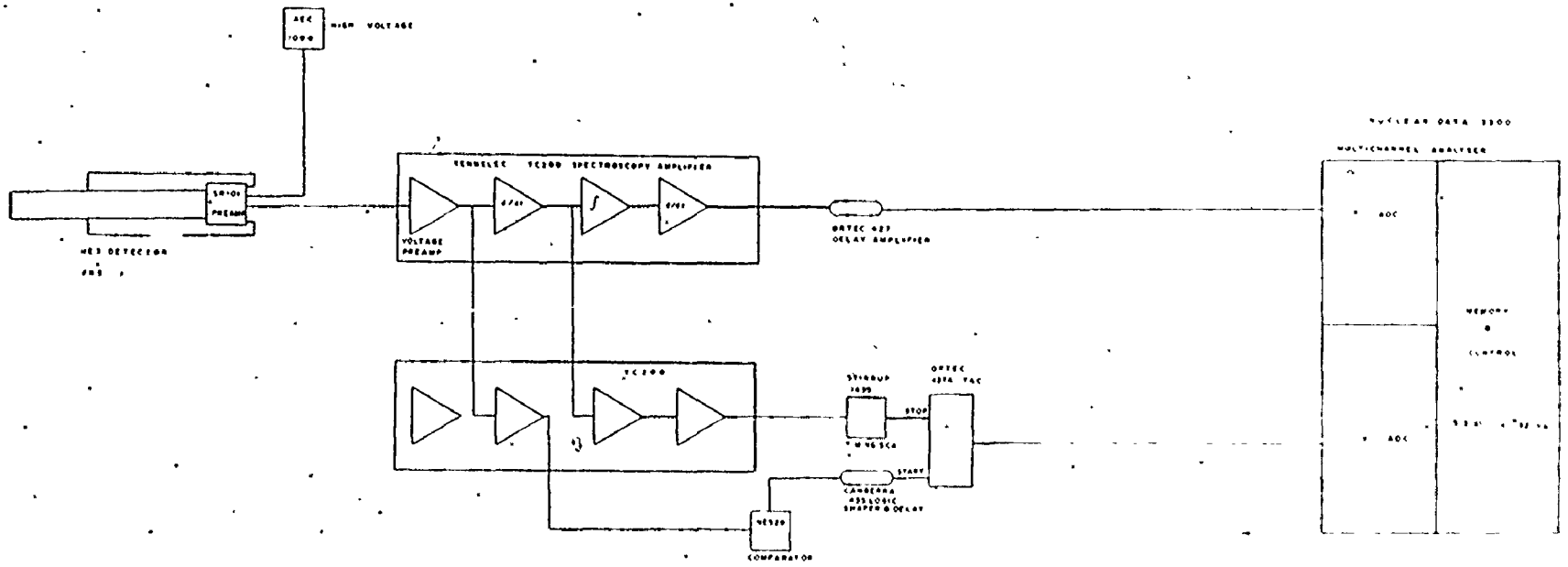

4.4 Electronics for energy-risetime analysis.

The preamplifier signal, instead of being differentiated directly, was first amplified using the gain of 2 voltage preamplifier, contained in the spectroscopy amplifier and then fanned out to the first stage differentiator of the risetime amplifier. The leading edge of the differentiator output was picked off using the NE529 comparator circuit shown in Fig. 4.5. The NE529 consists of a high speed (10 ns propagation delay) comparator input stage and two complementary TTL compatible gated outputs. In this circuit, the comparator input, with 50 Ω termination, was compared with a stable reference voltage formed by the forward biased diode and the ten turn potentiometer. In order to get a fast logic output, the inverting output A was differentiated using a .05μf capacitor and 50 Ω resistor and in addition a standard TTL output, B, was made available. All supply and reference voltages were derived from standard NIM voltages of ± 12V by using zener diodes and capacitive decoupling to minimize noise and crosstalk. Since the circuit was designed for high speed, in order to minimize ground loop pickup, the

NE 529 COMPARATOR CIRCUIT

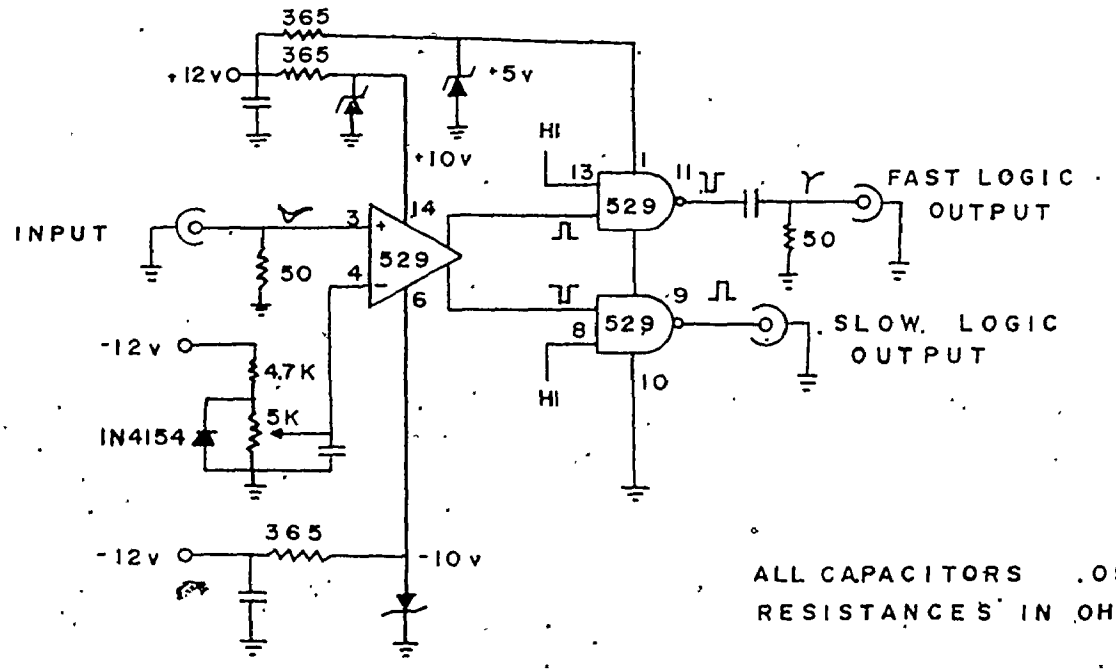

4.5 NE529 fast comparator circuit. Employed in the electronics of Figures 4.4 and 4.9.

circuit was mounted on a double sided printed circuit board with a large ground plane and shielded coaxial cables were used for input and output signals. The entire assembly was mounted in a standard single width NIM module. The fast logic output of the 529 comparator was then fed to a logic shaper and delay to allow full use of the TAC time range and then the fast logic output of the logic shaper was used as the start signal of the TAC (8 μs full scale).

In order to generate a stop signal for the TAC which would contain information concerning the crossover time, the output of the first differentiation stage of the spectroscopy amplifier was fed to the input of the integration and second differentiation stage of the rise-time amplifier. This output was then passed to a timing SCA used solely as a zero crossing detector and its fast logic output was then used as the TAC stop signal.

Finally the risetime amplifier output or time signal was fed to the Y ADC of a Nuclear Data 3300 multichannel analyser. The energy signal was delayed to get it in time with the time signal and then fed to

X ADC of the analyser. The energy-time coincidence spectrum was then encoded in a 512 channel (energy) by 32 channel (time) array in the memory of the analyser.

The selection of time constants for three stages of the risetime amplifier warranted consideration. The first differentiator was being used to shape the pre-amplifier pulses prior to the detection of the leading edge by the comparator. Thus the time constant must only be short enough that the comparator output would not exhibit large variations in width, an effect which could be significant at high count rates. Also, if the amplifier time constant were very short compared to the signal rise-time, signal attenuation would occur. As a compromise it was decided to choose a time constant of 0.2 μs which was approximately equal to the shortest risetimes encountered.

The selection of time constants used to form the bipolar pulse for crossover detection was much more difficult. Ideally, it was realized, the time constants should be varied to maximize three factors:

1) the signal to noise ratio
2) the slope of the signal at crossover, and
3) the sensitivity of crossover time with pulse risetime.

Cuttler (Cu69b) has done a detailed analysis of such an optimization for the case of a doubly differentiated exponential signal of time constant, τ, and has found that the optimum time constants for the first and second differentiation stages, T_1 and T_2 respectively, are $T_1 \geq 2\tau$ and $T_2 \geq 5\tau$. Using these criteria, for this experiment it would be necessary to choose $T_1 \gtrsim 10\mu s$ and $T_2 \gtrsim 25\mu s$ which would impose an inconveniently long delay between the time and energy signals. Furthermore, the Tennelec amplifier did not allow removal of the integration stage and the shortest time constant that could be selected for it was 0.05μs which was still appreciable compared to the shortest risetimes. Thus, it was decided to study the effect of using two differentiation stages and one integration stage. The equations for the pulse height as a function of time for both methods of crossover formation are derived in Appendix I. In order to minimize the number of variable parameters, the integration time constant was kept equal to the second differentiation time constant. Figure 4.6 shows the crossover time as a function of pulse risetime for a variety

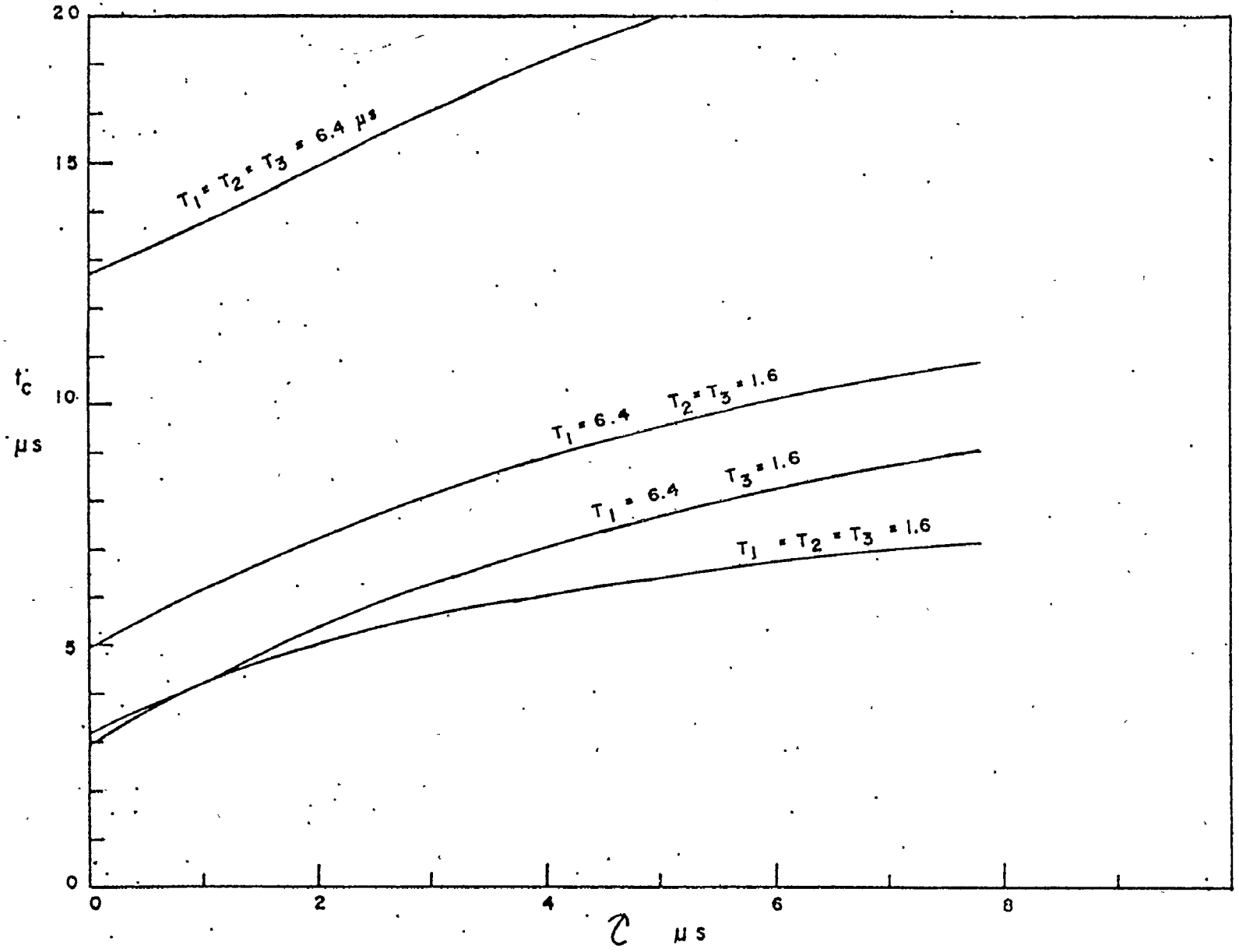

4.6 Crossover time as a function of pulse risetime for amplifiers with different RC shaping constants. Based on the equations of Appendix A1.

of different available time constants. Clearly, it would be desirable to maximize the slope of this graph, $dtc/d\tau$, which is called the crossover sensitivity. This is best satisfied by the choice of 6.4 μs for all three time constants. Unfortunately, this would require the use of several delay amplifiers in series after the spectroscopy amplifier to get the energy and risetime signals in time and thus would bring about an inherent decrease in the signal to noise ratio for the energy signal. Almost as good a choice is that of T_1 = 6.4 μs and $T_2 = T_3$ = 1.6 μs. This is almost identical in slope to the double differentiation case with the same time constants but with a slightly larger delay until crossover time. Table 4.1 shows the normalised slope and maximum pulse height for various different available time constants assuming an exponential input pulse of unit height and 1.0 μs time constant. It appears that the choice with the minimum sensitivity and maximum signal attenuation has the maximum slope at crossover and that in fact high sensitivity must be traded off to gain signal amplitude and maximize the slope at crossover. It is also apparent that the addition of an integration stage provides a

definite improvement since the slope at crossover is greater in addition to an increased signal to noise ratio provided by the narrowing of the amplifier bandwidth. Thus the uncertainty in crossover time is decreased at the expense of slight signal attenuation. It appears from the previously mentioned graph and table that optimum time constant choice lies in the middle; i.e. T_1 = 6.4 μs, $T_2 = T_3$ = 1.6 μs. This had the advantage that the output of the first differentiator of the spectroscopy amplifier could be used instead of an additional amplifier.

The uncertainty in the time between leading edge pickoff and crossover has also to be considered. One source of possible timing uncertainty would be the variation of triggering time with pulse height, commonly called walk. This would only affect the leading edge pickoff since the crossover time occurs at a constant fraction of charge collection and hence is independent of pulse height. If a linear risetime is assumed it can easily be shown that the maximum error in time pickoff due to walk is given by:

$$\Delta_{tw} = \frac{\tau V_t}{0.8} \left(\frac{1}{V_2} - \frac{1}{V_1} \right) \qquad (4.1)$$

where

Δ_{tw} is the timing error due to walk

τ is the risetime (10% to 90%)

V_t is the trigger level

V_1, V_2 are the maximum and minimum pulse heights of interest.

For a 1 MeV and a 500 keV neutron, which might have the same risetime; V_1 = 120 mV, V_2 = 86 mV, τ = 4 μs maximum and with a threshold level of 7 mV, we get a timing error due to walk of approximately 0.1 μs. For smaller pulse heights the risetime decreases and so the effect remains approximately the same. The other potential source of timing error was noise, commonly referred to as jitter, which would affect both the leading edge and crossover pickoffs. Again, assuming a linear risetime, it can easily be shown that timing uncertainty due to jitter, Δ_{tj}, is given by

$$\Delta_{tj} = \frac{N}{V} \frac{\tau}{0.4} \qquad (4.2)$$

where V is the pulse height and

N is the root mean square of the noise band.

Since the noise band was of the order of a few millivolts and the signals were of the order of volts for the crossover pulses, the uncertainty in crossover time due to jitter was negligible. On the leading edge, however, assuming N = 5 mV, τ = 2 μs and V_1 = 120 mV (1 MeV), (these values are justified as typical if one looks at the risetime distributions in Chapter 3) one finds that the timing jitter is approximately 0.2 μs. Since these errors add in quadrature, this gives a total timing error of approximately 0.2 μs which is less than one bin width of the analyzer.

4.3.3 Electronics for Risetime Discrimination

The circuit for risetime discrimination is shown in Fig. 4.7. It should be recognized that a large part of the electronics, namely the spectroscopy amplifier and delay amplifier and the risetime circuitry up to the TAC, was identical to that of the energy-risetime analysis electronics. The difference between the two sets of electronics occurred in what was done to the TAC output (now 4 μs full scale). A window was set on the TAC output using the single channel analyser (SCA).

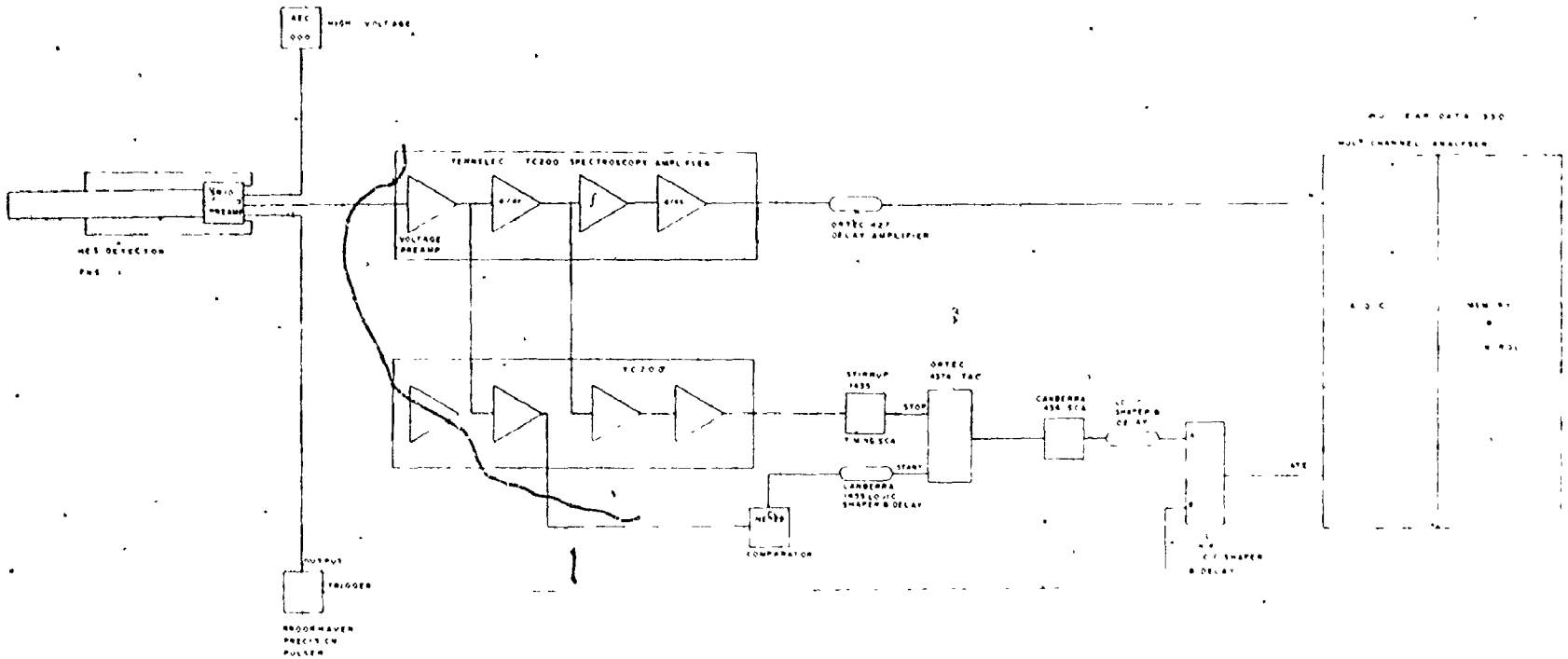

A.7 Electronics for neutron spectroscopy with risetime selection.

This logic signal was then delayed and a logical OR condition established between it and the delayed and stretched trigger output of the pulser. This latter operation was performed to allow the fixed risetime pulser to be accepted regardless of the risetime window imposed. The logic shaper and delay which followed the SCA and the combination delay stretcher and OR circuit were designed and built by the author and are shown in Figures 4.8 and 4.9 respectively. The logic shapers and delays were imposed to place the output of the OR gate in time with the energy signal and to make it wide enough to allow a coincidence to be performed. Thus with the electronics shown, only those pulses with risetimes falling within a range selected by the SCA would be analysed and stored.

4.4 The Beam Monitor

A nuclear reactor will exhibit power fluctuations with periods extending from minutes to days. In addition, over a period of a few weeks, as the flux density drops due to fuel burnup, there will be an attendant drop in photon flux from the beam port. Although variation of

LOGIC SHAPER & DELAY

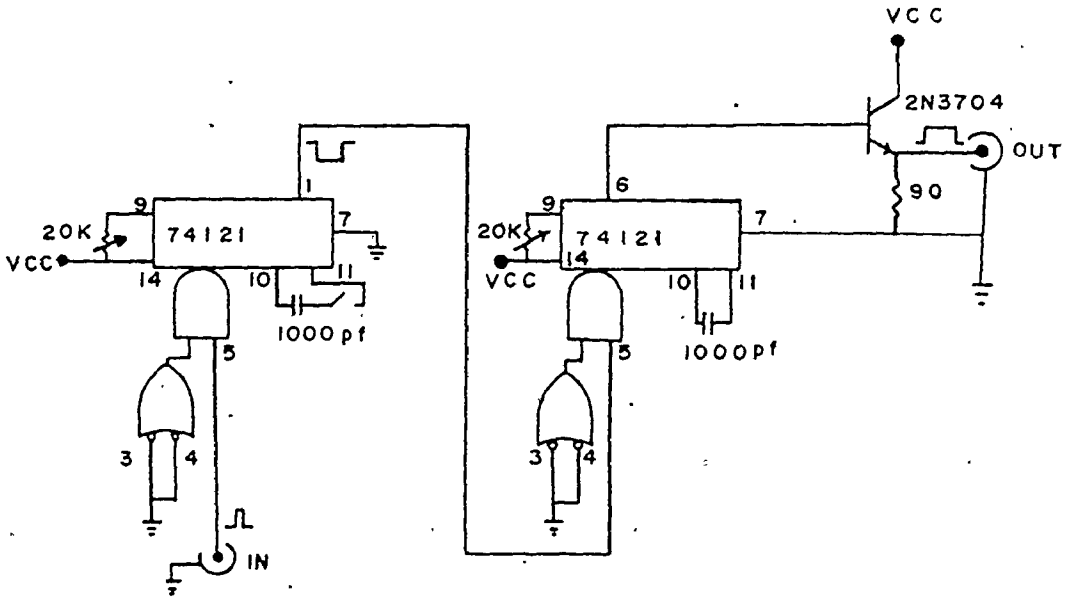

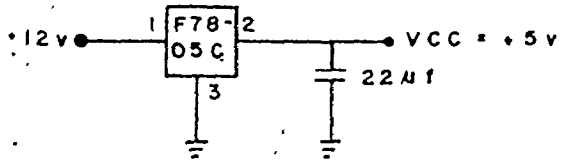

DELAY TIME . 1-12 μs SWITCH CLOSED
30 ns SWITCH OPEN

WIDTH . 1-12 μs

4.8 Logic shaper and delay circuit. Used in the electronics of Figure 4.7.

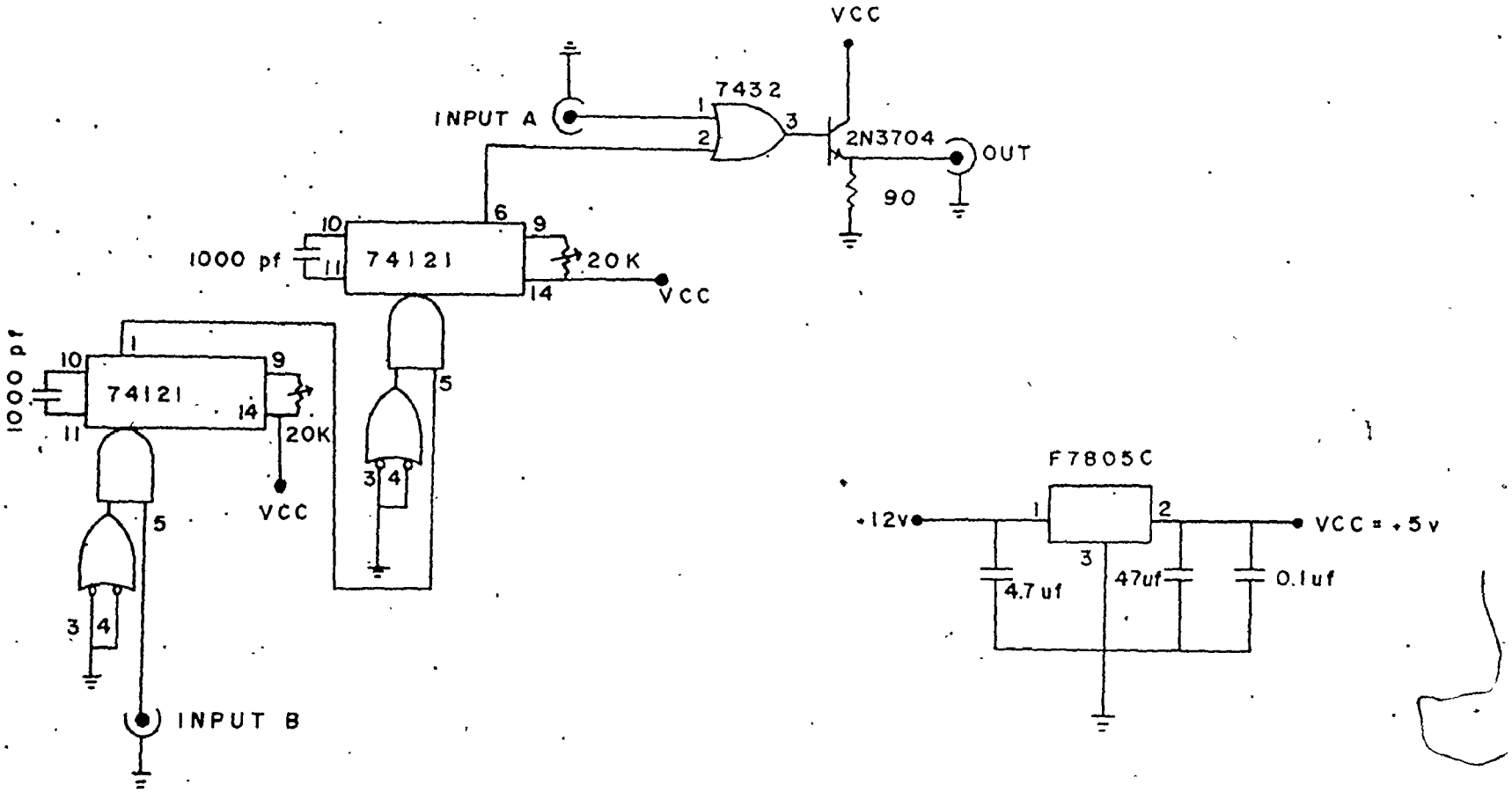

4.9 Logical OR gate with one input shaped and delayed. Used in the electronics of Figure 4.7.

photon flux due to the former effect can be easily corrected for by monitoring the reactor power the latter effect is more difficult to correct for since the control rods can be withdrawn to maintain constant power. For this reason it was decided to monitor the flux of the beam directly. For any good beam monitor, two conditions must necessarily be fulfilled:

1. The monitor count rate must be linear with beam count rate.
2. Any background component must be small with respect to the beam component.

To satisfy the first condition it was decided to use a NaI(Tℓ) detector arranged to look at the target or alternatively a scatterer in front of the target. The latter method had the advantage that for a given beam flux the count rate should be independent of target whereas, of course, the former would be target dependent. There was, however, a distinct disadvantage to the latter method in that the monitor scatterer would attenuate the beam intensity and change the energy spectrum of the beam. This could be an appreciable effect since the

scatterer would have had to be made quite thick in order to give a sufficient count rate in the monitor detector. Since it had already been decided to run bismuth photoneutron standards before and after each target as an independent check of gain and zero shifts, monitor rates could be normalized for each new target by using the bismuth monitor count rates taken a few minutes before a run and a few minutes after. For these reasons it was decided to use the targets as their own monitor scatterers.

High energy photons of approximately 10 MeV interact in matter primarily in two ways - via Compton scattering and pair production. Since a high energy photon scattered through an angle of $\pi/2$ with respect to the incident beam has an energy approximately equal to the electron rest mass, it was decided to place the monitor detector at right angles to the beam. By setting an energy window about 511 keV, it would be then possible to observe both Compton events and annihilation radiation. The window would also serve to decrease the background rate.

The monitor geometry and electronics are shown in Fig. 4.10. To further reduce background the detector was shielded on all sides by 10 cm of lead, and lead collimators, 2.5 cm inner diameter by 37 cm long, were placed in front of it to allow it to look only at the target. The face of the detector was placed approximately 90 cm from the target in order to define a scattering angle of approximately $\pi/2$ but at the same time yield a reasonable count rate.

A 3.8 cm x 3.8 cm Harshaw integral mount NaI(Tl) detector was chosen as the monitor. Its current output was integrated using a charge sensitive preamplifier, then amplified and fed to a single channel analyser. With no target in place, a ^{22}Na source was placed at the front entrance of the collimator to serve as a source of 511 keV photons for use in setting a rough energy window. After the window had been set, the source was removed and the target positioned on the aligning tray.

As stated previously the scattered radiation from the target would not be at exactly 511 keV due to the finite solid angle subtended by the collimated monitor.

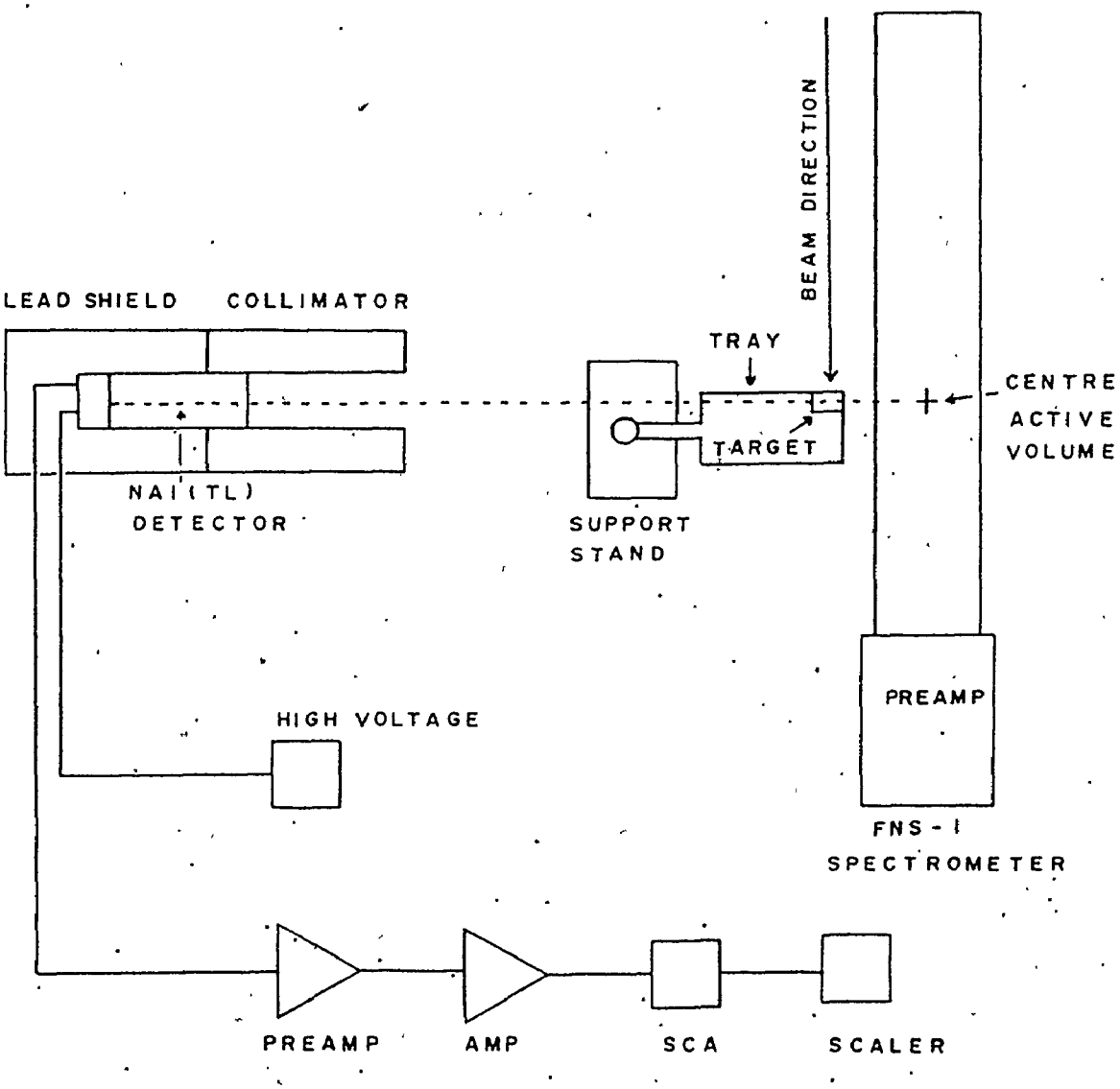

4.10 Experimental arrangement for cross section determination (parallel geometry) showing the NaI beam monitor and associated electronics. Not to scale.

Thus, it was necessary to vary the energy window slightly in order to find the optimum ratio of count rate with the target in position compared to that with the target out. Eventually, it was found that the lowest background rate at 1.5 MW, the normal operating power, was 2.3%. In addition, it was found that while the reactor was running in its normal manner at 1.5 MW, the background remained typically at around 2% presumably because the decay rate of ^{41}Ar in the room was at equilibrium. Thus since the background rate was small, it could be determined at regular intervals and then be subtracted from the daily monitor reading to give a number that was truly proportional to the beam rate. In doing so, however, it was necessary to remember that an experiment could not be started or continued until the ^{41}Ar in the room had reached equilibrium.

Next, an experiment was performed to test the linearity of monitor count rate as a function of reactor power. Prior to the experiment, the reactor was shut down for approximately six hours. Since the decay rate of ^{41}Ar is 109.8 minutes and the average time for one

complete replenishment of the reactor air is approximately one hour, there was effectively no ^{41}Ar activity in the air. The room background was measured and recorded by measuring the monitor count rate with the target removed. Then, with the target in place the reactor was increased in power to 1.5 MW, 2.5 MW, 3.5 MW and finally 5 MW. At each power level the reactor power was allowed to stabilize for ten minutes and then a ten minute count was performed to determine the monitor rate. Since the entire time span of the experiment was .727 half lives and since it had been previously shown (Ro74) that over an eight half life time span the argon background contribution was only twice the zero power background (or less than 1% of the total background in this case), it was deemed that the background rate was small enough and changing slowly enough to allow direct measurement of it at each power level.

The data after background subtraction were fitted to the equation of a straight line using a linear least squares fitting program written by the author. The data

were found to have a slope of $(74.73 \pm 0.78) MW^{-1}s^{-1}$ and a reduced chi square of 1.23. Although this clearly showed that the monitor count rate was a linear function of reactor power, it was noted that this would also be true for monitor rate versus beam intensity, since the calibration was done over a short period of time for which fuel burnup would be negligible.

To minimize the operational error of the beam monitor it was decided to run the experiments only at a nominal 1.5 MW. It was indicated by the reactor staff that power fluctuations of up to 10% could be expected on a weekly basis. Thus, due to the narrow range of power values and the high degree of linearity over a wide range of reactor powers, it was felt that any error produced by the beam monitor due to nonlinearity of power versus count rate would be of the order of one percent. It should also be noted that in one day typically 10^7 counts were recorded in the beam monitor and thus statistical error was negligble. Since the error in extracting the photoneutron peak areas was found to be typically between 5 and 10%, the error in

the beam monitor was considered sufficiently small.

Over the duration of the experiment, the monitor energy window was checked frequently by scaling the count rate from the ^{22}Na source placed at the front face of monitor collimator with the target removed.

4.5 The Targets

The major considerations for target selection are outlined in section 4.1. In order to minimize the mass of scattering material in the photon beam, it was decided to employ a thin aluminum tray and thus a flat bottomed target was necessary. Since it was also desired to have a target shape that would allow the easy calculation of absolute detector efficiency for fixed geometry, it was decided, in light of these two constraints, to use cubic targets.

There were also considerations to be made concerning the dimensions of the targets. Since the photoneutron cross sections were expected to be very small, it was desirable to make the targets wider than the beam width to ensure maximum count rate. In addition this would allow errors arising from measurement of the spacial intensity

distribution to be ignored. On the other hand, since the detector was situated parallel to the beam and beside the target the target width should be kept as small as possible to minimize neutron scattering in the target. The target could, of course, be made as thick as possible but a target thicker than a few mean free paths for the photon energies of interest would add little extra contribution to the photoneutron production rate. The beam area was found, by photographic means described in Chapter 5, to be mostly concentrated within a diameter of 2.5 cm and for the typical elements near atomic mass 200, a 2.54 cm thickness corresponds roughly to an attenuation of 70% for 9 MeV photons. Thus it was felt that cubic targets of approximately 2.54 cm length would be appropriate.

The natural lead, bismuth and thallium targets were melted, formed by use of a cubic mold and then machined to the appropriate size. The tantalum cube was composed of 2.54 cm square plates of varying thickness totalling 2.88 cm bonded tightly together by a single layer of 1.9 cm wide Scotch Brand transparent tape.

In a similar fashion the gold target was formed from 2.54 cm square gold plates of equal thickness.

The only exception to the 2.54 cm cubic geometry was the separated lead-208 sample. Since only 26.5 g of ^{208}Pb in thin sheet form were available for use, it could not be fashioned into a 2.54 cm cube and since melting it to form a smaller cube would result in some loss of the very expensive isotope, it was decided to roll the sheet into a tight cylinder of length 1.7 cm and diameter 1.5 cm.

The weight, density and isotopic abundance of the targets used is presented in Table 4.2. Trace impurities were considered to be of little concern due to the large amount of material required to observe photonuclear reactions at these energies.

CHAPTER 5

EXPERIMENTAL PROCEDURES

5.1 Measurement of the Photon Beam Spectral Components

Since the interpretation of relative photoneutron cross sections required a knowledge of the relative intensities of the spectral components for each photon source, it was decided that an independent measurement of these should be made. Although this could be carried out by using a Ge(Li) detector, it was realized that the photon beam would be too intense at the normal reactor power of 1.5 MW. This was solved by reducing the power to 1 KW and placing the detector at the normal target position but behind two 61 cm thick iron blocks which defined a slit of width 0.1 cm. It was noted that the reduced reactor power would not affect the relative intensities since the photons in the energy range of interest (greater than 5 MeV) were all produced by prompt thermal neutron capture. The output of the 15 cc Princeton-Gamma Tech. Ge(Li) detector and its attached charge sensitive preamplifier was sent to a Canberra 1413 spectroscopy amplifier and then fed into a Nuclear Data 3300 multichannel analyser. Data were collected over a three

hour period for the nickel source and a four hour period for the chromium. The spectra are presented in section 6.1.

In order to deduce the ratio of intensities of the spectral components, it was also necessary to know the relative efficiency of the Ge(Li) detector. Since the intensities and energies of the prompt gamma rays from thermal neutron capture by nitrogen are a well known standard for high energy photons (Be71), a spectrum of nitrogen could be obtained and then the relative efficiency determined. This was done by placing a sample of nitrogen-rich melamine in the tangential irradiation facility (Ni70). This facility is basically a hollow evacuated tube positioned at a tangent to the reactor core which allows an external detector to view a sample undergoing neutron capture, but not view the core gamma rays. The Ge(Li) detector was situated coaxially with the sample beam and inside a quadrasected NaI annulus (Ni70). A coincidence spectrum consisting of double escape events was taken over a one day period and is shown in Fig. 6.3.

The analysis of these data and the interpretation of the results are reported in section 6.1.

5.2 Measurement of the Beam Strength

5.2.1 Measurement of the Beam Profile

In determining the photoneutron cross sections it was necessary to know if the beam completely illuminated the target and, as we shall see shortly, a knowledge of the cross sectional area of the beam was necessary in the measurement of the absolute photon flux. For these reasons, it was decided to determine the profile of the beam. This was done by using standard Kodak AA Industrex X-ray photographic film in a sealed square aluminum holder of side 10 cm. The film holder was placed in a fixed position on a moveable jack whose location was marked on a large fixed aluminum platform on the beamport floor. Since this platform was the same one which supported the ^{3}He detector and target stand for the photoneutron experiments, it was also possible to determine the beam position relative to the detectors for these experiments. Photographs were taken at positions roughly perpendicular to the reactor wall face and approximately centered with respect to the

beam port collimator, 0.8 meters, 1.8, and 2.3 meters from the front face of the water tanks (Fig. 4.1). The 0.8 meter position was the location of targets for the photoneutron experiments. It was found by trial and error that an exposure of fifteen minutes was sufficient to define the beam profile. Photographs were developed at 20°C for 5 minutes in KODAK liquid X-ray Developer and Replenisher.

A quantitative evaluation was made by scanning the photograph taken at 0.8 meters using a Leitz-Wetzlar optical densitometer with colored filters removed. To facilitate ready analysis the photomultiplier output of the densitometer was digitized by utilizing the circuit shown in Fig. 5.1. The output of the photomultiplier of the densitometer was sent to a two stage amplifier. The first stage was comprised of a 741 operational amplifier acting as a high impedance buffer and the second stage which again consisted of a 741 operational amplifier acted as a gain of ten voltage amplifier. The amplifier output was fed to a Krohn-Hite 5200 function generator acting as a voltage to frequency converter (VFC) and its output was sent to the input of a TRACOR-NORTHERN TN1705 multichannel

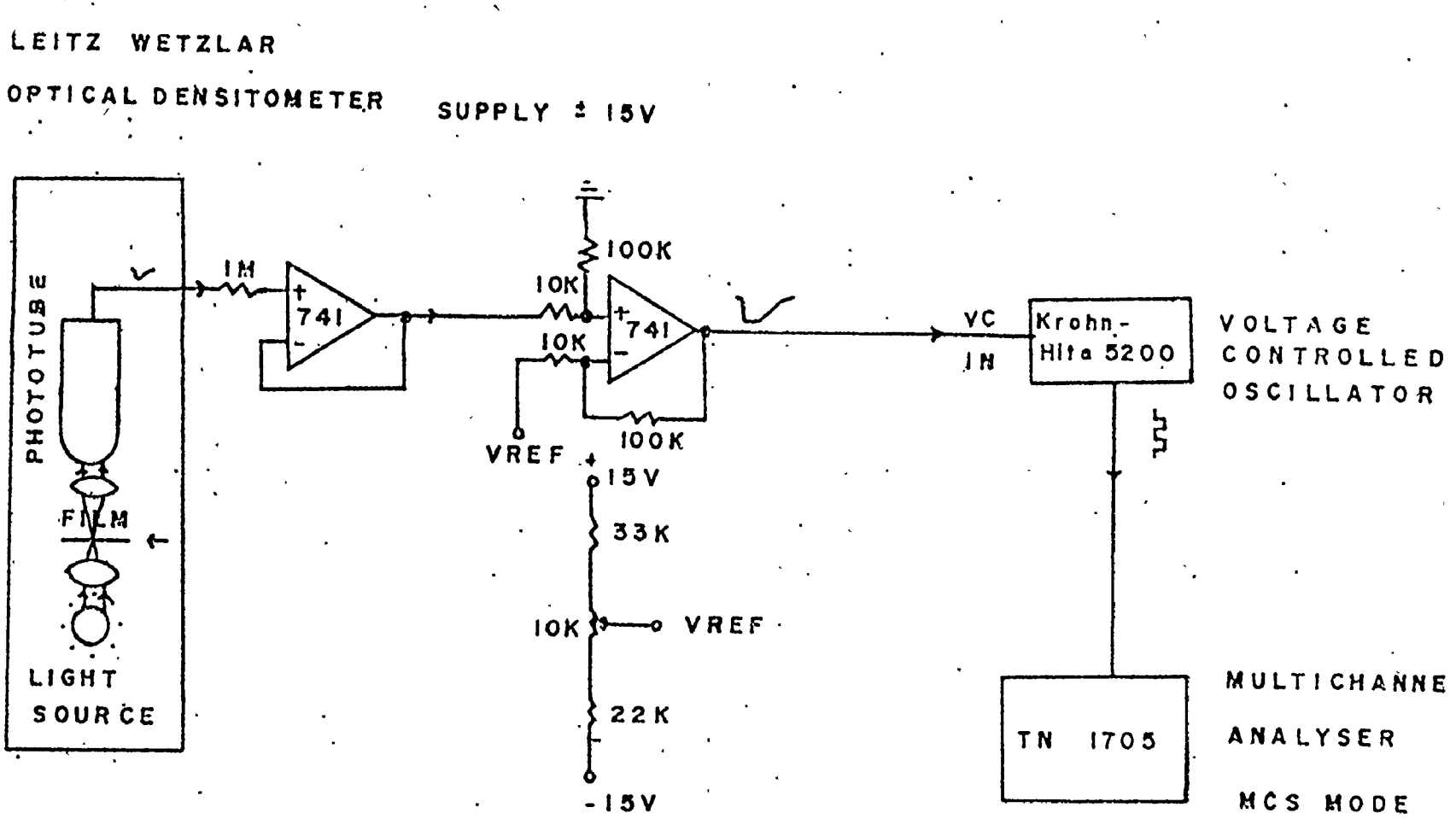

5.1 Experimental arrangement for measuring the density of film exposed in the γ-beam.

analyser. The analyser was operated in multiscaling mode with a dwell time of 900 milliseconds per channel. Since the scan speed of the densitometer was 0.005 cm per second this allowed a maximum scan length of 4.6 cm for the full 1024 channel memory which was quite sufficient. Pieces of over-exposed and unexposed X-ray film, developed at the same time as the film to be scanned, were used to determine the opaque and transparent states and the VFC frequencies corresponding to these states could be varied by adjusting VREF at the op. amp. stage. The dynamic range was thus adjusted such that the opaque state gave approximately zero counts per channel on a normal scan speed and the transparent state gave approximately 2300 counts per channel. The film was taped in a fixed position and scanned using a 1 mm slit length in 1 mm strips over its entire width. The results of this experiment and those of the absolute flux determination are presented in section 6.2.

5.2.2 Measurement of the Absolute Flux

The gamma ray flux emerging from the collimators was too intense to measure directly and furthermore, it was noted that photofractions are not known accurately

near 9 MeV photon energy. Hence a method was required that would indirectly measure a known fraction of the beam intensity. This was achieved by employing a NaI(Tℓ) detector in a good geometry experiment to observe the Compton scattered flux from a target placed in the beam. A carbon plate of thickness 2.45 cm and 10 cm square was chosen as the scatterer. The lateral dimensions were chosen to be much larger than the beam diameter of approximately 2.5 cm (see section 6.2) in order to avoid any possibility of the beam striking an edge of the plate. The thickness was chosen to provide a reasonable counting rate while at the same time minimizing self absorption effects and the geometry of the source of scattered radiation. The scattering angle was chosen to be approximately 30° since it provided an adequate scattered flux and ensured that the Compton scattered photons would be approximately 2.5 MeV. The latter reason was important to ensure that the energy of the scattered photons was well above that of most photons from the room background, the primary component being the 1.294 MeV photon from the beta decay of ^{41}Ar found in the reactor building air.

The experimental configuration is shown in Fig. 5.2. With no scatterer in place, the path of the direct beam of gamma rays was located and marked at positions 0.8, 1.8, and 2.3 meters behind the water tanks by means of a lead shielded Geiger counter and beam photographs. The path of the beam was delineated by means of a thin string stretched between a centering screw on the collimator and the mark at 2.3 meters.

A Harshaw 7.62 cm x 7.62 cm NaI(Tℓ) detector was placed in an open ended, form fitting lead shield, designed to constrain the crystal but allow direct viewing of the scatterer. The detector assembly was placed on top of additional lead shielding which in turn was situated on a moveable table and adjustments were made until the detector axis was in the same horizontal plane as the direct beam. A lead collimator 12.7 cm long with a 15.6 cm outer diameter and a 3.2 cm inner diameter was positioned coaxial to the detector and then lead bricks were placed around the detector on all sides to yield an approximate average thickness of 13 cm. It was noted that no apparent change was observed in the detector position.

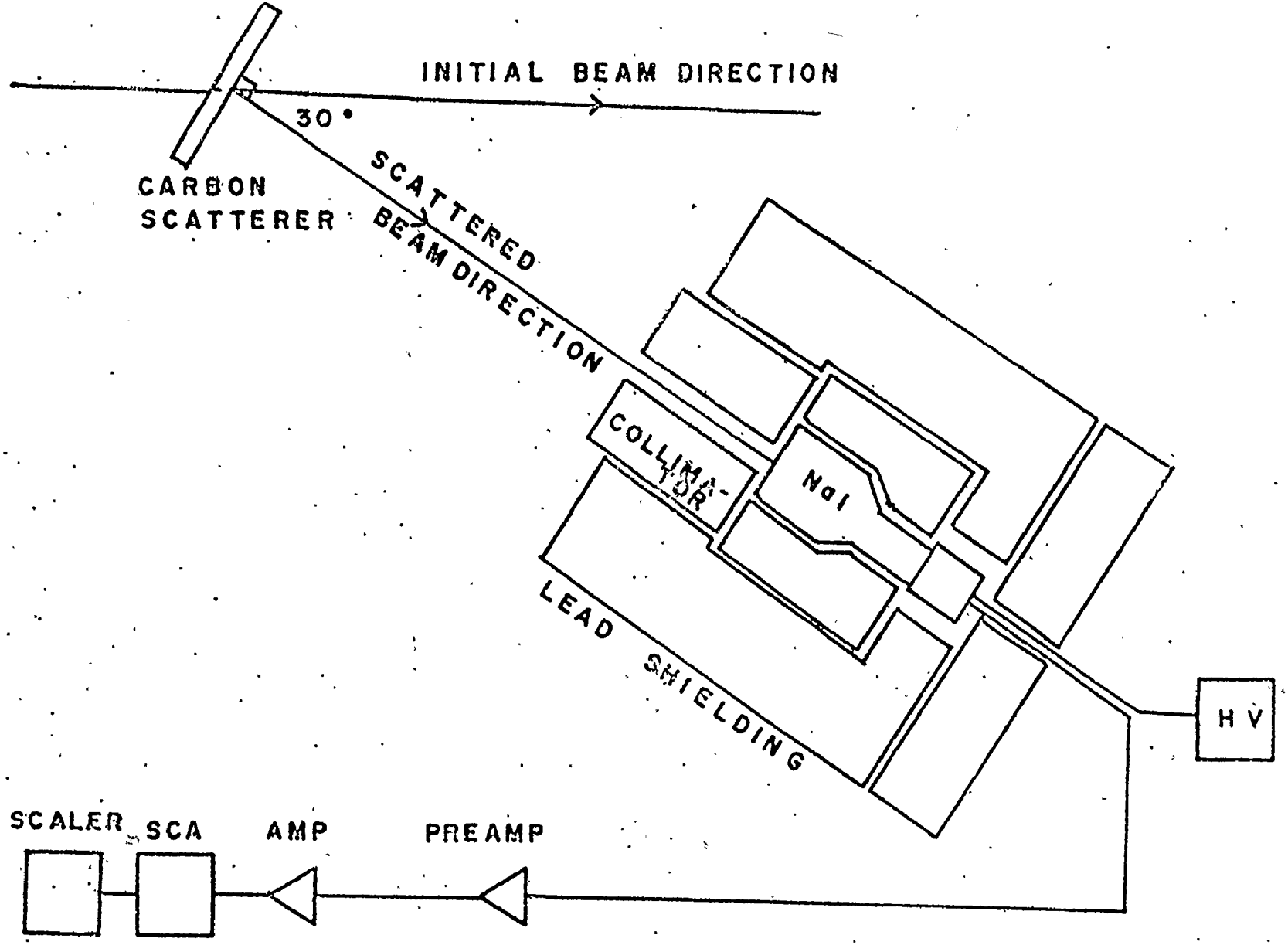

5.2 Experimental configuration for determination of the photon beam intensity by Compton scattering.

The supporting table was moved until the axis of the detector was oriented at an angle of 30° to the beam direction. Although the actual angle was attained roughly by using a large set square, it was determined accurately by triangulation employing the measured linear dimensions of the right triangle shown in Fig. 6.6. It was realized that the angle of scattering, an essential quantity, could also be determined by calibration of the energy of the scattered photons from the experiment, as an additional check of the triangulation method. It was found that the distance from detector face to the point of intersection of the detector axis and the direct beam was 102.5 cm and 145.2 cm respectively for the determination of the flux from the nickel and chromium sources. The set square was then used to orient the carbon scatterer about its point of intersection with the direct beam, until the face of the plate was parallel to the face of the detector.

The detector was operated at approximately 750 volts and the output signal was fed into a Canberra 1405 preamplifier. The preamplifier signal was sent to the input of a Canberra 1417 amplifier whose output in turn was sent

to a Nuclear Data 3300 multichannel analyser operating with a 512 channel conversion gain.

Data were collected for a 160 minutes live time and then for an additional 160 minutes live time in the subtraction mode with the scatterer removed, in order to correct for room background radiation and scattering of the direct beam by air molecules and collimators. The resultant spectra for the nickel and chromium sources are shown in section 6.2. During the entire experiment the reactor was operated at a 1.5 MW power level.

The energy of the Compton scattered peak was determined by means of a ^{60}Co calibration source, a ^{137}Cs source and a ^{22}Na source.

5.3 Measurement of Photoneutron Intensities

As intimated previously the measurement of photoneutron intensities was the primary investigation of this thesis. One of the targets listed in Table 4.2 was placed on the aluminum tray within a 2.54 cm marked square as shown in Fig. 4.10. The profile of the beam had previously been determined by photographic methods (section 5.2 and 6.2) and the position of the center of

the beam located. The horizontal direction of the beam was then delineated by means of a thin string in the same manner as in section 5.2 and its vertical position was marked on the beam port wall and sighted with a cathetometer. The target tray was then carefully moved horizontally and vertically on its support stand until the center of the target coincided with the center of the beam and the target face was perpendicular to the beam direction. After the positioning of the first target, subsequent targets could be positioned in the marked square of the sample tray and be assured of being in the beam. Even though the sample tray had been rendered immobile by placing lead weights on its base, periodic checks were made with the string and cathetometer to ensure that target position had not moved. The detector was placed on a platform consisting of a 45x15x1 cm sheet of foam rubber atop a plywood sheet of the same dimensions. This platform in turn was placed on two variable jacks. The detector was carefully moved until it was parallel to the beam and as close as possible to the sample to maximize solid angle without having its support legs

intersect the beam. This geometry has been analysed in detail in section 3.5.2. The center of the active volume, as determined from Fig. 3.9, was placed in the same x-y plane as the target center and then the jacks were elevated until the detector axis was parallel to and in the same horizontal plane as the axis of the beam. The detector was held stationary on the platform by two 4.5 kg lead blocks which also served to minimize microphonics but even so, as a precaution, the detector position was frequently checked. Both the detector and target holder were situated on a 0.65 cm thick levelled aluminum platform.

Next the beam monitor was set up facing the target and an energy window was set on its output at approximately 511 keV. This procedure has been described in detail in section 4.4. Approximately once every two weeks a ^{22}Na source was placed in a fixed position at the entrance of the monitor collimator and a 10 minute count taken to ensure that the SCA window had not widened or drifted considerably. In the event of such a drift (of which there were only two cases) the window was reset in the

same fashion as described in section 4.4 and the data taken after the last positive window check were discarded.

The electronics initially used were those without risetime discrimination, described in section 4.3.1. The nickel source was positioned in the core and a spectrum of photoneutrons from bismuth was collected over a one week period. After the bismuth data had been obtained spectra of natural lead, thallium, gold, and tantalum were taken for a period of one week each. Between each of the spectra and after the last one a four day spectrum of bismuth was obtained to ensure that the system gain stabilization was functioning correctly and to allow normalization of the beam monitor as discussed in section 4.4. Next the nickel source was replaced with the chromium source and spectra of bismuth, lead and enriched 208-lead were collected. The bismuth data were collected with and without risetime discrimination on alternate days over a two week period in order to determine the efficiency due to risetime discrimination (section 3.7). The lead data were each collected for a one week time interval and

again bismuth spectra were obtained for four days before and after each lead spectrum. With the exception of the first bismuth spectrum, all data taken with the chromium source in place were gathered using pulse risetime discrimination (sections 3.7 and 4.3.3). Finally, the chromium source was replaced with the nickel and a neutron spectrum was obtained for the enriched 208-lead target. Risetime discrimination was employed. At several times throughout the course of the experiment, background spectra were taken with the targets removed.

All spectra, taken using both chromium and nickel sources, are presented in section 6.3 together with a sample background spectrum. The identification of photoneutron groups and the subsequent analysis of data is discussed in section 6.3. Interpretation of the resultant data is discussed in Chapter 7.

5.4 Measurement of Fore-Aft Asymmetry of Photoneutron Emission in Lead

In an attempt to study multipole mixing for photoneutron reactions on lead, it was decided to perform an experiment to measure the relative neutron emission rate

in the forward and backward directions for angles symmetrical about 90° to the beam direction. The underlying theory behind such an experiment is discussed in Chapter 2.

The target tray was repositioned in the manner described in section 5.3 such that a target placed on it would be centered in the beam. The only difference was that the horizontal support rod was now parallel to but out of the beam. A target of natural lead 2.54 cm square and 0.64 cm thick was placed on the tray such that it was centered in the beam with its square face perpendicular to the beam. Two variable height jacks were bolted onto a four wheeled Dexion cart and a 45x15x1 cm sheet of plywood and similar sized sheet of foam rubber were placed on top of it. The detector was placed on top of the platform such that its axis was perpendicular to the beam direction and two 4.5 kg lead weights were placed on its base to render it immobile and minimize microphonics. The mobile detector assembly was constrained to move in a direction parallel to the beam by two 1.5 meter long "railroad tracks" made of

Dexion and held in position by lead bricks. The experimental layout is shown in Fig. 5.3. The jacks were independently varied in height until the detector axis was approximately 5 cm higher than the target center and in a plane parallel to that of the beam direction. With the detector assembly as far away from the target as possible, the center of the active volume, which had been previously marked on the outside of the detector was made to coincide with a string which denoted the beam direction (see section 5.2) and the axis was set perpendicular to the beam direction by using a large set square. Next the detector assembly was moved as far as possible to the other side of the target and if the mark on the detector failed to coincide with the string, the lead blocks on the Dexion tracks were lifted and the track direction adjusted. This process was repeated until the detector center coincided with the beam direction to less than 1 mm along its entire path, thus ensuring that the detector moved parallel to the beam. The detector was then positioned such that its axis was 7.6 cm away from the target center in the Z direction. Chocks were then placed tightly against the tracks and wheels and their position denoted

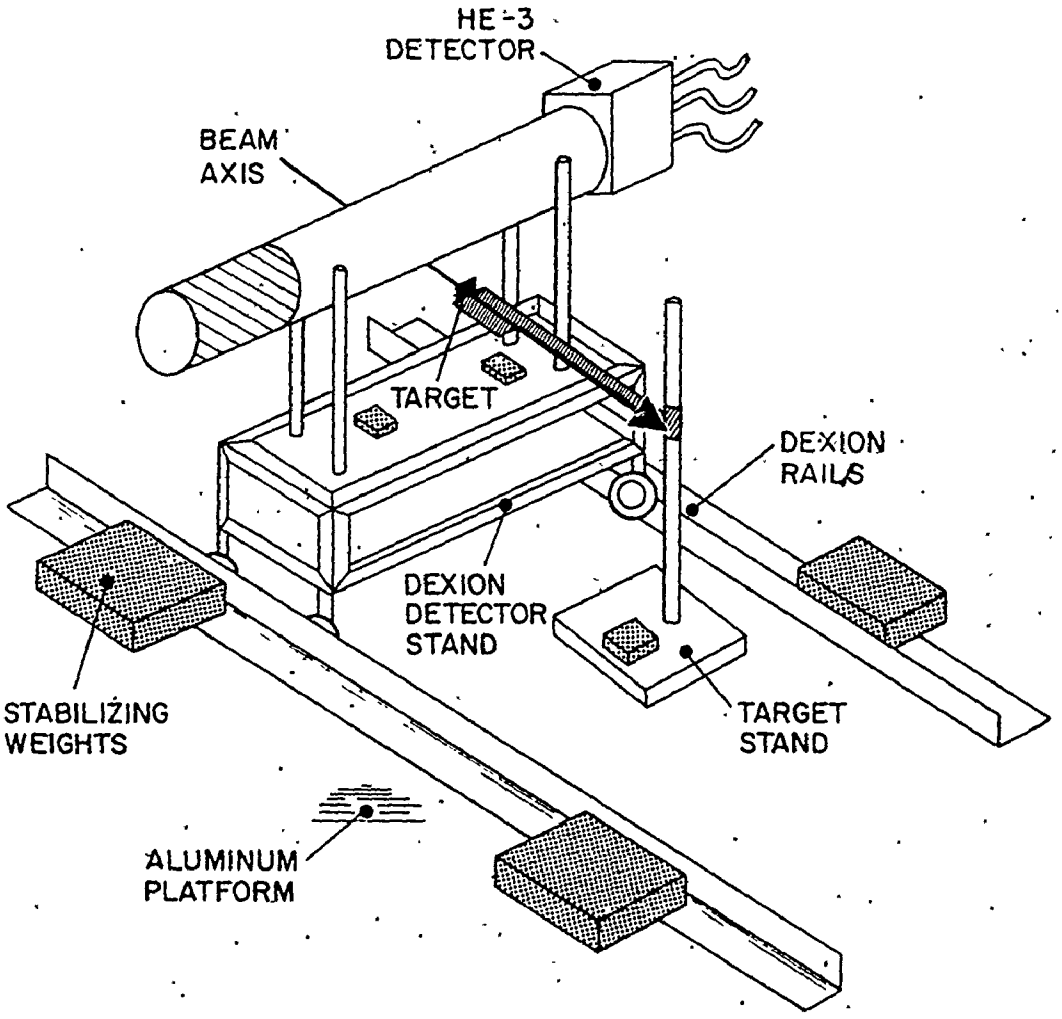

5.3 Experimental arrangement for determination of the fore-aft neutron emission asymmetry in lead. Detector moves along direction defined by the rails (parallel to beam axis) and is confined at two different positions by wheel chocks not shown. Beam monitor is also not shown.

with tape. The chocks were then removed and the detector moved to the other side of the target where the process was repeated. Afterwards the detector was moved back and forth several times between the two positions and the reproducibility in position was found to be ± 0.1 cm. This was also the error in the actual measured position. The actual detector positions used were chosen to satisfy four conditions :

1) to keep the detector out of the beam in order to minimize random adding
2) to look at polar angles close to 0° and 180° where the anisotropy should be largest (Chapter 2)
3) to be as close as possible to the target to maximize count rate
4) to be far enough from the target to define a reasonable angular resolution.

The angular resolution function for this geometry is derived in section 3.5.3. At the conclusion of the experiment the detector position was again measured and no observable change was seen.

The beam monitor was set up as in section 5.3 and 4.4. Since there might be a possible change in counting

rate in the monitor due to multiple scattering of photons when the detector was in the two different positions, it was decided to investigate this. Monitor counts were collected for twenty minute periods five times each with the helium-3 detector in both positions and in no case was there any observable difference in rate. As described in section 4.4, the beam monitor window was checked periodically to ensure that no drifts had occurred.

Data were collected over a four week period using the nickel photon source and then the chromium photon source. The electronics used employed no risetime discrimination and have been described in section 4.3.1. The detector was positioned in the forward and then backward direction on alternate days in order to minimize any unforeseeable long term effects due to a change in flux. The resultant spectra are presented in section 6.4 together with the analysis of the data. Interpretation of the results is discussed in Chapter 7.

CHAPTER 6

DATA AND ANALYSIS OF DATA

6.1 Photon Beam Spectral Components

The spectra of the nickel and chromium sources at the target position are shown in Figures 6.1 and 6.2 and the nitrogen calibration spectrum is shown in Figure 6.3. The double escape peaks are identified by the energy in keV of the incident photon noting that the nitrogen spectrum, taken with the Ge(Li) in the pair spectrometer mode, has no full energy or single escape peaks. Significant lines were identified for energies greater than 5.7 MeV for nickel and 5.0 MeV for chromium, since only a few nuclei (and certainly none in this experiment) have photoneutron thresholds below these energies. Lines in nitrogen were identified down to 1.8 MeV, since it was desired to obtain as many points as possible for the determination of the smoothed efficiency curve. Lines were identified initially by inspection and then, using the known energies of nickel (Ra67, Au75a, Au75b, Ki76), chromium (Ra67, Ra70, Au70, Ve70a) and nitrogen (Be71), a straight line least squares fit of channel number to energy was performed.

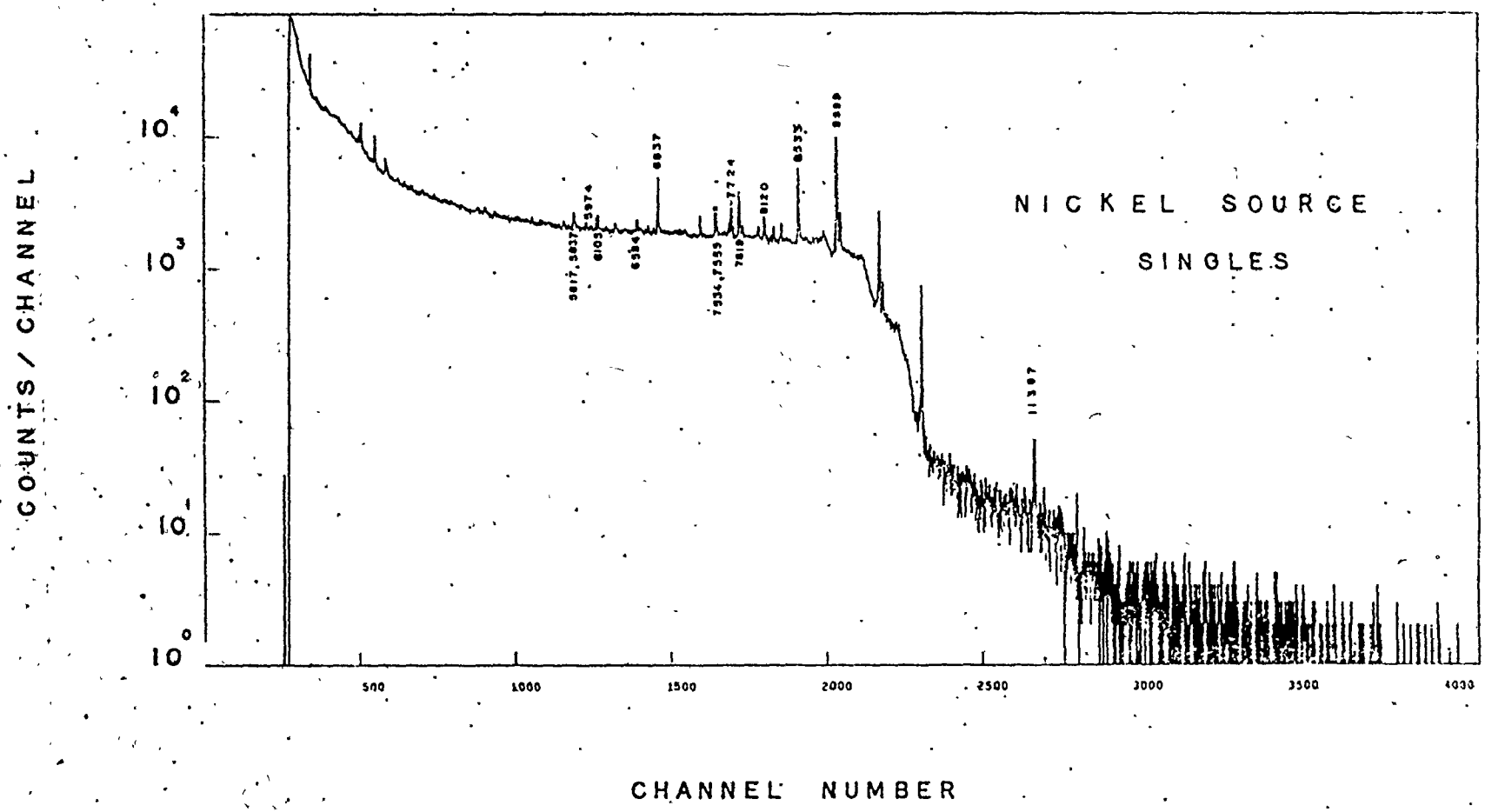

6.1 Spectrum of the beam of photons from the nickel source. Taken at target position using a Ge(Li) detector in singles mode.

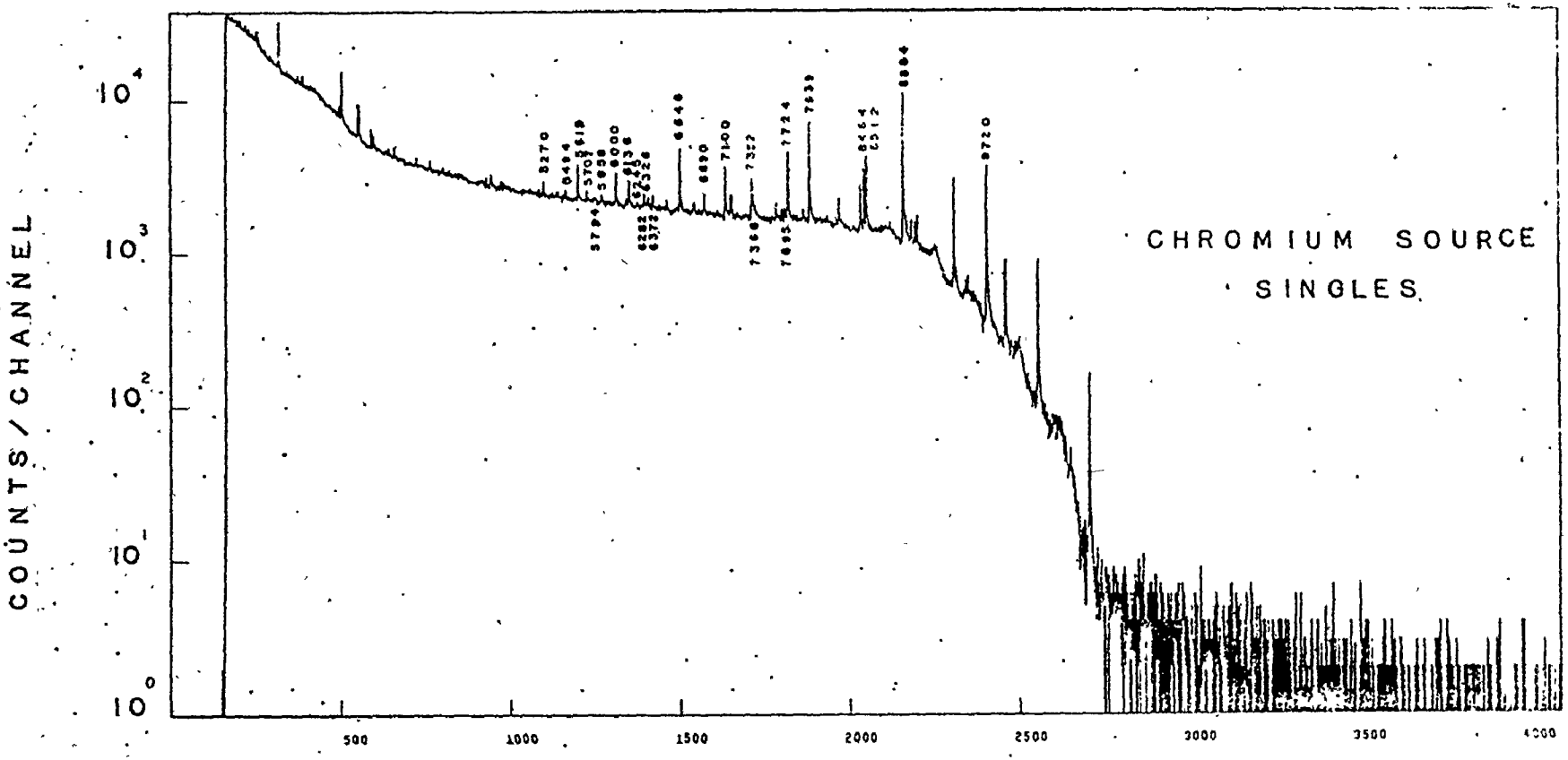

6.2 Spectrum of the beam of photons from the chromium source. Taken at target position using the same Ge(Li) detector in singles mode.

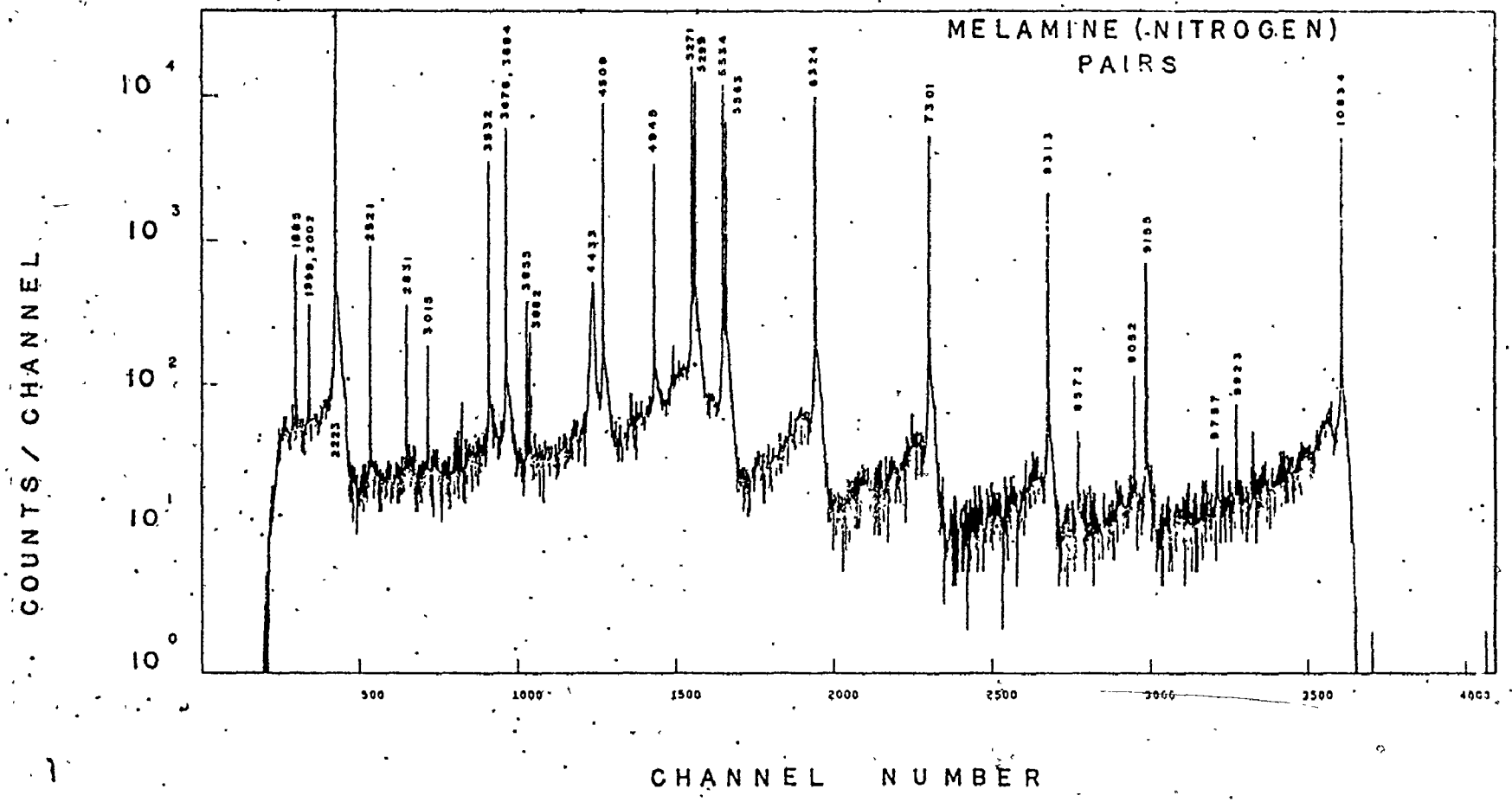

6.3. Calibration spectrum of a beam of nitrogen capture gamma rays from a melamine source. Source was placed in the McMaster tangential irradiation facility using a Ge(Li) detector and a NaI annulus in pair mode. Ge(Li) is the same used to obtain the Figures 6.1 and 6.2.

In all cases the reduced chi-square was approximately 1 and the results of the fit were then used to determine the energies of any unidentified lines.

A few points should be noted about the spectra. The nitrogen calibration spectrum possesses a strong peak at 2.223 MeV due to thermal neutron capture by hydrogen, strong peaks at 3.684, 4.433 and 4.945 MeV due to carbon, and a few small unidentified peaks presumably due to contaminants. Since the relative intensities of these lines were not known, they were excluded from the efficiency calibration. The spectrum of the nickel source is, with two exceptions, comprised entirely of lines from thermal neutron capture on stable nickel isotopes. The first exception is a line at 7.724 MeV due to thermal neutron capture on aluminum, presumably from the source holder and surrounding visible reactor core. The second is a line at 11.387 MeV due to thermal neutron capture on ^{59}Ni which in turn is produced by thermal neutron capture on ^{58}Ni. Since the half life of ^{59}Ni is approximately 8×10^4 years, it must be realized that the intensity of the 11.387 MeV photons will increase slowly with

irradiation time. This was not a consideration for our experiment, however, due to the low intensity of the line and its slow growth rate. The chromium spectrum was also comprised of peaks from thermal capture on stable chromium isotopes and aluminum. One line, quoted as 7.366 MeV by Rasmussen (Ra67) is actually seen to be a doublet at 7.377 and 7.363 ± .002 MeV. Furthermore, a low intensity unidentified line, presumably due to a contaminant, is seen at 7.695 ± .002 MeV.

A FORTRAN program was written to calculate the peak areas. Essentially the method was to choose several points on either side of the peak to serve as an estimate of the background and to fit a straight line to them using a linear least squares routine. The fitted background was then subtracted from the peak channel by channel and the resultant area under the peak was totalized. The percentage error in the area was taken as :

$$\Delta A = 100\sqrt{\sum_{I=IMin}^{IMax} (Y(I) - \sigma_A^2 + I^2\sigma_B^2 + 2I\sigma_{AB}^2)} \qquad (6.1)$$

where ΔA= error in area
I = channel number
IMin = minimum channel number of the peak

IMax = maximum channel number of the peak

Y(I) = number of counts in channel I

σ_A^2, σ_B^2, σ_{AB}^2 are the elements of the variance covariance matrix for the least squares fit of :

$$\text{BACKGROUND (I)} = A + BI \qquad (6.2)$$

A, B constants

Unresolved doublets were resolved by a trial and error procedure involving symmetrizing the unresolved portion of the two peaks, adding the estimated areas thus obtained and comparing with the total area. This was repeated until the sum of the areas was within statistical error and the peaks were reasonably symmetric. A similar procedure was done for triplets by first attempting to symmetrize the outer peaks and then calculating the shape of the middle peak.

The intensities of the twelve most intense lines of nitrogen were thus determined and were divided by the accepted values of the intensities (Be71) to yield the relative efficiency at each point. A linear least squares fit of the log of the efficiency as a function of energy was performed for polynomials of degree 2 to 8. The

best fit, with a reduced χ^2 of 0.5 was found for degree 5. The low value of χ^2 suggested that the error bars assigned to the points were 30% too small. The efficiency curve together with the calculated points and the percentage error in the curve is shown in Fig. 6.4. The percentage error for the curve was calculated using the variance-covariance matrix, namely:

$$P\Delta(E) = 100\sqrt{\sum_{I=0}^{N}\sum_{J=0}^{N} \sigma_{IJ}^2 \, E_\gamma^{I+J-2}} \cdot \mathrm{EXP}\left(\sum_{I=0}^{N} A_I E_\gamma^I\right) \qquad (6.3)$$

where $P\Delta(E)$ is the percentage error in the efficiency curve at photon energy E_γ

σ_{IJ}^2 are the elements of the variance-covariance matrix

N is the degree of the polynomial

I,J are integers

This efficiency curve was in turn used to determine the relative intensities for the photons from the nickel and chromium sources and the results are presented in Tables 6.1 and 6.2 respectively. Certain lines in

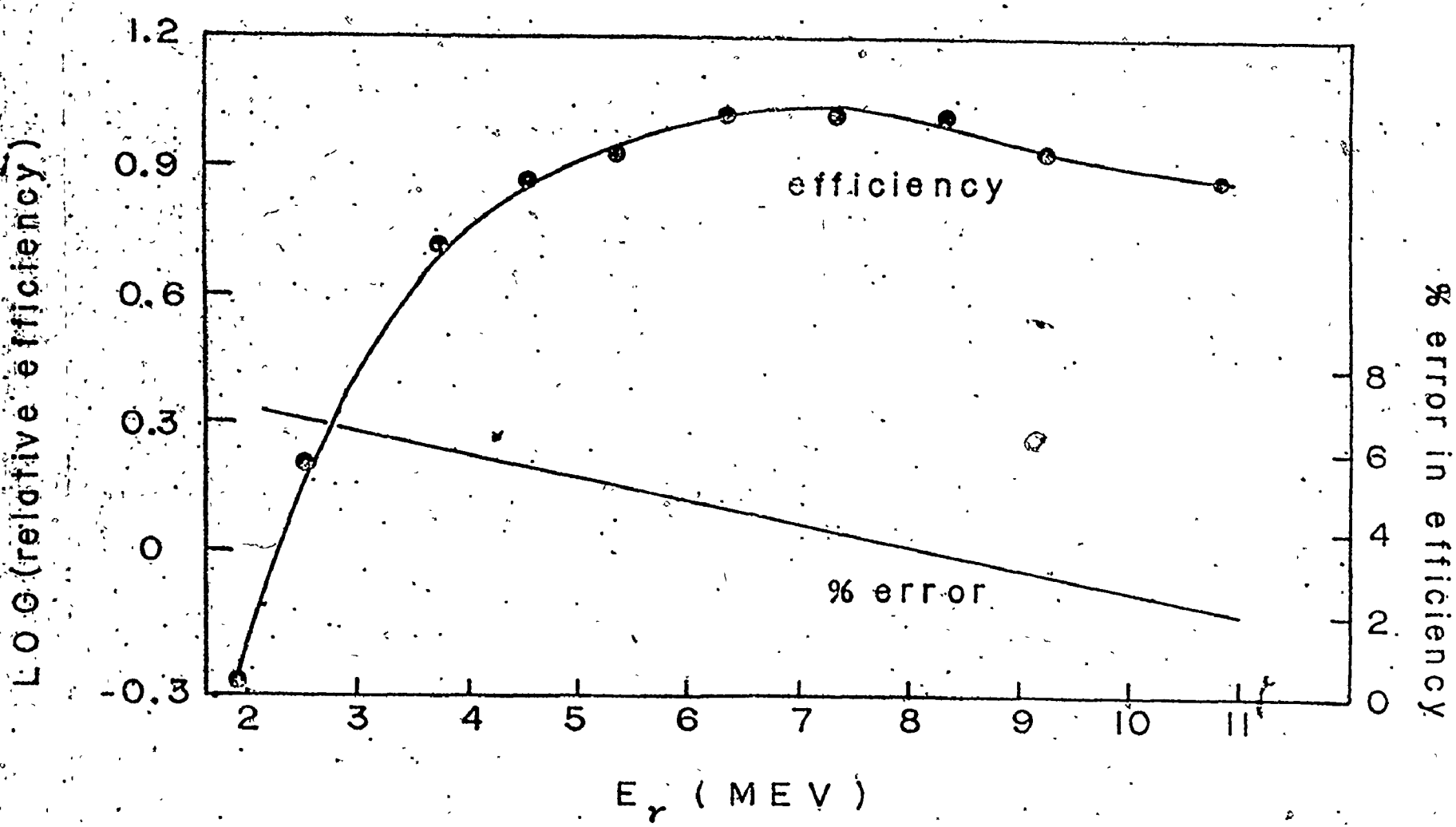

6.4 Relative efficiency of the Ge(Li) detector as a function of photon energy. Efficiency is determined for the double escape peaks only, using the nitrogen spectrum of Figure 6.3. Error bars are smaller than dots. Log of the efficiency has been fitted to a polynomial as shown. Percentage error is also shown.

chromium, namely the 5.707, 6.000, 6.136, and the 6.890 MeV line, contained a contribution from the single escape peak from a higher energy photon, or, as in the case of the 6.646 MeV double escape peak, a contribution from the full energy peak of one photon and the single escape peak of another. A correction for this was made by calculating the ratio of intensity of full energy and single escape peaks to the double escape peaks for well resolved lines. For the energy range of interest these ratios were constant within a few percent, being 0.21 for the single to double escape ratio. In most cases the correction was approximately ten percent of the peak area and, in one case, approximately twenty percent; and thus, errors resulting from this correction were felt to be less than a percent. The percentage error for a given peak is taken as the square root of the quadrature sum of the percentage error in the peak area and the percentage error in the efficiency curve. The tables also list the relative intensities for natural nickel and chromium taken from Rasmussen (Ra67) and the agreement is seen to be very good within experimental error.

6.2 The Beam Strength

6.2.1 The Beam Profile

The densitometer scans obtained from the experiments described in section 5.2.1, consisted of 34 - 1024 channel sets of data. The maximum counts per channel corresponding to a transmittance of 1, was 2325 and the minimum counts per channel which occurred for 0 transmittance was 0.

The transmittances were used to calculate the normalized density as given by :

$$D(J) = 1 - C(J)/2325 \qquad (6.4)$$

with $D(J)$ the normalized density at channel J
and $C(J)$ the number of counts in channel J

It was realized, however, that except for low photon intensities, density is not a linear function of intensity. For this reason, characteristic curves of density versus intensity were obtained from Eastman Kodak for Industrex AA film. These curves, however, were plotted over such a region that they did not approach saturation as closely as desired; and thus, it

was decided to find an analytical expression for the characteristic curve. A form suggested by Becker (Be66) is :

$$D = A(1 - EXP\ (-\ BI_\gamma)) \qquad (6.5)$$

where A and B are positive constants

D is density in arbitrary units

and I_γ is the relative photon intensity.

As a test of the model, the characteristic curves for different developing times were fitted using a nonlinear least squares fitting program. Since the errors assigned to the curves were unknown, the reduced χ^2 was meaningless, but in all cases visual inspection showed that the characteristic curves and model function very nearly equaled one another.

The density scale had previously been normalized from 0 to 1, but it was realized that maximum density could only occur for infinite intensity. Thus it was assumed that since the maximum number of counts per channel had been 2325 then the maximum density, D_{max}, (corresponding

to less than 1 count per channel) could be no less than $1 - {}^{1}/_{2325}$. Thus to a first approximation the normalized intensity could be given by :

$$I = \ln(1-D) \,/\, \ln(1-D_{max}) \qquad (6.6)$$

The intensities were then grouped into 1 mm x 0.9 mm bins and renormalized such that the maximum intensity per bin was 100. A contour plot is shown in Fig. 6.5 with the normal cubic target position (determined from section 5.3) superimposed. It is clear that from the large area of intensity 100 and sharp fall-off that the central region has not been completely corrected for saturation by our worst case approximation. This is adequate, however, since we are interested only in the general shape of the beam and the amount which misses the target.

The beam appears to be almost elliptical with a dense core and is apparently denser on the left side than the right as one faces the beam. This asymmetry may be due to the source not being completely aligned with the collimator and thus possibly the addition of

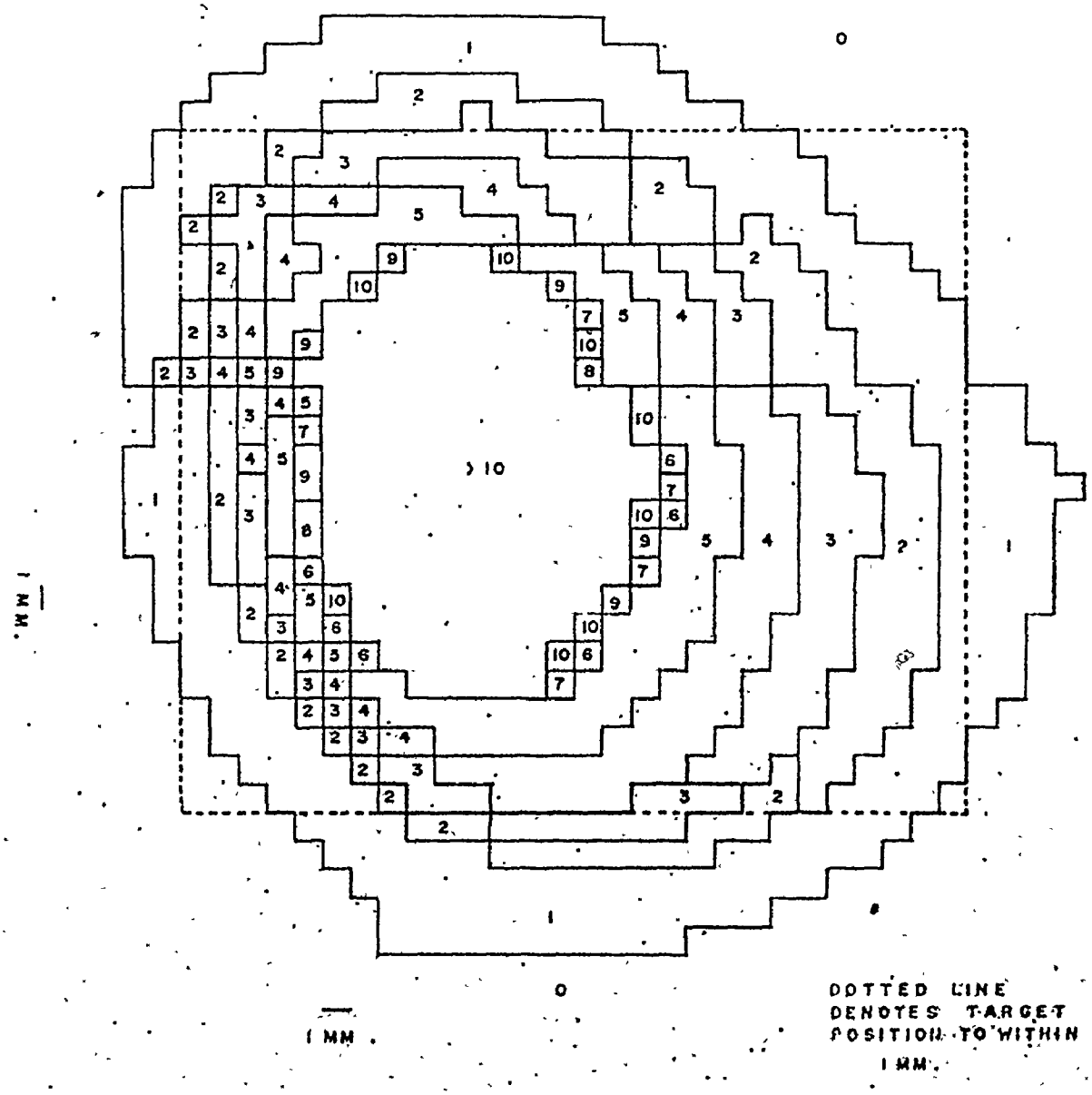

6.5. Contour plot of beam intensity profile. Numbers denote relative intensity as determined from measurements discussed in section 6.2.1. Position of standard 2.54 cm x 2.54 cm cross section targets is demarked by dotted line. Drawing is to scale as shown.

a source container in an adjacent fuel position might increase the photon intensity at the target.

The primary concern of this experiment was to determine how much of the beam missed the cubic targets. By adding the intensities and realizing the error in target positioning was ± 1 mm, this was found to be less than 4%. It must be realized that due to the crude approximation of the maximum intensity that the error may be much smaller. Nevertheless, as we shall see in section 6.2.2, the uncertainty in measurement of the total beam intensity is of the order of 10 to 14% and thus this correction is small in comparison.

One final point should be noted. The enriched 208-lead target, being much smaller than the cubic targets would be missed by a substantial portion of the beam. This was not deemed a problem since the isolated lines in the enriched target could be used to normalize the intensities to those of the cubic natural lead target.

6.2.2 The Absolute Flux

The spectra obtained during the absolute flux determination experiments for both nickel and chromium

sources are presented in figure 6.6 and several points are immediately obvious. The broad peak due to Compton scattering of high energy source photons is seen at approximately channel 200 for nickel and 358 for chromium. At a lower energy (approximately channel 106 for nickel and 188 for chromium) is a peak corresponding to Compton scattering of 2.223 MeV gamma rays from neutron capture by hydrogen in the reactor. Higher in energy than the Compton peaks is a broad spectrum thought to be due to bremsstrahlung production by high energy photons in the thick scatterer. Since all three features are due to events arising from beam photons, none would disappear when background was subtracted. The lower level discriminator of the ADC eliminated any annihilation photons which would be produced due to pair production in the scatterer.

The first step in the analysis was the elimination of the smooth background under the Compton peak. A non-linear fit to an exponential was done for data points between channels 234 and 314 (nickel) and channels 412 and 512 (chromium), where the log plot of the count rate versus channel number appeared to be a straight line. The fitted exponential was then extrapolated into the

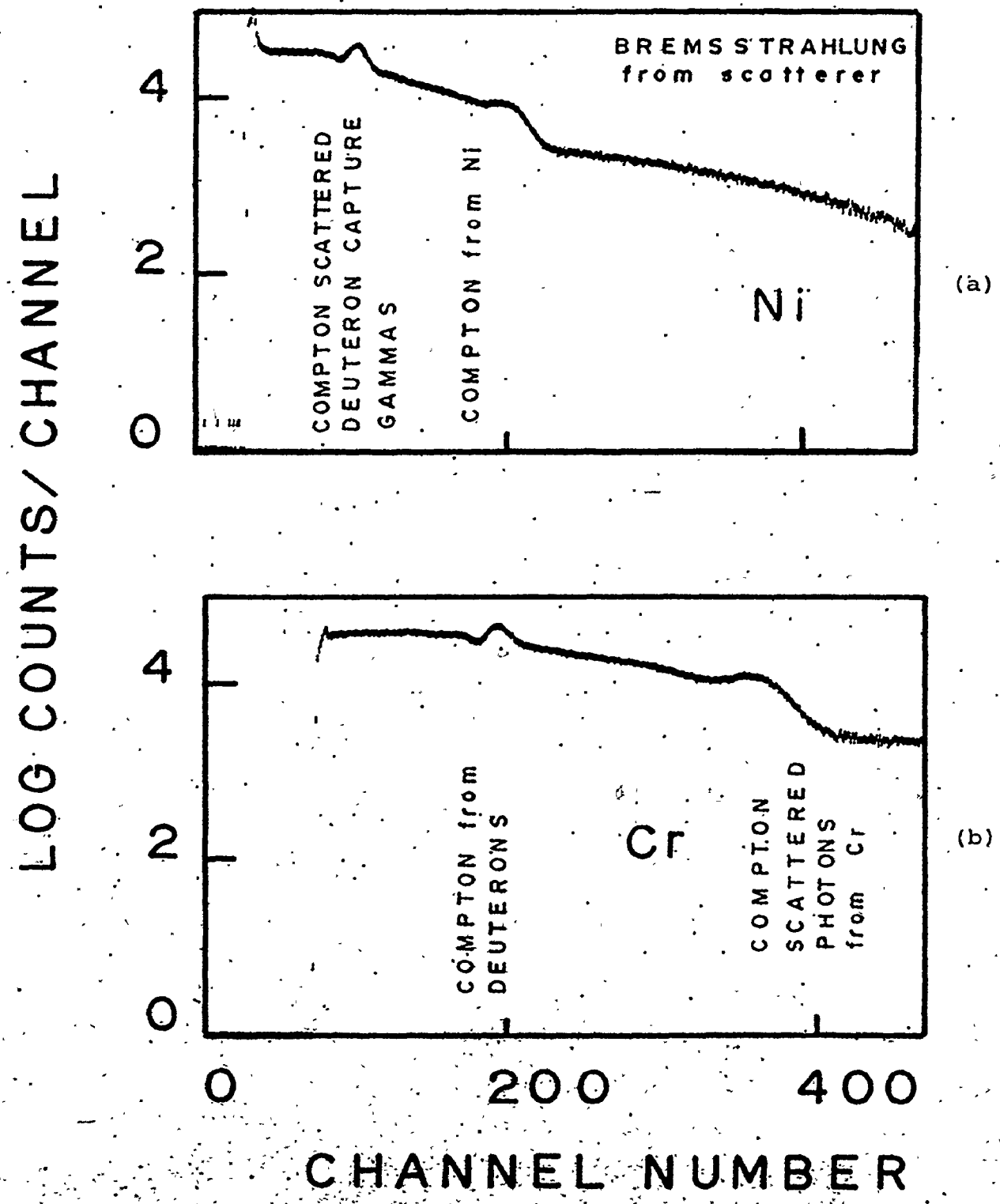

6.6 Spectra of photons Compton scattered from beam. Top is from nickel source and bottom is from chromium source.

region of the peak and then subtracted channel by channel from the peak. The region between channels 185 and 234 (nickel) and 335 and 412 (chromium) were then fitted to a Gaussian in order to determine the centroid. In a manner analogous to Heath (He64), the number of counts to the right of the centroids were determined and doubled, yielding 222000 ± 6000 for the nickel source and 210000 ± 5600 for the chromium source. The errors are seen to be larger than statistical errors due to an error in determination of the centroid and errors generated in fitting the background and peak. The latter is significant since the peak is actually a sum of Compton peaks at slightly different energies due to different incident photon energies and hence the peak is not truly Gaussian in shape.

In order to determine the centroid energy of the Compton scattered peaks, spectra of ^{60}Co and ^{22}Na were obtained. These yielded peaks at energies 1.173 and 1.333 for cobalt and 0.511, 1.275 and 1.786 MeV (sum peak) for sodium. Since NaI(Tl) detectors do not have a linear response for pulse height versus photon energy, the

relationship was empirically determined by fitting the energy, using a least squares method, to a second degree polynomial in channel number. The fit was then used to determine the centroids of the Compton scattered source peaks and Compton scattered deuteron peaks. These were seen to be at 2.515 MeV for the nickel source, 2.354 for the chromium source, 1.360 MeV for the scattered deuteron line from the nickel experiment and 1.330 MeV for the scattered deuteron line from the chromium experiment. By using the equation for Compton scattering:

$$E_\gamma^1 = \frac{E_\gamma}{1+\frac{E_\gamma}{mc^2}(1-\cos\theta)} \qquad (6.7)$$

where E_γ is the incident photon energy,

E_γ^1 is the energy of the photon scattered through an angle θ with respect to the incident beam, and mc^2 is the rest mass of the electron, the angle of scattering can be inferred from the peak energies. We get 31.40 ± 0.03 degrees for the nickel Compton scattered peak if an experimental initial intensity distribution, as given in Table 6.1, is used and 31.30 ± 0.03 degrees for the

deuteron Compton scattered peak from the nickel experiment. Likewise we get 31.90 ± 0.03 degrees and 32.26 ± 0.03 degrees and 32.26 ± 0.03 degrees for chromium when the experimental intensity distribution of Table 6.2 is used. The errors are associated mainly with uncertainty in determination of the peak centroids.

Next it was required to calculate the fraction of source photons scattered into the detector. A schematic of the idealized geometry is presented in Fig. 6.7 with the dimensions for both the nickel and chromium experiments. The thickness of the carbon scatterer was measured as 2.45 ± 0.02 cm using a micrometer, and the collimator diameter was 3.18 ± 0.10 cm. The lengths TP, TS and PS from Fig. 6.7 were found to be 118.2 cm, 102.7 cm, and 62.3 cm for the nickel experiment and 132.5 cm, 107.8 cm, and 76.0 cm for the chromium, all with an error of ± 0.1 cm. The point P was taken as a point in the center of the collimator, and was determined after the experiment was terminated, by removing the detector and stretching a string centered in the collimator. A point was then marked on the support platform directly under the string, either at the entrance of the collimator (for chromium)

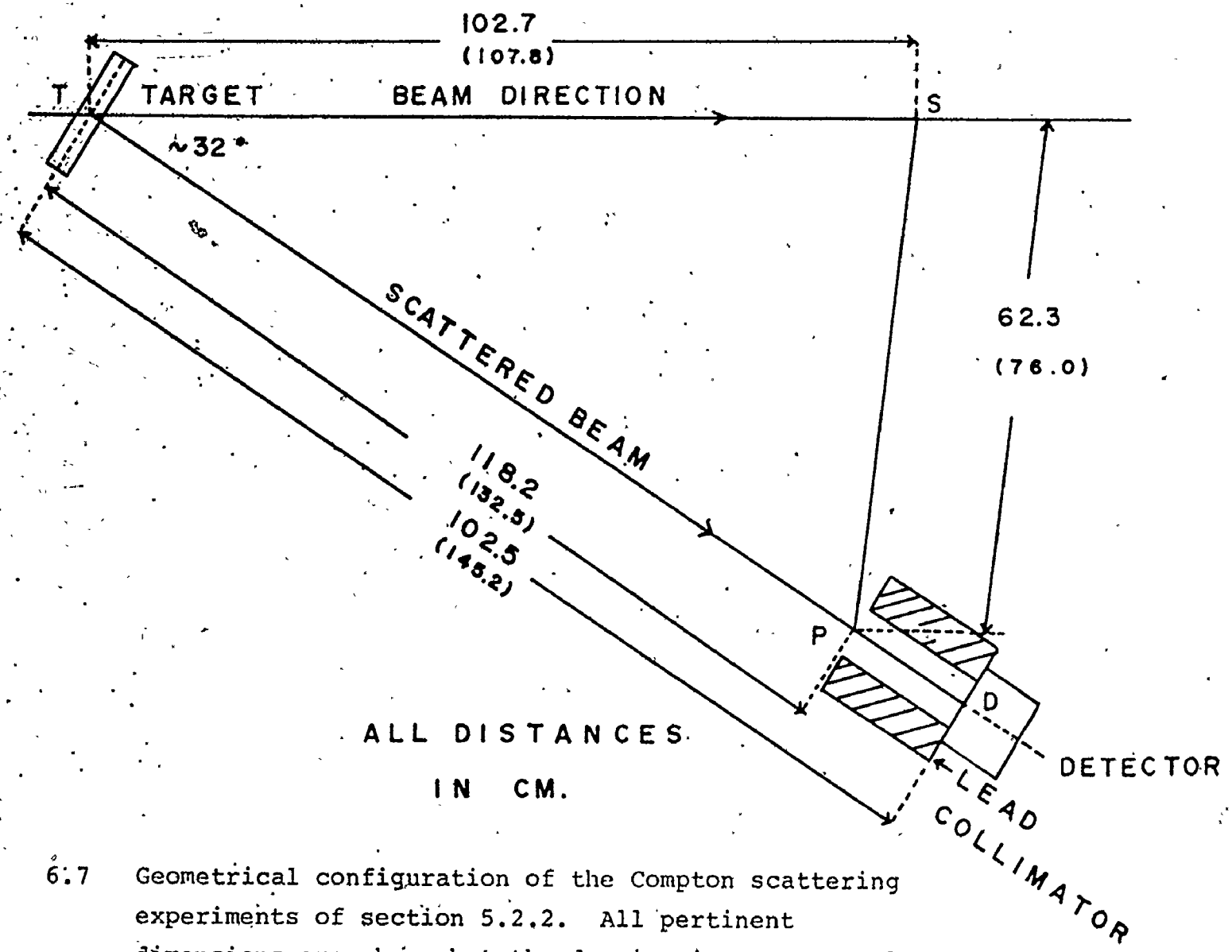

6.7 Geometrical configuration of the Compton scattering experiments of section 5.2.2. All pertinent dimensions are shown but the drawing is not to scale.

or behind it (for nickel). The angles of the triangle were calculated using the cosine law and then the angles were summed to check closure with 180 degrees. The difference from 180 degrees was used to estimate the error in θ. Thus, it was found that the measured angle θ was 31.8 ± 0.3 degrees for nickel and 32.0 ± 0.3 for chromium. Thus averaging with the angles determined from the spectra, it was felt reasonable to assign θ to be 31.5 ± 0.3 degrees for the nickel experiment and 32.1 ± 0.3 degrees for chromium. In contrast, the orientation of the carbon scatterer with respect to the beam direction could be measured to only 58 ± 1 degrees.

Several assumptions were made in order to simplify the calculation.

The incident gamma rays contributing to the Compton scattered peak were assumed to possess initial energies greater than 5.5 MeV for the nickel experiment and 5.6 MeV for the chromium. This was determined by taking the relative intensities of section 6.1 and multiplying them by their respective Compton scattering cross sections as determined by the Klein-Nishina equation :

$$\frac{d\sigma}{d\Omega} = \frac{r_o^2}{2}\left(\frac{E_\gamma^1}{E_\gamma}\right)^2 \left(\frac{E_\gamma}{E_\gamma^1} + \frac{E_\gamma^1}{E_\gamma} - \sin^2\theta\right) \qquad (6.8)$$

with $\frac{d\sigma}{d\Omega}$ is the cross section per electron for Compton scattering

r_o is the classical electron radius

E_γ is the incident photon energy

E_γ^1 is the scattered photon energy

and θ is the angle of scattering.

Next, equation 6.7 was used to determine a spectrum of relative scattered intensities. The energy resolution near 2.5 MeV was determined by extrapolating the widths of the calibration peaks using the equation :

$$\delta = \sqrt{A + BE_\gamma} \qquad (6.9)$$

where δ is the full width at half maximum

A,B are empirically determined constants

and E_γ is the photon energy.

Finally, the resolution function was folded into the relative intensity distribution and the percentage of initial photons contributing to the higher energy half of the peak was determined. It was thus found that energies lower than 5.5 MeV in nickel and 5.6 MeV in chromium

contributed only a few percent to the total scattered intensity and thus were neglected.

The total interaction rate of the incident beam with the scatterer was assumed to be concentrated at a point in the middle of the target. This was allowed since the probability of interaction for incident and scattered photons was small and because the target was far enough away from the detector to appear like a point source.

The scattered beam was assumed to strike the face of the detector at right angles, essentially ignoring the spread of up to ± 0.9 degrees about perpendicularity.

It has been shown in a more detailed calculation for a similar experiment (Ro74), that the last two assumptions introduce a change of only 0.5%, negligible with respect to the 5% to 10% uncertainties in the absorption coefficients (St70).

The average reaction rate was estimated as

$$R = 1 - \frac{\Sigma \exp\left(-\mu_1 t/\cos 32^\circ\right) I(E)}{\Sigma I(E)} \qquad (6.10)$$

with μ_1 being the linear absorption coefficient for photons of energy E in carbon,

I(E) the relative intensity of photons at energy E,

t the thickness of the scatterer, and the sum being over all photon energies above 5.5 MeV for nickel and 5.6 MeV for chromium. The self absorption for the target was taken to be

$$S = \exp(-\mu_2 t/2) \qquad (6.11)$$

where μ_2 is the linear absorption coefficient for the scattered radiation in carbon. The fraction of events scattered into the detector was taken as

$$F = Z \Sigma \frac{1}{\sigma_T} \frac{d\sigma}{d\Omega}(E,\theta)\Delta\Omega\, I(E)/\Sigma\, I(E) \qquad (6.12)$$

In the expression, Z is the atomic number of carbon, $d\sigma/d\Omega$ is the differential cross section per electron for Compton scattering given by equation 6.8 for photons of energy E and scattering angle θ ($31.8 \pm 0.3°$ for nickel, $32.0 \pm 0.3°$ for chromium), $\Delta\Omega$ is the small solid angle extending from the center of the scatterer to the rear of the collimator aperture, and σ_T is the total interaction cross section

for photons of energy E in carbon (St70). Again, the sum is over all discrete photon energies greater than 5.5 MeV for nickel and 5.6 MeV for chromium. The interaction rate in the 7.62 cm NaI(Tℓ) detector was seen to be

$$D = 1 - \exp(-7.62\mu_3) \tag{6.13}$$

with μ_3 being the linear absorption coefficient (cm^{-1}) in NaI at the mean scattered photon energy (Ha75). The probability of an event being found in the full energy peak was estimated to be

$$P = pRSFD \tag{6.14}$$

where p is the photofraction taken from the curves of Heath (He64) for a 7.62 cm NaI(Tℓ) detector. The flux of gamma rays could thus be calculated as

$$\phi = M/P \tag{6.15}$$

where ϕ is the flux for gamma rays of energy greater than 5.5 MeV (nickel) or 5.6 MeV (chromium) and M is the count rate (s^{-1}) taken from the spectra, namely $(23.13 \pm .62)s^{-1}$ for nickel and $(8.99 \pm .24)$ for chromium.

Finally, a first order correction was made for the transmission of scattered photons through small thicknesses of the lead collimator, an effect which would introduce an apparent small increase in the solid angle of the detector as viewed by the point source. The geometry for this calculation is illustrated in Fig. 6.8. The path length through the lead is given by :

$$\ell = \frac{r-R}{\sin\theta} = \frac{(r-R)\sqrt{r^2+(TD)^2}}{r} \qquad (6.16)$$

If unit flux irradiates the collimator aperture the flux per unit area can be approximated by :

$$\frac{d\phi}{dA} = \frac{1}{\pi R^2}$$

If we furthermore assume that the same flux would strike the detector outside radius R if the lead shielding were removed, the transmission through the walls of the collimator can be estimated as :

$$T = \int \frac{dA}{\pi R^2} \exp(-\mu_4 \ell) \qquad (6.17)$$

$$= \int_R^{R_1} \frac{2r}{R^2} \exp\left(-\mu_4 \frac{(r-R)\sqrt{r^2+(TD)^2}}{r}\right) dr \qquad (6.18)$$

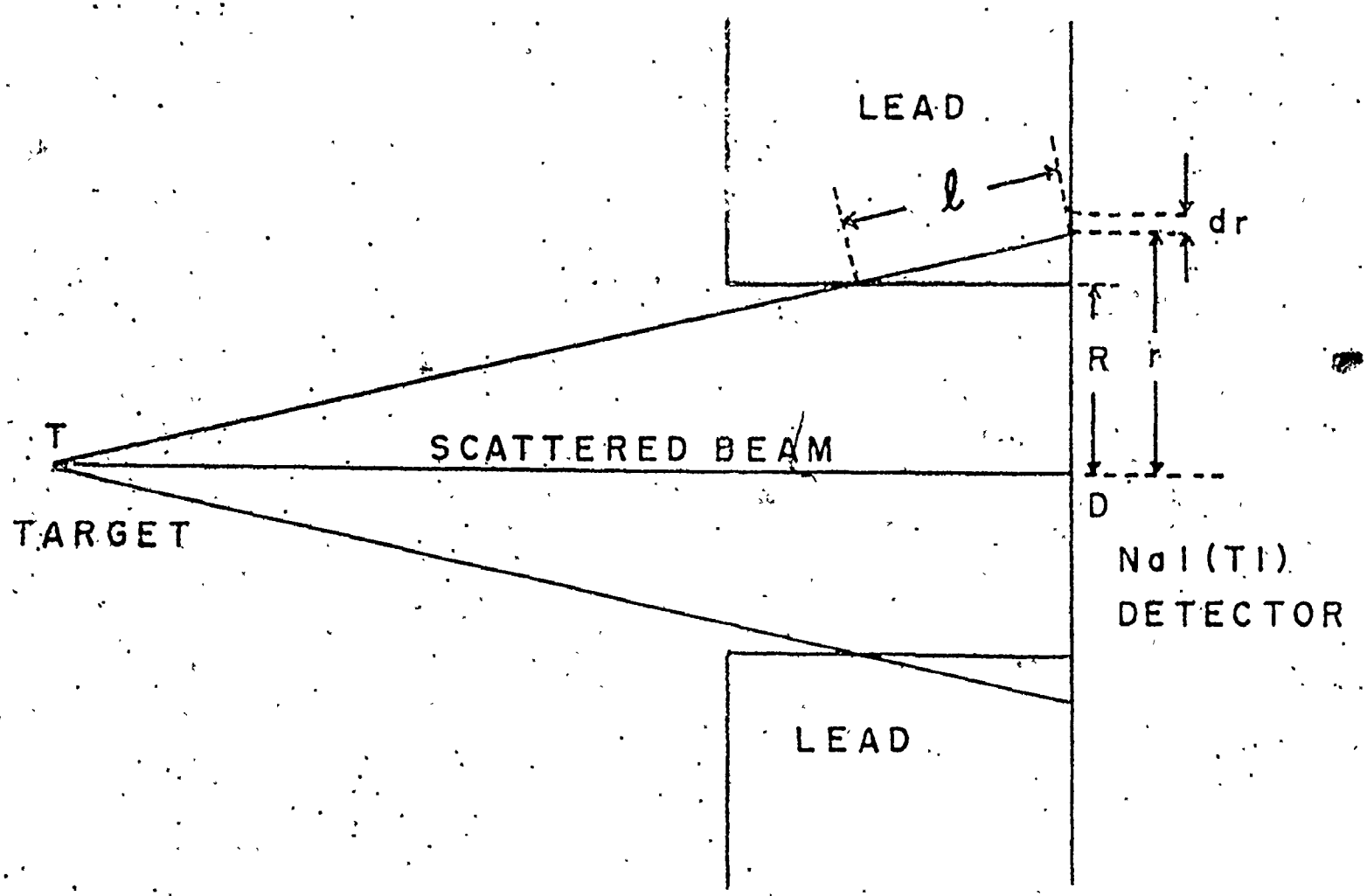

6.8 Geometry used in the calculation of the solid angle correction due to photon transmission through the collimator edge. Used in the analysis of Compton scattering experiments.

where μ_4 is the linear absorption coefficient for the scattered radiation in lead and R_1 is the maximum radius for significant contribution to the integral.

When all of the above considerations were taken into account, the total incident flux was found to be $(7.30 \pm 0.70)\times10^{6}s^{-1}$ for nickel photons of energy greater than 5.5 MeV or $(2.90 \pm 0.28)\times10^{6}s^{-1}$ for the 8.999 MeV photon on May 27, 1975. Similarly, it was found that the total flux for chromium gamma rays of energy greater than 5.6 MeV was $(3.23 \pm 0.43)\times10^{6}s^{-1}$ corresponding to a flux of $(3.44 \pm 0.50)\times10^{5}s^{-1}$ for the 9.719 MeV gamma ray on November 20, 1976. It was noted that these results were only valid at the target position for a 1.5 MW reactor power level and that less than 4% of the beam intensity missed the normal cubic targets (section 6.2.1).

6.3 Photoneutron Intensities

6.3.1 The Data

The photoneutron spectra collected during the experiments described in section 5.3 are presented in Figures 6.9 to 6.17. Each spectrum is identified by the name of the target material and it is indicated

whether or not risetime discrimination was employed. Peaks in the spectra are denoted by three numbers, A, E_x, E_γ, for polyisotopic elements and two numbers, E_x, E_γ, for monoisotopic elements. The first number, A, stands for the atomic mass of the residual nucleus and E_x stands for the excitation energy in keV of the particular nuclear level that is populated. The last number, E_γ, denotes the energy in keV of the exciting photon. Certain peaks which correspond to two or more unresolvable neutron groups have been denoted by a letter, and their components are tabulated in section 6.3.4 and 6.3.5. Identification of the photoneutron groups is described in section 6.3.4. Three groups in lead which were unable to be identified have been designated "UNASSIGNED 1, 2 and 3". These are discussed in Chapter 7. For comparison, a background spectrum collected over a similar time period is presented in Fig. 6.18. This spectrum is typical of those collected throughout the experimental period and clearly is entirely negligible in the energy region above the epithermal peak.

6.9 Neutron spectrum of the $^{209}Bi(\gamma,n)^{208}Bi$ reaction using photons from nickel source. Numbers used to identify neutron groups are explained in section 6.3.1.

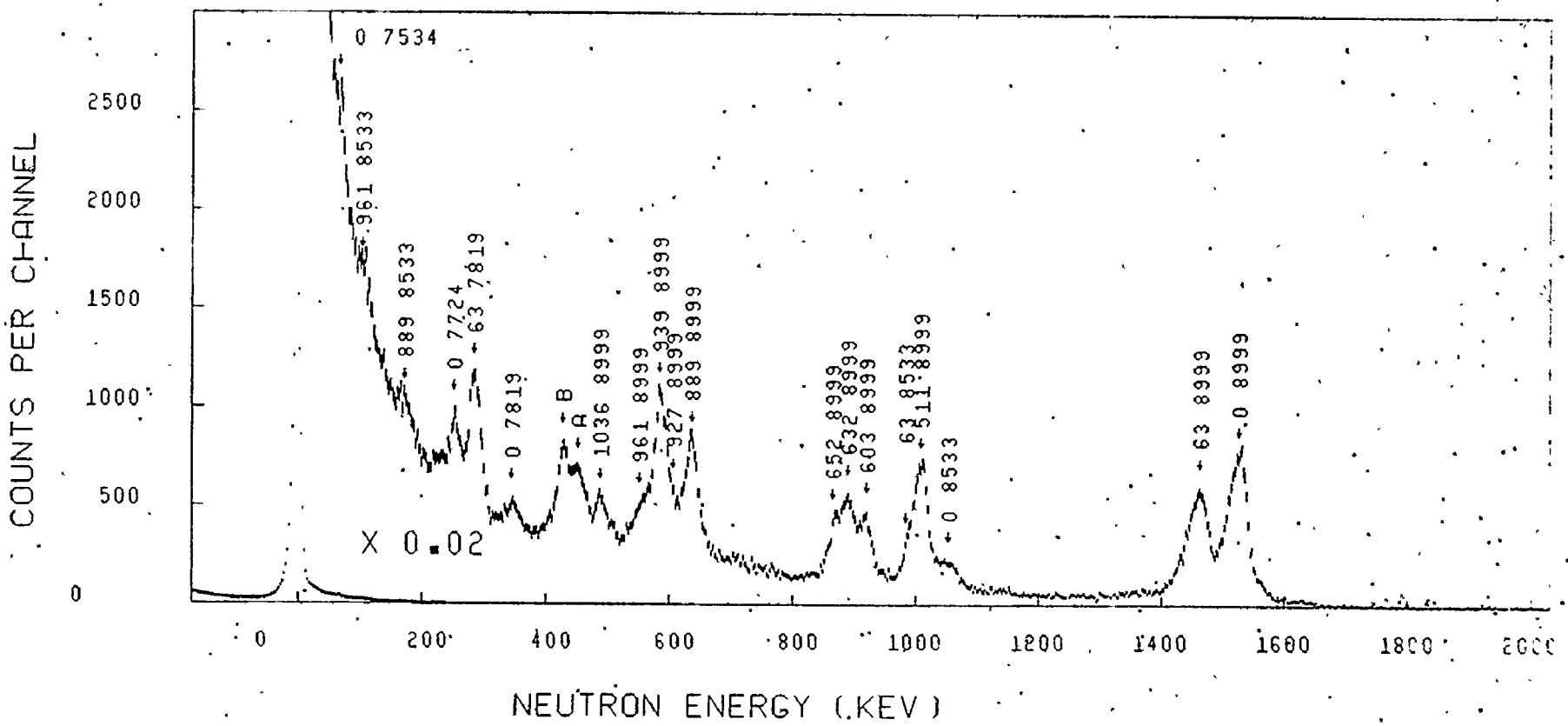

6.10 Neutron spectrum of the $^{209}Bi(\gamma,n)^{208}Bi$ reaction using photons from chromium source. Numbers used to identify neutron groups are explained in section 6.3.1.

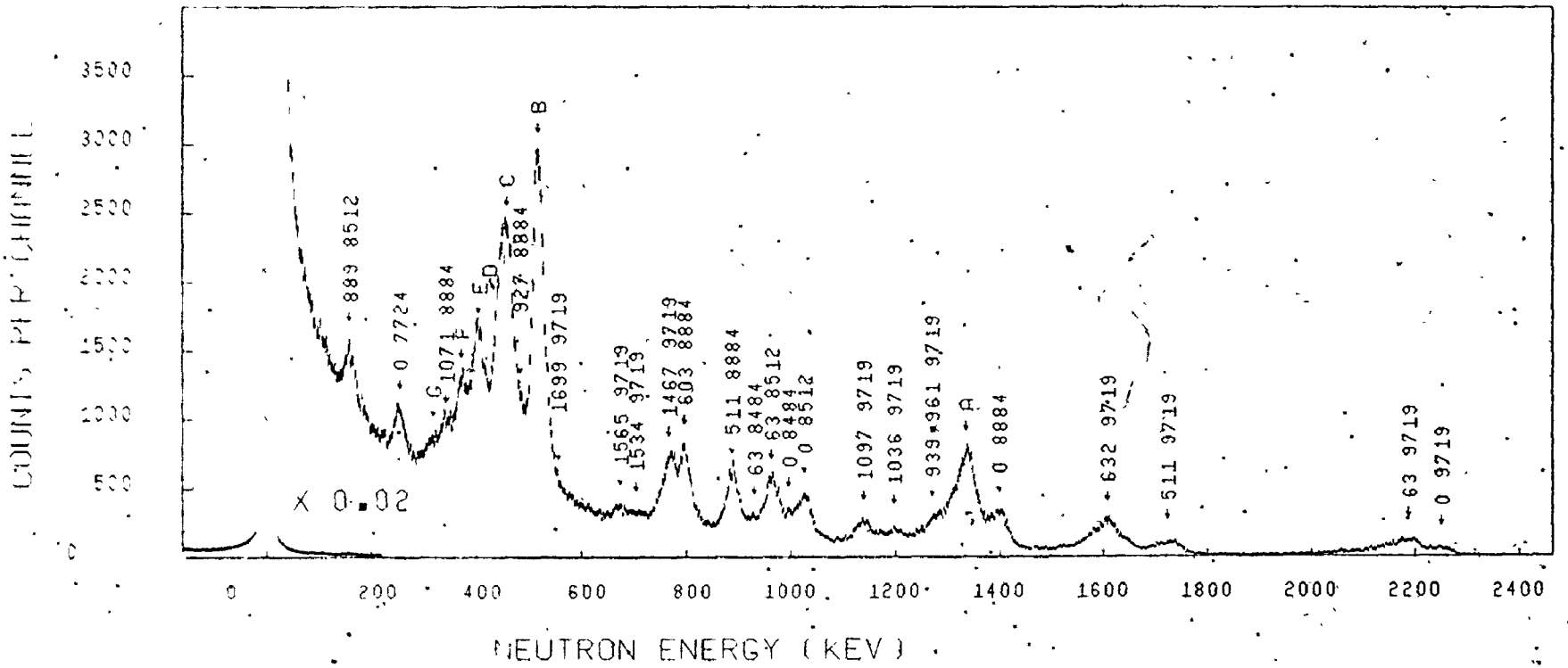

6.11 Neutron spectrum of the $^{nat}Pb(\gamma,n)$ reaction using nickel capture photons. Numbers used to identify neutron groups are explained in section 6.3.1.

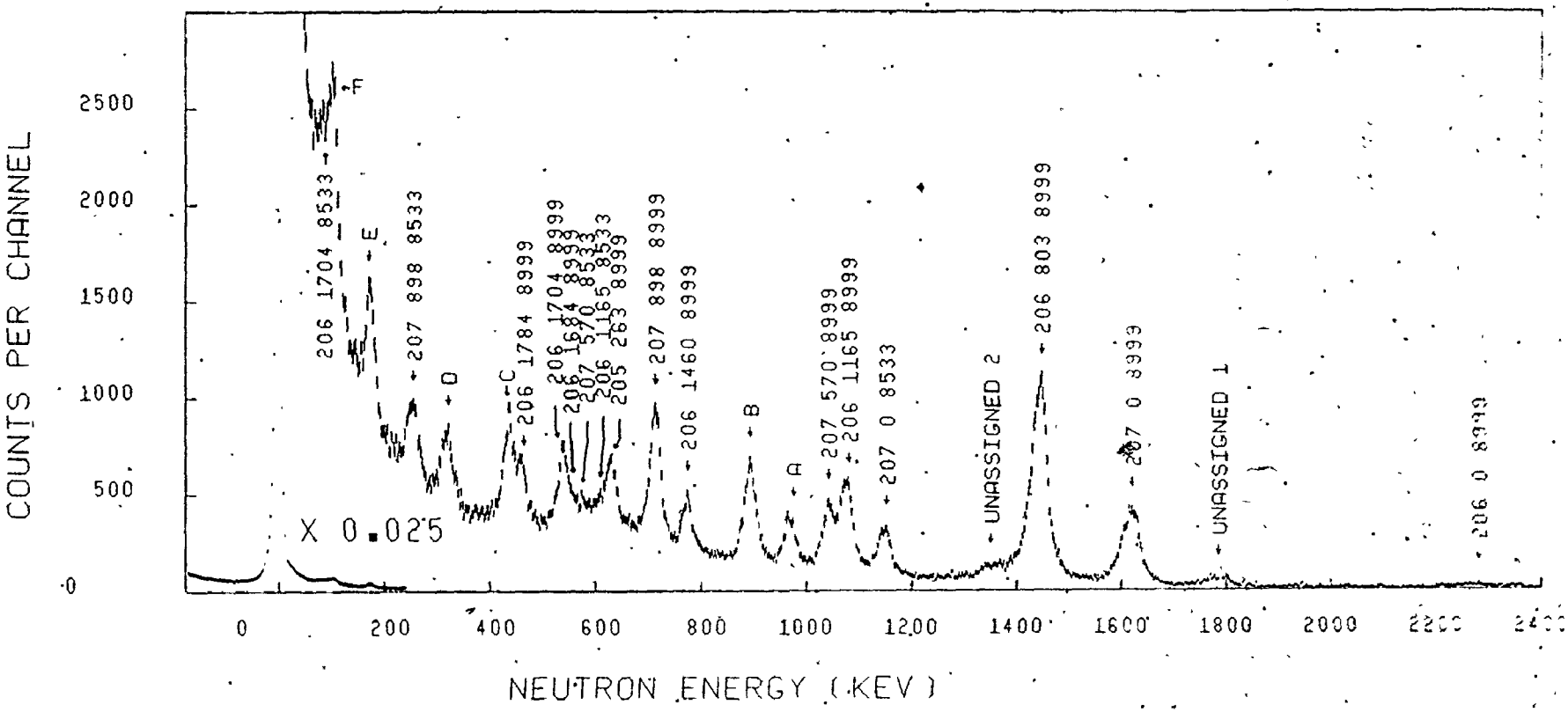

6.12 Neutron spectrum of the enriched $^{208}Pb(\gamma,n)$ reaction using nickel capture photons. Numbers used to identify neutron groups are explained in section 6.3.1.

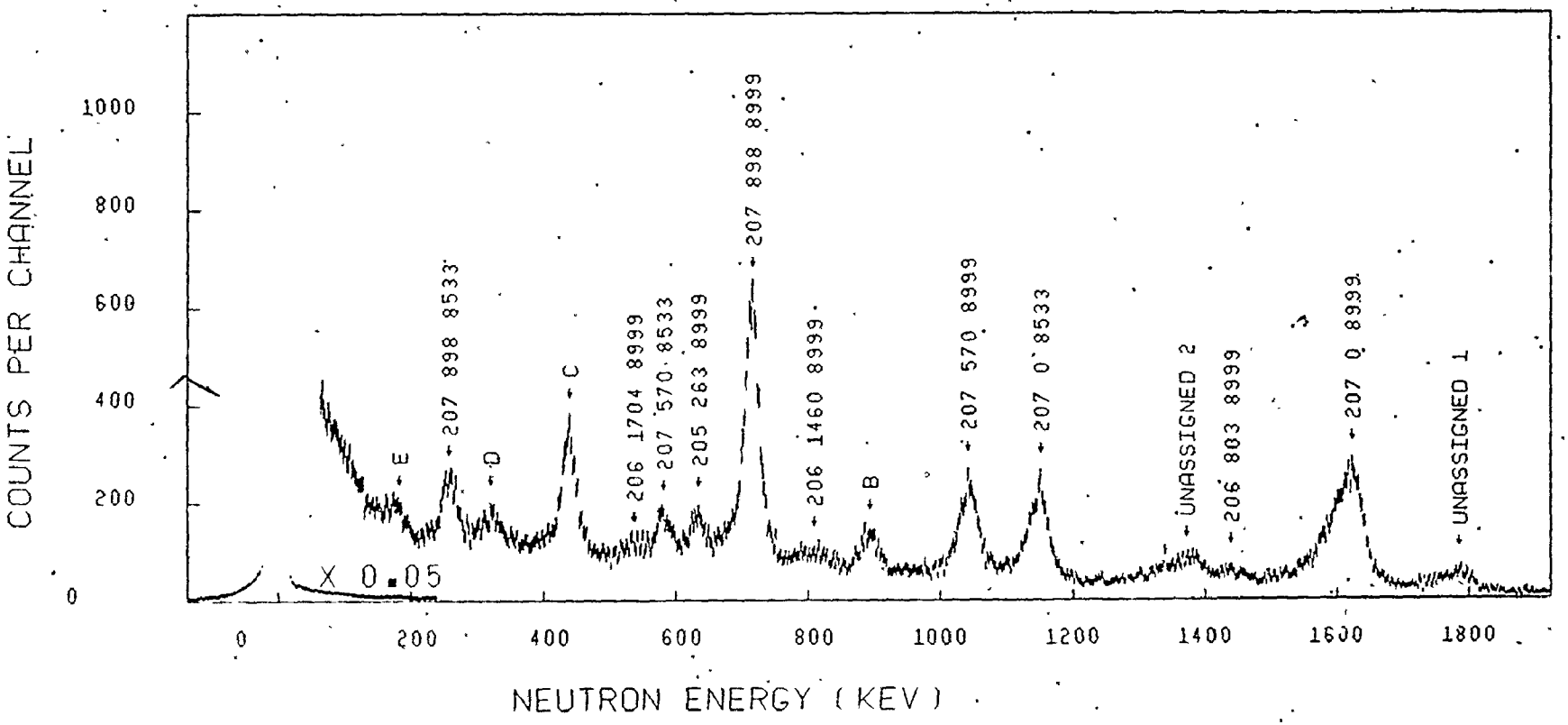

6.13 Neutron spectrum of the $^{nat}Pb(\gamma,n)$ reaction using chromium capture photons. Numbers used to identify neutron groups are explained in section 6.3.1.

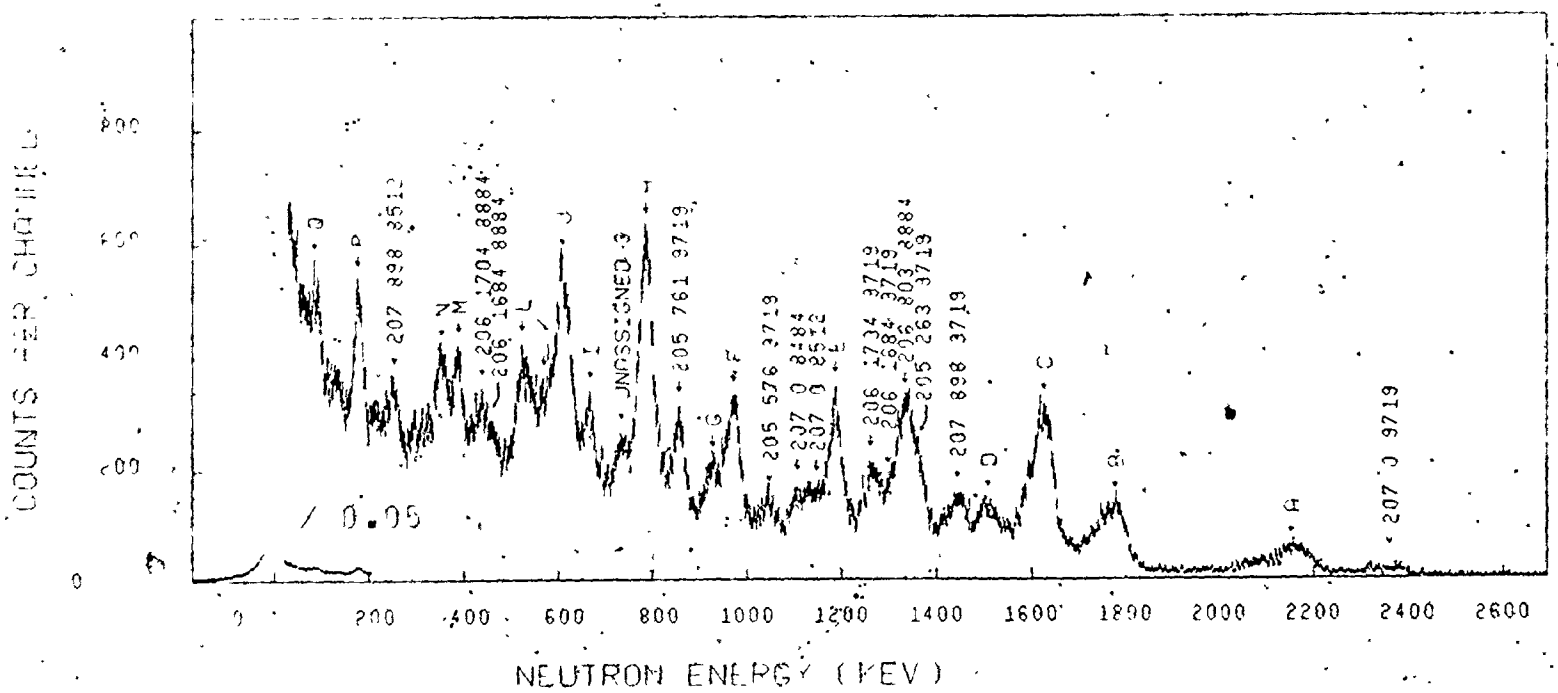

6.14 Neutron spectrum of the $^{enriched}Pb(\gamma,n)$ reaction using chromium capture photons. Numbers used to identify neutron groups are explained in section 6.3.1.

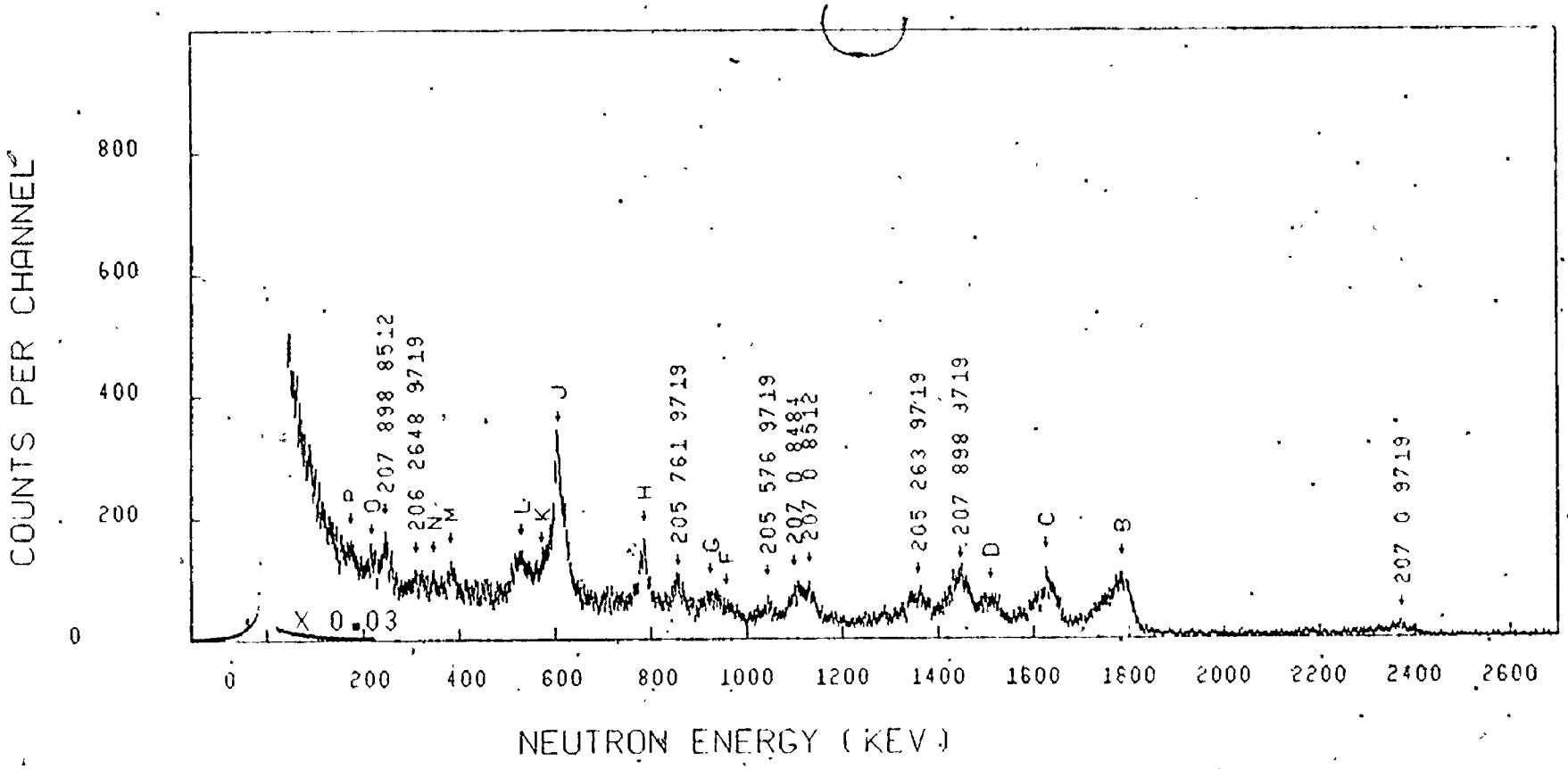

6.15 Neutron spectrum of the $^{nat}Tl(\gamma,n)$ reaction using nickel capture photons. Numbers used to identify neutron groups are explained in section 6.3.1.

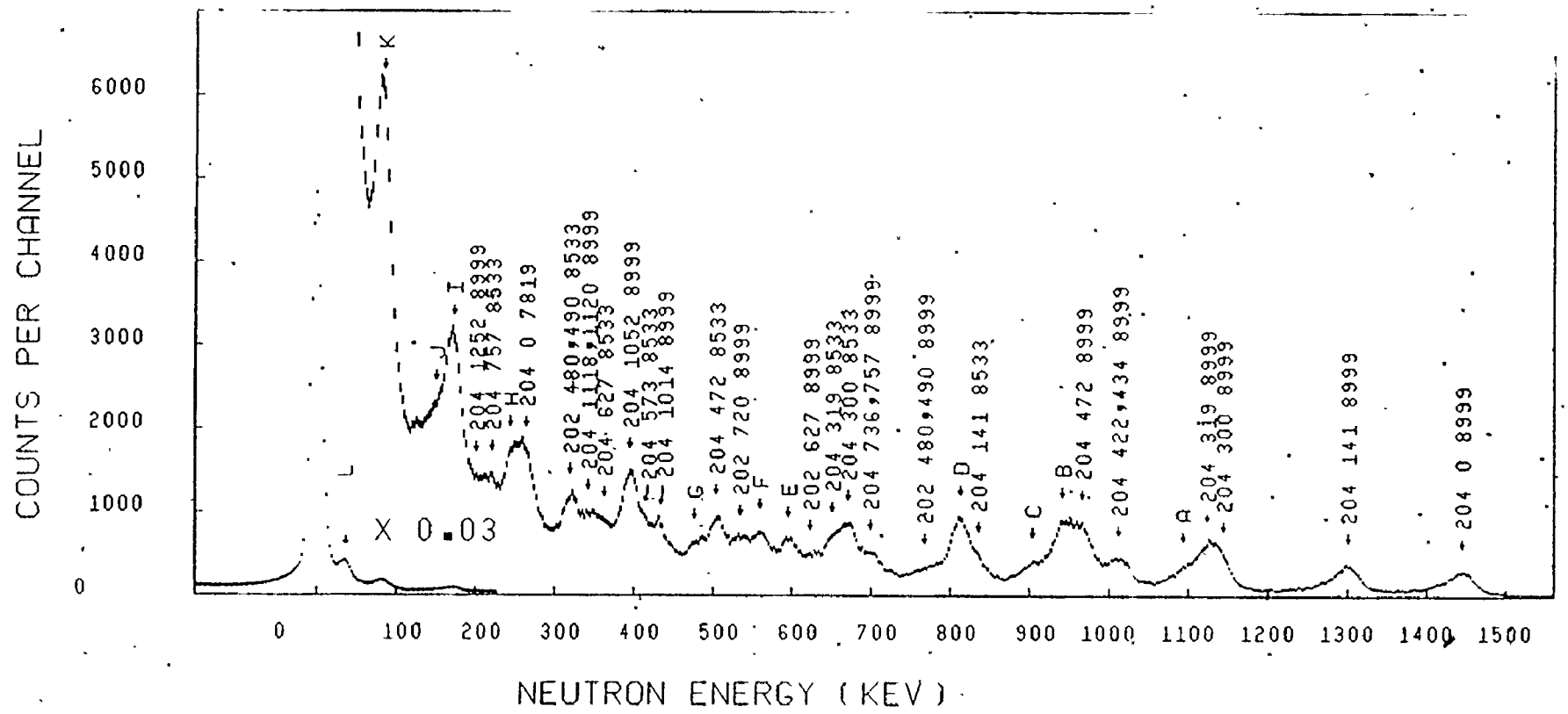

6.16 Neutron spectrum of the $^{197}Au(\gamma,n)^{196}Au$ reaction using nickel capture photons. Numbers used to identify neutron groups are explained in section 6.3.1. Brackets denote probable assignments as discussed in Chapter 6.

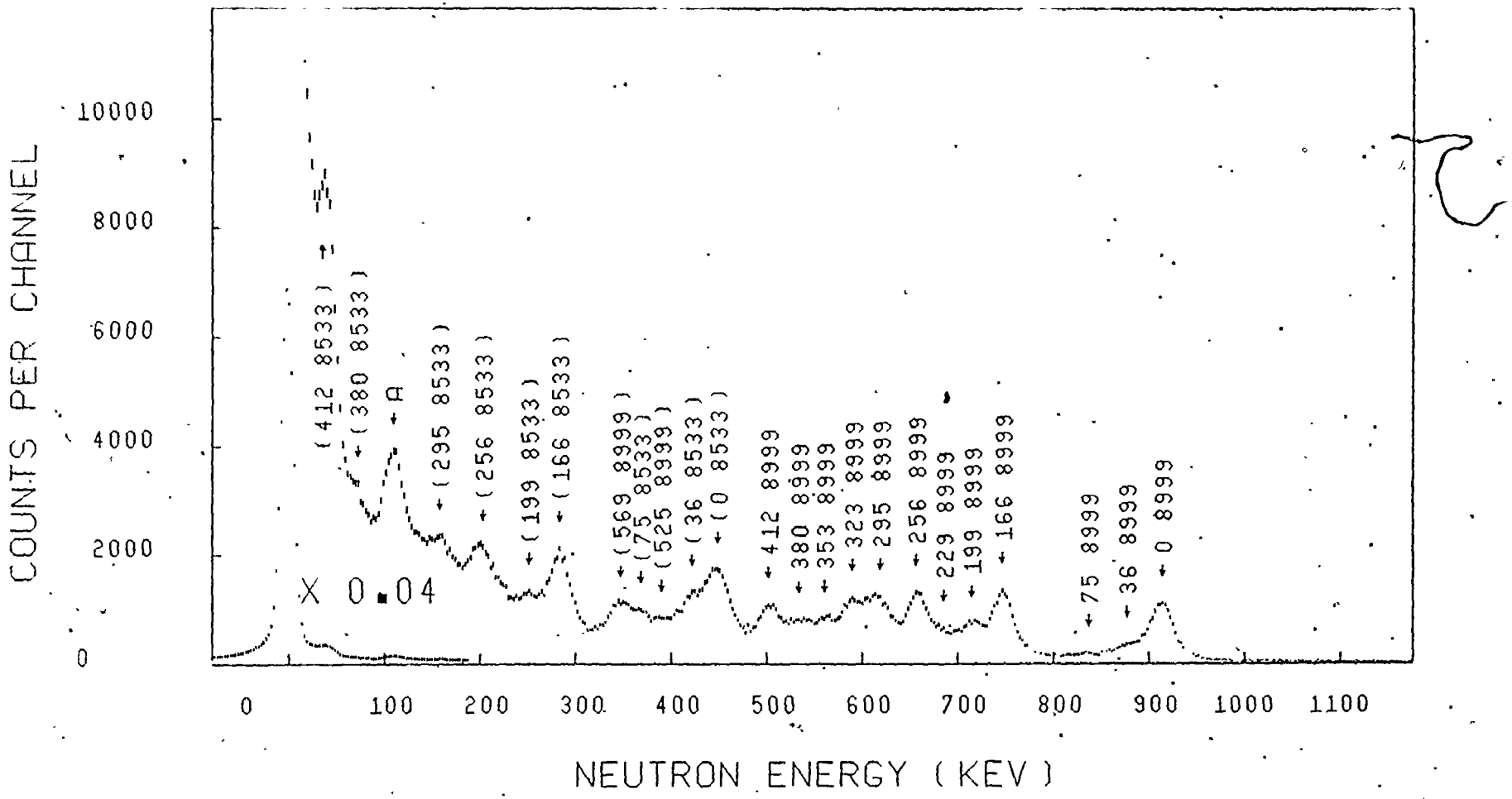

6.17 Neutron spectrum of the $^{181}Ta(\gamma,n)^{180}Ta$ reaction using nickel capture photons. Numbers used to identify neutron groups are explained in section 6.3.1. Brackets denote probable assignments as discussed in Chapter 6.

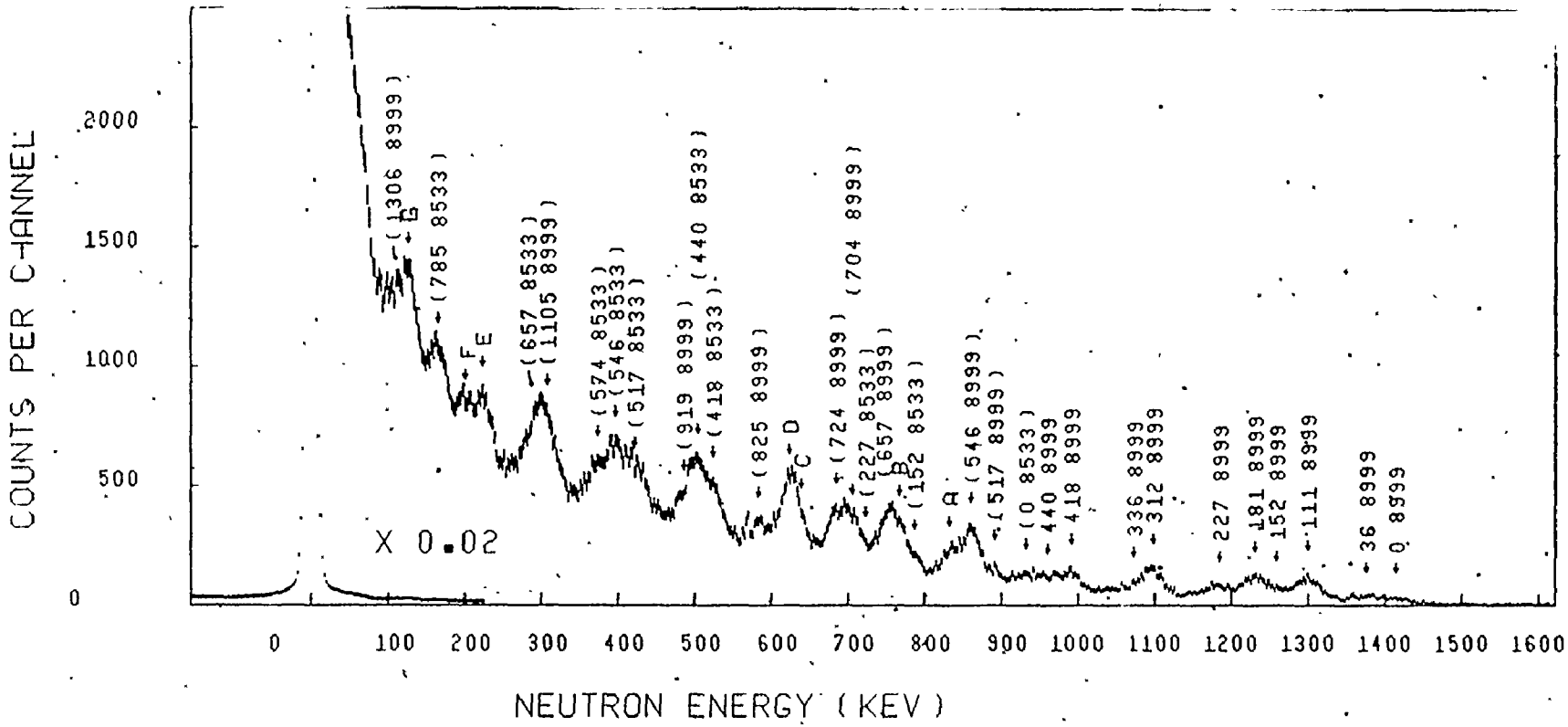

6.18 Background neutron spectrum. Taken at target site with target removed and beam open in the same geometry as for Figures 6.9 to 6.17. Collection time is about one half that used in the other figures.

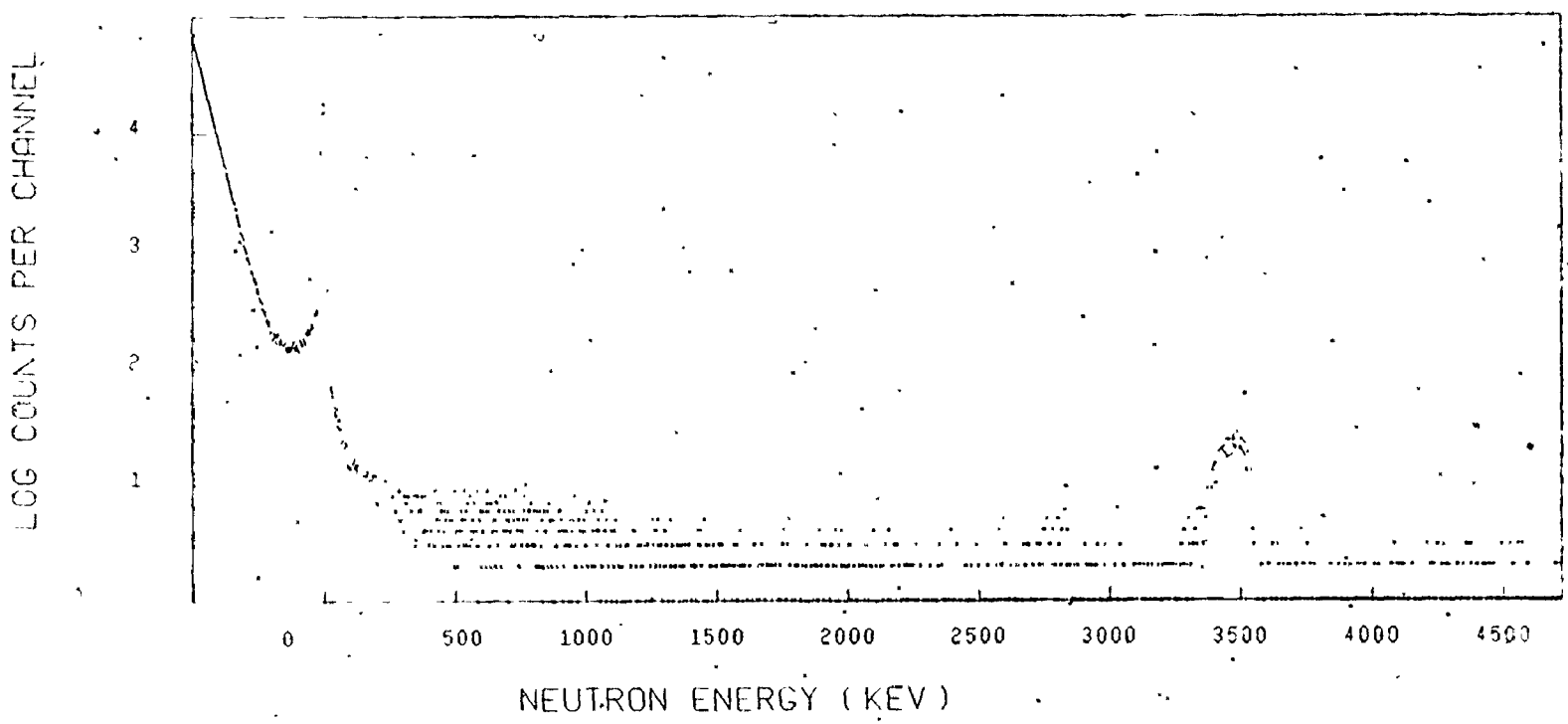

6.3.2 Extraction of Peak Areas and Centroids

The first step of the photoneutron data analysis was the determination of peak areas and centroids. This was accomplished by employing the FORTRAN code JSPLOT, a nonlinear least squares fit program for multiple peaks. The code assumed that a single isolated peak could be modelled to a Gaussian peak with a low energy exponential tail and, that within a region to be fitted the background would be linear. It can be seen by referring to Fig. 3.18 that the first two assumptions were not unreasonable approximations. It had to be borne in mind, however, that due to the rapid rise in the continuum, the assumption of a linear background at low energies would not be valid over large energy windows. To surmount this problem for low energy neutron groups, where a region about a peak or group of peaks could not be selected narrow enough to contain a linear background, a program was written to fit the background to polynomials of various degrees up to degree eight. This best fit background was then subtracted channel by channel from the data within the window and negative values were set to zero. The resultant data was

then fitted using JSPLOT. This was not necessary for data acquired using risetime discrimination, since the background at low energy was much flatter. It was furthermore recognized that deviations of the data from the assumed model would be reflected in the uncertainties of the areas and centroids as determined by the variance-covariance matrix of JSPLOT and indeed, these uncertainties tended to be higher by 75 to 90 percent than those expected from purely statistical fluctuations.

JSPLOT requires the programmer to supply a list of centroid estimates for each region to be fitted and thus a major concern was whether or not the code would generate artifacts or false peaks if the programmer asked it to fit for nonexistent neutron groups. In order to test this, several regions of various spectra were chosen that were known from published excitation energies (section 6.3) to have only a few neutron groups. These regions were then fitted using JSPLOT. The best fit cases were those with only the correct number of known groups. In no case was the inclusion of additional peaks by the programmer in the initial guess found to decrease the value of χ^2 and, in

fact, in most cases the code proceeded to determine the best fit by including the known peaks and rejecting the false groups. As a further precaution, the values of χ^2 ($\sim$ 0.8 to 1.2) determined from these fitted regions were then used as criteria for other regions. If the addition of a small peak was found to reduce the value of χ^2 such that it became less than the typical χ^2 values for the test regions, it was assumed that the region had been overfitted and the small peak was discarded. In all such cases, the inclusion of the additional peak was found to induce only a few percent change in the areas of the surrounding peaks and a negligible effect on the centroids.

Uncertainties in peak centroids were taken to be those assigned by JSPLOT. Uncertainties in peak areas were likewise chosen with the exception of those low energy peaks for which a polynomial background had been previously subtracted. Here the uncertainty in the sum of the background under the peak (as determined by the covariance matrix of the background fit program) was added in quadrature to the error estimated by JSPLOT.

6.3.3. Energy Calibration and Peak Identification

To aid in the identification of neutron groups and to allow the determination of photoneutron Q-values, it was necessary to know the neutron energy scale of the spectra. Unfortunately, unlike gamma ray work, there are no readily available sources of high energy mono-energetic neutrons aside from charged particle reactions. Since the energy scale must be frequently checked, the use of an accelerator for energy calibration would be inconvenient. In light of this, it was decided to use the neutrons from one of the photoneutron reactions to calibrate the energy scale and a method was worked out which would require only the known excitation energies of the residual nucleus and the peak centroids. Bismuth was chosen since its excitation energies are accurately known and it has a number of well separated photoneutron peaks spaced over a wide neutron energy range (~ 0 to 1.5 MeV).

It can be shown (Appendix II) that, to well within the errors of centroid determination, the neutron energy is given by the relationship

$$E_n\ (1 + 1/A) = E_\gamma - Q - E_x \qquad (6.19)$$

with

E_n the neutron energy

A the mass of the residual nucleus in AMU's

E_γ the incident photon energy

Q the photoneutron Q-value

and E_x the excitation energy of the residual nucleus.

Now, a preamp-amplifier-multichannel analyser system frequently does not yield a completely linear relationship for energy versus channel number and thus a second order term in channel number is often added to correct for this small nonlinearity. Thus, if we assume that the neutron energy versus channel number relationship is of the form:

$$E_n = a\ I^2 + b\ I + c \qquad (6.20)$$

where a,b,c are constants.

and I is the channel number,

then E_x obeys the relationship

$$E_x = a'\ I^2 + b'\ I + c'$$

with

$$a' = a(1 + {}^1/_A) \qquad (6.21)$$

$$b' = b(1 + {}^1/_A) \qquad (6.22)$$

$$c' = c(1 + {}^1/_A) - (E_\gamma - Q) \qquad (6.23)$$

By making a linear least squares fit to the well resolved observed peak positions and the known excitation energies, one could obtain a', b' and c'. Different photon energies could be incorporated by using the normal excitation energies for levels populated by the photon of highest energy, $E_{\gamma 1}$, and excitation energies of the form $(E_{\gamma 1} - E_{\gamma 2}) + E_x$ for photons of a lower energy, $E_{\gamma 2}$. By knowing the position, T, of the centroid of the thermal peak, the following equation could be obtained :

$$a\ T^2 + b\ T + c = 0 \qquad (6.24)$$

Direct substitution of equations 6.21 to 6.23 into 6.24 yields

$$Q = E_\gamma + a^1\ T^2 + b^1\ T + c^1 \qquad (6.25)$$

Thus the Q-value could be obtained using only the position of the thermal peak and the excitation energies of the levels in the product nucleus.

To get an absolute calibration of the neutron energy scale equations 6.20 to 6.23 could be used and then unknown levels could be obtained using the equation :

$$E_x = E_\gamma - Q - E_n\,(1 + {}^{1}/_{A}) \qquad (6.26)$$

The levels in bismuth employed in the initial fit were identified by using the thermal peak as zero neutron energy and by assuming the highest energy peak corresponded to the ground state transition. The Q-value taken from the compilation of Wapstra (Wa71) was used to determine the approximate neutron energy of this group and then a linear pulser was used to determine the approximate energies of the well resolved groups in between. The least squares fit was then performed using known excitation energies (Aℓ71, Eℓ73, Cr73) to yield a reduced χ^2 of approximately 1.5 for 13 degrees of freedom. The good fit suggested that the initial assignments were correct, and thus, the energies of the other neutron groups were calculated and used to determine their excitation energies. The levels of bismuth are tabulated in Table 6.4 and the measured Q-value is given in Table 6.3.

The photoneutron groups of the other reactions were identified by determining the neutron energy scale from bismuth data taken before and after the spectrum was collected. This was valid provided that the bismuth spectra

agreed with respect to gain and zero parameters, and in all cases this was found to be true. Levels were identified by using Wapstra's Q-value data (Wa71) and comparing values of $E_\gamma - Q - E_x$ to $E_n\ (1 + {}^{1}/_{A})$ determined from the bismuth data. The possible levels thus identified are presented, together with the relative intensities corrected for detector efficiency, in Tables 6.4 to 6.12. Some neutron groups, such as those of gold and tantalum, could not be uniquely identified due to a lack of information concerning excitation levels in the residual nucleus. If $E_{\gamma 1}$, $E_{\gamma 2}$, $E_{\gamma 3}$ ... are the energies of the photon spectrum in descending order, then for $E_{\gamma 2} - Q < E_n\ (1 + {}^{1}/_{A}) \leq E_{\gamma 1} - Q$, the excitation energy of the residual nucleus corresponding to a given neutron group can be uniquely determined for monoisotopic targets. For neutron energies less than $E_{\gamma 2} - Q$, the assignments are not unique if the excitation energies are unknown; since, for two excited levels E_{x1}, E_{x2}, it is possible, for example, to have $E_{\gamma 2} - Q - E_{x2}$ equal to $E_{\gamma 1} - Q - E_{x1}$. Even in the case of some targets with known excitation levels, unique assignments could not be

made for some neutron groups; since, some combinations of E_γ, Q and E_x would yield similar neutron energies. Some possible assignments could be eliminated on the basis of angular momentum selection and other considerations, and this is discussed in section 6.3.4.

The Q-values for the other reactions were next determined. For all nuclei except gold and tantalum, an estimate of the Q-value was obtained using the values of $E_n\ (1 + {}^{1}/_{A})$ determined from the bismuth standard and the values of E_x taken from the literature (references are in Tables 6.13 to 6.19). This was done for all uniquely identified neutron groups with errors being assigned from the centroid uncertainties as estimated by JSPLOT (6.3.2). Finally, the Q-value and associated error were obtained by taking a weighted average of the individual estimates of the Q-value and their errors. This method had the advantage that it only required three variable parameters to determine all the Q-values, namely a', b', and c' for the fit to the bismuth data. As an internal check, however, those nuclei with a sufficient number of uniquely identified groups were fitted in the same manner as for bismuth. Good

values of χ^2 were obtained and the Q-values thus obtained agreed well with the estimates previously described.

In the case of gold and tantalum, the Q-values could not be obtained in a similar manner since the excitation energies of the residual nuclei were not known. In these cases, the Q-value was determined by assuming that the highest energy neutron group corresponded to the ground state transition. The uncertainty assigned is just the uncertainty in estimation of the group centroid, as determined by JSPLOT. The measured reaction Q-values are listed in Table 6.3 together with the published values of Wapstra et al. The agreement is seen to be good with the exception of tantalum. A possible reason for this discrepancy is discussed in section 7.1.

6.3.4 The Reduced Neutron Widths

The possible components listed for the various neutron groups of Tables 6.4 through 6.12 were assigned on the basis of energy alone. The criterion used in the assignment was, that if a possible component calculated using the tabulated Q-values and excitation energies,

could occur within two standard deviations of the estimated peak centroid, then it was included. For nuclei possessing large uncertainties in the tabulated Q-values, the procedure was first to estimate the Q-value more accurately by using isolated groups that could be uniquely determined and then to use this Q-value to search for unresolved components.

It was realized, however, that some possible components could be eliminated on other grounds. An elementary calculation of the relative component intensities was performed, assuming that the intensities were proportional to the isotopic abundance, incident photon flux and the optical model transmission coefficients. The latter have been calculated (Au62) using Perey-Buck and Bjorklund-Fernbach optical potentials, and an example of such is plotted in Fig. 2.3 for s, p, d, f and g wave neutrons with A=200. It was noted that the emission of ℓ-wave neutrons was determined by the spin and parity of the initial $(J_i^{\pi_i})$ and final $(J_f^{\pi_f})$ states, according to the normal quantum mechanical rules governing strong and electromagnetic interactions. These may be stated as :

$$\pi^i \, \pi^L = \pi^f \, \pi^\ell$$

where L is the photon multipolarity (6.27)

and

$$\vec{J}_i + \vec{L} = \vec{J}_f + \vec{\ell}$$

It can be seen that certain values of J_i, J_f and L, and certain ℓ-values could not exist. In such a case this could be accounted for by setting the corresponding transmission coefficient to zero.

In light of the above, the ℓ-values for the elementary intensity calculation, if allowed, were taken to be 0 and 2 if a parity change occurred and 1 and 3 if no parity change occurred between the initial and final states. This essentially assumed an E1 interaction and this assumption is discussed later. The calculations showed that some components should be of negligible intensity because of the low flux for a particular exciting photon or because of low probability for transmission of the neutrons through the optical potential barrier. It was noted that several neutron groups, which were calculated to be of very low intensity compared to surrounding groups, such as those due to the 8120 keV photon, but which were

capable of being resolved, were not resolved. Thus, although our calculation was considered too simplistic to accurately predict the relative intensities of the neutron groups, it was felt to be adequate to determine which unresolved groups could be neglected. The neutron group components, their relative intensities, as well as the angular momentum and parity of the residual nuclear states corresponding to the components, are listed in Tables 6.13 to 6.19.

The determination of components for tantalum and gold was more difficult, since, as previously stated, the excitation energies are not well known. For neutron groups corresponding to excitation energies less than 465 keV (8999 less 8533 keV) the excitation energy could be uniquely determined. For groups corresponding to higher energy it was assumed that, to a lowest order approximation, the spectrum due to the 8999 keV photons would be duplicated by the 8533 keV photons. Thus, if a group corresponded to E_x for an 8533 keV photon and E_x^1 for 8999 keV, then E_x assignment was chosen if E_x had been observed for the 8999 keV case. If the E_x^1 assignment

were chosen, the choice could be further strengthened if a lower energy group corresponded to E_x^1 for an 8533 keV photon. It was, of course, realized that there were a few cases for nuclei with known excitation energies where a low lying excited state was populated by a low energy photon and not by the higher energy gamma ray. Furthermore, there was still no guarantee that a group arising from a higher energy excited state and a 9 MeV photon did not interfere with a group assigned to be due to a low excitation energy and low energy photon. Thus, although these assignments are probably for the most part correct, the results and subsequent discussion must be viewed with some caution; and thus, such levels have been bracketed in the spectra.

In order to examine the intrinsic nuclear properties of the neutron intensities, it is desirable to remove the energy-dependent factor arising from the neutron penetration probability through the centrifugal barrier. In the case of an s-wave neutron, this probability, called the penetrability, is proportional to the square root of the neutron energy, E_n, for a given nucleus (section 2.3). Thus, for a given

isotope, the measured intensities can be readily made independent of energy if the neutrons can be characterized as s-wave. Unfortunately, a glance at Fig. 2.3 reveals that, in a large portion of the neutron energy range of interest, the neutron transmission coefficients suggest that a significant contribution by p-, d- and sometimes even f- wave emission is possible. Their penetrabilities are not merely proportional to the square root of the neutron energy; and thus, division by $\sqrt{E_n}$ would not completely remove the energy dependence. If the photon interaction were pure E1 then the emitted neutrons would be s-, d- g- ... wave if the parity of parent and daughter states were opposite and p-, f-, ... wave if the parities were the same. For the low-lying states of the nuclei in question, the former is normally the case with only a few exceptions. For nuclei near mass A=200, the isoscalar E2 resonance should occur around 10 to 11 MeV photon energy and, in fact, in the case of ^{208}Pb there is evidence from inelastic electron scattering (Bu72, Pi74) to suggest that an E2 resonance might occur at 9 MeV. It has been pointed out, however, that in the case of photoneutron reactions on ^{208}Pb (Ve70b, Pi74) the

$E2/E1$ mixing fraction is small, and this has also been implied by our angular distribution studies on natural lead (section 6.4). Photoneutron cross sections for bismuth, lead, gold and tantalum observed using partly monochromatic photons (Be75) can be fitted reasonably well to a Lorentzian centered at the giant dipole energy, and near 9 to 10 MeV there are no large peaks added to the giant dipole portion of the cross section. Thus it was felt reasonable to assume that the $E2/E1$ mixing fraction was to a lowest order approximation negligible. Although no information was available on thallium, it too was assumed to have negligible E2-E1 mixing.

Our studies concerning the angular distribution of photoneutrons from lead (section 6.4) have indicated that a generally small but finite mixing fraction exists at these energies. Based on a model derived in Chapter 2, the mixing fraction has been estimated and these estimates have been used to calculate the reduced widths of lead. It is interesting to note that these finite mixing fractions do not alter the ratios of reduced widths drastically except for those in which s-wave emission is

prohibited at low neutron energies. For example, using the estimated fraction of 0.04 for the 8999 keV photon incident on ^{208}Pb, one finds that the ratios of reduced widths differ by less than 1 percent for the groups that possess an s-wave component and 9 percent for the one group that does not have an s-wave term. Similarly for 8533 keV photons incident on ^{208}Pb the estimated mixing fraction is 0.11, altering the ratio of reduced widths by 6 percent for groups with s-wave emission allowed and 70 percent for the one group which cannot be formed by s-wave emission. For neutron energies greater than about 1.5 MeV, deviations do not exceed approximately 15% even for mixing fractions as high as 0.5.

In order to estimate the amount of angular momentum mixing, it was decided that, as a first approximation, the relative intensities of different ℓ-values would be proportional to the optical model transmission coefficients.

The neutron intensities were thus assumed to be given to first order by :

$$I = I_o \sum_{\ell=o} f^{\ell}_{EL_1, EL_2} T_{\ell}^{j} \qquad (6.28)$$

where T_ℓ^j is the transmission coefficient for neutrons emitted from a nucleus of mass A with orbital angular momentum ℓ and total angular momentum j, I_o is a constant, $f^{\ell}_{EL1,EL2}$ is the ratio of the square of matrix elements corresponding to E_{L2} and E_{L1} interactions (called the E_{L2}/E_{L1} mixing fraction), assumed to be j independent. In particular, for a parity change between initial and final states, we have $f^{\ell even}_{E1,\ E1} = 1$, $f^{\ell odd}_{E1,E2} = \alpha = 0$, all others being zero. For no parity change we have $f^{\ell odd}_{E1,E1} = 1$, $f^{\ell even}_{E1,E2} = \alpha = 0$, all others being zero.

Now in general (section 2.3), T_ℓ^j can be written as :

$$T_\ell^j = P_\ell\ T_\ell^{1j} \qquad (6.29)$$

where P_ℓ is the neutron penetrability for ℓ-wave emission and T_ℓ^{1j} is a reduced transmission coefficient which is a function of the nuclear potential. It was furthermore assumed that, to first order, an intensity, independent of neutron energy and designated a reduced width, could be obtained by using the following equation :

$$I_R = \frac{I}{f_o P_o + f_1 P_1 + f_2 P_2 + f_3 P_3} \qquad (6.30)$$

with I_R the reduced width and f_o, f_1, f_2 and f_3 fractions to be determined. Under the assumption of equation (6.28), to first order we have :

$$f_\ell = \frac{T_\ell{}^j}{T_o{}^j + T_2{}^j + \alpha\,(T_1{}^j + T_3{}^j)} \qquad \ell = 0,2,\ \pi^i\pi^f = -1.$$

$$f_\ell = \frac{f_{E2,E1}\ T_\ell{}^j}{T_o{}^j + T_2{}^j + \alpha\,(T_1{}^j + T_3{}^j)} \qquad \ell = 1,3\ \pi^i\pi^f = -1 \quad (6.31)$$
$$j = \ell \pm 1/2$$

$$f_\ell = \frac{f_{E2,E1} T_\ell{}^j}{T_1{}^j + T_3{}^j + \alpha\,(T_0{}^j + T_2{}^j)} \qquad \ell = 0,2\ \pi^i\pi^f = +1 \quad (6.32)$$

$$f_\ell = \frac{T_\ell{}^j}{T_1{}^j + T_3 + \alpha(T_o{}^j + T_2{}^j)} \qquad \ell = 1,3\ \pi^i\pi^f = +1$$

where π^i, π^f are the parities of the initial and final nuclear states respectively.

If j can have only one value, due to angular momentum selection rules, that value was used, otherwise, an average value of $T_\ell{}^{\ell-1/2}$ and $T_\ell{}^{\ell+1/2}$ was used. In

either case the results were very similar.

The values of T_ℓ^j are again taken from Auerbach and Perey's compilation (Au62). For transitions where a given value of ℓ cannot occur due to the values of the initial and final state angular momenta and parities, the corresponding value of f_ℓ was set to zero.

6.3.5 Photoneutron cross-sections

The calculation of a cross section for an individual photoneutron group is quite straightforward. If the detector senses R neutrons per second corresponding to photoneutron events instigated by photons of energy E_γ, which leave the residual nucleus of mass A with excitation energy E_x, then the expression relating R to the cross section is :

$$R(A,E_x,E_\gamma)=\phi(E_\gamma)\,(1-EXP(-\textstyle\sum_j n_j \sigma_\gamma{}^j t))\,\dfrac{n_A \sigma_{\gamma n}(A,E_x,E_\gamma)}{\sum_j n_j \sigma_\gamma{}^j}\,\dfrac{M}{M_o}\,\varepsilon(E_n) \quad \ldots(6.33)$$

where n_j is the number of nuclei per unit volume of the j^{th} isotope

n_A is the number of nuclei per unit volume of the isotope of mass A

$\sigma_\gamma{}^j$ is the total photon interaction cross section for energy E_γ and the j^{th} isotope

t is the target thickness

σ_γ is the photoneutron cross section

M is the monitor rate for the experiment

M_o is the monitor rate when the beam intensity was determined

$\epsilon(E_n)$ is the efficiency of the detector for neutrons of energy E_n (given in equation 6.19)

and

$\phi(E_\gamma)$ is the total flux (s^{-1}) for photons of energy E_γ incident on the target.

Since photoneutron cross sections near 9 MeV typically have values of a few millibarns whereas total cross sections near these energies are typically 15 barns, to a very good approximation all σ_γ^j are the same and hence are denoted by σ_γ. Thus

$$\sum_j n_j \sigma_\gamma^j = n\sigma_\gamma$$

where n is the total number of nuclei per unit volume. Then if $Y_A = n_A/n$ we have :

$$\sigma_{\gamma n}(A,E_x,E_\gamma) = \frac{R\sigma_\gamma}{\phi(E_\gamma)(1-EXP(-n\sigma_\gamma))Y_A\epsilon(E_n)} \frac{M_o}{M} \qquad (6.34)$$

The above equation has implicit in it several assumptions. In the first place it is assumed that the beam cross section is smaller than the target and, as has been discussed in section 6.2.1, this is a good approximation. Secondly, it has been assumed that the measurement of the total photoneutron cross section is insensitive to anisotropy in the angular distribution. This is indeed the case as is discussed in Appendix III. Nonelastic and elastic scattering of neutrons in the target have been neglected and this too is justified in Appendix III. Finally, deadtime and random adding have been neglected since observations of the stabilization pulser show these effects to be negligible.

The uncertainty in the cross section for a single line was calculated by use of the standard equations for the propagation of errors. The uncertainty in most of the quantities has been previously discussed. Values of σ_γ were taken from the compilation of Storm and Israel (St70) and over the energy range of interest are seen to possess a slowly varying linear relationship with respect to photon energy, allowing easy interpolation. Storm

suggests an uncertainty of up to 10% for these values. When the various experimental and tabulation uncertainties were combined, it was found that the experimental percentage error in the cross section was typically the quadrature sum of the percentage error in the peak area plus 25% for the nickel source and 27% for the chromium source, with slight variations depending on the particular photon in question (see Tables 6.1 and 6.2).

As mentioned previously, some neutron groups were comprised of two or more components. Equation 6.28 can be extended to determine cross sections for the individual components, provided that the ratios of the intensities of the components are known. This was done for certain groups in lead consisting of two components from two different isotopes, by comparing the normalized intensity of the group in natural lead with that in enriched lead, and by utilizing the known isotopic abundances. In other cases, however, the ratio of intensities within an unresolved group could not be determined, and thus, the intensity of the group could only be used to obtain an upper limit to the cross section for each component within a group. The

individual neutron group cross sections are presented in Tables 6.13 to 6.19 and are discussed in Chapter 7. For unresolved groups, a cross section was calculated for each component of the group as if it alone constituted the whole group. These values were used to yield an estimate for the upper limit to the photoneutron cross sections for a given energy and isotope, where unresolved groups are concerned.

Table 6.20 lists the total photoneutron cross sections for all eight isotopes as a function of photon energy. For each isotope and photon energy there are two numbers. The first is the sum of cross sections for all isolated components for that isotope and energy and is called the lower limit to the cross section. The second number is the lower limit to the cross section plus the sum of cross sections from all unresolved groups having a component corresponding to that isotope and photon energy. This is the upper limit to the cross section. The upper and lower limits to the total cross sections have an uncertainty of approximately 25% for data obtained with the nickel source and 27% for data obtained with the chromium source. The total photoneutron cross sections are discussed in Chapter 7.

6.4 Fore-Aft Asymmetry of Photoneutron Emission in Lead

The spectra collected during the experiment described in section 5.4 are presented in Figures 6.19 and 6.20. The former is that taken with the nickel photon source and the latter is that obtained using the chromium source. Both forward and backward angle spectra, normalized to the same monitor rate, are shown for each source, and the resolvable lines are labelled. Due to the decreased solid angle subtended by the detector and the thinner target as compared to the natural lead experiments of section 6.3, the counting statistics were poorer. Consequently more groups were incapable of being resolved and these have not been labelled, since further analysis was not possible. Group identification, centroids and peak areas were obtained in the same manner as in section 6.3.

If $I(\bar{\theta})$ and $I(\pi-\bar{\theta})$ were the intensities observed at the average angle $\bar{\theta}$ and $\pi-\bar{\theta}$ respectively, then we can define an asymmetry parameter, A, by the expression

$$A = \frac{I(\pi-\bar{\theta}) - I(\bar{\theta})}{I(\pi-\bar{\theta}) + I(\bar{\theta})} \qquad (6.35)$$

The resolved groups, their corresponding asymmetry parameters, and the uncertainty in the asymmetry parameters

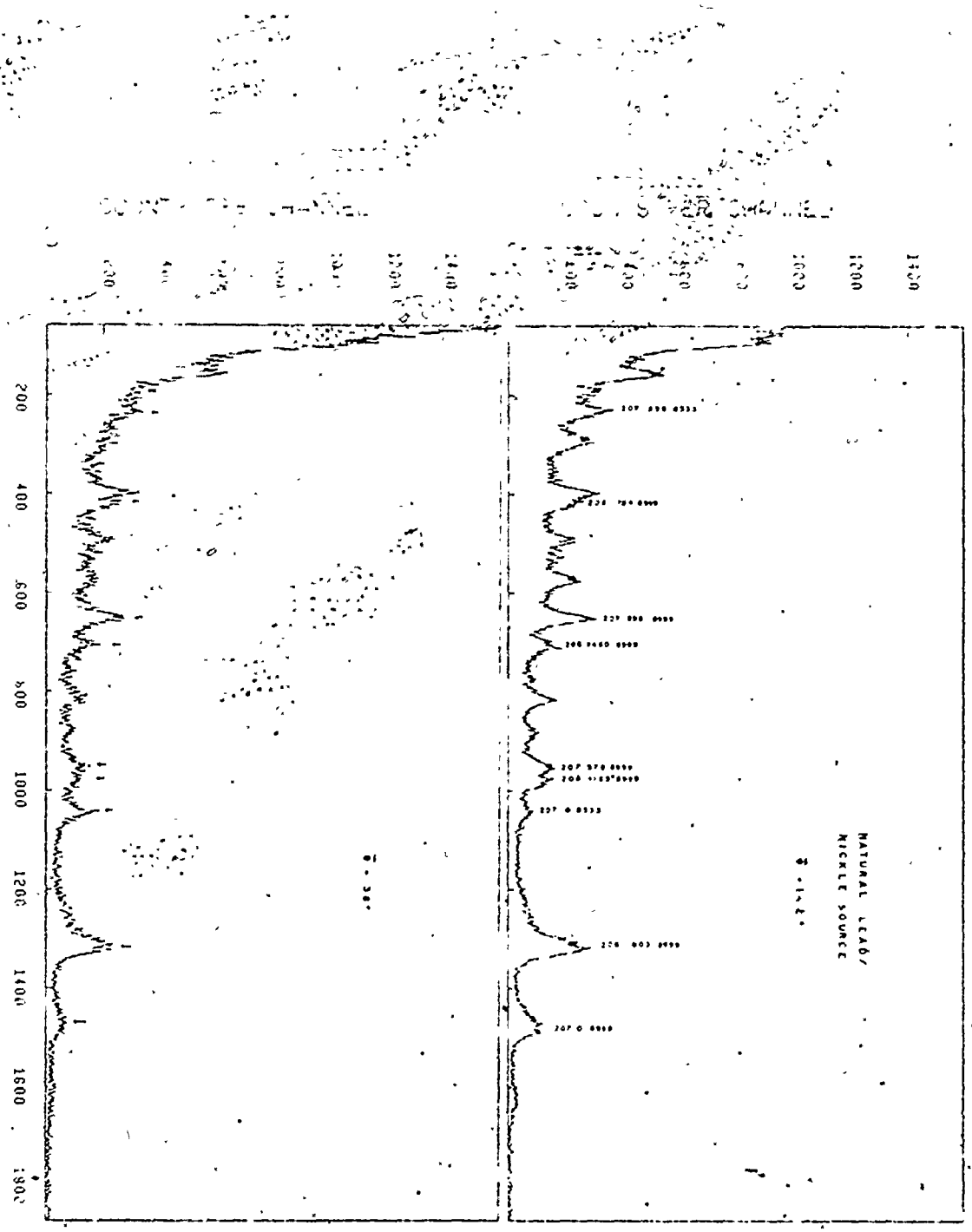

6.19 Photoneutron spectra of natural lead using nickel capture photons collected at forward and backward angles symmetric about $\theta=\pi/2$. Only resolved neutron groups consisting of a single isotope, residual excited state and photon energy have been identified. These are labelled in the upper diagram and the corresponding groups are denoted by an arrow in the lower diagram. Spectra have been normalized to the same integrated photon flux.

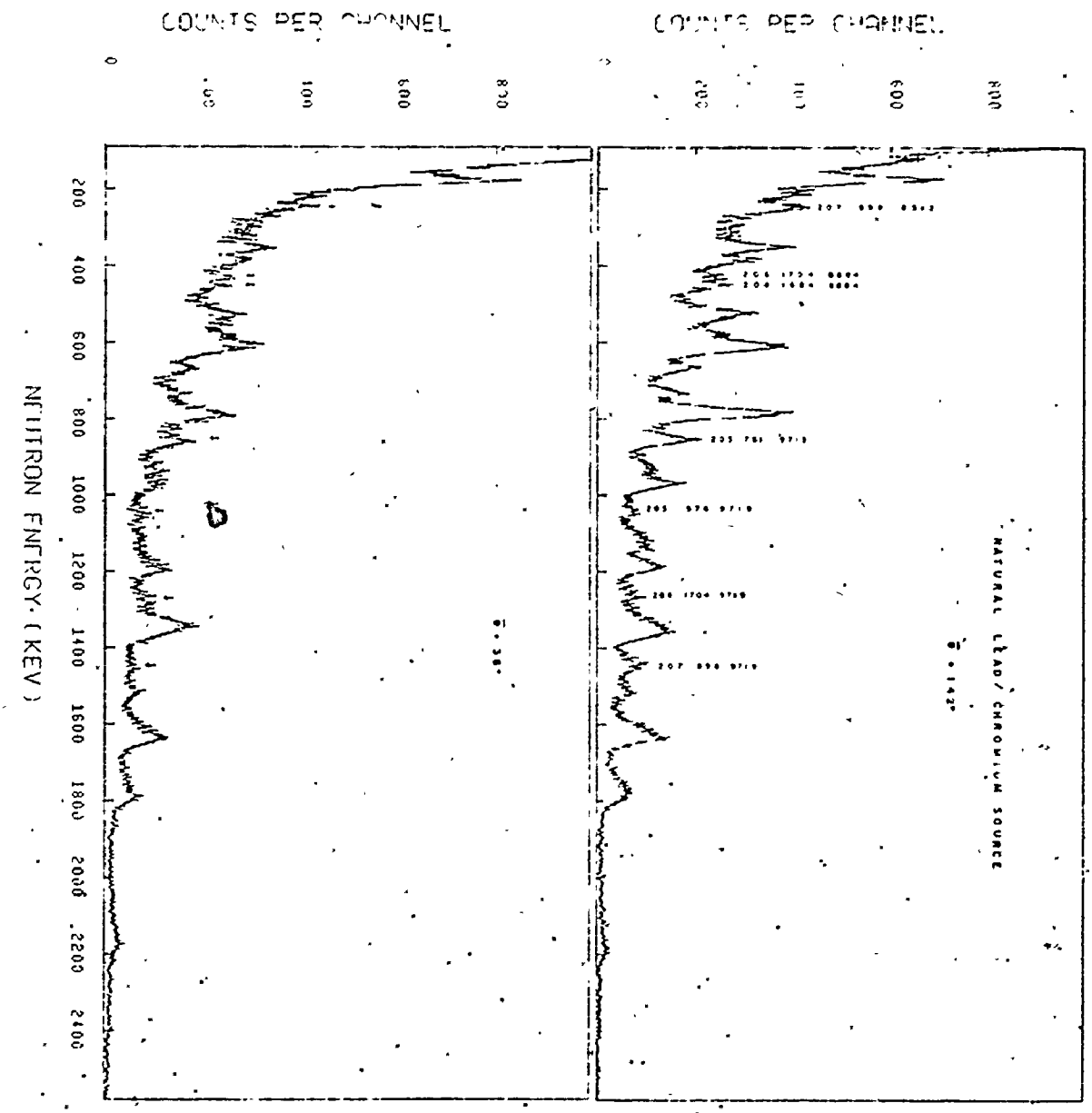

6.20 Photoneutron spectra of natural lead using chromium capture photons collected at forward and backward angles symmetric about $\theta=\pi/2$. Only resolved neutron groups consisting of a single isotope, residual excited state and photon energy have been identified. These are labelled in the upper diagram and the corresponding groups are denoted by an arrow in the lower diagram. Spectra have been normalized to the same integrated photon flux

are shown in Table 6.21. The latter were calculated from the uncertainties in the peak areas using the standard rules of statistics for first order propagation of errors. Peak area uncertainties were those determined by the peak fitting. It was realized that high energy photons would be scattered by the target preferentially in the forward direction, and that differences in the fore-aft count rate could be produced by the pulse pile-up or increased deadtime caused by such forward scattered photons reaching the detector. Observations of the area and shape of the stabilization pulser for both forward and backward angle spectra indicated that such effects were negligible.

Since the main objective of this experiment was to determine the degree of E2/E1 mixing in the photon interaction, it was desirable to be able to relate the asymmetry parameter to the E2/E1 mixing fraction, α, as defined in section 6.3.4. In general we have

$$I(\bar{\theta}) = K\int_{o}^{\pi/2} \frac{d\sigma}{d\Omega}(\theta)\frac{d\varepsilon(\theta)}{d\theta}\, d\theta \qquad (6.36)$$

$$I(\pi-\bar{\theta}) = K\int_{\pi/2}^{\pi} \frac{d\sigma}{d\Omega}(\theta)\frac{d\varepsilon(\theta)}{d\theta}\, d\theta$$

where $d\sigma/d\Omega$ is the differential cross section for photoneutron emission , K is a constant, and $d\varepsilon/d\theta$ is the differential efficiency of the neutron detector derived in section 3.5.3 and is symmetric about $\theta=\pi/2$. Clearly, if $d\sigma/d\Omega$ is a function of α and θ only, the asymmetry parameter could be used to determine α. Unfortunately, the differential cross section is a sum of Legendre polynomials multiplied by their respective coefficients. These coefficients (Chapter 2) are in turn a function of various angular momenta and the matrix elements corresponding to these angular momenta. The magnitude and phase of these matrix elements are not known; and thus, even for the simplest case of a 0^+ to $1/2^-$ transition, 16 measurements at different angles would be needed to uniquely determine all matrix elements.

Thus, it was decided to derive a simple model for the differential cross section based on several simplifying assumptions. It was assumed initially that a matrix element could be separated into two terms; one corresponding to the photon interaction matrix element of a specific multipole and a matrix element determined by the orbital

angular momentum and channel spin of a neutron in an optical potential. Secondly, it was assumed that the square of the neutron matrix element was equal to its corresponding optical model transmission coefficient. Thirdly, the ratio of the squares of the photon interaction matrix elements were taken to be 1 for an E1/E1 or E2/E2 ratio, α for an E2/E1 ratio and zero for any M1 contributions. These last two assertions contained the implicit assumption that the phase factors for all matrix elements were set to one, an assumption which is probably not completely correct and whose implications are discussed later. The detailed calculations for various spin transitions are derived in section 2.4.

Using this model and equation 6.36, the asymmetry parameter could be plotted as a function of α and then, by utilizing the experimentally determined values of A, α could be estimated for various energies of photons incident on 208- and 206- lead. As noted in Chapter 2, due to the ambiguity of the intermediate spin, this could not be done for 207- lead targets. The values of α, thus determined, and their corresponding uncertainties are tabulated in

Table 6.21. It should be pointed out that, for a given transition and a given asymmetry parameter, there exist in fact two values of α, one corresponding to E1 dominance and one corresponding to E2 dominance. The former has been chosen since, as mentioned in Chapter 1, research to date indicates that any E2 contribution is smaller than the E1 contribution for the photon energies of interest.

One point of interest may be seen in Table 6.21. For given photon energies and nuclei where the mixing fraction may be determined by more than one transition, α appears to be reasonably similar. This would tend to suggest that the assumptions made, since they should manifest themselves differently for different transitions, are at least qualitatively correct.

The implications of the estimated mixing fractions are further discussed in Chapter 7.

CHAPTER 7

CONCLUSIONS

7.1 Bismuth

The various neutron groups were seen to correspond to within a 5 keV standard deviation to the known existing excitation energies of ^{208}Bi. An average Q-value of 7459±2 keV was calculated for the reaction (Table 6.3) and was found to be in good agreement with, but considerably more precise than the tabulated value of Wapstra (Wa71).

The total photoneutron cross section is found to increase slowly with photon energy (Table 6.20) from 2.2 mb at 7534 keV to approximately 18 mb at 8999 keV. There are small deviations from this pattern such as the cross sections at 8512 and 8533 keV which differ from each other by a factor of nine and do not follow the general energy trend. The cross section at 8512 keV is seen to be at least 27 mb, and that at 9719 keV is at least 62 mb. Since the cross section averaged over resonances is approximately 50 mb at 8.5 MeV and 80 mb at 9.7 MeV (Be75), this suggests that at most energies the reactions occur off resonance and that at

8512 and 9719 keV, the reactions occur closer to a resonance. If this were the case, one might expect the distribution of reduced widths to have a lower correlation with the (p,d) and (d,t) spectroscopic factors at 8512 and 9719 keV. In fact, one sees in Table 7.1 strong correlations with the (p,d) factors at only two energies; 9719 keV with a 93% confidence level and 8533 keV with a 79% confidence. The (d,t) spectroscopic factors exhibit no strong correlations with the reduced widths. It must be recalled, however, that since the intermediate state is ambiguous, a correlation suggests that the reaction has a significant direct component, whereas a lack of correlation or an anticorrelation does not prohibit such a component (Chapter 2). Furthermore, since the level density of ^{209}Bi is not known for the excitation energies in question, it is impossible to tell what the peak resonance cross section should be and hence how close to resonance the reactions are at 8512 and 9719 keV.

As one scrutinizes the distribution of intensities, several interesting points come to light. The relative intensities exhibit fluctuations which range roughly over

a factor of up to 10 and there appears to be no readily observable trend with neutron energy. Clearly, the nature of such an intensity distribution is not that of an evaporation spectrum, signifying that the level density in ^{209}Bi at these energies is low enough that a large amount of level overlap does not occur. The reduced widths vary over a factor of up to 6 and also have no apparent trend with either neutron energy or excitation energy.

Estimates of the number of degrees of freedom for the distribution of reduced widths are presented in Table 7.2. The reactions at 9719, 8999 and 8533 keV yield values of ν significantly greater than one and hence suggest, even in light of the uncertainties in the reduced widths, a multichannel process due either to a direct or semidirect interaction or to multiple exit channels caused by mixed ℓ- wave neutron emission. The reaction at 8884 keV yields an estimate of $\nu \sim 0$. Because of the uncertainty in the reduced widths, this may indicate that the parent width distribution is not chi-squared in nature (such as a direct or semidirect reaction might yield) or is unichannel

compound (ν=1). Thus, the results are inconclusive for this photon energy.

There is difficulty in determining whether the partial cross sections for population of various excited states have a common trend with photon energy. This is because resolution problems generally only allow comparison of levels for less than three different photon energies. There are, however, four levels which can be compared for three or more photon energies - the ground state, 63, 511 and 889 keV states. The linear correlation coefficients and confidence levels (section 2.2) have been calculated for the latter three transitions with respect to the ground state and are presented in Table 7.3. As can be seen, all three exhibit photon energy dependent correlations with the ground state. The 63 keV and 889 keV transitions are very strongly correlated with 91% and 97% confidence levels respectively, while the 511 keV transition is not quite as strongly correlated with a 75% confidence level. A possible explanation for such a correlation might lie in the existence of a common doorway state which dominates the transition, having strong matrix elements connecting

it to the final states. Such matrix elements would be expected to be strongest for final states which closely resembled the doorway state such as might be the case for a few step semidirect interaction.

The low lying states in ^{208}Bi may be interpreted as consisting of particle-hole multiplets arising from the coupling of a single proton with a neutron hole outside a ^{208}Pb spherical core. The previous studies of single particle transfer reactions (Aℓ71, Eℓ73, Cr73) have established the simple particle-hole multiplet structure of these states. The lowest lying multiplets are the $h_{9/2}p^{-1}_{1/2}$ doublet consisting of the ground and 63 keV states; the $h_{9/2}f^{-1}_{5/2}$ multiplet consisting of the 511, 603, 631, 652 and 927 keV states; the $h_{9/2}p^{-1}_{3/2}$ multiplet of 889, 961, 1071 and 1097 keV states and the $f_{7/2}p^{-1}_{1/2}$ doublet which is comprised of the 939 and 1036 keV states. This last doublet is of interest since it is the lowest lying multiplet corresponding to excitation of the proton outside the ^{208}Pb core. During a direct photoneutron reaction on ^{209}Bi, which consists of one proton outside the closed lead shell, one would in the simplest situation expect the proton to be initially

excited and in turn transfer most of its energy to a neutron just beneath the Fermi surface which would then be ejected. Since the proton would de-excite in this process, one would simplistically expect to find multiplets corresponding to proton excitations populated to a lesser degree than multiplets in which the proton is in its lowest state. This is not found to be the case for the $^{209}Bi(\gamma,n)$ reaction which leads us to believe that the reaction is not a direct one step process. It may, however, still be a few step semidirect process.

7.2 Lead

All of the neutron groups excepting three were seen to correspond to known existing levels to within a 5 keV standard deviation. This demonstrates both the validity of using bismuth as an energy standard and the accuracy of the centroid determination and energy fitting techniques. The average Q-values were seen to be in good agreement with the more precise values of Wapstra's compilation with the exception of the value for the $^{206}Pb(\gamma,n)^{205}Pb$ reaction obtained with the natural sample which differed by two standard deviations.

Three groups have been found that cannot, for one of a variety of reasons, be assigned to photoneutron reactions on any of the three lead isotopes. Two of these groups found using nickel source photons and designated "UNASSIGNED 1" and "UNASSIGNED 2", have neutron energies of 1784 and 1360 keV respectively which would correspond to the 206 0 8533 and 206 0 8120 groups. Neither, however, disappear when the enriched 208- lead target is used and, in fact, their intensity relative to the strong groups corresponding to a 208-lead target remains the same within errors. This suggests that the two groups correspond to photoneutron reactions on a 208- lead target or an impurity which remains in the same relative abundance as the 208-lead. The latter is unlikely since the samples come from two different ore types - the enriched Saclay sample presumably from thorium deposits and the natural sample probably from thorium and uranium ores. There are also only a limited number of target materials with Q-values below the minimum 7215 keV required for a 9 MeV photon to produce a neutron group with the same energy as "UNASSIGNED 1" (or U1 for short). All of those that do, as determined from the Q-values of Wapstra (Wa71), would

be expected to yield additional groups that are not observed and it should be noted that 204-, 206- and 208-lead are not included amongst these.

If the groups are due to photoneutron reactions on 208- lead, the U2 group could be due to a previously undiscovered level in 207- lead at an energy of 264±5 keV. This is possible if thermal capture data on ^{208}Pb has been misinterpreted but the numerous studies of this reaction make the hypothesis appear unlikely. The last recourse is the hypothesis that the groups are due to photons that do not arise from neutron capture on nickel or aluminum, as observed in Chapters 5 and 6. If so, and if the reactions took place on 208- lead nuclei, the U1 group would require a photon energy of 9161±5 keV (assuming a ground state transition). Natural selenium and titanium, strontium and ^{15}N all have photons in this energy range but it is difficult to understand, in light of the fact that kilograms are required to get an observable effect, how these materials could be present. Furthermore, additional groups corresponding to excited states of ^{207}Pb which should be populated by the photons are not seen. Finally, a detailed study of the beam spectra has failed to find

any indication of contaminant photons other than those listed in Tables 6.1 and 6.2.

A third group designated "UNASSIGNED 3" has been found using the chromium source and a natural lead target. It does not correspond to any known excited state or source photon for any of the naturally occurring lead isotopes, but since it is not seen with the enriched target, it is assumed to be due to photoneutron reactions on 207- lead. The possible excitation energies of 206- lead would be 2231, 1396, 1024, 996, 451 or 236 keV depending on which energy photon populated the neutron group. As far as is known from the literature, no such levels in 206- lead have been found. These three anomalous groups point out the need for further photoneutron spectroscopic studies of separated isotopes of lead and such work will soon be undertaken using targets of 99% or greater enrichment.

The total photoneutron cross section for the $^{208}Pb(\gamma,n)$ reaction increases slowly with photon energy, being less than 1.5 mb at 7724 keV, 6.5 mb at 8533 keV and approximately 20 mb at 9719 keV. The first value

is particularly interesting since it is at an energy only 300 keV greater than that used in Jackson's determination of the off resonance cross section (Ja74). The author deduced a value of $1.3^{+2.7}_{-0.7}$ mb for the off resonance component, which is in excellent agreement with our value. Jackson was able to attribute this value to neighbouring resonances plus a small direct component. Since the average level spacing in ^{208}Pb for the present excitation energies is no more than 15 keV (Bo69), electromagnetic monochromatic photon experiments still average over resonances and off resonance regions. These yield typical values (Be75) of 43, 50 and 80 mb at 8.5, 9.0 and 9.7 MeV respectively, and thus suggest that in our experiments the reactions occur off resonance. As explained in section 2.2, this is in agreement with the expectations based on the photoneutron strength functions.

Cross sections for $^{206}Pb(\gamma,n)$ follow similar trends as do those for $^{208}Pb(\gamma,n)$, and again the reaction apparently occurs off resonance. One unusual feature is the cross section at 8484 which is five times higher than that at 8512 keV. It is possible that the reaction at 8484 keV

may occur on the tail of a nearby narrow resonance. The $^{207}Pb(\gamma,n)$ reaction is also peculiar in that, at those energies where the cross section has fairly narrow limits, it appears to be a factor of 4 to 5 greater than those for the other two lead isotopes or for any of the other isotopes studied. Although the cross sections are less than those averaged over resonances, the probability of the occurrence of even two or more reactions close to resonance is considered to be quite small. As yet no other reason for this behaviour has been found.

Inspection of the spectra verifies that they are not characteristic of those related to neutron evaporation. Furthermore, observation of the relative intensities reveals that for all isotopes there are no apparent trends with excitation energy or neutron energy. A few groups from the $^{207}Pb(\gamma,n)$ reaction, such as the 206 803 8999 and 206 1704 8583 groups, have much larger than normal partial cross sections, which accounts in part for the anomalously large total cross sections for this target nucleus. As with bismuth, correlations between strengths of excited states as a function of photon energy can only

be obtained for a few states. Specifically these are the ground state, 570 keV and 898 keV states of the ^{207}Pb residual nucleus. The linear correlation coefficients and confidence levels of the latter two with respect to the ground state are -.997 (95%) and -.318 (40%). This high degree of anticorrelation in the first case and moderate degree of anticorrelation in the second case may indicate that the reaction has an appreciable multistep (compound or semidirect) component.

The reduced widths exhibit random fluctuations over a factor of roughly 2 for ^{208}Pb target nuclei, up to 7 for ^{206}Pb and up to 60 for ^{207}Pb. There appears to be no obvious energy trend. Two groups have unusually large reduced widths; specifically the 206 1998 8999 and 206 1684 8512 groups. In both cases the relative intensities are not large, but because of the neutron energy, the penetrabilities are small. For the former case, a calculation of ν indicates that the probability of occurrence of a reduced width of such magnitude is .08, which is small but nevertheless finite. The latter case cannot be compared to other groups corresponding to the same energy photons since

they are coincident with other components. Nevertheless, it seems unlikely that the others would have huge reduced widths since this is not observed for other photons. Such a large value may be due to an incorrect spin assignment in the literature which is likely since d- wave transmission coefficients at 90 keV are small.

Estimates of the number of degrees of freedom can only be obtained for the ^{207}Pb target, mainly because of the low level density of the other residual nuclei and the finite detector resolution. Values between 0 and 1 are found at three different photon energies and because of the uncertainties in the values of ν, it is difficult to use these values to interpret the nature of the interaction.

Table 7.1 lists the correlation coefficients between the reduced widths and the (p,d) and (d,t) spectroscopic factors. A high degree of correlation exists for the ^{208}Pb target at 8999 keV which suggests the existence of an appreciable direct component to the interaction. No correlation is seen at the other photon energies, however, but we must be reminded that for a sample space of three elements, $P_c(r,3)$ is a very broad function which falls off slowly with

r. For the 8884 keV photon incident on a ^{207}Pb target, a moderate correlation is seen with the (p,d) spectroscopic factors. Again, as with bismuth, a lack of correlation at the other energies does not rule out a direct component, due to the ambiguity in spin of the intermediate state. No significant correlations are seen to exist for the ^{206}Pb target.

Table 6.21 contains the photoneutron emission asymmetry parameters, A, and the E2/E1 mixing fractions, α, for resolvable neutron groups. It is seen that all have asymmetrical emission rates and that with the exception of two groups (207 0 8533, 206 1784 8999) all emit photoneutrons more strongly in the backward direction (A>0). The fore-aft asymmetry itself is direct evidence that parity mixing is occurring, caused by the existence of both odd and even L photon interactions. Furthermore, as pointed out by Evans Hayward (Ha65), the stronger photoneutron emission rate at backward angles is theoretically expected of a direct photoneutron reaction with multipole mixing. The two exceptions may have a stronger multistep nature. The failings of the theory which was derived to calculate

the mixing fraction (section 2.4) is clearly shown by the fact that for the 207 898 9719 group the theoretical curve of α versus A yields a maximum for $\Lambda = 0.58$, whereas the measured value is $0.66 \pm .05$. We can, however, say that α is greater than 0.25 with a 95% confidence. For a given target nucleus and photon energy, we find that the mixing fractions are generally in reasonable agreement even though the final spins differ. This tends to support the validity of the assumptions made in the theory, at least as to the qualitative results of the mixing fractions.

It is seen then that for the ^{208}Pb and ^{206}Pb targets and for the resolvable corresponding neutron groups, there appears to be a generally small but finite percentage ($\sim$ 4-10%) of multipole mixing. This is not altogether surprising considering that the reactions occur at energies just below the theoretical peak of the isoscalar quadrupole resonance and on the tail of the giant dipole resonance. It is impossible, however, to determine what resonance or indeed if only one resonance contributes to the even parity multipole component, and thus the controversy concerning the assignment of the 8.85 MeV resonance (Chapter 1) remains

unresolved. All that can be stated with reasonable certainty is that in the range of photon energies between 8512 and 9719 keV, there exists in the off resonance region, a small but finite odd parity magnetic or even parity electric multipole contribution to the photoneutron reaction.

7.3 Thallium, Gold and Tantalum

7.3.1 Thallium

The neutron groups were seen to correspond to within a 5 keV standard deviation to known existing levels in ^{204}Tℓ and ^{202}Tℓ. Since the level densities in these two nuclei are quite high, many groups were not capable of being resolved. Most possible groups in both isotopes that are capable of being resolved (based on the known excitation levels) are seen. A few, such as the 204 0 8533 and 204 345 8533 groups are barely able to be resolved and are not seen, a fact which suggests that they are weakly populated and masked by the response tails of other nearby groups. The Q-value for the ^{205}Tℓ(γ,n) reaction (Table 6.3) is found to be 7 keV higher than the value of Wapstra. This represents a difference of

approximately two standard deviations. The $^{203}Tl(\gamma,n)$ reaction yields a Q-value which is 17 keV higher than the value tabulated by Wapstra, but it is well within the error bars of the latter and considerably more precise.

Total cross sections for both reactions are seen to be in general small, although the limits of resolution prohibit accurate determination of total cross sections in most cases. The cross section for the $^{205}Tl(\gamma,n)$ reaction is less than 10 mb at 7819 keV and less than 22 to 28 mb at most other energies. The cross section for the $^{203}Tl(\gamma,n)$ reaction has narrow limits for only two energies, being between 3 and 11 mb at 8999 keV and less than 27 mb at 7819 keV. Data is not available concerning the photoneutron cross section averaged over resonances for the thallium isotopes, but it is reasonable to assume that the average cross sections at these energies are similar to those of the other isotopes in this mass range - namely 30 to 70 mb. Thus, it seems likely that the interaction proceeds off resonance.

Inspection reveals, as for bismuth and lead, that the neutrons do not form an evaporation spectrum. Direct

observation indicates that the partial cross sections do not undergo large fluctuations, either with excitation energy or photon energy, although insufficient data is available to study energy trends. The same is true of the reduced widths, with one exception. The 204 1118, 1120 8999 group has a reduced width, assuming f-wave emission of at least a factor of 160 greater than the others at that photon energy. In calculating the reduced width it was realized that the possible spin-parity assignment, 7^+, would require h-wave neutrons whose transmission coefficient and penetrability is essentially zero at these neutron energies. Instead, the next lower ℓ-wave with the same parity was used (f-wave) since the 7^+ assignment given in the reference, was not certain. It appears, however, based on the huge reduced width, that the penetrability of the group has been grossly underestimated and that in fact neutrons of $\ell \mp 2$ or less are emitted. This would suggest that the spin of one of the two levels is 4 or less. In the absence of known spins and parities, it has been assumed that s-wave and higher even ℓ value neutrons are emitted, since this is predominantly

the case for lead and bismuth. For the case of 8999 and 8533 keV photons incident on ^{205}Tℓ, there are sufficient groups such that the number of degrees of freedom for the distribution of reduced widths can be calculated. The value of ν is found to be 4.4 for 8999 keV photons and 4.3 for 8533 keV photons incident on ^{205}Tℓ. In order to obtain the first result, ν was calculated with and without the 204 1118, 1120 8999 group. Based on the estimate of ν excluding this group, the probability for occurrence of such a large value of reduced width is vanishingly small, and thus the estimate of ν was chosen which excluded this group. The large value of ν, which is significantly greater than one, again suggests a multichannel process or a direct/semidirect nature.

There is no existing data for (p,d) and (d,t) reactions on ^{205}Tℓ or ^{203}Tℓ and hence it was not possible to study correlations between reduced widths and spectroscopic factors.

7.3.2 Gold

The analysis of the results of the $^{197}Au(\gamma,n)$ reaction are hindered, mainly through ambiguities in level assignments (Chapter 6), by a lack of knowledge of the excited states of ^{196}Au. Since the levels in ^{196}Au are known from the decay of the 12^- 595 keV state, they are of high spin and require the emission of f-wave or higher ℓ neutrons to be populated by an E1 photoneutron reaction on a $3/2^+$ ^{197}Au nucleus. Thus it is assumed that most of these six known excited states are not populated in the photoneutron reactions although some calculated level energies appear close to the known levels. In particular, the estimated 380 and 412 keV levels are in all probability not 6^+ or (6^+, 8^+) levels respectively, since, for the 8533 keV excitation, the neutron energy is so low that the probability for f- wave and higher ℓ emission is effectively zero. Thus, the 380 keV level may correspond to the known 370 keV level whose 6^+ assignment is uncertain, but the 412 keV level could not correspond to the known 401 (6^+) or 421 (8^+) levels.

The 229 keV level, although near in energy to the

known 232 keV level, cannot be identified with the latter since this requires h- wave emission, which has essentially a zero penetration factor at that neutron energy. Similarly, the 75 keV level is discounted as being equivalent to the known 5^+ 85 keV level. Reduced widths have been calculated, in the absence of spin information, as if s- wave emission and higher even ℓ-values could occur.

In making the above assumptions, it has been implicitly assumed that the interaction is predominantly E1, based on reasons stated in section 2.4 and the results of the lead angular distributions. It should be recognized, however, that a strong E2 component could possibly populate the high spin levels of ^{196}Au.

The reaction Q-value is found to be in excellent agreement with that of Wapstra but is considerably more precise. This is, of course based solely on the highest energy group, which is apparently the ground state transition. The total (γ,n) cross section is found to be between 15 and 17 mb at 8533 keV and between 14 and 15 mb at 8999 keV. The similarity between these cross sections and the others at the same energies suggests that the level assignments

of Chapter 6 are not grossly in error. In addition, the value of $\sigma_{\gamma n}$ compared with the cross sections averaged over many levels (Be75), namely 30 mb at 8.5 MeV and 50 mb at 9 MeV, suggests that the interactions are probably off resonance although they may be quite near to a resonance peak.

Examining the spectrum, we find the average level spacing of approximately 43 keV to be quite low compared to that of the nuclei nearer to the closed shells of ^{208}Pb (Table 7.4). This is, of course, no great surprise, since far from the closed shell the low lying nuclear levels no longer consist of just simple shell model configurations, and other levels due to collective oscillations and non-sphericity come into play. The partial cross sections vary over a range of about a factor of five in a manner not characteristic of an evaporation spectrum, and there are generally small fluctuations in partial cross sections both upwards and downwards as the photon energy changes from 8999 to 8533. The reduced widths also exhibit small, apparently random, fluctuations with both excitation energy and photon energy; and an estimate of ν yields a value of

$\sim$ 5 at 8999 keV and $\sim$ .2 at 8533 keV.

Insufficient numbers of photon energies and a lack of (p,d) and (d,t) reaction data have excluded any correlation studies on this nucleus.

7.3.3 Tantalum

Again, as in gold, a lack of information concerning the excited states of the residual nucleus hampers the analysis of results, and a lack of (p,d) and (d,t) reaction data eliminates attempts to compare reduced widths and spectroscopic factors. Only two excited states of ^{180}Ta are known; a 1^+ level near 32 keV and a $1^{(-)}$ level near 210±10 keV. The former must be populated by f- wave or higher odd ℓ neutron emission for an E1 photon and the latter by d- wave or higher even ℓ emission, but at the neutron energies of concern the transmission coefficients are not prohibitive. Thus, the observed 36 keV and 227 keV levels probably correspond to the 32 and 210 keV levels of the references (Gr75, Le68). The ground state has a possible 8^+ spin parity assignment from the literature, but the low value of the transmission coefficient at this energy

suggests that the spin is such that d- waves or lower ℓ- values populate it. This assumption is further strengthened by the disappearance of the group corresponding to the 1^+ 36 keV level for 8533 keV photons since the f- wave transmission factor at this neutron energy is quite low. The possible d- wave-populated 227 keV level is seen, however, for 8533 keV photons and thus this suggests that the ground state is spin 7 or less. This is also why the possible 36 7819 component has been omitted from group F. In the absence of spin information, the reduced widths have been calculated as if s- wave or high even ℓ neutrons were emitted.

The estimated Q-value of 7580 ± 5 keV, based on the highest energy neutron group, is seen to be 64 keV lower than the mean value of 7644 keV assigned by Wapstra and even though the latter has a large uncertainty of 22 keV, our value is still well outside its limits. It must be recalled, however, that the 7644 keV value is based on bremsstrahlung threshold methods which observe the energy at which photoneutrons first begin to be emitted by the target. Since the first two states (0, 36 keV) are each a factor five less strongly populated

than the 111 keV state at 9 MeV, it is possible that the same is true near threshold and that at energies which only populate the ground and first excited states, weak neutron emission has been interpreted as a background component. This would then give a Q-value which is 111 keV too high, making the "true" value 7533±22. This is within two standard deviations of our result.

The total (γ,n) cross sections have been found to be between 10 and 18 mb for E_γ = 8533 keV and between 7 and 10 mb at 8999 keV. These are again in rough agreement with other cross sections at these energies, strengthening trust in the level assignments. They are, also, significantly lower than the 30 to 50 mb average cross section (Be75) indicating that the reaction proceeds off resonance.

The average spacing of levels in ^{180}Ta is seen, as in the case of ^{196}Au, to be much lower than the nuclei nearer the closed shells. The spacing of 40 keV for excitation energies less than 600 keV is equal to that of gold and is in turn roughly an order of magnitude less than that of the lead isotopes. The spacing for excitation energies less than 1400 keV is 65 keV suggesting by the

increase that the higher levels at least are not simple shell model configurations. This might reasonably be expected for a deformed nucleus such as tantalum. Observation of the spectrum indicates that it is not an evaporation spectrum and inspection of the partial cross sections shows them to fluctuate randomly over a narrow range with excitation energy. The cross sections for all levels increase by a factor of 1.3 to roughly 5 as the photon energy decreases, and this loose correlation may indicate a semidirect reaction or at least a doorway state common to the various exit channels (section 7.1). The fact that the partial (and in fact, total) cross sections increase with decreasing photon energy may also suggest that the interactions are occurring on the tail of a resonance residing at an energy less than 8.5 MeV. It is not possible to tell if this has any connection with tantalum's deformed nature.

The reduced widths exhibit moderate random fluctuations both with E_γ and E_x. The number of degrees of freedom of the reduced width distribution is estimated to be $\sim$3 at 8533 keV and $\sim$7 at 8999 keV. Both may

suggest semidirect or multichannel processes.

7.4 Summary of Photoneutron Reaction Properties Near A=200

The reaction Q-values are seen to be in good agreement with the tabulated values of Wapstra (Wa71) and in many cases are as accurate or indeed more accurate than the latter. Most groups correspond well with known residual nuclear excitation energies, the only exception being three groups in natural lead which have not been identified.

Although the total cross sections generally have an upward trend with energy, they can fluctuate quite dramatically over a small range of photon energies. Thus, it is difficult to compare our values at 8.53 and 8.51 MeV with the 8.56 MeV values of Donahue et al. (We61, Gr64, Hu67) but we can do a comparison at 9 MeV. These values (which have been averaged if measured more than once) are presented in brackets under our values in Table 6.20. Donahue's cross section for ^{206}Pb is in agreement with ours since it is merely a large valued upper bound. The present values are roughly within one standard deviation of Donahue's cross sections for ^{209}Bi and ^{208}Pb but are considerably smaller for gold and tantalum. Also, for

the $^{181}Ta(\gamma,n)^{180m}Ta$ reaction, Donahue obtains a value of 44±15 mb, whereas if we assume the 227 keV level of our data is the 8.1 hour isomeric level, we obtain a cross section of 0.2 mb. These discrepancies are likely due to the fact that, since the system of Donahue had no energy information, if a given source had photons of different energies, the authors could not directly determine the number of neutrons corresponding to each photon. To correct for this, the authors used sources whose energies roughly agreed with the lower energy photons and subtracted the count rates thus obtained in order to determine the count rate due to the highest energy photon. As just mentioned, this is not always valid since occasionally cross sections can vary widely over only 20 keV.

Total cross sections are seen to be substantially smaller than those determined by electromagnetically generated photon sources. Since the latter generally average over the resonance structure of the excited target for heavy nuclei, this suggests that the interaction occurs off resonance in most cases. Although this also appears to be so for the ^{207}Pb target, its cross sections at most

energies are seen to be anomalously large compared to the other nuclei. Most of the other nuclei have roughly equal cross sections for a given energy although a few exceptions occur.

The distribution of reduced widths suggests that for all nuclei of concern at most photon energies, the reaction process is probably not strongly unichannel compound in nature. It should be recalled, however, that the uncertainty in ν is based on that of the reduced widths which in turn is not known. Thus, although the values of ν have qualitative meaning, the meaning of the actual numbers should be viewed with caution.

Correlation of reduced widths and (p,d) and (d,t) spectroscopic factors indicates that for ^{209}Bi at 9.7 MeV, ^{208}Pb at 9.0 MeV and ^{207}Pb at 8.9 MeV, the reactions probably occur with a substantial direct or semidirect contribution. For other photon energies incident on ^{209}Bi and ^{207}Pb, intermediate spin ambiguities cannot rule out such a contribution even though an anticorrelation or no correlation exists. Single particle pickup data is not available for the other nuclei.

The trends of partial cross sections for individual excited states of the residual nucleus could only be investigated for four levels in ^{208}Bi and three levels in ^{207}Pb due to resolution problems. In the former case a high degree of correlation was found, suggestive of a common doorway state connecting the four residual levels. In the latter case, the ground state was found to be strongly anticorrelated with the first excited state and moderately anticorrelated with the second. The significance of this is not fully understood but may be due to the presence of a multistep interaction, such as a compound reaction or a strong doorway state.

Thus the majority of the evidence presented seems to indicate that the photoneutron reactions observed occur off resonance and possess a strong semidirect component. This is in agreement with the theoretical predictions of a multiparticle-multihole continuum far from resonance.

7.5 Critique of the Experiment and Future Goals

It should be stressed that this is a new experimental field and as such there is no existing body of knowledge to guide one. This, of course, will develop with time and will make future analysis easier. There are, however, certain

problems inherent to the method that make data analysis difficult. Among these are the inability to continuously vary the photon energy and the inability to exclude more than one excitation process.

The major single drawback of our method of photoneutron spectroscopy is that of finite energy resolution. This creates an inability to determine accurate total cross sections, to follow energy trends of groups corresponding to various levels in the residual nucleus and to study angular distributions of a large number of groups. To some degree, this can never be completely prevented, because with different energy photons it is always possible to find different residual nuclear energy levels which yield neutron groups of almost the same energy. The problem can, however, be minimized in three different ways.

The choice of targets can significantly reduce the amount of overlap of neutron groups. Residual nuclei with low level densities such as those near closed shells and monoisotopic target nuclei are ideal for such purposes. In many cases separated isotopes in the large quantities required can be obtained on loan.

The second solution to neutron group overlap is improvement of the resolution of the detector. The technique of risetime discrimination was discussed in Chapter 3 and was found to provide minimal improvement in energy resolution. This is mainly because the largest portion of the resolution is due to the gain dependence of the amplifier with pulse risetime resulting in a series of slightly shifted peaks at different risetimes for a given neutron energy. One method of improving the resolution would be to collect data two dimensionally as a function of risetime and energy and determine an energy-risetime dependent shift correction that could be applied to the spectra. Spectra at each risetime window could then be shifted and added off line, yielding a final spectrum with much higher resolution. In doing so, there would be no loss of efficiency and, if necessary, low risetimes could still be rejected to eliminate continuum events. Neutron count rates are low enough that buffered tape writing techniques could easily be used, allowing 2048 x 32 energy-time spectra to be collected.

Finally, given a fixed resolution, it is possible to improve methods of extracting barely resolved multiplets. The method presently in use (Chapter 6) requires guesses as to the number of peaks and centroid position and has difficulty extracting multiplets of small and large closely spaced peaks. Furthermore, since it is written for a non-interactive machine, analysis time for one spectrum is lengthy. A recent method for peak extraction developed by Kennett et al. (Ke77) employs a deconvolution technique based on Bayes' Theorem. It is written for a small interactive computer and requires no initial guesses as to centroid or peak number. It does, however, as does the present program, require a knowledge of spectral response function but it is not extremely sensitive to it. Using this method, very small and poorly resolved peaks have been observed in test spectra that could not be resolved using the present program. Since it is an iterative technique, and separation of peaks improves with time, most peaks can be resolved if the program is allowed to run long enough. Future work will make extensive use of this method for peak extraction.

As we have seen in section 7.2, there are certain anomalies in the spectra of natural lead and enriched 208-lead. Two groups appear which have energies corresponding to a 207- lead target but which for reasons explained in section 7.2, do not appear to correspond to this or any other lead target. In an attempt to explain this mystery, steps have been taken to borrow separated lead isotopes with enrichments greater than 99%. It is hoped that a study of these isotopes will clarify the anomalies which currently exist. Studies of the photoneutron angular distributions for the lead isotopes will also be undertaken using more forward and backward angles than the two used in these experiments. Although many angles are required to uniquely determine the matrix elements (section 6.4) it is possible, using a larger number of angles than at present, to make fewer assumptions and thus fit the data to a more sophisticated model. With fewer degrees of freedom, it may also be possible to estimate the branching ratio to multiple intermediate spin states when targets which are not even-even are studied.

Attempts will also be made to push the study of both photoneutron cross sections and angular distributions to

elements of lower mass. Since reactions on these nuclei should occur on the tail of the isoscalar E2 resonance, far from the centroid, one would expect significantly different mixing ratios to occur. It would also be interesting to see if reaction mechanisms are substantially the same for nuclei of different mass regions. Initial studies of nuclei near the closed proton shell of tin such as antimony and cadmium have shown that such studies are feasible, and nuclei with mass number as low as 93 (niobium) have yielded reasonable photoneutron rates.

Lastly, there is a need for detailed single particle pickup reaction studies on the isotopes of thallium, gold and tantalum, in order to allow correct interpretation of the photoneutron spectra which have been obtained. Such studies would also allow a more detailed analysis of the type of photoneutron reaction to be undertaken.

APPENDIX 1

Calculation of the Output Pulse Shape of an RC Amplifier

An amplifier acting as a low pass or high pass filter may be replaced by its RC or CR equivalent. The RC equivalent circuit for a high pass filter (differentiator) is shown in Fig. A1.1a and that for a low pass filter (integrator) is shown in Fig. A1.1b. If v_i denotes the input voltage; v_o, the output voltage; C and R, the capacitance and resistance respectively; i, the current through the resistor and Q, the charge on the capacitor, then for high pass filter we find :

$$v_i = \frac{Q}{C} + Ri \qquad \text{(A1.1)}$$

differentiating with respect to time

$$\frac{dv_i}{dt} = \frac{1}{C}\frac{dQ}{dt} + R\frac{di}{dt} \qquad \text{(A1.2)}$$

but

$$\frac{dQ}{dt} = i \text{ and } Ri = v_o$$

and substitution thus yields

$$\frac{dv_o}{dt} + \frac{v_o}{T} = \frac{dv_i}{dt} \qquad \text{(A1.3)}$$

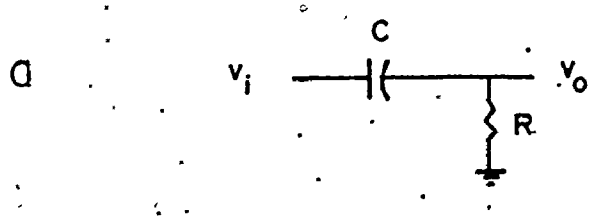

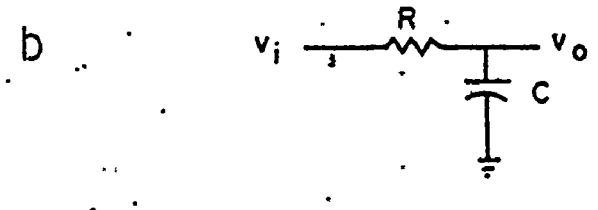

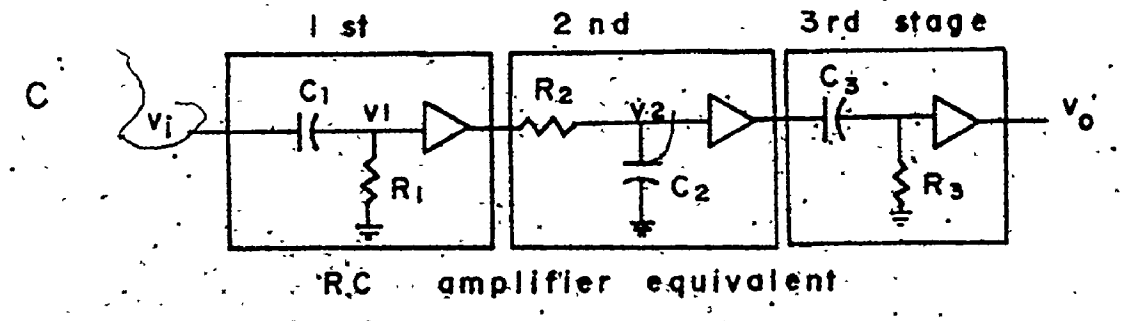

Al.1. Equivalent circuits for RC amplifier analysis. Figure (a) and (b) are the high and low pass filter equivalents respectively. Figure (c) is the RC equivalent of a three stage spectroscopy amplifier.

where $T = RC$ (A1.4)

In a similar manner we find for the low pass filter :

$$\frac{dv_o}{dt} + \frac{v_o}{T} = \frac{v_i}{T} \qquad \text{(A1.5)}$$

Now we wish to analyze the 3 stage amplifier shown schematically in Fig. A1.1c. We assume an exponential input of the form

$$v_i = v(1-e^{-t/\tau}) \qquad \text{(A1.6)}$$

where v and τ are constants. As an example we shall derive the output voltage for the case

$$R_1C_1 \neq R_2C_2 \neq R_3C_3 \neq \tau ,$$

since all other cases are derived in a very similar manner.

We have as initial conditions

$$v_i = v_1 = v_2 = v_o = o \text{ at } t = o \qquad \text{(A1.7)}$$

where

v_1 is the output voltage of the first stage

v_2 is the output voltage of the second stage

v_o is the final output voltage

and we assume that the amplifiers have an infinite bandwidth, i.e. only multiply the output voltage by a constant factor which can be set to unity. We also write $R_1C_1 = T_1$, $R_2C_2 = T_2$ and $R_3C_3 = T_3$. We then have for the first stage :

$$\frac{dv_1}{dt} + \frac{v_1}{T_1} = \frac{dv_i}{dt} = \frac{v}{\tau} e^{-t/\tau} \qquad \text{(A1.8)}$$

The solution for this type of first order differential equation may be obtained from any standard text book on differential equations.

Thus for equation (A1.8) we have :

$$v_1 = e^{-t/T_1} \int^{t} e^{\frac{x}{T_1}} \frac{v}{\tau} e^{\frac{-x}{\tau}} dx + C e^{-t/T_1}$$

and applying the initial conditions (A1.7) we find

$$v_1 = \frac{vT_1}{\tau - T_1} (e^{-t/\tau} - e^{-t/T_1}) \qquad \text{(A1.9)}$$

For the second stage we have :

$$\frac{dv_2}{dt} + \frac{v_2}{T_2} = \frac{v_1}{T_2} = \frac{vT_1}{T_2(\tau - T_1)} (e^{-t/\tau} - e^{-t/T_1}) \qquad \text{(A1.10)}$$

and this is solved in the same manner as (A1.8) to yield :

$$v_2 = \frac{vT_1}{\tau-T_1}\left[\frac{\tau}{\tau-T_2}e^{-t/\tau} - \frac{T_1}{T_1-T_2}e^{-t/T_1} + \frac{T_2(\tau-T_1)}{(T_1-T_2)(\tau-T_2)}e^{-t/T_2}\right] \quad \text{(A1.11)}$$

The equation for the third stage is :

$$\frac{dv_o}{dt} + \frac{v_o}{T_3} = \frac{dv_2}{dt} = \frac{vT_1}{\tau-T_1}\left[\frac{-e^{-t/\tau}}{\tau-T_2} + \frac{e^{-t/T_1}}{T_1-T_2} - \frac{(\tau-T_1)e^{-t/T_2}}{(T_1-T_2)(\tau-T_2)}\right] \quad \text{(A1.12)}$$

This may again be solved in a fashion analogous to equation (A1.8) and we thus obtain :

$$v_o = \frac{vT_1T_3}{\tau-T_1}\left[\frac{-\tau}{(\tau-T_2)(\tau-T_3)}e^{-t/\tau} + \frac{T_1e^{-t/T_1}}{(T_1-T_2)(T_1-T_3)} - \frac{T_2(\tau-T_1)e^{-t/T_2}}{(T_1-T_2)(\tau-T_2)(T_2-T_3)}\right.$$

$$\left. + \left\{\frac{\tau}{(\tau-T_2)(\tau-T_3)} - \frac{T_1}{(T_1-T_2)(T_1-T_3)} + \frac{T_2(\tau-T_1)}{(T_1-T_2)(\tau-T_2)(T_2-T_3)}\right\}e^{-t/T_3}\right]$$

for $\tau \neq T_1 \neq T_2 \neq T_3$ (A1.13)

It should be noted that if any of the parameters τ, T_1, T_2 or T_3 are equal, we get an indefinite 0/0 solution. However, it can be shown by using L'Hospital's Rule, that in the limit as any of the four parameters become equal to one another, a finite solution exists. These solutions can also be derived in the same manner as above but equating the appropriate time constants where necessary. As explained in Chapter 3, only cases with $T_2 = T_3$ were considered and the results for these special cases are presented below.

$$v_o = \frac{vT_1}{\tau-T_1}\left[\frac{-T_2\tau}{(\tau-T_2)^2}\, e^{-t/\tau} + \frac{T_1T_2}{(T_1-T_2)^2}\, e^{-t/T_1} - \frac{t(\tau-T_1)e^{-t/T_2}}{(T_1-T_2)(\tau-T_2)}\right.$$

$$\left. + \left\{\frac{T_2\tau}{(\tau-T_2)^2} - \frac{T_1T_2}{(T_1-T_2)^2}\right\}\, e^{-t/T_2}\right]$$

for $\tau \neq T_1 \neq T_2 = T_3$ (A1.14)

$$v_o = \frac{vT_1T_2}{(T_1-T_2)^2}\left[\frac{-t}{T_1}e^{t/T_1} + \frac{T_1+T_2}{T_1-T_2}\, e^{-t/T_1} - \frac{t}{T_2}e^{-t/T_2} + \frac{T_1+T_2}{T_1-T_2}\, e^{-t/T_2}\right]$$

for $\tau = T_1 \neq T_2 = T_3$ (A1.15)

$$v_o = \frac{vT_1}{T_2(T_2-T_1)}\left[\frac{-t^2}{2T_2}e^{-t/T_2} - \frac{T_2 t}{T_1-T_2}e^{-t/T_2} - \frac{T_1T_2^2}{(T_1-T_2)^2}e^{-t/T_2} + \frac{T_1T_2^2}{(T_1-T_2)^2}e^{-t/T_1}\right]$$

for $\tau = T_2 = T_3 \neq T_1$ (A1.16)

$$v_o = \frac{v}{\tau-T_1}\left[\frac{-T_1^2\tau}{(\tau-T_1)^2}e^{-t/\tau} + \frac{t^2}{2T_1}e^{-t/T_1} + \frac{T_1 t}{\tau-T_1}e^{-t/T_1} + \frac{T_1^2\tau}{(\tau-T_1)^2}e^{-t/T_1}\right]$$

for $\tau \neq T_1 = T_2 = T_3$ (A1.17)

and $$v_o = \frac{ve^{-t/T_1}}{2T_1^2}\left[\frac{-t^3}{3T_1} + t^2\right]$$

for $\tau = T_1 = T_2 = T_3$ (A1.18)

The equations for the case of double differentiation can be derived in the same way or by the use of Laplace transforms and these may be found in Cuttler's paper (Cu69b). A computer program was written to generate waveforms using the above equations for double differentiation, with and without an integration stage, for various time constants and risetimes. Graphs of crossover time, tc, versus τ and a table of normalized slope, $\frac{1}{V_o}(\frac{dV}{dt})\ t=t_c$, and maximum pulse height, V_o, for different time constants are presented in Chapter 3.

APPENDIX II

Recoil Correction for Photoneutron Decay

If we consider a photon of energy E_γ incident on a nucleus, to produce a photoneutron of energy E_n at an angle θ with the incident photon direction, and a recoiling residual nucleus of energy E_M at an angle of ϕ with respect to the photon direction, then the balance of energy and momentum require that :

$$E_\gamma - Q - E_x = E_n + E_M \qquad \text{(A2.1)}$$

$$P_M \sin\phi = P_n \sin\theta \qquad \text{(A2.2)}$$

$$E_\gamma/c = P_M \cos\phi + P_n \cos\theta \qquad \text{(A2.3)}$$

where

Q is the photoneutron Q-value

E_x is the excitation energy of the residual nucleus

P_n is the norm of the neutron momentum

and

P_M is the norm of the momentum of the recoiling nucleus.

If we further assume that particle energies are nonrelativistic,

then :

$$P_n^2 = 2 m E_n \qquad (A2.4)$$

$$P_M^2 = 2 M E_M \qquad (A2.5)$$

with m the rest mass of the neutron

and M = Am the rest mass of the residual nucleus. A solution of equations A2.1 to A2.5 yields the following equation for the neutron energy :

$$E_n = \frac{A}{1+A}(E_\gamma - Q - E_x) - \frac{E_\gamma^2}{2mc^2(1+A)} + \frac{2E_\gamma}{(1+A)}\sqrt{\frac{E_n}{2mc^2}}\,\mathrm{Cos}\Theta \qquad (A2.6)$$

For our work the first term will never be less than ∿25 keV. The second term will be largest for large values of E_γ and low values of A. For a worst case estimate using E_γ = 12 MeV and A = 100, we get for the second term - 0.758 keV and thus it can be neglected since centroid errors alone account for 2.5 keV uncertainties. For the third term such a worst case estimate yields 10.9 keV ($|\mathrm{Cos}\Theta|=1$). For more typical values such as A=200 and E_n = 2.5 MeV and 1 MeV we get values of 4.4 keV and 2.7 keV respectively.

For the experiments which measure photoneutron cross sections (section 5.3), the third term can again be neglected if, to first order, the probability of emission of neutrons is symmetric about $\theta = \pi/2$. For such a case we get :

$$\text{3rd term} = \int_0^{\pi} \frac{2E_\gamma}{1+A}\sqrt{\frac{E_n}{2mc^2}}\,\varepsilon(\theta)P(\theta)\cos\theta d\theta \Big/ \int_0^{\pi} \varepsilon(\theta)P(\theta)d\theta \quad \text{(A2.7)}$$

where $P(\theta)$ is the probability of neutron emission into an angle, θ

$\varepsilon(\theta)$ is the detector efficiency which is symmetric about $\theta=\pi/2$ (section 3.5.2) thus

$$\text{3rd term} = \frac{2E_\gamma}{1+A}\sqrt{\frac{E_n}{2mc^2}} \int_0^{\pi} \varepsilon(\theta)P(\theta)\cos\theta d\theta \Big/ \int_0^{\pi} \varepsilon(\theta)P(\theta)d\theta \quad \text{(A2.8)}$$

Now $\cos\theta$ is antisymmetric about $\theta=\pi/2$ and thus the first integral is zero. Therefore

$$\text{3rd term} = 0 \quad \text{(A2.8)}$$

The assumption of symmetry about $\theta=\pi/2$ is equivalent to stating that parity mixing is small. As is discussed in

Chapter 7 this is indeed the case.

For the asymmetry experiment on lead (section 5.4), we no longer have an integral from 0 to π but rather 0 to $\pi/2$. As discussed in section 6.4, the mean polar angle for the detector efficiency is approximately 42° and thus we get for the third term in equation A2.6 an average value of 2.6 keV for E_γ = 10 MeV, A=200 and E_n = 2.5 MeV. Values of 1.7 keV and 1.2 keV are obtained for E_n = 1 MeV and 0.5 MeV respectively. The dispersion due to this term is seen to be much less than the typical peak widths of 15 (E_n=0) to 35 keV (E_n=1.5 MeV) f.w.h.m.. It is also less than the typical 5 keV energy centroid uncertainties.

Photoneutron energies are also shifted due to elastic scattering in the target materials. It may be shown in a straightforward manner that an elastic collision by a nonrelativistic neutron of energy E_n through an angle θ by a nucleus of atomic mass A yields a new neutron energy E_n^1 according to the equation :

$$\frac{E_n^1}{E_n} = \frac{2\cos^2\theta + A^2 - 1 \pm 2\cos\theta\sqrt{\cos^2\theta + A^2 - 1}}{(1+A)^2} \qquad \text{(A2.9)}$$

Given that A is approximately 200, this yields a maximum value of 1% for the energy shift per collision which is at least twice as small as the detector resolution (2.7% at 1 MeV, 2% at 2 MeV). If neutron emission is isotropic, the spectrum for initially monoenergetic photoneutrons becomes complicated but would have a mean energy shift approximately one half of the maximum shift of 1%. If one then considers that the probability of elastic scattering is no greater than 50% for the targets of concern, this makes the effective centroid shift of the order of 0.25% or approximately 2,5 keV at 1 MeV. This is effectively negligible with respect to previously mentioned uncertainties and systematic errors,

APPENDIX III

Corrections for Cross Section Calculations

We shall first address ourselves to the matter of errors induced by anisotropic photoneutron angular distributions. If, as many researchers have done for direct reactions (Fu60, Ha71), we assume a differential cross section, $\sigma(\Theta)$, of the form :

$$\sigma(\Theta) = a + b \, Sin^2\Theta \qquad (A3.1)$$

where Θ is the polar angle and a, b are constants then the total cross section is given by :

$$\sigma_T = \int_{\Theta=0}^{2\pi} a + b \, Sin^2\Theta \, d\Theta = (2a + b)\pi \qquad (A3.2)$$

The measured total cross section is given by

$$\sigma_M = 2\pi \int_{\Theta=0}^{2\pi} \varepsilon(\Theta)\sigma(\Theta)d\Theta \Big/ \int_{\Theta=0}^{2\pi} \varepsilon(\Theta)d\Theta \qquad (A3.2)$$

with ε being the angular dependent detector efficiency function.

As a first approximation for the efficiency (see section 3.5.2) we assume that ε is given by :

$$\varepsilon = h \quad \text{for} \quad \theta_2 \leq \theta \leq \pi - \theta_2 \tag{A3.3}$$

where h is a constant

$$\varepsilon = h(\theta-\theta_1)/(\theta_2-\theta_1) \text{ for } 0\leq\theta\leq\theta_1$$

$$\Big) \qquad \text{and } \pi-\theta_1\leq\theta\leq\pi$$

$$\varepsilon = 0 \quad \text{elsewhere.}$$

We find by direct integration of A3.2 that the value of the constant h does not matter and that

$$\frac{\sigma M}{\sigma T} = 1 + \frac{1}{(a/b+1/2)} \frac{1}{(\pi-\theta_1-\theta_2)} \left(\frac{\theta_1 \text{Sin}2\theta_1 - \theta_2 \text{Sin}2\theta_2}{2} + \frac{\text{Cos}2\theta_1 - \text{Cos}2\theta_2}{4} \right.$$

$$\left. - \frac{\theta_1}{\theta_2-\theta_1} \text{Cos}\theta_1 \text{Sin}\theta_1 + \frac{2\theta_1-\theta_2}{\theta_2-\theta_1} \text{Cos}\theta_2 \text{Sin}\theta_2 \right) \tag{A3.4}$$

For the present configuration, $\theta_1 \approx 20°$ and $\theta_2 \approx 50°$ and thus

$$\frac{\sigma_M}{\sigma_T} \approx 1 - \frac{.0105}{(a/b + 1/2)}$$

Values of a/b tend to be small (see for example Lo72) but nevertheless even for the worst case of $a/b = 0$ (no isotropic contribution) we have $\sigma_M/\sigma_T = .979$ which is much smaller than the uncertainty in the measured cross section.

Elastic scattering and absorption of photoneutrons may also cause an error in estimating the cross section. Although elastic scattering cross sections are appreciable, yielding mean free paths of 1.5 to 7.7 cm for the targets in question, it can be argued that the effect of elastic scattering upon the measurement of the photoneutron cross section will be negligible. If the elastic scattering cross section were sharply forward peaked, most neutrons would continue in their initial direction with only a small loss in energy as described in Appendix II. In the other extreme, if the photoneutron cross sections were isotropic, those neutrons initially directed at the detector but scattered away from it would on the average be compensated for by neutrons initially directed away from the detector, but scattered into it. Again there would be a small

energy loss but this would be much smaller than the detector resolution. Nonelastic scattering of neutrons cannot be neglected in this manner. Fortunately the cross sections for nonelastic events tend to be much smaller than those for elastic scattering. The transmittances vary from average values of .96 to 0.98 for the gold, thallium, bismuth and lead targets to a low of .94 for the tantalum target. Since the photoneutron cross sections measurements have an inherent uncertainty of at least 25% (section 6.3.5) nonelastic scattering is entirely negligible. In a similar fashion, it is seen that neutron capture processes, with average transmittances of 0.97 or better, are negligible.

TABLE 1.I

Comparison of Photoneutron Facilities

Photon Source	Effective photon[1.] intensity at target position $eV^{-1}cm^{-1}sec^{-1}$	Energy[1.] spread $\Delta E_\gamma/E_\gamma$ %	Possible Detection Methods	Energy[6.] Resolution $\Delta E_n/E_n$ % 0.5 MeV	1 MeV
Bremsstrahlung monochromator	$(.05-1)\times10^{-3}$	1	fast scintillator		
Bremsstrahlung threshold (cyclotron)	1	3	time of flight	0.3[2.]	0.4[2.]
			large liquid scintillators	-	-
			BF_3	-	-
Bremsstrahlung threshold (Linac)	10	3	Same as for Bremsstrahlung cyclotron		
Positron annihilation in flight	10^{-2}	4	large liquid scintillators	-	-
$^{19}F(p,\gamma\alpha)$	1	1.8[4.]	time of flight	0.3[2.]	0.4[2.]
$^{7}Li(p,\gamma)$	10	0.07[4.]	BF_3	-	-
$^{3}H(p,\gamma)$	10	<0.2[4.]	^{3}He[5.]	4.2[3.]	2.7[3.]
(n,γ) followed by Compton scattering	1	2	BF_3	-	-
(n,γ)	10^{6}	10^{-4}	BF_3	-	-
			^{3}He	4.2[3.]	2.7[3]
			large liquid scintillators		

1. Reference Ar73 except as noted.
2. For 10 m flight path, 1 ns time resolution.
3. Best resolution to date from FNS-1 spectrometer (Chapter 3).
4. Reference Ha65.
5. Has not been utilized in such an experiment.
6. Blank space denotes no useful energy information.

TABLE 2.1

S=0 Low Energy Giant Collective Resonances

EL	T	Simple Harmonic Oscillator Energy	with the inclusion of residual two body interactions	Energy ($MeV\text{-}A^{-1/3}$) 2.	3.
E0	0	$2\hbar\omega$	$1.5\hbar\omega$	-	62
E0	1	$2\hbar\omega$	$4\hbar\omega$	173	164
E1	0[1]	-	-	-	-
E1	1	$1\hbar\omega$	$2\hbar\omega$	80	82
E2	0	$0\hbar\omega$	$0\hbar\omega$	-	0
E2	0	$2\hbar\omega$	$1.5\hbar\omega$	-	62
E2	1	$2\hbar\omega$	$3\hbar\omega$	128	123

1. Thompson scattering. Does not disrupt internal nuclear coordinates.
2. Based on the hydrodynamic model.
3. Based on equation 2.

TABLE 3.1

Maximum Proton Ranges for given Neutron Energies

Neutron Energy E_n (MeV)	Maximum Available Energy, E_t (MeV)	Range of Proton of Energy E_t in dry air at 1 atm, 15°C (Ev55) (cm)	Range of Proton of Energy E_t in detector gas[1]. (cm)
1.000	1.764	5.70	1.19
0.667	1.431	4.05	0.84
0.333	1.091	2.70	0.56
0.000	0.764	1.50	0.31

[1] gas consists of 6 atmospheres of Argon and 3 atmospheres of Helium-3

TABLE 4.1

Maximum Pulse Height and Normalized Slope[1] for Different Amplifier Time Constants

T_1 (μs)	T_2 (μs)	T_3 (μs)	V_o	$\frac{1}{V_o}\left(\frac{dV}{dt}\right)_{t=tc}$ μs^{-1}
1.6	1.6	1.6	0.161	.408
6.4	1.6	1.6	0.248	.207
6.4	-	1.6	0.339	.184
6.4	6.4	6.4	0.220	.082

T_1 = time constant of the first differentiator,

T_2 = time constant of the integrator

T_3 = time constant of the second differentiator

V_o = maximum pulse height

$(dV/dt)_{t=tc}$ = slope of the pulse at crossover

[1] an exponential input of the form $V = 1-e^{-t/\tau}$ is assumed where

t is the time

τ is the risetime constant = 1 μs

TABLE 4.2

Targets

Element	Atomic Number	Weight (±.05g)	Density (CRC72) (g/cm^3)	Isotope (Atomic mass)	Fraction (Le68) %
Tantalum	73	306.9	16.65	180	.0123
				181	99.988
Gold	79	312.5	19.32	197	100.
Thallium	81	191.0	11.85	203	29.50
				205	70.50
Lead	82	193.4	11.35	204	1.48
				206	23.6
				207	22.6
				208	52.3
Separated[1] Lead	82	26.5	11.35	204[2]	<0.03[3]
				206	14.
				207	1.
				208	85.
Bismuth	83		9.75	209	100.

[1] cut from the Saclay sample

[2] contains trace activity of ^{210}Po

[3] determined by spark source mass spectrometry by N.R.C., Ottawa. Error is ± 3% of the value quoted.

TABLE 6.1

Nickel Source Intensities

Energy (MeV)	Relative Intensity[a]	Accepted Intensity[a,b]
11.387	5.8 ± 0.5	c
8.999	1000.0 ± 8.0	1000 ± 1
8.533	434.4 ± 5.9	450 ± 1
8.120	76.7 ± 3.5	83 ± 1
7.819	215.7 ± 4.8	217 ± 1
7.724	154.3 ± 4.0	d
7.555	112.3 ± 3.8[e]	60 ± 1
7.534		58 ± 1
6.837	284.7 ± 4.6	286 ± 1
6.584	38.1 ± 3.4	47 ± 1
6.105	49.2 ± 4.1	50 ± 1
5.974	19.0 ± 3.9	18 ± 1
5.837	75.1 ± 4.5[e]	16 ± 1
5.817		56 ± 1

[a] Arbitrary units. Unless otherwise stated lines arise from thermal neutron capture on stable nickel isotopes.

[b] Reference Ra67.

[c] From thermal neutron capture on ^{59}Ni and thus the intensity is dependent on irradiation time. Intensity was determined May 20, 1975.

[d] From thermal neutron capture on aluminum.

[e] Intensity of two lines which could not be resolved.

TABLE 6.2

Chromium Source Intensities

Energy (MeV)	Relative Intensity[a]	Accepted Intensity[a,b]
9.720	393 ± 15	407 ± 1
8.884	1000 ± 30	1000 ± 1
8.512	258 ± 10	228 ± 1
8.484	168 ± 8	168 ± 1
7.939	485 ± 20	473 ± 1
7.724	211 ± 10	[c]
7.695	26 ± 6	[d]
7.377	108 ± 7	279 ± 1[e]
7.363	167 ± 8	
7.100	161 ± 8	161 ± 1
6.890	48 ± 6	43 ± 1
6.646	214 ± 10	219 ± 1
6.372	29 ± 6	30 ± 1
6.326	28 ± 6	20 ± 1
6.282	38 ± 6	49 ± 1
6.246	7 ± 6	11 ± 1
6.136	67 ± 6	69 ± 1
6.000	87 ± 6	94 ± 1
5.858	22 ± 6	29 ± 1
5.794	9 ± 6	14 ± 1
5.707	26 ± 6	30 ± 1
5.619	139 ± 7	143 ± 1
5.494	29 ± 6	27 ± 1
5.270	44 ± 6	47 ± 1

[a] Arbitrary units. Unless otherwise stated lines arise from thermal neutron capture on stable chromium isotopes.

[b] Reference Ra67.

[c] From thermal neutron capture on aluminum.

[d] Unidentified contaminant.

[e] Sum of two unresolved components.

TABLE 6.3

Photoneutron Q - values

Initial Isotope	Nickel Source (keV)	Chromium Source (keV)	Weighted Average (keV)	Wapstra (Wa71) (keV)
^{209}Bi	7462 ± 3	7456 ± 3[1.]	7459 ± 2	7453 ± 11
^{208}Pb[2.]	7371 ± 1	7363 ± 3	7371 ± 3	7368.2±1.4
^{208}Pb[3.]	7376 ± 5	7365 ± 4	7369 ± 4	7368.2±1.4
^{207}Pb[2.]	6742 ± 2	6744 ± 5	6742 ± 3	6740.7±1.4
^{207}Pb[3.]	6737 ± 5	-	6737 ± 5	6740.7±1.4
^{206}Pb[2.]	8089 ± 5	8086 ± 4	8087 ± 3	8081.0±1.4
^{206}Pb[3.]	-	8083 ± 5	8083 ± 5	8081.0±1.4
^{205}Tl	7548 ± 3	-	7548 ± 3	7541.4±3.8
^{203}Tl	7737 ± 3	-	7737 ± 3	7720 ± 20
^{197}Au	8080 ± 5[4.]	-	8080 ± 5	8080 ± 12
^{181}Ta	7580 ± 5[4.]	-	7580 ± 5	7644 ± 22

1. Average of data with and without risetime selection.
2. From natural sample.
3. From enriched sample.
4. Based on highest energy neutron group.

TABLE 4

Observed Neutron Groups from Bismuth using a Nickel Source

Possible Components

	E_n [1] (keV)	E_x (keV)	E_γ (keV)	Relative Intensity [3]	Error [3]
	1530	0	8999	1000	22
	1466	63	8999	678	21
	1063	0	8533	149	8
	1020	511	8999	579	33
	1001 [2]	63	8533	74	33
	930	603	8999	293	14
	901	632	8999	305	30
	881	652	8999	184	33
	647	889	8999	429	13
		0	8120		
	617	927	8999	156	15
	595	939	8999	540	17
		63	8120		
	564 [2]	961	8999	138	11
	498	1036	8999	144	10
A	463	1071	8999	223	13
A		603	8533		
B	437	1097	8999	264	13
B		632	8533		
	354	0	7819	82	10
	292	63	7819	328	12
	259	0	7724	138	11
	178	889	8533	59	12
	108	961	8533	43	12
	70	0	7534	33	12

1. Error is ± 5 keV except as noted.
2. Error is ± 10 keV.
3. Arbitrary units.

TABLE 6.5

Observed Neutron Groups from Bismuth using a Chromium Source

E_n (keV)[1]		Possible Components E_x (keV)	E_γ (keV)	Relative[3] Intensity	Error[3]
2252		0	9719	387	19
2191		63	9719	633	18
1741		511	9719	365	19
1629		632	9719	1012	31
1422		.0	8884	1000	48
1361	A	889	9719	2355	65
		63	8884		
1296[2]		939	9719	299	50
		961	9719		
1223		1036	9719	343	26
1166		1097	9719	494	35
1052[2]		0	8512	503	18
1023[2]		0	8484	258	17
989[2]		63	8512	708	25
955[2]		63	8484	165	15
913		511	8884	710	26
822		603	8884	908	33
791		1467	9719	719	24
727[2]		1534	9719	63	18
696[2]		1565	9719	112	20
		1576	9719		
564		1699	9719	375	36
538	B	1721	9719	3493	54
		1734	9719		
		889	8884		
		511	8512		
502		927	8884	778	49
477	C	939	8884	2327	72
		0	7939		
456	D	1792	9719	1353	84
		1806	9719		
		961	8884		
		603	8512		
421	E	1844	9719	1503	34
		631	8512		
		603	8484		
		63	7939		
389	F	1036	8884	876	31
		652	8512		
		631	8484		
358		1071	8884	403	31
331[2]		1925	9719	164	29
		1097	8884		
265		0	7724	318	20
168		889	8512	252	16

1. Error is ± 5 keV except as noted.
2. Error is ± 10 keV.
3. Arbitrary units.

TABLE 6.6

Observed Neutron Groups from Natural Lead Using a Nickel Source

(possible components)

E_n (keV)[1]	Residual Isotope	E_x (keV)	E_γ (keV)	Intensity[4]	Error[4]
2260[3]	206	0	8999	53	8
1784	206	0	8533	145	13
1621	207	0	8999	1000	24
1448	206	803	8999	2353	32
1360	206	0	8120	146	12
1157	207	0	8533	425	15
1086	206	1165	8999	841	21
1052	207	570	8999	519	19
980	206	803	8533	415	17
	206	0	7724		
905[2]	206	1340	8999	874	22
	205	0	8999		
	205	2	8999		
785	206	1460	8999	396	16
	206	0	7534		
725	207	898	8999	1068	25
641	205	263	8999	625	22
616	206	1165	8533	258	21
591	207	570	8533	247	22
568[2]	206	1684	8999	232	26
	206	803	8120		
547	206	1704	8999	603	30
470	206	1784	8999	434	21
444	207	0	7819	632	23
	206	1340	8533		
	205	0	8533		
	205	2	8533		
327	206	1460	8533	385	24
	205	576	8999		
266[3]	207	898	8533	155	102
256[3]	206	1998	8999	211	101
179	207	570	8120	431	22
	207	0	7555		
	206	803	7724		
	205	263	8533		
108	206	2150	8999	438	17
	206	1684	8533		
	205	803	8999		
89	206	1704	8533	132	16

1. Error ± 5 keV except as noted.
2. Error ± 7 keV.
3. Error ± 10 keV.
4. Arbitrary units.

TABLE 6.7

Observed Neutron Groups from Enriched ^{208}Pb using a Nickel Source

(possible components)

E_n (keV)[1]	Residual Isotope	E_x (keV)	E_γ (keV)	Relative[4] Intensity	Error[4]
1782[2]	206	0	8533	168	64
1621	207	0	8999	1000	44
1444[2]	206	803	8999	94	20
1378	206	0	8120	211	24
1159	207	0	8533	468	30
1055	207	570	8999	465	32
905	206	1340	8999	132	22
	205	0	8999		
	205	2	8999		
820[2]	206	1460	8999	47	20
	206	0	7555		
	206	0	7534		
728	207	898	8999	1089	46
645	205	263	8999	180	26
593	207	570	8533	179	30
550[3]	206	1704	8999	39	26
448	207	0	7819	533	40
	206	1340	8533		
	205	0	8533		
	205	2	8533		
329	206	1460	8533	137	30
	205	576	8999		
265	207	898	8533	321	40
187	207	570	8120	103	26
	207	0	7555		
	206	803	7724		
	205	263	8533		

1. Error ± 5 keV except as noted.
2. Error ± 10 keV.
3. Error ± 15 keV.
4. Arbitrary units.

TABLE 6.8

Observed Neutron Groups from Natural Lead using a Chromium Source

E_n (keV)[1]	Residual Isotope	(Possible components) E_x (keV)	E_γ (keV)	Relative[4] Intensity	Error[4]
2344[2]	207	0	9719	117	13
2141	206	803	9719	506	31
	206	0	8884		
1770	207	570	9719	1000	48
	206	0	8512		
1629	206	1340	9719	2095	90
	205	0	9719		
	205	2	9719		
1512	207	0	8884	429	57
	206	1460	9719		
1448	207	898	9719	456	68
1367[2]	205	263	9719	573	66
1339[2]	206	803	8884	944	58
1305[3]	206	1684	9719	187	54
1271[2]	206	1704	9719	442	36
1195	206	1784	9719	953	68
	206	0	7939		
1146[2]	207	0	8512	230	40
1117[3]	207	0	8484	170	36
1054[2]	205	576	9719	207	33
979[2]	206	1998	9719	1002	48
	206	1165	8884		
	206	803	8512		
	206	0	7724		
935[2]	207	570	8884	340	36
	206	803	8484		
	205	703	9719		
862[2]	205	761	9719	681	53
795[2]	206	1340	8884	2319	84
	205	0	8884		
	205	2	8884		
743[2]	unassigned 3				
671[3]	206	2314	9719	617	78
	206	1460	8884		
618[3]	207	898	8884	2000	204
	206	0	7377		
	206	0	7363		
	205	1014	9719		
579[3]	207	570	8512	743	102
	207	0	7939		
	206	2384	9719		
	206	2391	9719		
	206	1165	8484		
	205	1044	9719		
536[3]	207	570	8484	1048	105
	206	2428	9719		
	205	263	8884		
464[2]	206	1684	8884	166	41
442	206	1704	8884	294	42
393	206	1340	8484	706	50
	206	803	7939		
	205	0	8484		
	205	2	8484		
359	207	0	7724	666	39
	206	1784	8884		
	206	0	7100		
257[2]	207	898	8512	308	69
181[3]	206	803	7724	763	97
	205	263	8512		
90[2]	206	1684	8512	443	151
	205	703	8884		

1. Error ± 5 keV except as noted.
2. Error ± 7 keV.
3. Error ± 10 keV.
4.

TABLE 6.9

Observed Neutron Groups from Enriched ^{208}Pb using a Chromium Source

(Possible components)

E_n (keV)[1]	Residual Isotope	E_x (keV)	E_γ (keV)	Relative Intensity[4]	Error[4]
2346[3]	207	0	9719	216	55
1781	207	570	9719	1000	114
	206	0	8512		
1632	206	1340	9719	753	120
	205	0	9719		
	205	2	9719		
1513[2]	207	0	8884	255	74
	206	1460	9719		
1451	207	898	9719	535	70
1364	205	263	9719	284	46
1141[2]	207	0	8512	200	38
1114[2]	207	0	8484	203	40
1054[2]	205	576	9719	78	28
967[2]	206	1998	9719	46	17
	206	1165	8884		
	206	803	8512		
	206	0	7724		
940[2]	207	570	8884	112	38
	206	803	8484		
	205	703	9719		
867	205	761	9719	167	40
796	206	1340	8884	349	50
	205	0	8884		
	205	2	8884		
618	207	898	8884	1246	100
	206	0	7377		
	206	0	7363		
	205	1014	9719		
581[2]	207	570	8512	247	66
	207	0	7939		
	206	2384	9719		
	206	2391	9719		
	206	1165	8484		
	205	1044	9719		
538	207	570	8484	358	60
	206	2428	9719		
	205	263	8884		
392[2]	206	1340	8484	180	36
	206	803	7939		
	205	0	8484		
	205	2	8484		
352[2]	207	0	7724	79	48
	206	1784	8884		
	206	0	7100		
324[2]	206	2648	9719	77	58
	206	2659	9719		
255	207	898	8512	266	62
225[2]	207	898	8484	116	34
	205	576	8884		
182[3]	206	803	7724	73	32
	205	263	8512		

1. Error ± 5 keV except as noted.
2. Error ± 7 keV.
3. Error ± 10 keV.
4. Arbitrary units.

TABLE 6.10

Observed Neutron Groups from Thallium using a Nickel Source

(Possible components)

E_n (keV)[1]	Residual Isotope	E_x (keV)	E_γ (keV)	Relative Intensity[4]	Error[4]
1446	204	0	8999	1000	19
1303	204	141	8999	1068	16
1146	204	300	8999	1048	111
1128	204	319	8999	1065	100
1098	204	345	8999	393	31
	202	188	8999		
1018	204	422	8999	1006	23
	204	434	8999		
974	204	472	8999	1796	50
948	204	489	8999	1623	49
	202	315	8999		
910	204	536	8999	356	27
	202	351	8999		
842	204	141	8533	508	46
819	204	627	8999	1809	62
	202	0	8533		
774[2]	202	480	8999	221	31
	202	490	8999		
706	204	736	8999	526	29
	204	757	8999		
678	204	300	8533	1197	57
657	204	319	8533	618	55
630[2]	202	627	8999	264	32
602	204	389	8533	727	35
	202	188	8533		
567	204	900	8999	815	41
	204	422	8533		
	204	434	8533		
540	202	720	8999	605	43
511	204	472	8533	1083	49
482	204	960	8999	363	50
	202	315	8533		
437	204	1014	8999	596	61
	204	141	8120		
417[3]	204	573	8533	410	76
400	204	1052	8999	1539	94
	202	0	8120		
367[2]	204	627	8533	370	74
	204	616	8533		
350[2]	204	1118	8999	496	68
	204	1120	8999		
325	202	950	8999	876	55
	202	480	8533		
	202	490	8533		
269	204	0	7819	1084	38
251	204	1202	8999	933	39
	204	736	8533		
	204	319	8120		
221	204	757	8533	393	50
	204	345	8120		
204[2]	204	1252	8999	201	43
	204	389	8120		
	202	188	8120		
176	204	1280	8999	1835	48
	204	0	7724		
	202	1099	8999		
	202	627	8533		
154[2]	204	422	8120	476	41
	204	434	8120		
	204	141	7819		
96	204	1375	8999	1742	40
	204	900	8533		
	204	489	8120		
	202	720	8533		
	202	0	7819		
36	204	960	8533	1210	40
	204	536	8120		
	204	141	7724		
	202	351	8120		

1. Error ± 5 keV except as noted.
2. Error ± 7 keV.
3. Error ± 10 keV.
4. Arbitrary units.

TABLE 6.11

Observed Neutron Groups from Gold using a Nickel Source

(Possible components)

E_n (keV)[1]	E_x (keV)	E_γ (keV)	Relative Intensity[3]	Error[3]
914	0	8999	1000	20
878	36	8999	210	12
840[2]	75	8999	50	10
749	166	8999	973	23
716	199	8999	480	17
687	229	8999	295	18
659	256	8999	912	25
621	295	8999	841	30
593	323	8999	753	24
563	353	8999	435	24
536	380	8999	415	25
505	412	8999	657	30
452	465	8999	1167	142
	0	8533		
423	494	8999	492	45
	29	8533		
392[2]	525	8999	156	46
	60	8533		
369[2]	548	8999	283	50
	83	8533		
348[2]	569	8999	427	64
	104	8533		
285	633	8999	783	79
	168	8533		
252[2]	665	8999	144	53
	200	8533		
203	715	8999	278	51
	250	8533		
158	760	8999	94	18
	295	8533		
110	808	8999	382	31
	343	8533		
73	846	8999	23	7
	381	8533		
41	878	8999	268	50
	413	8533		
	0	8120		

1. Error is ± 5 keV except as noted.
2. Error is ± 10 keV.
3. Arbitrary units.

TABLE 6.12

Observed Neutron Groups from Tantalum using a Nickel Source

(Possible Components)

E_n (keV)[1]	E_x (keV)	E_γ (keV)	Relative[5] Intensity	Error[5]
1412[2]	0	8999	165	25
1375[2]	36	8999	203	28
1301	111	8999	1000	44
1260	152	8999	360	48
1231	181	8999	899	55
1185	227	8999	391	44
1101	312	8999	1132	91
1077[3]	336	8999	223	87
996	418	8999	656	55
967[3]	440	8999	373	55
938[2]	475	8999	377	55
	10	8533		
897[2]	517	8999	363	62
	52	8533		
868	546	8999	1932	85
	81	8533		
840	574	8999	895	80
	109	8533		
793[3]	622	8999	476	130
	157	8533		
773[3]	642	8999	1352	274
	177	8533		
757[2]	657	8999	1440	337
	192	8533		
730[4]	685	8999	389	173
	220	8533		
711[3]	704	8999	1297	159
	239	8533		
691	724	8999	1414	155
	259	8533		
645[3]	770	8999	598	212
	305	8533		
631	785	8999	2264	214
	320	8533		
591	825	8999	448	113
	360	8533		
532	884	8999	1195	108
	419	8533		
	5	8120		
511	905	8999	1538	215
	440	8533		
	26	8120		
497[3]	919	8999	748	240
	454	8533		
	40	8120		

TABLE 6.12

(con't'd)

Observed Neutron Groups from Tantalum using a Nickel Source

(Possible Components)

E_n (keV)[1.]	E_x (keV)	E_γ (keV)	Relative[5.] Intensity	Error[5.]
428	988	8999	1366	89
	523	8533		
	109	8120		
403	1014	8999	1579	98
	549	8533		
	135	8120		
379	1037	8999	792	94
	572	8533		
	158	8120		
312	1105	8999	1511	123
	640	8533		
	226	8120		
295	1122	8999	1167	119
	657	8533		
	243	8120		
229	1189	8999	937	73
	724	8533		
	310	8120		
	9	7819		
205	1213	8999	452	87
	748	8533		
	334	8120		
	33	7819		
168	1250	8999	591	47
	785	8533		
	371	8120		
	70	7819		
129	1289	8999	757	71
	824	8533		
	410	8120		
	181	7819		
	14	7724		
112[2.]	1306	8999	238	64
	841	8533		
	427	8120		
	126	7819		
	31	7724		

1. Error ± 5 keV except as noted.
2. Error ± 7 keV.
3. Error ± 10 keV.
4. Error ± 15 keV.
5. Arbitrary units.

TABLE 6.13

The Low Lying States of ^{208}Bi Populated by a Nickel Source

	E_γ (keV)	E_x [1] (keV)	J^π [1]	Relative Intensity per unit photon flux [2]	σ_{Yn} [3] (mb)	Reduced Width [4]
	8999	0	5^+	100 (2)	3.8(9)	121
		63	4^+	68 (2)	2.6(7)	80
		511	6^+	58 (3)	2.2(6)	89
		603	4^+	29 (1)	1.1(3)	48
		632	$(3^+,5^+)$	31 (3)	1.2(3)	55
		652	7^+	18 (3)	.7(2)	80
		889	5^+	43 (1)	1.6(4)	85
		927	2^+	16 (1)	.6(1)	143
		939	3^+	54 (2)	2.1(5)	113
		961	4^+	13 (1)	.5(1)	25
		1036	4^+	14 (1)	.6(1)	26
	8533	0	5^+	34 (2)	1.3(3)	54
		63	4^+	17 (7)	.7(3)	27
		889	5^+	14 (3)	.5(2)	31
		961	4^+	10 (3)	.4(2)	22
	7819	0	5^+	38 (5)	1.4(4)	84
		63	4^+	152 (6)	5.7(14)	298
	7724	0	5^+	89 (7)	3.4(9)	203
	7534	0	5^+	60 (22)	2.2(9)	163
			Unresolved Groups			
A	8999	1071		22 (1)	.9(2)	
	8533	603			2.0(5)	
B	8999	1097		26 (1)	1.0(2)	
	8533	632			2.3(6)	

1. Reference (Cr73).
2. Arbitrary units. Unresolved groups are normalized as if due to the 8999 keV photons. Numbers in brackets represent the uncertainty in the value.
3. Numbers in brackets represent the uncertainty times ten. The cross section is given for each possible component of an unresolved group as if that component solely constituted the group.
4. Arbitrary units. See 6.3.4.

TABLE 6.14

The Low Lying States of ^{208}Bi Populated by a Chromium Source

	E_γ (keV)	E_x [1] (keV)	J^π [1]	Relative Intensity per unit photon flux [2]	$\sigma_{\gamma n}$ [3] (mb)	Reduced Width [4]
	9719	0	5^+	39 (2)	5.0(13)	33
		63	4^+	63 (2)	8.1(22)	53
		511	6^+	37 (2)	4.7(13)	38
		632	$(3^+,5^+)$	102 (3)	13.1(36)	116
		939	3^+	30 (5)	3.8(12)	-
		961	4^+			
		1036	4^+	34 (3)	4.4(13)	47
		1097	6^+	49 (4)	6.3(18)	70
		1467	-	72 (2)	9.2(25)	130
		1534	-	6 (2)	0.8(35)	11
		1565	-	11 (2)	1.4(5)	21
		1699	5^-	38 (4)	4.9(14)	76
	8884	0	5^+	39 (2)	4.8(13)	50
		511	4^+	28 (1)	3.4(9)	1
		603	4^+	36 (1)	4.4(12)	60
		927	2^+	31 (2)	3.8(11)	425
		1071	3^+	16 (1)	2.0(6)	35
	8512	0	5^+	76 (3)	9.3(26)	122
		63	4^+	108 (5)	13.2(37)	170
		889	5^+	38 (3)	4.7(13)	85
	8484	0	5^+	61 (5)	7.5(21)	100
		63	4^+	40 (5)	4.9(15)	65
	7724	0	5^+	60 (4)	7.2(20)	134
			Unresolved Groups			
A	9719	889	5^+	235 (7)	30.1(83)	
	8884	63	4^+		11.4(31)	
B	9719	1721	$(6^-,7^-)$	349 (5)	44.7(123)	
		1734	-		44.7(123)	
	8884	889	5^+		16.9(46)	
	8512	511	6^+		65.9(180)	
C	8884	939	3^+	233 (7)	11.3(31)	
	7939	0	5^+		22.7(62)	
D	9719	1806	-	135 (8)	17.3(48)	
	8884	961	4^+		6.5(18)	
	8512	603	4^+		25.1(70)	
E	9719	1844	4^-	150 (3)	19.2(53)	
	8512	631	$(3^+,5^+)$		27.9(77)	
	8484	603	4^+		43.2(119)	
	7939	63	4^+		14.6(40)	
F	8884	1036	4^+	88 (3)	4.3(119)	
	8512	652	7^+		16.4(45)	
	8484	631	$(3^+,5^+)$		25.3(70)	
G	9719	1925	3^-	16 (3)	2.1(7)	
	8884	1097	6^+		0.8(3)	

1. Reference (Cr73).
2. Arbitrary units. Unresolved groups are normalized as if due to the 9719 keV photons. Numbers in brackets represent the uncertainty in the value.
3. Numbers in brackets represent the uncertainty times ten. The cross section is given for each possible component of an unresolved group as if that component solely constituted the group.
4. Arbitrary units. See section 6.3.4.

TABLE 6.15

The Low Lying States of ^{207}Pb, ^{206}Pb and ^{205}Pb Populated using a Nickel Source

	Residual Isotope	E_γ (keV)	E_x [1] (keV)	J^π [1]	Relative Intensity per unit Photon Flux per atom [2] Enriched Pb	Natural Pb	Accepted	$\sigma_{\gamma n}$ [3] (mb)	Reduced width [4]
	207	8999	0	$1/2^-$	100(4)	100(2)	100(2)	3.4(8)	112
			570	$5/2^-$	47(4)	52(2)	52(2)	1.7(4)	154
			898	$3/2^-$	109(4)	107(3)	107(3)	3.6(10)	196
		8533	0	$1/2^-$	108(8)	98(3)	98(3)	3.2(8)	146
			570	$5/2^-$	41(12)	57(5)	57(5)	2.0(6)	316
			898	$3/2^-$	74(20)	36(24)	36(24)	1.3(3)	79
	206	8999	0	0^+	-	12(2)	12(12)	0.4(1)	10
			803	2^+	799(170)	545(7)	545(7)	18.3(46)	674
			1165	0^+	-	195(5)	195(5)	6.6(17)	315
			1460	2^+	40(16)	92(4)	92(4)	3.1(8)	170
			1684	4^+	-	54(6)	54(6)	1.8(6)	580
			1704	1^+	332(220)	140(7)	140(7)	4.8(13)	274
			1784	2^+	-	100(5)	100(5)	3.4(8)	216
			1998	4^+	-	49(23)	49(23)	1.7(8)	3065
		8533	1165	0^+	-	138(11)	138(11)	4.6(13)	289
			1704	1^+	-	704(9)	704(9)	23.7(59)	2594
	205	8999	263	$3/2^-$	109(16)	140(5)	140(5)	4.8(13)	267
					Unresolved Groups				
A	206	8533	803	2^+	-	42(2)	42(2)	7.6(20)	-
	206	7724	0	0^+				21.1(53)	
B	206	8999	1340	3^+	13(2)	87(2)	129(25)	4.3(14)	553
	205	8999	0	$5/2^-$			69(14)	2.4(7)	-
	205	8999	2	$1/2^-$					
C	207	7819	0	$1/2^-$	53(4)	63(2)	63(2)	9.8(25)	-
	206	8533	1340	3^+				11.3(28)	-
	205	8533	0	$5/2^-$				10.8(27)	-
	205	8533	2	$1/2^-$				10.8(27)	-

TABLE 6.15
(cont'd)

The Low Lying States of ^{207}Pb, ^{206}Pb and ^{205}Pb Populated using a Nickel Source

	Residual Isotope	E_γ (keV)	E_x [1] (keV)	J^π [1]	Relative Intensity per unit Photon Flux per atom [2]			$\sigma_{\gamma n}$ [3] (mb)	Reduced width [4]
					Enriched Pb	Natural Pb	Accepted Pb		
D	206	8533	1460	2^+	14(3)	39(2)	9(2)	0.3(1)	18
	205	8999	576	$3/2^-$			83(18)	2.8(10)	153
E	207	8120	570	$5/2^-$	10(3)	43(2)	43(2)	18.8(48)	-
	207	7555	0	$1/2^-$				24.1(60)	-
	206	7724	803	2^+				21.7(55)	-
	205	8533	263	$3/2^-$				7.4(13)	-
F	206	8999	2150	(2^+)	-	44(2)	44(2)	3.4(8)	-
	206	8533	1684	4^+				7.7(20)	-
	205	8999	803	2^+				3.2(8)	-

UNASSIGNED GROUPS

Neutron Energy (keV)	Intensity		
1784	17(6)	15(1)	-
1360	21(2)	15(1)	-

1. References for level energies, spins and parities are: ^{207}Pb - (Sc71), ^{206}Pb - (Se72), ^{205}Pb-(Ha72)
2. Arbitrary units. Unresolved groups are normalized as if due to the 8999 keV photons. Groups which have been resolved by comparison with the enriched lead data are included in the unresolved group section. Accepted intensities for resolved groups are those obtained using natural lead since the statistics are much better. Accepted values for unresolved groups are either those of the natural lead data if the relative component intensities could not be deduced or the relative component intensities obtained by comparison of the enriched and natural lead data. Numbers in brackets are the uncertainty in the value.
3. Calculated from the accepted values of the intensities (see footnote No. 2) Numbers in brackets are the uncertainty times ten. For groups in which the relative component intensities could not be obtained the cross section is given for each component as if it alone constituted the group.
4. Arbitrary units. See section 6.3.4.

TABLE 6.16

The Low Lying States of ^{207}Pb, ^{206}Pb, and ^{205}Pb using a Chromium Source

	Residual Isotope	E_γ (keV)	E_x (keV)	J^π	Relative Intensity per unit Photon flux per atom			$\sigma_{\gamma n}$ (mb)	Reduced Width
					Enriched Pb	Natural Pb	Accepted		
	207	9719	0	$1/2^-$	22(6)	12(1)	12(1)	1.5(4)	10
			898	$3/2^-$	54(7)	46(7)	46(7)	5.8(18)	57
		8512	0	$1/2^-$	31(6)	35(6)	35(6)	4.4(14)	51
			898	$3/2^-$	41(9)	47(11)	47(11)	5.9(21)	103
		8484	0	$1/2^-$	47(9)	40(9)	40(9)	5.0(18)	60
	206	9719	1684	4^+	-	43(12)	43(12)	5.4(21)	98
			1704	1^+	-	102(8)	102(8)	12.8(36)	142
			2648	3^-	654(493)	-	0	0	0
		8884	803	2^+	-	86(5)	86(5)	10.6(29)	114
			1684	4^+	-	15(4)	15(4)	1.8(7)	247
			1704	1^+	-	27(4)	27(4)	3.3(10)	60
	205	9719	263	$3/2^-$	172(28)	127(15)	127(15)	15.9(47)	165
			576	$3/2^-$	47(17)	46(7)	46(7)	5.8(18)	69
			761	$5/2^-$	101(24)	151(12)	151(12)	18.9(54)	480
					UNRESOLVED GROUPS				
A	206	9719	803	2^+	-	118(7)	118(7)	14.8(41)	-
	206	8884	0	0^+				5.7(16)	-
B	207	9719	570	$5/2^-$	100(5)	100(5)	100(5)	12.5(35)	142
	206	8512	0	0^+			~ 0	~ 0	0
C	206	9719	1340	3^+	75(1)	210(9)	12(1)	1.5(4)	19
	205	9719	0	$5/2^-$			455(46)	56.9(166)	-
	205	9719	2	$1/2^-$					
D	207	8884	0	$1/2^-$	26(7)	43(6)	10(2)	1.2(4)	12
	206	9719	1460	2^+			42(8)	5.3(18)	50

TABLE 6.16
(cont'd)

The Low Lying States of ^{207}Pb, ^{206}Pb, and ^{205}Pb using a Chromium Source

	Residual Isotope	E_γ l. (keV)	E_x (keV)	J^π	Relative Intensity per unit Photon flux per atom			$\sigma_{\gamma n}$ (mb)	Reduced Width
					Enriched Pb	Natural Pb	Accepted Pb		
E	206	9719	1784	2^+	-	220(16)	220(16)	27.5(78)	-
	206	7939	0	0^+				21.7(61)	-
F	206	9719	1998	4^+	391(144)	231(12)	231(12)	28.8(80)	
	206	8884	1165	0^+				11.12(31)	-
	206	8512	803	2^+				43.3(120)	-
	206	7724	0	0^+				52.2(145)	-
G	207	8884	570	$5/2^-$	11(4)	34(4)	34(4)	4.3(13)	-
	206	8484	803	2^+				22.6(67)	-
	205	9719	703	$7/2^-$				9.4(28)	-
H	206	8884	1340	3^+	35(5)	232(8)	134(20)	16.5(51)	734
	205	8884	0	$5/2^-$			74(11)	9.1(28)	-
	205	8884	2	$1/2^-$					
I	206	9719	2314	0^+	-	143(19)	143(19)	17.9(54)	-
	206	8884	1460	2^+				6.9(21)	-
J	207	8884	898	$3/2^-$	125(10)	200(20)	48(6)	5.9(18)	92
	206	7377	0	0^+			179(22)	30.9(93)	-
	206	7363	0	0^+					
K	207	8512	570	$5/2^-$	25(7)	74(10)	74(10)	13.9(42)	-
	207	7939	0	$1/2^-$				7.3(22)	-
	206	9719	2391	(4^+)				21.4(65)	-
	206	8484	1165	0^+				49.3(150)	-
	205	9719	1044	$7/2^-$				20.5(63)	-
L	207	8484	570	$5/2^-$	36(6)	105(11)	105(11)	30.2(88)	-
	206	9719	2428	2^+				30.3(88)	-
	205	8884	263	$3/2^-$				11.3(33)	

TABLE 6.16
(cont'd)

The Low Lying States of ^{207}Pb, ^{206}Pb, and ^{205}Pb using a Chromium Source

	Residual Isotope	E_γ (keV)	E_x (keV)	J^π	Relative Intensity per unit Photon flux per atom			$\sigma_{\gamma n}$ (mb)	Reduced Width
					Enriched Pb	Natural Pb	Accepted		
M	206	8484	1340	3^+	18(4)	71(5)	54(11)	15.5(52)	-
	206	7939	803	2^+				5.3(18)	-
	205	8484	0	$5/2^-$			247(52)	30.4(105)	-
	205	8484	2	$1/2^-$					-
N	207	7724	0	$1/2^-$	8(5)	67(4)	12(4)	1.5(6)	25
	206	8884	1784	2^+			141(47)	6.8(29)	-
	206	7100	0	0^+				4.14(179)	-
O	207	8484	898	$3/2^-$	12(3)	-	12(3)	3.5(13)	-
	205	8884	576	$3/2^-$				3.5(13)	-
P	206	7724	803	2^+	7(3)	76(10)	260(114)	31.6(163)	548
	205	8512	263	$3/2^-$			53(23)	6.5(33)	112
Q	206	8512	1684	4^+	-	44(15)	44(15)	5.4(24)	33440
	205	8884	703	$7/2^-$			~ 0	~ 0	0

UNASSIGNED GROUP

Neutron Energy (keV)	Intensity
743	37(5)

1. Same footnotes apply as for Table 6.15 except that normalization of unresolved groups is to the 9719 keV photon.

TABLE 6.17

The Low Lying States of ^{204}Tl and ^{202}Tl observed using a Nickel Source

Residual Isotope	E_γ (keV)	E_x [1] (keV)	J^π [1]	Relative Intensity per unit Photon flux per atom [2]	$\sigma_{\gamma n}$ (mb) [3]	Reduced Width [4]
204	8999	0	2^-	100(2)	1.4(4)	125
		141	-	107(2)	1.5(4)	146
		300	-	105(11)	1.5(4)	159
		319	-	107(10)	1.5(4)	160
		422	(4^-)	101(2)	1.4(4)	-
		434	-			
		472	-	180(5)	2.5(6)	316
		736	-	53(3)	.7(2)	-
		757	-			
		1014	-	60(6)	.8(2)	116
		1052	-	154(9)	2.2(6)	312
		1118	(7^+)	50(7)	.7(2)	52178
		1120	(7^+)			
		1252	-	20(4)	.3(1)	40
	8533	141	-	118(12)	1.6(4)	212
		300	-	276(14)	3.8(9)	550
		319	-	142(14)	1.9(5)	290
		472	-	249(12)	3.4(9)	508
		573	-	94(18)	1.3(4)	186
		616				
		627	-	85(16)	1.2(4)	181
		757	-	90(12)	1.2(3)	172
	7819	0	2^-	500(19)	6.9(17)	
202	8999	480	-	53(7)	.7(2)	-
		490	4^-			
		627	-	62(7)	.8(2)	121
		720	-	146(10)	1.9(5)	284
	8533	480	-	485(33)	6.6(17)	-
		490	4^-			
			Unresolved Groups			
A 204	8999	345	-	39(3)	.5(1)	
202	8999	188	-		1.2(3)	
B 204	8999	489	-	162(5)	2.3(6)	
202	8999	315	-		5.1(13)	
C 204	8999	536	-	36(3)	.5(1)	
202	8999	351	-		1.1(3)	
D 204	8999	627	-	181(6)	2.5(6)	
202	8533	0	2^-		13.6(34)	

TABLE 6.17
(Cont'd)

The Low Lying States of ^{204}Tl and ^{202}Tl observed using a Nickel Source

Residual Isotope	E_γ (keV)	E_x[1] (keV)	J^π[1]	Relative Intensity per unit Photon flux per atom[2]	$\sigma_{\gamma n}$[3] (mb)	Reduced Width[4]
E 204	8533	389	-	73(4)	2.3(6)	
202	8533	188	-		5.5(14)	
F 204	8999	900	-	82(4)	1.1(3)	
	8533	422	(4^-)		2.6(7)	
	8533	434	-		2.6(7)	
G 204	8999	960	-	36(5)	.5(1)	
202	8533	315	-		2.7(8)	
H 204	8999	1202	-	93(4)	1.3(3)	
	8533	736	-		2.9(7)	
I 204	8999	1280	-	184(5)	2.6(7)	
	7724	0	2^-		16.7(42)	
202	8533	627	-		13.8(35)	
J 204	8120	422	4^-	48(4)	8.6(23)	
	8120	434	-		8.6(23)	
	7819	141	-		3.1(8)	
K 204	8999	1375	-	174(4)	2.4(6)	
202	8533	720	-		13.1(32)	
	7819	0	2^-		26.8(67)	
L 204	8120	536	-	121(4)	21.7(54)	
	7724	141	-		11.0(28)	
202	8120	351	-		51.8(130)	

1. Reference (Ma71, Au71, Fu73).

2. Arbitrary units. Unresolved groups are normalized as if due to the 8999 keV photons. Numbers in brackets represent the uncertainty of the value.

3. Numbers in brackets represent the uncertainty in the value times ten. The cross section is given for each possible component of an unresolved group as if that component solely constituted the group.

4. Arbitrary units. See section 6.3.4.

TABLE 6.18

The Low Lying States of ^{196}Au Observed using a Nickel Source

E_γ (keV)	E_x [1] (keV)	J^π [2]	Relative Intensity [3]	$\sigma_{\gamma n}$ [4] (mb)	Reduced Width [5]
8999	0	2^-	100(2)	1.9(5)	182
	36	-	21(1)	.4(1)	39
	75	5^+?	5(1)	.1(0)	10
	166	-	97(2)	1.8(4)	197
	199	-	48(2)	.9(2)	95
	229	7^+?	30(2)	.6(1)	65
	256	-	91(2)	1.7(4)	191
	295	-	84(3)	1.6(4)	166
	323	-	75(2)	1.4(4)	153
	353	-	43(2)	.8(2)	91
	380	6^+?	42(3)	.8(2)	88
	412	$6^+,8^+$?	66(3)	1.3(3)	147
	(525)	-	16(5)	0.3(1)	33
	(569)	-	43(6)	0.8(2)	84
8533	(0)	2^-	117(14)	5.1(14)	223
	(36)	-	49(4)	2.1(4)	97
	(75)	5^+?	28(5)	1.1(4)	53
	(166)	-	78(8)	3.4(10)	170
	(199)	-	14(5)	0.6(2)	32
	(256)	-	28(5)	1.1(4)	57
	(295)	-	9(2)	0.4(2)	21
	(380)	6^+?	2(1)	0.1(0)	5
	(412)	$6^+,8^+$?	27(5)	1.1(4)	57
		Ambiguous Groups			
8999	808	-	38(3)	0.7(2)	
8533	353	-		1.7(4)	

1. Level energies are determined by using the highest energy neutron group (assumed to be the ground state group due to the 8999 keV photon) and equation 6.26. Bracketed level energies are suggested assignments as described in the text and may have contributions from other energy photons and residual excitation energies.
2. Reference Sc72. Spins and parities with question marks would correspond to f-wave neutron emission or higher. Due to the low transmission coefficients, these levels are probably not the same as those of the reference. See text.
3. Arbitrary units. Ambiguous groups are normalized as if due to the 8999 keV photons. Numbers in brackets represent the uncertainty in the value.
4. Numbers in brackets represent the uncertainty in the value times ten. The cross section is given for each possible component of an ambiguous group as if that component solely constituted the group.
5. Arbitrary units. See section 6.3.4.

TABLE 6.19

The Low Lying States of ^{180}Ta Observed using a Nickel Source

E_γ (keV)	E_x [1] (keV)	J^π [2]	Relative Intensity [3]	$\sigma_{\gamma n}$ [4] (mb)	Reduced Width [5]
8999	0	(8^+)	17(3)	0.1(0)	27
	36	1^+	20(3)	0.1(0)	272
	111	-	100(4)	0.5(1)	156
	152	-	36(5)	0.2(0)	58
	181	-	90(5)	0.4(1)	147
	227	$1^{(-)}$	39(4)	0.2(0)	52
	312	-	113(9)	0.5(1)	200
	336	-	22(9)	0.1(0)	40
	418	-	66(6)	0.3(1)	125
	440	-	37(6)	0.2(0)	72
	(517)	-	36(6)	0.2(0)	72
	(546)	-	193(9)	0.9(2)	400
	(657)	-	144(34)	0.7(2)	321
	(704)	-	130(16)	0.6(2)	283
	(724)	-	141(16)	0.7(2)	314
	(825)	-	45(11)	0.2(1)	103
	(919)	-	75(24)	0.4(1)	173
	(1105)	-	151(12)	0.7(2)	325
	(1306)	-	24(6)	0.1(0)	68
8533	(0)	(8^+)	38(6)	0.4(1)	45
	(152)	-	48(13)	0.5(2)	103
	(227)	$1^{(-)}$	39(17)	0.4(2)	66
	(418)	-	120(11)	1.3(3)	265
	(440)	-	154(22)	1.7(5)	348
	(517)	-	137(9)	1.5(4)	286
	(546)	-	158(10)	1.7(4)	341
	(574)	-	79(9)	0.9(2)	177
	(657)	-	117(12)	1.3(4)	260
	(785)	-	59(5)	0.6(2)	135
7819	(36)	1^+	45(9)	1.0(3)	283
		Ambiguous Groups			
8999	574	-	90(8)	0.4(1)	
8533	111	-		1.0(3)	
8999	642	-	135(27)	0.6(2)	
8533	181	-		1.5(5)	
8999	770	-	60(21)	0.3(1)	
8533	305	-		0.7(3)	
8999	785	-	226(21)	1.1(3)	
8533	320	-		2.4(7)	

TABLE 6.19

The Low Lying States of ^{180}Ta Observed using a Nickel Source

E_γ (keV)	E_x [1] (keV)	J^π [2]	Relative Intensity [3]	$\sigma_{\gamma n}$ [4] (mb)	Reduced Width [5]
E 8533	724	-	94(7)	1.0(3)	
7819	0	(8^+)		2.1(6)	
F 8999	1250	-	45(9)	0.2(1)	
8533	785	-		0.5(2)	
G 8533	824	-	76(7)	0.8(2)	
7819	181	-		1.7(4)	

1. Level energies are determined by using the highest energy neutron group (assumed to be the ground state group due to the 8999 keV photon) and equation 6.26. Bracketed level energies are suggested assignments as described in the text and may have contributions from photons of other energies and other residual excitation levels.

2. Reference Gr75 and Le68. Bracketed spins and parities are uncertain.

3. Arbitrary units. Ambiguous groups are normalized as if due to the 8999 keV photons. Numbers in brackets represent the uncertainty in the value.

4. Numbers in brackets represent the uncertainty in the value times ten. The cross section is given for each possible component of an ambiguous group as if that component solely constituted the group.

5. Arbitrary units. See section 6.3.4.

Table 6.20

Photoneutron Cross Sections [1]

Photon Energy (keV)

Isotope	7100		7370		7534		7555		7724		7819		7939		8120		8484		8512		8533		8884		8999		9719	
^{209}Bi	-	-	-	-	2.2[4]	2.2[4]	-	-	5.3	5.3[2]	7.2	7.2	0	37.3	-	-	12.4	80.9	27.2	162.5	2.8	7.1	18.4	69.6	17.0	18.8	61.7	175.1
^{208}Pb	-	-	-	-	-	-	0	24.1[6]	0	1.5	0	9.8	0	7.3	0	18.8[6]	5.0	38.7	10.3	24.2	6.5	6.5	7.1	11.4	(36±12) 8.7	8.7	19.8	19.8
^{207}Pb	0	41.4	30.9	30.9[5]	-	-	-	-	0	42.8	-	-	0	27.0	-	-	0	87.4	5.4	48.7	28.3	55.2	32.2	62.8	(23±11) 40.1	47.8	25.0	165.7
^{206}Pb	-	-	-	-	-	-	-	-	-	-	-	-	-	-	-	-	30.4	30.4	6.5	6.5	0	18.2	9.1	23.9	4.8	13.2	97.5	127.4
^{205}Tl	-	-	-	-	-	-	-	-	0	27.7	6.9	10.0	-	-	0	38.9[6]	-	-	-	-	14.4	22.2	-	-	(< 34) 14.5	28.2	-	-
^{203}Tl	-	-	-	-	-	-	-	-	-	-	0	26.8	-	-	0	51.8[6]	-	-	-	-	6.6	55.3	-	-	3.4	10.8	-	-
^{197}Au	-	-	-	-	-	-	-	-	-	-	-	-	-	-	-	-	-	-	-	-	15.0	16.7[3]	-	-	14.4	15.5[3]	-	-
^{181}Ta	-	-	-	-	-	-	-	-	-	-	-	-	-	-	-	-	-	-	-	-	10.3	18.3[3]	-	-	(44±3) 7.1	9.7[3]	-	-
																									(45±3)			

1. Left hand number for each photon energy is the lower bound to the cross section in millibarns as explained in section 6.3. Right hand number is the upper bound in millibarns. Uncertainty is 25% for data obtained with the nickel source and 27% for data obtained using the chromium source except as noted. Numbers in brackets are from the experiments of Donahue et al. (We61, Gr64, Hu67).
2. Average of data obtained using chromium and nickel sources.
3. Dependent on group assignments. See section 6.3.
4. Uncertainty is 40%.
5. Sum of 7363 and 7377 keV photons.
6. Estimates are not very significant since photon intensities are very weak and only well isolated groups can be observed.

TABLE 6.21

Fore-Aft Asymmetry in Lead at $\bar{0} = 38°$

E_γ	E_x	J_f^π	$A \pm \sigma_A$		$\alpha \pm \sigma_\alpha$	
			$^{208}Pb(\gamma,n)^{207}Pb$		$J_i^\pi = 0^+$	
9719	898	$3/2^-$	.66	.05	-[2]	-[2]
8999	0	$1/2^-$	.293	.008	.025	.005
	570	$5/2^-$	.122	.005	.055	.005
	898	$3/2^-$	.020	.001	.0005	.0001
					$<\alpha> = .043$[1]	.003[1]
8533	0	$1/2^-$	-.49	.01	.11	.01
	898	$3/2^-$	.27	.02	.115	$+.015$ $-.025$
					$<\alpha> = .111$[1]	.008[1]
8512	898	$3/2^-$	.33	.04	.13	$+.09$ $-.04$
			$^{207}Pb(\gamma,n)^{206}Pb$		$J_i^\pi = 1/2^-$	
9719	1704	1^+	.11	.01	-	
8999	803	2^+	.25	.02	-	
	1165	0^+	.184	.008	-	
	1460	2^+	.032	.002	-	
	1784	2^+	-.075	.004	-	
8884	1684	4^+	.40	.06	-	
	1704	1^+	.12	.03	-	
			$^{206}Pb(\gamma,n)^{205}Pb$		$J_i^\pi = 0^+$	
9719	576	$3/2^-$	.43	.09	.30	-[3]
	761	$5/2^-$	.22	.01	.15	$\pm$ .18
					$<\alpha> = .16$[1]	.03[1]

1. Weighted average.
2. Curve of asymmetry versus alpha peaks at A = 0.58. Alpha is greater than 0.25 with a 95% confidence.
3. Upper range of uncertainty is greater than the maximum of the asymmetry versus alpha curve.

TABLE 7.1

Correlations of Reduced Widths and Spectroscopic Factors

Target	E_γ (keV)	(p,d) N	(p,d) r	(p,d) $(1-P_c(r,N))$	(d,t) N	(d,t) r	(d,t) $(1-P_c(r,N))$
^{209}Bi[1]	9719	6	.77	.93	8	.18	.34
	8889	9	-.27	.52	10	.10	.21
	8884	5	-.69	.80	5	-.72	.83
	8533	4	.79	.79	4	.39	.39
	8512	3	-.82	.61	3	-.99	.94
^{208}Pb[2]	9719	3	.16	.10	3	.26	.17
	8999	3	.98	.88	3	.99	.94
	8533	3	-.46	.30	3	-.36	.24
^{207}Pb[3]	9719	4	-.51	.51	3	-.85	.65
	8999	9	-.42	.74	7	-.28	.46
	8884	4	.65	.65	2	[5]	-
	8533	3	.41	.27	3	.06	.04
^{206}Pb[4]	9719	3	-.29	.19	3	-.29	.19

1. References: (p,d) - (Cr73) (d,t) - (Al71)
2. References: (p,d) - (Sc71) (d,t) - (Sc71)
3. References: (p,d) - (La74) (d,t) - (Ti68)
4. References: (p,d) - (Ya68) (d,t) - (Ti69)
5. Insufficient resolved lines exist to match the (d,t) data.

TABLE 7.2

Estimate of Number of Degrees of Freedom, ν[1] of Reduced Width Distributions

Target Isotope	Photon Energy (keV) 9719	8999	8884	8533
^{209}Bi	3.4(10)	6.6(11)	0.0(5)	3.2(4)
^{208}Pb	-	-	-	-
^{207}Pb	0.7(4)	0.5(9)	0.2(4)	-
^{206}Pb	-	-	-	-
^{205}Tℓ	-	4.4(8)	-	4.3(7)
^{203}Tℓ	-	-	-	-
^{197}Au	-	5.1(14)	-	1.6(9)
^{181}Ta	-	3.6(19)	-	6.6(9)

1. Numbers in brackets are the sample size. Sample spaces with 3 or less samples have been omitted. Uncertainties are based on the uncertainties of the reduced widths as discussed in section 6.3.4.

TABLE 7.3

Correlation of the Energy Dependence of Partial Cross Sections for Differing Excitation Energies with Respect to the Ground State

E_x (keV)	r	N	$(1-P_c(r,N))$
	$^{209}Bi(\gamma,n)$	^{208}Bi	
63	0.740	6	0.91
511	0.925	3	0.75
889	0.998	3	0.97
	$^{208}Pb(\gamma,n)$	^{207}Pb	
570	-0.997	3	0.95
898	-0.318	5	0.40

TABLE 7.4

Approximate Level Spacing of the Residual Nuclei

Nucleus	E_x<600 keV (keV)	E_x<1400 keV (keV)	Reference
^{208}Bi	140	95	Cr73
^{207}Pb	285	360	Sc71
^{206}Pb	800	325	Se72
^{205}Pb	140	130	Ha72
^{204}Tl	50	50	Ma71, Fu71
^{202}Tl	90	110	Au71
^{196}Au	40	-	present work
^{180}Ta	40	65	present work

BIBLIOGRAPHY

A&60 W.D. Allen, in Fast Neutron Physics, Part I (Interscience Publishers, New York, 1960.

A&71 W.P. Alford, J.P. Schiffer and J.J. Schwartz, Phys. Rev. C3 (1971) 860.

Ar73 B. Arad and G. Ben-David, Rev. Mod. Phys. 45 (1973) 230.

Au62 E.H. Auerbach and F.G.J. Perey, Brookhaven National Laboratory Report No. BNL-765, 1962.

Au70 R.L. Auble and M.N. Rao, Nucl. Data B3 (1970) 127.

Au71 R.L. Auble, Nucl. Data B5 (1971) 581.

Au75a R.L. Auble, Nucl. Data B14 (1975) 119.

Au75b R.L. Auble, Nucl. Data B16 (1975) 1.

Ba55 R. Batchelor, R. Aves and T.H.R. Skyrme, Rev. Sci. Instr. 26 (1955) 1037.

Ba60 R. Batchelor and G.C. Morrison, in Fast Neutron Physics, Part I (Interscience Publishers, New York, 1960) 413.

Ba64 R. Batchelor and K. Parker, AWRE 0-78/64, 1964.

Ba73 G.A. Bartholomew, E.D. Earle, A.J. Ferguson, J.W. Knowles and M.A. Lone, in Advances in Nuclear Physics, Vol 7 (Plenum, New York, 1973) 229.

Be66 K. Becker, Film Dosimetry (Focal Press, London, 1966).

Be69 P.R. Bevington, Data Reduction and Error Analysis for the Physical Sciences (McGraw-Hill, New York, 1969) 122.

Be71 D. Bellman, Atomkernenergie 17 (1971) 145.

Be75 B.L. Berman, Nucl. Data A15 (1975) 319.

Bo63 L.M. Bollinger, R.E. Coté, R.T. Carpenter and J.P. Marion, Phys. Rev. 132 (1963) 1640.

Bo69 C.D. Bowman, R.J. Baglan and B.L. Berman, Phys. Rev. Lett. 23 (1969) 796.

Bo70a L.M. Bollinger, in Experimental Neutron Resonance Spectroscopy (Academic Press, New York, 1970) 235.

Bo70b C.D. Bowman, R.J. Baglan, B.L. Berman and T.W. Phillips, Phys. Rev. Lett. 25 (1970) 1302.

Br55 D.M. Brink, Thesis, University of Oxford, 1955.

Bu72 F.R. Buskirk, H. Graf, R. Pitthan, H. Theissen, O. Titze and Th. Walcher, Phys. Rev. Lett. (1972) 194.

Ca53 K.M. Case, F. DeHoffmann and G. Placzek, Introduction to the Theory of Neutron Diffusion, Vol. 1 (Los Alamos Scientific Laboratory, Los Alamos, New Mexico, (1953).

Ca60 E.E. Carroll and W.E. Stephens, Phys. Rev. 118 (1960) 1256.

Ca71 R.W. Carr and J.E.E. Baglin, Nucl. Data A10 (1971) 143.

Co67 E.U. Condon and H. Odishaw, ed. Handbook of Physics, second edition (McGraw-Hill, New York, 1967) 14-3.

Cr73 G.M. Crawley, E. Kashy, W. Lanford and H.G. Blosser, Phys. Rev. C8 (1973) 2477.

Cu69a J.M. Cuttler, S. Shalev and Y. Dagan, Trans. Am. Nucl. Soc. 12 (1969) 63.

Cu69b J.M. Cuttler, S. Greenberger and S. Shalev, Nucl. Instr. and Meth. 75 (1969) 309.

Cu71a J.M. Cuttler, Ph.D. Thesis, Technion, 1971.

Cu71b J.M. Cuttler, Y. Dagan and S. Shalev, Trans. Am. Nucl. 14 (1971) 417.

Cu73 J.M. Cuttler, Private communication, 1973.

Da58 M. Danos, Nucl. Phys. 5 (1958) 23.

El73 C.E. Ellegaard and P.D. Barnes, Phys. Rev. C1 (1973) 742.

Em63 W.S. Emmerick, in Fast Neutron Physics, Part II (Interscience Publishers, New York, 1963) 1057.

En66 H.A. Enge, Introduction to Nuclear Physics (Addison-Wesley, Reading, Mass., 1966) 147.

Ev55 R.D. Evans, The Atomic Nucleus (McGraw-Hill, New York, 1955).

Fi70 F.W.K. Firk and E. Melkonian, in Experimental Neutron Spectroscopy (Academic Press, New York, 1970) 101.

Fr73 H. Franz, Private communication to J.M. Cuttler, 1973.

Fu60 E.G. Fuller and Evans Hayward, Proceedings of International Conference on Nuclear Structure (University of Toronto Press, Toronto, 1960) 941.

Fu62a E.G. Fuller and Evans Hayward, Nucl. Phys. 33 (1962) 431.

Fu62b E.G. Fuller and Evans Hayward, in Nuclear Reactions Vol.II (North-Holland, Amsterdam, 1962) 113.

Fu73 A. Fubini, R. Alberini and D. Lattanzi, Nuovo Cimento 18A (1973) 711.

Gi53 A.B. Gillespie, Signal, noise and resolution in nuclear counter amplifiers (Pergamon Press, London, 1953).

Gi60 J.H. Gibbons and H.W. Newson, in Fast Neutron Physics, Part I (Interscience Publishers, New York, 1960).

Go48 M. Goldhaber and E. Teller, Phys. Rev. 74 (1948) 1046.

Go66 M.D. Goldberg, S.F. Mughabghab, S.N. Purohit, B.A. Magurno and V.M. May, Neutron Cross Sections, Second edition, Supplement No. 2, BNL-325 (Brookhaven National Laboratories, Upton, New York, 1966).

Go72 N.B. Gove and A.H. Wapstra, Nucl. Data A11 (1972) 128.

Gr64 L. Green and D.J. Donahue, Phys. Rev. 135 (1964) 703.

Gr75 L.R. Greenwood, Nucl. Data B15 (1975) 559.

Ha47 A.O. Hanson and J.L. McKibben, Phys. Rev. 72 (1947) 673.

Ha65 Evans Hayward, in Nuclear Structure and Electromagnetic Interactions (Oliver and Boyd, Edinburgh, 1965) 141.

Ha72 J.H. Hamilton, V. Ananthakrishan, A.V. Ramayya, W.M. LaCasse, D.C. Camp, J.J. Pinajian, L.H. Kern and J.C. Manthuruthil, Phys. Rev. C6 (1972) 1265.

Ha74 Evans Hayward, Private communication.

He64 R.L. Heath, Scintillation Spectrometry, AEC (U.S.) Report TID-4500, Idaho, 1964.

Hi72 A.M. Hillas, Cosmic Rays (Pergamon Press, Toronto, 1972).

Hu53 G.S. Hurst and R.H. Ritchie, Rev. Sci. Instr. 24 (1953) 664.

Hu58 D.J. Hughes and R.B. Schwartz, Neutron Cross Sections, Second Edition, BNL-325 (Brookhaven National Laboratories, Upton, New York, 1958).

Hu67 R.R. Hurst and D.J. Donahue, Nucl. Phys. A91 (1967) 365.

Ja48 L. Janossy, Cosmic Rays (Oxford University Press, Oxford, 1948) 251.

Ja74 H.E. Jackson, Phys. Rev. C9 (1974) 1148.

Ke46 M.G. Kendall, The Advanced Theory of Statistics, Vol. II (Griffen Press, London, 1946) Chapter 17.

Ke77 T.J. Kennett, W.V. Prestwich and A. Robertson, submitted to Nucl. Instr. and Meth.

Ki68 C. Kittel, Introduction to Solid State Physics (Wiley Press, New York, 1968) 278.

Ki76 H.J. Kin, Nucl. Data B17 (1976) 485.

Kn66 J.W. Knowles and N.M. Ahmed, Atomic Energy of Canada Ltd. Report No. 2535, 1966.

La71 A.M. Lane, Ann. Phys. 63 (1971) 171.

La74 W.A. Lanford and G.M. Crawley, Phys. Rev. C9 (1974) 646.

Le60 J.S. Levinger, Nuclear Photodisintegration (Oxford University Press, Oxford, 1960)

Le68 C.M. Lederer, J.M. Hollander and I. Perlman, Table of the Isotopes, Sixth Edition (Wiley Press, New York, 1968).

Ly69 H. Lycklama, T.J. Kennett and L.B. Hughes, Can. J. Phys. 47 (1969) 666.

Ma62 A.V.H. Masket and W.C. Rodgers, United States Atomic Energy Commission (Dept. of Technical Information) Report No. TID-14975.

Ma71 M.J. Martin, Nucl. Data B5 (1971) 601.

Ma74 R.E. Maute, D.P. D'Amato and S.L. Blatt, Nucl. Data A13 (1974) 500.

Mc75 J.E. McFee, A.F.M. Ishaq, T.J. Kennett and W.V. Prestwich, Phys. Lett. 55B (1975) 369.

Mc76 J.E. McFee, W.V. Prestwich and T.J. Kennett, Phys. Rev. C13 (1976) 1864.

Mo71 R.A. Moyer, B.L. Cohen and R.C. Diehl, Phys. Rev. C2 (1971) 1898.

Ni70 L. Nichol, A.M. Lopez, A. Robertson, W.V. Prestwich and T.J. Kennett, Nucl. Instr. and Meth. 81 (1970) 263.

Ni74 P.W. Nicholson, Nuclear Electronics (Wiley Press, New York, 1974).

Pe58 A.S. Penfold and J.E. Leiss, Analysis of Photo Cross Sections (University of Illinois Press, Urbana, 1958).

Pi74 R. Pitthan, F.R. Buskirk, E.B. Dally, J.N. Dyer and X.K. Maruyama, Phys. Rev. Lett. 33 (1974) 849.

Po56 C.E. Porter and R.G. Thomas, Phys. Rev. 104 (1956) 483.

Pr62 M.A. Preston, Physics of the Nucleus (Addison-Wesley, Reading, Mass., 1962). Chapter 17.

Ra67 N.C. Rasmussen, Y. Hukai, T. Inouye and V.J. Orphan, Massachusetts Institute of Technology Report No. MITNE-85, 1967.

Ra70 M.N. Rao and J.R. Rapaport, Nucl. Data B3 (1970) 37.

Re60 K. Reibel and A.K. Mann, Phys. Rev. 118 (1960) 701.

Re65 F. Reif, Fundamentals of Statistical and Thermal Physics (McGraw-Hill, New York, 1965).

Ro49 B. Rossi and H. Staub, Ionization Chambers and Counters (McGraw-Hill, New York, 1949).

Ro67 R.R. Roy and B.P. Nigam, Nuclear Physics (Wiley Press, New York, 1967).

Ro74 A. Robertson, Ph.D. Thesis, McMaster University, 1974.

Ru75 P.A. Russo, P.A. Dickey, J.R. Calarco and P. Axel, in Proceedings of the Spring Meeting of the American Physical Society, Washington, 1975.

Sa74 G.R. Satchler, Physics Reports 14 (1974) 99.

Sc71 M.R. Schmorak and R.L. Auble, Nucl. Data B5 (1971) 207.

Sc72 M.R. Schmorak, Nucl. Data B7 (1972) 395.

Se72 K.K. Seth, Nucl. Data B7 (1972) 161.

Sh69 S. Shalev, Z. Fishelson and J.M. Cuttler, Nucl. Instr. and Meth. 71 (1969) 292.

Sh71 S. Shalev, Progress Report No. 2, TNSD-R/404, Dept. of Nuclear Science, Technion, Israel (1969) 14.

Sh72 S. Shalev, J.M. Cuttler amd Y. Dagan, Proc. Conf. on Nuclear Structure Study with Neutrons, Budapest, 1972.

Sp69 B.M. Spicer, in Advances in Nuclear Physics, Vol 2 (Plenum Press, New York, 1969) 1.

St50 H. Steinwedel, J.H.D. Jenson and P. Jenson, Phys. Rev. 79 (1950) 1019.

St70 E. Storm and H. Israel, Nucl. Data A7 (1970) 566.

Ti68 R. Tickle and J. Bardwick, Phys. Rev. 166 (1968) 1167.

Ti69 R. Tickle and J. Bardwick, Phys. Rev. 178 (1969) 2006.

To72 R.E. Toohey and H.E. Jackson, Phys. Rev. C6 (1972) 1440.

Ve70a H. Verheul, Nucl. Data B3 (1970) 161.

Ve70b A. Veyssiere, H. Beil, R. Bergere, P. Carlos and A. Lepretre, Nucl. Phys. A159 (1970) 561.

Wa71 A.H. Wapstra and N.B. Gove, Nucl. Data A9 (1971) 267.

We61 R.E. Welsh and D.J. Donahue, Phys. Rev. 121 (1961) 880.

Wi50 D.H. Wilkinson, Ionization Chambers and Counters (University Press, Cambridge, 1950).

Wo58 M.M. Wolff and W.E. Stephens, Phys. Rev. 112 (1958) 890.

Ya68 K. Yagi, T. Ishimatsu, Y. Ishizaki and Y. Saji, Nucl. Phys. A121 (1968) 161.